Processes Affecting the Cycling of Iron in the Atlantic Ocean

A thesis submitted for the degree of Doctor of Philosophy of
The University of Liverpool

Nicholas Rogan

School of Ocean and Earth Sciences, The University of Liverpool
Liverpool, UK

February 2014

Declaration

This thesis is an account of research undertaken between September 2009 and February 2014 at the School of Environmental Sciences, University of Liverpool, Liverpool, United Kingdom. Except where acknowledged in the customary manner, the material presented in this thesis is, to the best of my knowledge, original and has not been submitted in whole or part for a degree in any university.

Nicholas Rogan

February 2014

Contents

Declaration i

Abstract ix

Acknowledgments xi

1 Why is Iron Important? 13

1.1 Introduction 13

1.1.1 The importance of iron to biological communities 14

1.1.2 Iron processes 15

1.1.3 Uncertainty in the iron system 16

1.2 Aim of the thesis 16

2 Global Iron Distributions 19

2.1 Introduction 19

2.2 Iron sources 20

2.2.1 Aeolian supply of dust 20

2.2.2 Hydrothermal vent sources of iron 21

2.2.3 Continental Shelf Sediment Supply 24

2.2.4 Iron Source Summary 27

2.3 A global dataset 28

2.3.1 Methods 29

2.3.2 Atlantic Ocean 32

2.3.3 Pacific Ocean 36

2.4 The Sub-Polar North Atlantic 42

2.4.1 Introduction 42

2.4.2 Water masses of the region 43

2.4.3 Nutrient distributions 47

2.4.4 Phosphate derivatives 54

2.4.5 Micronutrients in the sub-polar North Atlantic 62

2.4.6 The importance of physical processes and biogeochemical regimes in the sub polar North Atlantic . 67

2.5 The Tropical Atlantic 70

2.5.1 Physics of the tropical Atlantic 70

2.5.2 Macronutrient distributions and hydrography 74

2.5.3 Iron in the tropical Atlantic 79

2.5.4 Importance of physical processes and biogeochemical regimes in the Tropical Atlantic 83

2.6 What Drives the Variation in Iron Regimes? 84

3 Quantifying Trace Metal Scavenging Rates 87

3.1 Introduction 87

3.2 Method 89

3.2.1 ^{234}Th / ^{238}U Scavenging Models 89

3.2.2 Calculation of the Rate Constants 91

3.2.3 Error quantification model 94

3.3 Results and Discussion 97

3.3.1 Model error quantification 98

3.3.2 Adsorption and fallout rates in the subpolar North Atlantic 101

3.3.2.1 Calculation of net rates 101

3.3.2.2 Iron fluxes 106

3.3.3 Determining the drivers behind scavenging rate variability 111

3.3.4 Is volcanic ash deposition a potential sink of iron? 112

3.3.5 Implications of volcanic ash control on particle scavenging 116

3.4 Summary and Conclusions 117

4 Developing the MITgcm Iron Closures 119

4.1 Motivation for modelling work 119

4.2 Iron in General Circulation Models 120

4.3 The MITgcm 123

4.3.1 Iron in the MITgcm 124

4.3.2 Limitations 127

4.3.2.1 Sub-polar North Atlantic 127

4.3.2.2 Atlantic basin 129

4.3.2.3 Nutrient limitation distribution 132

4.3.3 Attempts to reconcile the model $[Fe_T]$ with data values . . 134

4.4 Comparisons with NEMO-PISCES 135
4.4.1 Introduction 135
4.4.2 The NEMO-PISCES iron closure 136
4.4.3 Comparison of model parameters in MITgcm and NEMO-PISCES 138
4.5 Improvements to the MITgcm 141
4.5.1 Inclusion of sedimentary sources 141
4.5.2 Hydrothermal vent supplies of iron 142
4.5.3 Scavenging regime 143
4.5.4 Remineralisation of scavenged iron 145
4.5.5 Variable iron to phosphate uptake ratios 146
4.5.6 Other processes included in the new MITgcm closure . . 148
4.6 New Model Distributions and Processes 148
4.6.1 Subpolar North Atlantic 150
4.6.2 Tropical Atlantic 152
4.6.3 Atlantic and Global comparison 157
4.6.4 Old and new model comparison 161
4.7 Summary 164

5 Developing a Preformed, Regenerated and Scavenged Iron Model Framework 167

5.1 Introduction 167
5.2 Iron Framework 171
5.2.1 Framework definition 171

5.2.1.1 Mixed layer preformed iron 172

5.2.1.2 Benthic source preformed iron 173

5.2.1.3 Regenerated iron 175

5.2.1.4 Scavenged iron 175

5.3 Initial Tracer fields 176

5.3.1 Comparison between macronutrient and iron frameworks 176

5.3.2 Dominant balances within the iron framework 178

5.3.3 Caveats to the derived iron partitioning framework 180

5.3.4 Implications for the observational community 182

5.4 Summary 183

6 Sensitivity of the Preformed Iron Framework 185

6.1 Introduction 185

6.2 Method and Approach 186

6.3 Results and Discussion 190

6.3.1 Impact on total dissolved iron 190

6.3.2 What controls preformed iron? 194

6.3.3 What controls the regeneration imprint? 196

6.3.3.1 Effect of iron speciation on Reg_{ex} 200

6.3.3.2 Sensitivity of Reg_{ex} to stoichiometry 201

6.3.3.3 Effects of Sources on Reg_{ex} 202

6.3.4 Comparison of iron and phosphate frameworks 206

6.3.4.1 Relationship between the preformed and regenerated tracers 206

6.3.4.2 Variation in responses of Fe_{pre} and P_{pre} to model experiments 208

6.3.4.3 The regeneration imprint of phosphate 210

6.4 Summary 215

7 Conclusions **217**

7.1 Key outcomes 217

7.2 Open questions 221

References **225**

Abstract

Iron is important in determining the biogeochemistry of the oceans and has a strong control on ocean productivity. The sources of iron vary from atmospheric supply of desert dust, resuspension of oceanic sediments and fluxing of volcanic material out of vents into the deep ocean. Iron is very reactive in the water column and interacts with organic ligands, to form metal complexes, and particles via surface association. The interaction of these processes determines the ocean basin-wide distribution of total dissolved iron.

Observational measurements of 234^{Th} and ^{238}U were used to estimate the particle scavenging fluxes of iron in the subpolar North Atlantic, resulting in mean iron losses of 1.03±0.89 $pM\ Fe\ d^{-1}$ and 7.1±5.9 $pM\ Fe\ d^{-1}$ between spring and summer. During the spring a volcanic eruption deposited large amounts of ash into the North Atlantic, this had a strong effect on the scavenging and fallout of iron.

A novel iron model framework is presented. Diagnosis of this framework implies two important balances:

- The total iron (Fe_T) distribution is determined by the distribution of mixed layer preformed tracer (Fe_{pre}) and two new tracers representing sediment source and hydrothermal source, thus $Fe_T = Fe_{pre} + Fe_{sed} + Fe_{hyd}$.

- Regeneration (Fe_{reg}) and scavenging (Fe_{scav}) nearly cancel each other out. Though the size of the terms are bigger than the preformed tracer they have a very limited net impact. The excess regeneration resulting from the balance of these terms, ($Fe_{reg} + Fe_{scav}$) indicates whether

the regeneration of iron is important for setting the total dissolved iron distribution. For the majority of the ocean there is no regeneration imprint.

Organic ligands play a central role in determining the dissolved iron distribution. Ligands form organic complexes with inorganic free iron and increase the solubility of iron within the water column. These organic complexes then protect the iron from scavenging. Thus, the presence of ligands enhances the transport of iron-rich water throughout the Atlantic basin.

Acknowledgments

Firstly, my thanks go to my supervisors Ric. Williams, Alessandro Tagliabue and Eric Achterberg. Of course I would not be here without their continued guidance, assistance and patience. Thank you, I really appreciate the effort you have all put in, particularly over the two months in the run up to my hand-in when time was at a premium. I would also like to thank Vassil Roussenov and Jon Lauderdale, who both put in significant amounts of time debugging my code and explaining the intricacies of running a General Circulation Model. I would also like to thank the captain, the crew and the scientific serving on the RRS Discovery during the IBIS cruise in June 2010. I had a truly memorable time at sea and hope that it wasn't my last time. I also thank the University of Liverpool and the Natural Environment Research Council for financial support during my research.

y colleagues in Nicholson Rm 205 showed continued support and provided the odd opportunity to procrastinate, it was a great help.

I am purely a product of my upbringing and my time in school, so I would like to extend my thanks to all of the people who have encouraged me to question everything around me. Thanks, Mum and Dad, I am so proud to be your son and I hope that in some small way this makes you think it was somehow all worth it.

And lastly I'd like to thank Hannah Whitby, for being by my side and always saying the right thing.

List of Figures

2.1 Plot showing yearly average log deposition of iron, $g\ m^{-2}yr^{-1}$ . . 22

2.2 Plot showing yearly average supply of iron along plate boundaries, $\mu molFem^{-2}yr^{-1}$, (Tagliabue et al., 2010) 23

2.3 Plot showing every 25m bathymetry contours between 0 and 500m depth. These regions of continental shelf are likely to provide sedimentary iron to the water column. 25

2.4 A compendium of global modelled iron source distribution 27

2.5 Plot showing, (a), regional binning of iron data (colours for illustrative purposes only), and, (b), actual data locations (Red). 28

2.6 Apparent Oxygen Utilisation from the World Ocean Atlas 2009, (Garcia et al., 2010) 31

2.7 Boxplots showing annual mean iron at 120m, 120 to 550m, 550 to 1080m, 1080 to 2250m and $>$2250m depths for Atlantic regions. Red line indicates median value, the box represents upper and lower quartiles and whiskers represent spread of data excepting outliers. 33

2.8 Boxplots showing available monthly data ranges for iron at 120m, 120 to 550m, 550 to 1080m, and >2250m in the Atlantic North subtropical gyre. Red line indicates median value, the box represents upper and lower quartiles and whiskers represent spread of data excepting outliers. 34

2.9 Boxplots showing annual mean iron at 120m, 120 to 550m, 550 to 1080m, 1080 to 2250m and >2250m depths for Pacific regions. Red line indicates median value, the box represents upper and lower quartiles and whiskers represent spread of data excepting outliers. 38

2.10 Boxplots showing available monthly data ranges for iron at 120m, 120 to 550m, 550 to 1080m, and >2250m in the Pacific North subtropical gyre. Red line indicates median value, the box represents upper and lower quartiles and whiskers represent spread of data excepting outliers. 40

2.11 Showing the section locations used in this study. The map shows the North Atlantic. Greenland is in the top left and the UK mid-right. 43

2.12 T/S plot coloured with pressure for D354 labelled with water mass information 46

2.13 T/O plot coloured with pressure for D354 labelled with water mass information 48

2.14 Section A Nutrient Sections. Black crosses represent bottle positions. 49

2.15 Section B Nutrient Sections. Black crosses represent bottle positions. 51

2.16 Section D Nutrient Sections. Black crosses represent bottle positions. 54

2.17 Temperature-salinity and temperature-oxygen plots with $P*$ for the whole domain 57

2.18 P^* and PO_4^{reg} for section A. 58

2.19 Temperature-salinity and temperature-oxygen plots with $P*$ for section A. 59

2.20 $P*$ and PO_4^{reg} for section B. 60

2.21 Temperature-salinity and temperature-oxygen plots with $P*$ for section B 61

2.22 $P*$ and PO_4^{reg} for section D. 61

2.23 Temperature-salinity and temperature-oxygen plots with $P*$ for section D 62

2.24 Temperature-oxygen plots with Fe and Al (nM) for the Entire domain. 63

2.25 Fe and Al for section B. 64

2.26 Temperature-salinity and temperature-oxygen plots with Fe and Al (nM)for the $60°$N Section: B. 65

2.27 Fe and Al for section D. 66

2.28 Temperature-salinity and temperature-oxygen plots with Fe and Al (nM) for the Irminger Basin: Section D. 66

2.29 D361 Station Locations, colours represent cast number 71

2.30 D361 Station Locations and T/S plots, colours represent cast number. From left to right the regions are: coastal, central, southern and northern 72

2.31 D361 T/S and T/O plots coloured by cast depth and latitude, The depth plots include an indication of water masses 74

2.32 Tropical Atlantic south-north ($\sim$ 28°W) nutrient sections. Black crosses represent bottle positions. 75

2.33 Tropical Atlantic west-east (13°N) nutrient sections. Black crosses represent bottle positions. 77

2.34 D361 T/S and T/O plots coloured by PO_4, $\mu mol\ l^{-1}$ 78

2.35 D361 T/S and T/O plots coloured by $P*$ 79

2.36 D361 contoured sections of Fe (nM), note differing axes. 80

2.37 D361 T/S and T/O plots coloured by Fe (nM), note differing axes between T/S and T/O plots. 82

3.1 Schematic of a two-box export model. Dissolved (Th_d) and particulate (Th_p) thorium are controlled by forward ($k'f$) and reverse (kr) sorption processes and the physical fallout (λ_{part}) of particles. 91

3.2 Examples of simulated [POC] time-series 96

3.3 Station location and Irminger and Iceland basin partitioning plot for D350 (blue) and D354 (red), with bathymetric contours at 250m, 500m, 1000m, 2000m, 3000m and 4000m 97

3.4 Plot showing examples of idealised single and double bloom [POC] seasonal cycles (Black, left y-axis). Quantified errors in diagnosed adsorption rates associated with these [POC] time series are also shown (Red right-hand y-axis) 98

3.5 Plots of normalised adsorption error over the seasonal cycle for D350, dotted line shows timing of in situ measurements $\pm$ 10 days. 100

3.6 Plots of normalised fallout rate error over the seasonal cycle for D350, dotted line shows timing of in situ measurements $\pm$ 10 days. 100

3.7 Plots of normalised adsorption error over the seasonal cycle for D354, dotted line shows timing of in situ measurements $\pm$ 10 days. 101

3.8 Plots of normalised fallout rate error over the seasonal cycle for D354, dotted line shows timing of in situ measurements $\pm$ 10 days. 101

3.9 Relationship between $\log_{10}$ adsorption rate and $\log_{10}$ POC concentration for 'Small' (1-53 μm), 'Large' ($>$53 μm) and 'All' ($>$1 μm) particles 112

3.10 Relationship between $\log_{10}$ fallout rate and $\log_{10}$ POC concentration for 'Small' (1-53 μm), 'Large' ($>$53 μm) and 'All' ($>$1 μm) particles 113

3.11 Maps showing the deposition of volcanic ash from the Eyjafjallajokull Eruption, units are $log(g\ m^{-2}\ d^{-1})$. Greenland can be seen in the top left of the maps and mainland Europe in the bottom right, (Stohl et al., 2011) 114

3.12 Scatter plots showing the relationship between volcanic ash deposition, $log(g\ m^{-2}\ d^{-1})$, and adsorption rates, d^{-1}, at 150m . 115

3.13 Scatter plots showing the relationship between volcanic ash deposition, $log(g\ m^{-2}\ d^{-1})$, and fallout rates, d^{-1}, at 150m 115

4.1 Subpolar North Atlantic data scattered onto MITgcm 60°N July average dissolved iron distributions, $mol\ m^{-3}$ 127

4.2 Subpolar North Atlantic phosphate data scattered onto MITgcm 60°N July average phosphate distributions, $mol\ m^{-3}$ 129

4.3 MITgcm surface Atlantic dissolved iron $(left)$ and MITgcm Atlantic basin zonal mean dissolved iron $(right)$, with observational iron concentrations (Tagliabue et al., 2012) scattered over the modelled iron distributions. 130

4.4 Figure showing Tropical Atlantic iron data comparison 131

4.5 Figure showing Tropical Atlantic phosphate data comparison, $mol\ m^{-3}$. The contoured section is model output; data values are scattered onto the model field. 132

4.6 Nutrient limitation characteristics 133

4.7 Modelled NEMO-PISCES iron distributions at the surface and 1000m depth, taken from Aumont and Bopp (2006) 137

4.8 MITgcm, λ = 1.14 yr^{-1}, Iron distribution (nM) for 60N 141

4.9 Figure showing iron supply rate dependence on depth 143

4.10 Figure showing $R_{Fe:P}$ dependence on Fe_T 147

4.11 Summary of the new iron closure developed for the MITgcm . . . 149

4.12 MITgcm new closure 60°N dissolved iron distributions, $mol\ m^{-3}$. The contoured section is model output; data values are scattered onto the model field. 150

4.13 MITgcm new closure 60°N phosphate distributions, $mol\ m^{-3}$. The contoured section is model output; data values are scattered onto the model field. 152

4.14 MITgcm new closure 11°N dissolved iron distributions, $mol\ m^{-3}$. The contoured section is model output; data values are scattered onto the model field. 153

4.15 MITgcm new closure 28°W dissolved iron distributions, $mol\ m^{-3}$. The contoured section is model output; data values are scattered onto the model field. 154

4.16 MITgcm new closure 28°W phosphate distributions, $mol\ m^{-3}$. The contoured section is model output; data values are scattered onto the model field. 156

4.17 Observational iron data scattered over new closure MITgcm dissolved iron distributions for the Atlantic, $mol\ m^{-3}$ 158

4.18 MITgcm new closure Atlantic dissolved iron box and whisker plots, $mol\ m^{-3}$. O and M refer to observations and model values. The first letter following the hyphen then designates North or South followed by either one or two letters referring to "Polar-P", "Subpolar-SP", "Subtropical-ST" and "Tropical-T" regions. The red lines represent the median value, box limits represent the upper and lower quartiles and the whiskers then indicate extreme values not considered outliers (effectively $\pm$ 2.7σ or 99.4% of the data). 160

5.1 Schematic of a generic ocean basin illustrating the framework for investigating preformed iron 172

5.2 Atlantic zonal mean sections for Fe and PO_4 tracers 179

5.3 Atlantic zonal mean Sections of Benthic tracers and Fe_{scav} 181

6.1 Scatter plot of all sensitivity experiments showing percentage change of Fe_T and Atlantic integral export production from the control 189

6.2 Zonal mean plots of Fe_T anomalies from the Control run at three depths for the source experiments. From Left to right plots show zonal mean values for the upper 120m, 120-1800m and $>$1800m. Lines represent -50% and +50% perturbations for the three sources of iron, Atmospheric (ATM), Sedimentary (SED) and Hydrothermal (HYD). 190

6.3 Zonal-depth mean plots of Fe_T anomalies from the Control run at three depths for the speciation experiments. From Left to right plots show zonal-depth mean values for the upper 120m,120-1800m and +1800m. Lines represent -50% and +50% perturbations for the $[L_T]$ and 191

6.4 Meridional section of Fe_T ($mmol\ L^{-1}$) anomalies for total ligand concentration experiments 192

6.5 Zonal-depth mean plots of Fe_T anomalies from the Control run at three depths for the source experiments. From Left to right plots show zonal-depth mean values for the upper 120m,120-1800m and +1800m. Lines represent -50% and +50% perturbations for the three sources of iron, Atmospheric (ATM), Sedimentary (SED) and Hydrothermal (HYD). 193

6.6 Scatter plot of all sensitivity experiments showing percentage change of Fe_T and Fe_{pre} from the control 194

6.7 Zonal-depth mean plots of Fe_{pre} anomalies from the Control run at three depths for source and speciation experiment subsets. . . 195

6.8 Meridional section of Fe_{pre} anomalies ($mmol\ \ L^{-1}$) for Atmospheric and sediment source and total ligand concentration experiments 197

6.9 Meridional mean sections of Fe_{reg} and Fe_{scav} diagnostics from the control run, dashed white line indicates boundaries of ”net scavenging” and ”net regeneration” regimes. i.e $Reg_{ex} < 0$ are ”net scavenging” regimes and $Reg_{ex} > 0$ are ”net regeneration” regimes. The white dashed lines as a boundary between net scavenging and net regeneration regimes will be used in subsequent figures. 198

6.10 Scatter plot of all sensitivity experiments showing percentage change of Reg_{ex} and $\frac{Fe_{reg}}{-Fe_{scav}}$ from the control. Gridlines represent $\frac{Fe_{reg}}{-Fe_{scav}} = \frac{Fe_{reg}}{-Fe_{scav\,control}}$ and $Reg_{ex} = 0$, the latter is the boundary between net regeneration and net scavenging 199

6.11 Meridional section of Reg_{ex} anomalies ($mmol\ L^{-1}$) for total ligand concentration experiments. White dashed line denotes the boundaries between net scavenging and net regeneration regimes determined by Reg_{ex} distribution. 201

6.12 Figure demonstrating latitudinal variation of $Fe : C$, note $C : P = 117$, and its effect on Reg_{ex}. 202

6.13 Plot of Reg_{ex} anomaly ($mmol\ L^{-1}$) for constant $Fe : P$ experiment 202

6.14 (a) to (d) Meridional section of Reg_{ex} anomalies ($mmol\ L^{-1}$) for stoichiometry and source experiments. White dashed line denotes the boundaries between net scavenging and net regeneration regimes determined by Reg_{ex} distribution. (e) & (f)Meridional section of control L_{sat} ($mmol\ L^{-1}$) and the anomaly of L_{sat} for the SED OFF scenario. White dashed line denotes $L_{sat} = 0$ 205

6.15 Plot showing anomalies in basin mean P_{pre} and P_{reg} for the model experiments 207

6.16 Plot showing anomalies in basin mean Fe_{pre} and Fe_{reg} and the effects of selected experiments. Dotted arrows and label boxes represent the spectrum of results for particular groups of experiments. 208

6.17 Plot showing anomalies in basin mean Fe_{pre} and P_{pre}. Dotted arrows and label boxes represent the spectrum of results for particular groups of experiments. 209

6.18 Meridional Atlantic sections of preformed tracer anomalies for the Sediment-OFF scenario for (a) Iron and (b) Phosphate . . . 209

6.19 Control meridional Atlantic section of the fractional contribution of regenerated nutrient to total nutrient for phosphate and iron . . 210

6.20 Plot showing basin mean Fe_{RR} and P_{RR} for the experiment runs for (a) Phosphate and (a) Iron 211

6.21 Meridional sections of P_{RR} and Fe_{RR} anomalies for biological consumption rate experiments. White dashed line denotes the zero contour 212

6.22 Latitudinal variation in zonal mean $Fe : P$ uptake ratio for biological consumption rate perturbations 213

6.23 Meridional sections of P_{RR} and Fe_{RR} anomalies for iron source experiments. White dashed line denotes the zero contour. 214

List of Tables

2.1 Table detailing geographical breakdown of the iron database, based on large-scale nutrient regimes and circulatory features. The table provides regional coordinates and estimates of iron sources. 30

2.2 Table detailing Water Mass Characteristics for North Atlantic . . 44

3.1 Values used for Time series component parameters 96

3.2 Table showing rates derived from ^{234}Th for D350 data at depths of 150m and 50m. (***Bold-italicized numbers are from 150m***) . 102

3.3 Table showing rates derived from ^{234}Th for D354 data at depths of 150m and 50m. (***Bold-italicized numbers are from 150m***) . 103

3.4 Table showing comparison of rates from other studies,[a] NEMO-PISCES model as Aumont and Bopp (2006); Tagliabue et al. (2010), [b] MITgcm as described in Chapter 4. Numerical model studies are italicised. 104

3.5 Table showing the basin mean net adsorption and fallout rates for D350 and D354 105

3.6 Table showing derived iron fluxes for D350 data from ”free”, ”colloidal” and ”Total” iron pools at depths of 150m and 50m. (***Bold-italicized numbers are from 150m***) 107

3.7 Table showing derived iron fluxes for D354 data from ”free”, ”colloidal” and ”Total” iron pools at depths of 150m and 50m. (***Bold-italicized numbers are from 150m***) 108

3.8 Table showing approximations of iron supply rates and fluxes from observations or diagnosed within the MITgcm (Italicized), see Chapter 4. The model utilises input fields from Mahowald et al. (2006); Aumont and Bopp (2006); Tagliabue et al. (2010). . 110

4.1 MITgcm Parameter table 125

4.2 Comparison of parameters for the MITgcm and NEMO-PISCES iron closures 139

4.3 Comparison of old and new MITgcm closures 163

6.1 Table detailing sensitivity experiments carried out, each model run has a positive and negative perturbation, except for runs 4, 5 and 22 which are source turned off and variable Fe:P removed. The symbols represent the groupings of experiments: $\bigcirc$ = Sources, $\square$ = Scavenging, $\bigtriangledown$ = Speciation, $\diamond$ = Biological processes, $\bigtriangleup$ = Stoichiometry, $\triangleright$ = Transport via wind speed perturbations and $*$ = Control. 187

Chapter 1

Why is Iron Important?

1.1 Introduction

The importance of iron to marine scientists has evolved from an interest in the specific chemical interactions that it undergoes in seawater to being one of the most important elements affecting biological activity in the ocean. The importance of iron as a limiting nutrient was hypothesised in the late 1980's (Martin and Fitzwater, 1988; Martin, 1990) in terms of potentially being a major determining factor behind observed glacial-interglacial changes in CO_2. Biological activity is a process which consumes inorganic nutrients in the surface ocean, mainly through photosynthetic plants known as phytoplankton. Primary production fixes inorganic nutrients into organic material. This organic material is then processed and recycled by zooplankton grazing (Jackson, 1980) or respiration (Smith, 1978), converting nutrients between organic and inorganic forms. This process is not 100% efficient and some of the organic material can leave the surface ocean (Legendre and Gosselin, 1989). This removal of organic material can occur through physical fallout of deceased phytoplankton, excretion and sloppy eating by the zooplankton or by physical transport of water from the surface to the deep (Siegel et al., 2002; Benner et al., 2005). The combination of these processes results in the removal

of nutrients from the surface, which can lead to their sequestration in the thermocline, deep and bottom water as well as in deepwater sediments (Lackner, 2003). The process of removal and sequestration of nutrients and carbon to the deep ocean is balanced by interactions between the surface ocean, the atmosphere and the lithosphere. Inorganic nutrients, particularly iron, are supplied from sediments, rivers and other terrestrial sources. Air-sea exchange also allows any biological system that is consuming CO_2 during the course of photosynthesis to drawdown further CO_2 from the atmosphere (Siegenthaler and Sarmiento, 1993). Thus, Martin (1990) hypothesised the control of atmospheric CO_2 by iron via the processes of iron limitation, fertilisation, primary production and sequestration of CO_2. Although the work of Martin (1990) is not entirely supported now, the work instigated significant scientific interest leading to steady progression in the iron cycle. This thesis aims to further the community's understanding of the biogeochemical processes influencing iron.

1.1.1 The importance of iron to biological communities

In the time since Martin (1990)'s iron hypothesis, a large number of iron enrichment studies have been carried out to identify regions of the ocean that exhibit iron limitation of primary production. Contrasting nutrient regimes have been found to be limited by iron. The High-Nutrient Low-Chlorophyll regions of the high latitudes exhibited increased production following iron addition experiments (Baar et al., 2005). Fertilisation of nutrient-poor low-latitude regions with iron can lead to nitrogen-fixation, thus alleviating these regions from both macronutrient and iron limitation (Moore et al., 2009). In total, up to half of the global ocean may have primary productivity that is controlled by iron (Moore et al., 2001).

Our need for an understanding of the carbon cycle has increased as a consequence of anthropogenic climate change. The change in climatic conditions has arisen from fossil fuel consumption and production of large amounts of CO_2, which has been freely pumped into the atmosphere (Stocker

et al., 2013). Iron is clearly important if one wishes to understand the response of the marine biological community to any perturbations made to the system. There has been a large amount of work aimed at gaining insights into the mechanisms by which iron controls biological activity, and consequently affects the global carbon cycle.

1.1.2 Iron processes

Iron is the fourth most abundant element in the Earth's crust behind oxygen, silicon and aluminium. Consequently, there is significant supply of terrigenous iron to the ocean. The supply comes from numerous sources: transport of lithogenic dust to the the ocean by the atmosphere (Zhu et al., 1992; Zhuang et al., 1992), riverine supply of sedimentary material to coastal ocean (Mayer, 1982*b*,*a*), the provision of iron from oceanic sediments (Sawlan and Murray, 1983; Shaw et al., 1990) and the supply of mantle material through the Earth's crust via hydrothermal vents (Dutay et al., 2004; Boyle et al., 2005). Despite the large amounts of iron supplied, almost half the ocean is iron-limited. A range of processes combine to modify the residence time and bioavailabilty of iron within the water column.

The solubility of free inorganic iron in the ocean is temperature dependent, but of the order of 0.2 nM (Liu and Millero, 2002). We see ambient total iron concentrations much higher than this in the ocean. Organic ligands within the ocean interact with inorganic iron to form organic complexes (Gledhill and van den Berg, 1994). The solubility of iron increases with the presence of these iron-binding molecules and allows retention of iron in solution above its natural inorganic solubility. As well as this increase in solubility provided by organic ligands, there is a protection of dissolved iron from the process of particle scavenging (Goldberg, 1954). Iron has a tendency to interact with lithogenic and biogenic particles in the water column (Turekian, 1977; Honeyman et al., 1988), which following fallout of particulate material, can lead to a net loss of iron from the surface water. The complexations formed with organic ligands are much stronger than the surface associations formed with particles. However,

if the iron concentrations are higher than the total ligand concentration then there is still the potential for scavenging of any excess free inorganic iron. The process of colloidal aggregation of the organic complexes also results in iron associated with particles, which falls out of the surface water (Wen et al., 1997). Even with the presence of organic ligands there are still processes that remove iron from the water column, such as the coagulation of organic ligands forming particulate material, which is removed (Honeyman and Santschi, 1989). The combination of these processes in addition to the regional variability of the iron sources results in a range of iron regimes seen across the ocean.

1.1.3 Uncertainty in the iron system

There are some key areas of the iron system still lacking understanding. One concerns how the iron sources affect basin-wide distribution of iron. There are regions of the ocean that are remote from any iron sources and yet are not permanently iron-limited, such as the Peru Basin (Bruland et al., 2005); it is important to try to gain an understanding of why these regimes exist. Conversely, there are regions that are abundantly supplied with iron of varying sources that experience iron-limitation and persistent macronutrients at the end of the phytoplankton growth season (Nielsdóttir et al., 2009; Ye et al., 2010). A second area of uncertainty is the role of organic ligands. This ligand control is parameterised in most General Circulation Models as a constant ligand concentration. The scavenging of iron by particles is related strongly to the organic ligands as the total ligand concentration determines the quantity of free inorganic iron that can be rapidly scavenged onto particles, as well as the amount of organic ligands that may coagulate to form organic aggregates.

1.2 Aim of the thesis

The aim of this thesis is focussed on gaining an improved understanding of how the global distributions of iron are determined. With this ultimate goal I set

out the following more specific aims to be addressed in the following work:

- Establish the first order drivers behind basin-wide and regional observed iron distributions within the North Atlantic basin.

  A global dataset of historical iron data is used to analyse the geographical distribution and variability of total iron concentrations in relation to maps of modelled iron sources. A first order estimate of the drivers of the iron distributions is made. Two specific cruise datasets are also used to analyse two contrasting biological regimes in the Atlantic ocean. The subpolar gyre of the North Atlantic and the mid-latitude Atlantic are used as case studies to explore the regional variation of iron and reveal the controlling processes responsible.

- Quantify scavenging rates from direct measurements to determine regional variation and drivers of particle scavenging.

  Using direct measurements of ^{234}Th and ^{238}U, in situ scavenging rates of iron are calculated. The drivers of these scavenging rates are found using analysis of particle concentration and volcanic ash deposition fields. The inter-basin variability of scavenging is quantified; informing on the scavenging regimes present in the Iceland and Irminger basins of the North Atlantic.

- Develop an appropriate model platform to investigate the iron partitioning and distribution.

  The current iron modelling techniques are discussed with respect to selecting and developing a general circulation model that is suitable for exploring how the iron distribution is controlled. A model appropriate for running long-term experiments including iron transports and a suitable iron cycle is vital.

- Define an iron partitioning model framework to reveal the importance of sources, regeneration and scavenging on total dissolved iron distributions.

A framework for preformed iron (Broecker, 1974; Broecker et al., 1985; Toggweiler et al., 2003; Ito and Follows, 2005) is further developed and applied to iron. In addition to the two traditional preformed and regenerated tracers, two new tracers are defined. This novel framework provides insight on the relative contributions of iron sources, regeneration and scavenging.

- Explore the importance of iron processes in determining preformed and regenerated iron distributions.

  To test the model platform and framework, a range of sensitivity experiments and parameter perturbation model runs are conducted. The iron partitioning framework is aimed at revealing the driving factors behind the total iron distribution and identifying the processes that control variation from the integrated basin-wide view. The importance of processes such as subsurface regeneration and scavenging of iron are quantified relative to the iron sources to assess their impact on iron distribution.

Chapter 2

Global Iron Distributions

2.1 Introduction

The growth of phytoplankton is one of the key foundations upon which the marine ecosystem is built. Iron is a key nutrient in the Ocean, often determining the timing, magnitude and locations of phytoplankton blooms across the world. Our understanding of iron is necessary in order for us to understand how the ocean ecosystem works. The key drivers behind the initial distribution of iron are the sources. The primary signals of iron sources are apparent in the surface where a supply of iron can trigger a rapid response.

In this chapter a discussion of the key iron sources is followed by implications of their impact on total dissolved iron concentrations. The initial assertions made from our knowledge of the iron sources and the underlying physical transport in the oceans are tested using a global database of iron measurements, in addition to two more specific case studies in the tropical Atlantic and subpolar North Atlantic.

2.2 Iron sources

To provide further context to the discussion in this chapter it is important to set out our current knowledge of the iron supply to the global ocean. The method of analysing global iron data distribution, described in more detail later, focuses on geographical regions of two oceanic basins: Atlantic and Pacific. To best enable us to get some meaningful results from this analysis, it is essential to detail the global distribution of iron sources. The three major 'sources' of iron to the open ocean are aeolian supply of atmospheric iron, continental shelf sediments and hydrothermal vent systems. Here I discuss these sources and their delivery processes in more detail.

2.2.1 Aeolian supply of dust

The atmospheric deposition of dust from the world's deserts acts as a supply of lithogenic particles to the ocean, supplying approximately 16.5 x $10^{12}\ g\ Fe\ yr^{-1}$ (no error supplied) (Jickells and Spokes, 2002), equivalent to 2.98 x$10^{11}\ mol\ Fe\ yr^{-1}$, to the global ocean. This process can be very important, particularly because it is able to provide iron to areas of the ocean that are remote from coastal regions by vast distances of open ocean, for example deposition of the order of 4 $mmolFe\ m^{-2}\ yr^{-1}$ is seen in the central Pacific at distances of 6500 kilometres from the nearest continent (Mahowald et al., 2006).

In addition to the actual supply of lithogenic material, the processes that act to transport the dust from its source also cause further changes to this material. Whilst in the atmosphere these terrigenous particles undergo significant chemical interactions. An increase in solubility of crustal iron and aluminium results from acidification in the atmosphere. In addition to this, the accumulation of secondary acids and other nutrients, such as nitrate, from other air-masses (Zhu et al., 1992; Sullivan et al., 2007) provide alterations to lithogenic material that is beneficial to marine organisms. These processes

often act to increase the solubility of the iron within the dust particles, resulting in greater bioavailability to the phytoplankton once the dust is deposited. The solubility of these dust particles has been found to be related to the distance from source (Zhuang et al., 1992), and is also affected by the mineralogy of source region, photochemical processing and aerosol size. In addition, meteorological conditions affect the ultimate deposition location (Schlosser et al., 2014) as well as affecting solubility by the inter-mixing of air-masses of different characteristics (Sullivan et al., 2007).

These observational studies have been a great tool for examining the regional variation in iron cycling dynamics. However, biogeochemical ocean modellers in particular have always emphasised the importance of realistic global distribution fields in order to improve the accuracy of model ocean simulations. To provide these fields it is necessary to combine the characteristics of the source region, composition of anthropogenic emissions and atmospheric chemical process modelling with atmospheric circulation models to provide global estimates of dust, or iron, deposition to the surface ocean. The deposition fields from Mahowald et al. (2009) are shown in figure 2.1. Early estimates were based on average dust deposition fields by weight from reanalysis models (Luo et al., 2003; Ginoux et al., 2004; Tegen et al., 2004). More recent model estimates include a combination of atmospherically-processed lithogenic dust particles and anthropogenic particles from combustion, whose distributions are determined by complex atmospheric circulation models. These processes are further derived to provide flux estimates for deposited soluble iron.

2.2.2 Hydrothermal vent sources of iron

Throughout the ocean there are a large number of active hydrothermal vent systems. Many of the vent systems reside in locations known to be tectonically active, such as the mid-Atlantic ridge that runs the length of the Atlantic basin, and the Nazca plate boundaries in the south-east Pacific. Both of these regions are actively ejecting material of mantle origin into the water column

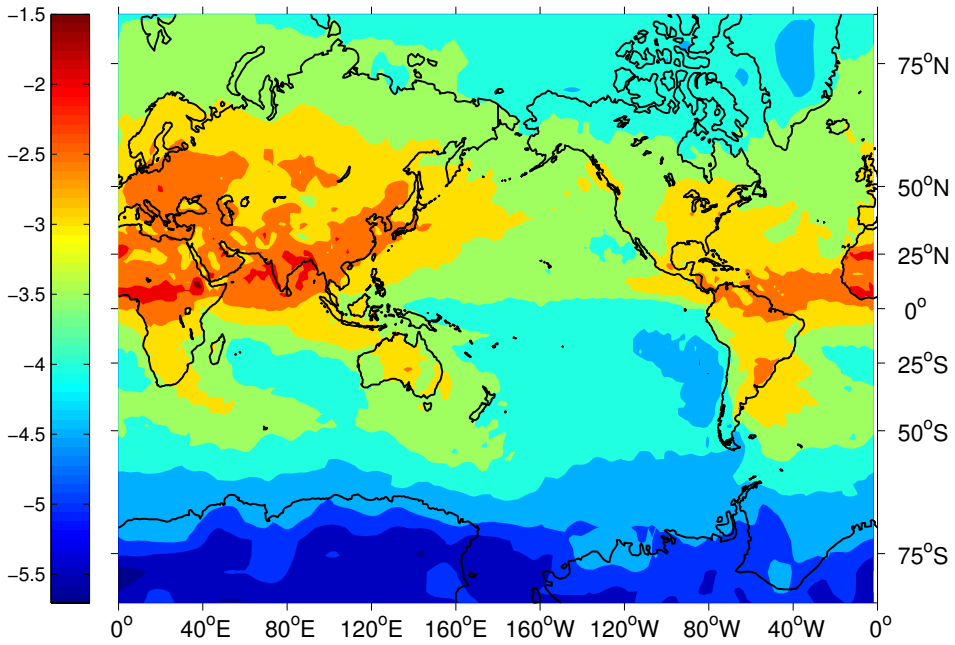

Figure 2.1: Plot showing yearly average log deposition of iron, $g\ m^{-2}yr^{-1}$

(Mahowald et al., 2009)

at rates that are, to first order, dependent on the spreading rates between the tectonic plates that are positioned at either side of these boundaries (Farley et al., 1995). The Earth's mantle is significantly enriched in many elements that are relatively rare in the ocean. Iron is amongst these elements and as a consequence is supplied into the abyssal regions of the oceans, as well as into volcanically active regions closer to the surface, such as islands like Iceland in the North Atlantic or the Solomon Islands in the South-West Pacific.

Despite these significant sources of iron into the ocean, for many years it was believed that much of this iron was inaccessible to phytoplankton due to rapid formation of particulates, which quickly fall out and are buried in deep-sea sediments before they can reach the surface (Elderfield and Schultz, 1996). In the last decade, this conclusion has been challenged as more evidence for the importance of hydrothermal iron in the global iron cycle has been found. Correlations between ^3He and nutrients, observed by Jenkins et al. (2007), suggested that there was a significant relationship between the ^3He that was ejected from hydrothermal vents and carried throughout the ocean and other elements that were accompanying it during its release from the Earth's crust.

Amongst these elements was iron, implying that iron that originated from these vent systems was able to spread over the ocean interior. Boyle et al. (2005) and Boyle and Jenkins (2008) also see important relationships between ^3He and dissolved iron in other locations supporting the inference that there is a robust relationship between ^3He and iron.

The key mechanism enabling iron to avoid being trapped within local iron cycle systems around the vent is effectively the same mechanism that increases bioavailability and residence times of iron in the surface waters. Organic iron-binding ligands have been found to exist around vents (Bennett et al., 2008),as well as over much of the rest of the ocean. Toner et al. (2009) find these organic compounds harvest the iron from within the hydrothermal plumes and allow the iron to remain in solution and undergo transport from the region, augmenting the deep-sea iron reservoirs by increasing the local iron solubility. Hence, hydrothermal vent systems are now accepted as a key iron source to oceanic waters (Farley et al., 1995; Dutay et al., 2004).

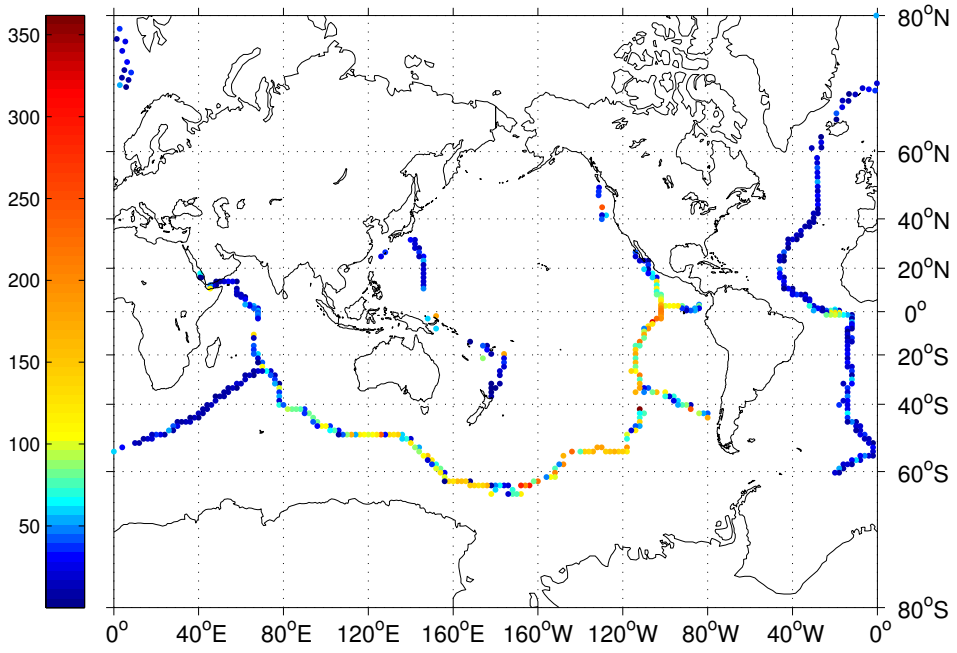

Figure 2.2: Plot showing yearly average supply of iron along plate boundaries, $\mu molFem^{-2}yr^{-1}$, (Tagliabue et al., 2010)

Drawing on the observed $Fe :^3 He$ ratios Tagliabue et al. (2010), carried out a model study investigating the impact of a hydrothermal source of iron using a

global ocean model (NEMO-PISCES). The inclusion of this source resulted in a drastic improvement in correlation between modelled dissolved iron fields and observational iron data. While there is a sparsity of dissolved iron data in all of the regions affected by a hydrothermal source, there is a general improvement in the modelling of deep ocean iron distributions. The model study found that the iron concentration increased by 0.5 nM in the deep Eastern Pacific, with the largest surface increases of 0.25 nM found in the North Atlantic sub polar gyre, a region with close proximity to the hydrothermal vents around Iceland.

The distribution of the hydrothermal sources follows the plate boundaries. Iron supply rates are strongest in the East Pacific and Southern Ocean, figure 2.2; these rates are derived from observed tectonic plate spreading rates and assume a $Fe :^3 He$ ratio of $4 \times 10^6\ molFe\ mol\ ^3He^{-1}$, following Tagliabue et al. (2010).

2.2.3 Continental Shelf Sediment Supply

The third major process that acts to provide dissolved iron into the water column is a direct benthic flux from oceanic sediments. Historically this process was believed to be dominated by a diffusive flux of iron from sediment pore-waters into adjacent marine water, dependent on the gradient between the two regions (Sawlan and Murray, 1983; Shaw et al., 1990). The magnitude of the contribution to surface productivity from these sediment sources was very small compared to the estimates of iron supply from aerosols. However, Elrod et al. (2004) showed that the potential supply from shelf sediments as a result of direct measurements of benthic flux over a five year period were much greater than were predicted using the pore-water gradient model applied previously, due to the inclusion of processes other than diffusion.

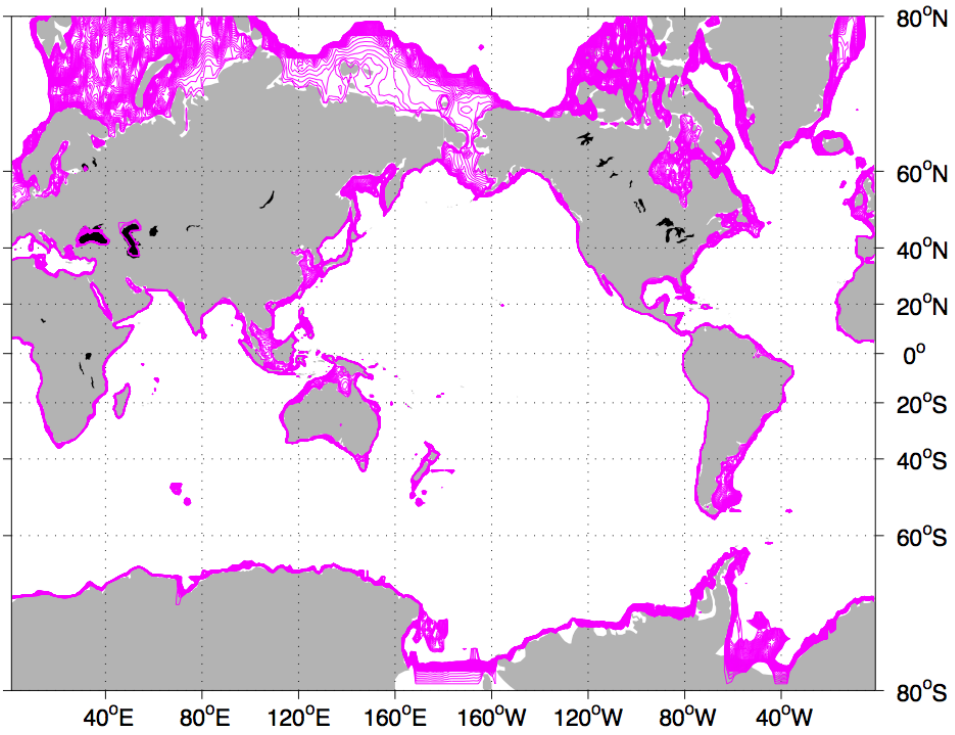

Figure 2.3: Plot showing every 25m bathymetry contours between 0 and 500m depth. These regions of continental shelf are likely to provide sedimentary iron to the water column.

Bio-irrigation, the tunnelling and manipulation of sediments by benthic fauna, is a process that can provide fluxes of radon 10 x greater than those seen for diffusion alone (Berelson et al., 2003; Green et al., 2002). The high measurements of iron fluxes suggest that bio-irrigation has a much greater impact relative to diffusion for iron as it does for inert elements such as radon. The increased estimates of sedimentary iron supply were based on a number of isolated experiments, in varying benthic environments. The global estimate was based on a mean carbon oxidation rate from the experiments being applied to the global continental shelf area. The oxidation of carbon would be accompanied by oxidation of iron within the sediments, meaning that applying a robust estimate of the ratio of iron to oxidised carbon in these environments gives us a total global sedimentary supply of iron, $8.9 \times 10^{10} molyr^{-1}$ (no error supplied) (Elrod et al., 2004), approximately a third of total atmospheric supply. The integral approximations do not take into account the relative solubility of the two supplies; sedimentary supply is carried out in tandem with resupply

of other organic material, including ligands. This can result in an increased solubility of supply relative to the atmospheric source (Elrod et al., 2004).

To provide a global distribution of sediment supply, one needs to assume that continental shelf regions shallower than 500m will provide a flux of iron by oxidation of organic material. A map showing the bathymetry of the ocean effectively shows regions where sedimentary iron fluxes to the ocean will occur (Figure 2.3):

- The South-East Asian archipelago and the area around Australia has a large area of shallow continental shelf, ideal conditions for the oxidation of organic material in the sediments, and subsequent release of nutrients back into the water column. South-East Asia is a potential source of iron to surface waters across the western central Pacific due to their proximity to one another.
- Considerable sedimentary supply across much of the Antarctic continental shelf, particularly around the Ross Sea, Antarctic Peninsula and Weddell Sea is inferred.
- The Arctic shelf, and the subsequent Arctic through flow into the North Atlantic is also significant supply of sedimentary iron.

This approximation is analogous to the way GCMs use shelf area to parameterise sediment supply, as a global database of observations does not exist.

2.2.4 Iron Source Summary

Analysis and discussion of the global iron database later in this chapter will be assisted by an overview of the iron supply distributions. It may not be possible to identify precisely the origin of iron in particular locations due to the lack of further supporting data for the observations, such as trace metal source tracers like alumnium and manganese, as well as hydrographic and nutrient data used to elucidate the characteristics of each individual dataset. However, a first step would be identifying relationships between the iron sources and iron distributions.

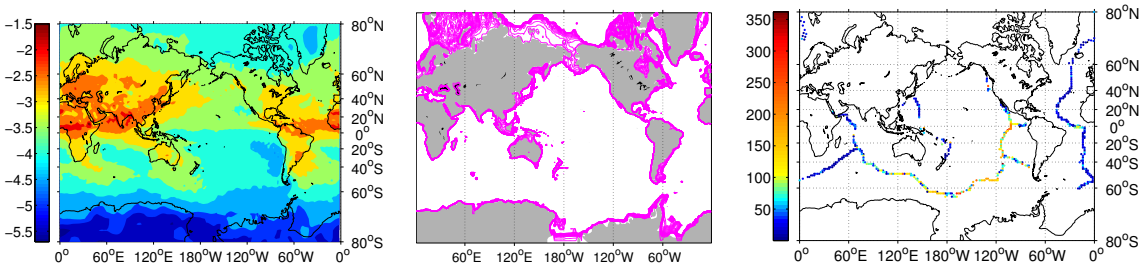

(a) Atmospheric, log iron supply, $g\ m{-}2\ yr^{-1}$

(b) Regions of sedimentary iron supply

(c) Hydrothermal iron supply, $\mu mol\ Fe\ m^{-2}\ yr^{-1}$

Figure 2.4: A compendium of global modelled iron source distribution

Assuming that iron sources are the dominant driver of the global iron distribution, a combination of the iron supply fields, figure 2.4, should help us to predict the first order distribution of dissolved iron. In order to make a comparison between sources and distribution of iron it is important to lay out a geographical framework which can be used to test the predictions made from the supply fields and observational dissolved iron data. These geographical regions can be seen in Table 2.1.

The thermohaline circulation can also be taken into account in addition to the direct iron supply. Iron is rapidly lost from the surface either through biological consumption or chemical processes. The introduction of this iron at depth

through remineralisation of particulate matter or from transport means that high concentrations of iron are found in these deep waters. Thus, when setting out predictions for the global distribution of dissolved iron, upwelling regions also need to be taken into account. These regions will often experience an influx of nutrients within the deep waters that are returning to the surface. The Peruvian Pacific coast, the California current, the Gulf of guinea and Japanese Continental Shelf are all regions that experience upwelling of deep, nutrient-rich waters (Tarazona and Arntz, 2001; Bruland et al., 2005).

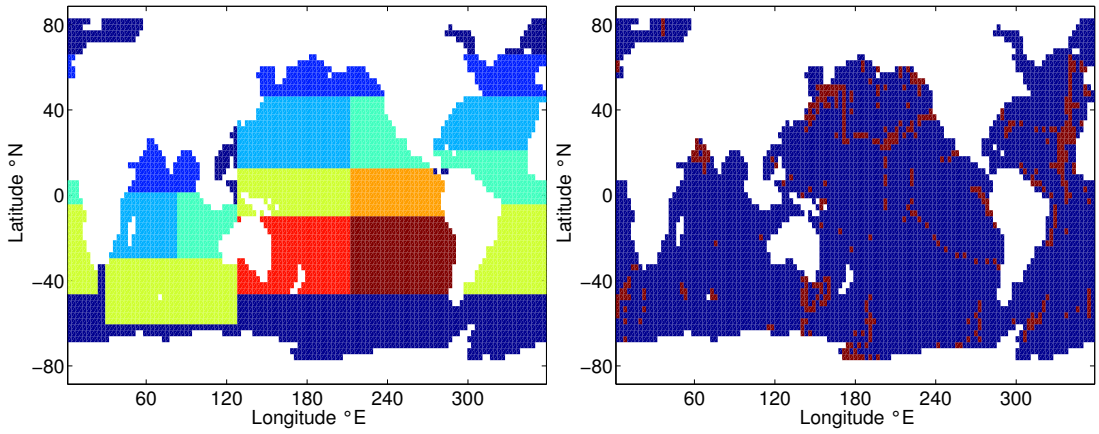

(a) Geographical regions **(b) Observation locations**

Figure 2.5: Plot showing, (a), regional binning of iron data (colours for illustrative purposes only), and, (b), actual data locations (Red).

2.3 A global dataset

Tagliabue et al. (2012) compiled a global dataset of iron observations, a preliminary step towards a climatology for iron, like those that exist for the hydrography and macronutrients. There was recognition of iron as a major limiting, or co-limiting, nutrient in large areas of the ocean following Martin (1990). The difficulties when trying to accurately determine concentrations from water samples have made it very difficult to build a comprehensive global survey of iron. This is changing now with contributions from the GEOTRACES programme adding to existing iron datasets. A more thorough coverage of iron concentrations across the globe will soon exist. Until that time, the work of

Tagliabue et al. (2012) has been invaluable to allow access to large amounts of global iron data for observationalists and modellers. In this section I take on the geographical framework defined in table 2.1 and displayed in figure 2.5a, along with the partitioning of data into depth bins, 0 to 120m, 120 to 550m, 550 to 1080m, 1080 to 2250m and 2250m+, to explore the large-scale distribution of iron across the globe, including seasonal variability where data permits. The conclusions from section 2.2 are also used to provide an insight into the reasons behind large-scale iron distributions. The distribution of the observations in the dataset are shown in figure 2.5b.

2.3.1 Methods

The data were first grouped into geographical regions, reflecting physical and biogeochemical regimes. The aim of this data binning is to try to isolate first order variability, as a result of the effects discussed previously in this chapter. This enables discussion about further processes and allows meaningful comparison between geographical regions. The data were further binned into depth layers, again to group depth layers where similar processes will dominate. The reasons behind the depth bin choices are strongly linked to processes that affect the distribution of iron in the ocean.

The surface bin, from 0 to 120m, is where the large majority of biological activity occurs. Biological activity affects the cycling of iron, affecting the export and retention of nutrients. In addition to this the largest supply of sedimentary and aeolian iron occur near the surface.

There is considerably less primary production below the surface layer, from 120 to 550m, although there is still significant biological activity from heterotrophic organisms able to function without light. There is remineralisation of particulate organic matter that leaves the surface layer (Boyd and Ellwood, 2010). This reintroduction of inorganic nutrients, including iron, leads to a subsurface increase in concentrations. The depths down to 500m are also where sediment supply is still important.

Table 2.1: Table detailing geographical breakdown of the iron database, based on large-scale nutrient regimes and circulatory features. The table provides regional coordinates and estimates of iron sources.

Region	Lat. limits	Lon. limits	Iron Sources, $Mt\ yr^{-1}$			Other features
			Atm.	Hyd.	Sed.	
North Subpolar Atlantic	45 to 65°N	-	73	3	33	North Atlantic Drift
North Subtropical Atlantic	20 to 45°N	-	328	4	25	Gulf of Mexico
Tropical Atlantic	5°S to 20°N	-	576	9	19	Gulf of Guinea upwelling
South Subtropical Atlantic	5 to 45°S	-	12	11	20	Agulhas Rings
North Subpolar Pacific	45 to 65°N	-	67	1	38	Aleutian Upwelling
Northwest Subtropical Pacific	10 to 45°N	W. of 290°E	114	5	7	Japanese upwelling
Northeast Subtropical Pacific	10 to 45°N	E. of 290°E	23	11	3	Californian Upwelling
Western Central Pacific	10°S to 10°N	W. of 290°E	7	3	30	Equatorial current and Peruvian upwelling
Eastern Central Pacific	10°S to 10°N	E. of 290°E	29	28	2	Peruvian upwelling via Boundary current
Southwest Subtropical Pacific	10 to 45°S	W. of 290°E	64	9	25	Peruvian upwelling
Southeast Subtropical Pacific	10 to 45°S	E. of 290°E	48	48	4	as Peruvian upwelling

Basin-scale circulation can cause localised transport of nutrients in boundary currents. For example, long distance transport of residual nutrients via subsurface western boundary currents in the Atlantic, known as nutrient streams, (Pelegri et al., 1996; Pelegrí et al., 2006; Williams et al., 2006) often occur between 300 and 1200m, therefore the depth bin of 550 to 1080m can capture some of these processes.

Intermediate water-masses influence depths between 1080 to 2250m providing a redistribution of subducted nutrients. At these depth levels there is a reduction in dissolved iron concentrations, contrasting with the generic nutrient-like profile of macronutrients. This is a consequence of the removal of dissolved iron by particles.

At depths greater than 2250m, the hydrothermal supplies will provide iron. Following the fallout of particulate iron through the dual processes of biological export and particle scavenging, remineralisation of particles augments deep dissolved iron reservoirs. This regeneration of particulate material is seen in observed Apparent Oxygen Utilisation, AOU, (Figure 2.6) with strong respiration beneath areas of strong biological activity in deep waters where dissolved organic nutrients and particles can accumulate through transport and fallout.

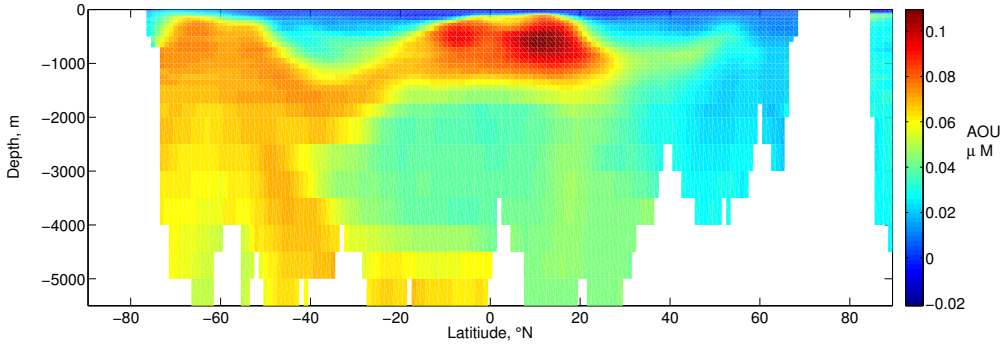

Figure 2.6: Apparent Oxygen Utilisation from the World Ocean Atlas 2009, (Garcia et al., 2010)

Once the data had been binned according to depth and geographical region it can be presented in the form of box and whisker plots. These box and whisker plots enable provision of several aspects of a particular subset of the

data. The red line in the middle of the box represents the median value of the dataset. The box itself represents the interquartile range, i.e. the 25th and 75th percentiles. The whiskers show the range of the data excluding points considered ”outliers”. Any points outside +/-2.7 σ are considered to be outliers.

2.3.2 Atlantic Ocean

Order of magnitude predictions of iron distributions were made from the iron source fields in section 2.2.4. The box and whisker plots for the four regions of the Atlantic were analysed with respect to these approximations to provide qualification of these crude estimates.

The northern subpolar gyre region has low atmospheric sources, a strong shallow hydrothermal source as a result of the activity on the Reykjanes ridge and moderate supplies of sediment from the north-west european shelf. There is also the possibility of a signal of iron from the sediment sources around Newfoundland being carried into the sub polar gyre via the North Atlantic Current (NAC). The observed surface iron concentrations in the sub-polar gyre are the highest surface values for the whole of the Atlantic subset (Figure 2.7a). This signal could well be a consequence of the Eyjafjalljokull Volcanic eruption which took place during April and May 2010, the period which the entire data for this region was collected, in addition to strong, shallow hydrothermal sources in the area (Tagliabue et al., 2010). The limited amount of data available for the Sub-polar gyre means there could be some bias towards atypical conditions as a result of the volcanic eruption (Achterberg et al., 2013).

The Northern subtropical gyre region has a very high supply of atmospheric iron. There is very little hydrothermal influence in this region, but significant sediment sources from the east of the North American continental shelf. A stream of sedimentary material could be carried into the subtropical gyre from the Gulf of Mexico by the Gulf Stream. Despite the apparent abundance of iron supplies the surface concentrations of iron here are lower than the sub-polar gyre. The North Atlantic subtropical gyre is an oligotrophic region, with very low

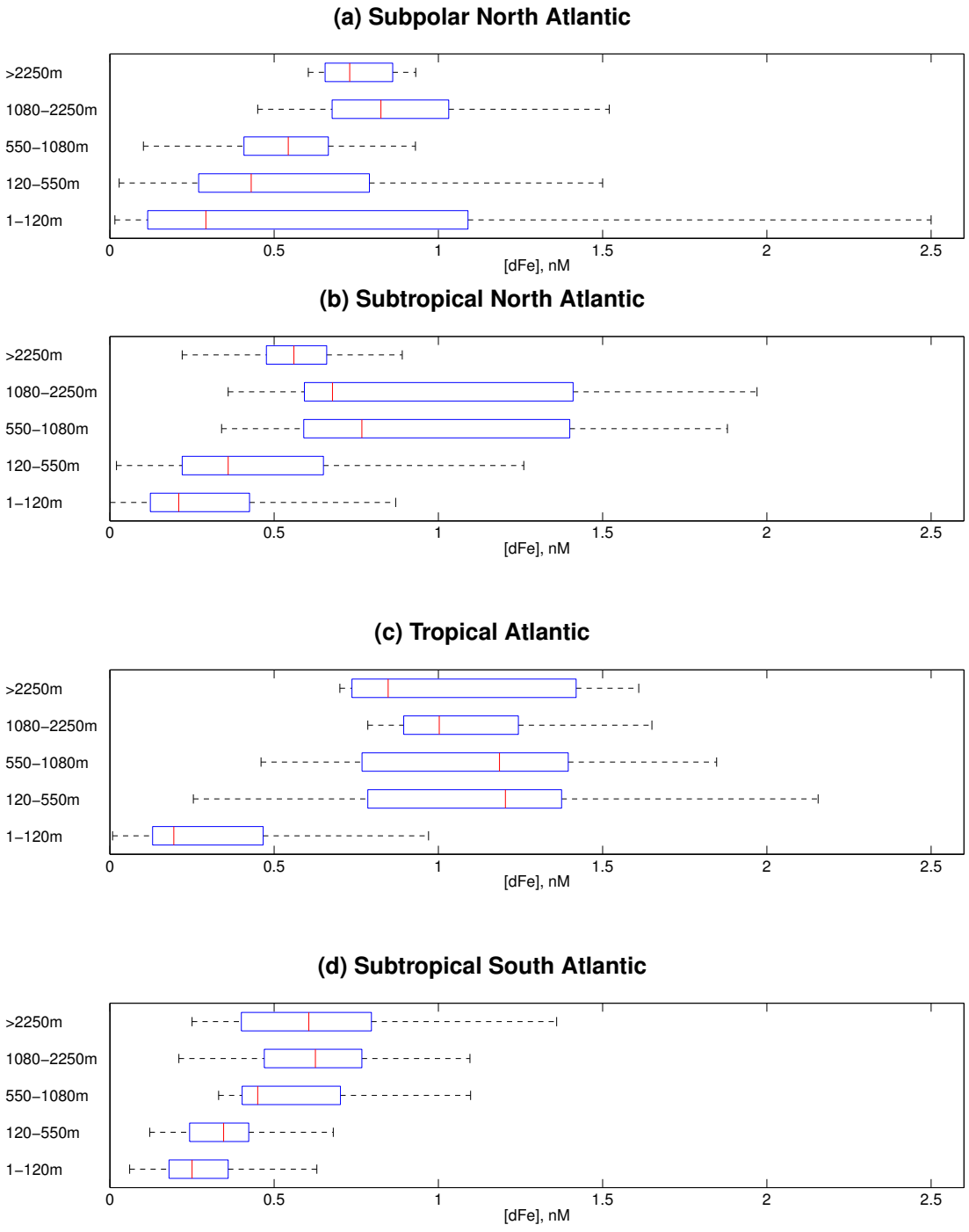

Figure 2.7: Boxplots showing annual mean iron at 120m, 120 to 550m, 550 to 1080m, 1080 to 2250m and >2250m depths for Atlantic regions. Red line indicates median value, the box represents upper and lower quartiles and whiskers represent spread of data excepting outliers.

amounts of residual nutrients residing in the centre of the gyre. The low surface iron concentrations are explained by the fact that the biology in the region utilise

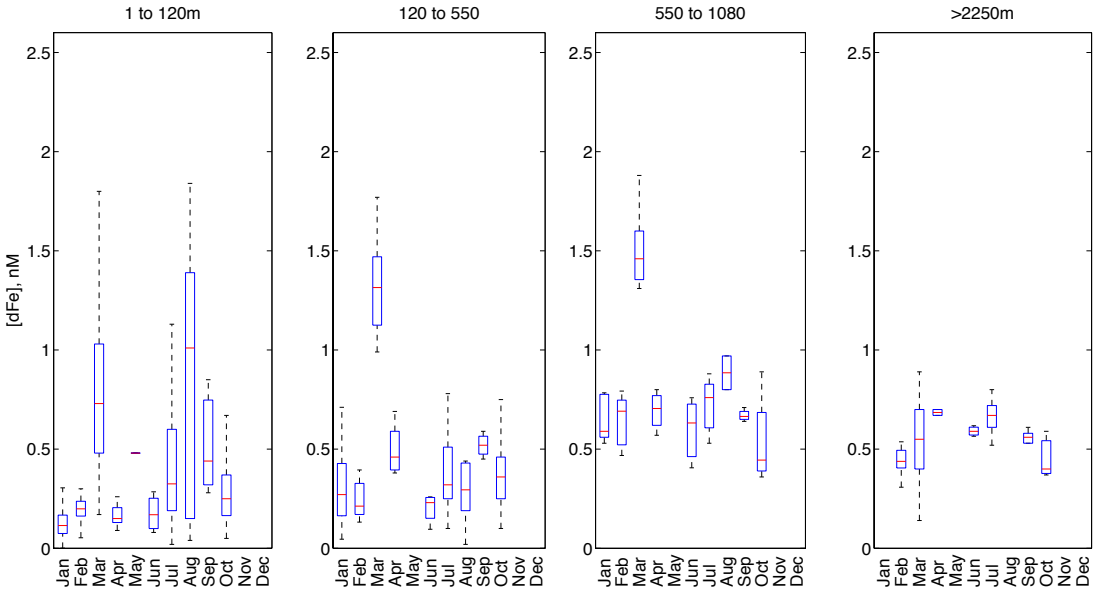

Figure 2.8: Boxplots showing available monthly data ranges for iron at 120m, 120 to 550m, 550 to 1080m, and >2250m in the Atlantic North subtropical gyre. Red line indicates median value, the box represents upper and lower quartiles and whiskers represent spread of data excepting outliers.

iron in the system alongside the effects of particle scavenging and deep winter convective mixing (Sedwick et al., 2005). In effect, iron concentrations remain low along with limiting macronutrients despite the large aeolian supply.

Between 120 and 550m depth the average iron concentration remains low (0.2 to 0.3 nM, but there is a large range of observed values, up to 1.2 nM. This signal might indicate sporadic recycling and regeneration of nutrients occurring in the upper regions of the thermocline, or alternatively represent the time-varying physical processes that act to induct nutrients into, or remove nutrients from, the surface mixed-layer, depending on the respective concentrations above and below the thermocline. These processes can often inject nutrient rich water from deeper regions into shallower waters. Strong deep winter mixing occurs most years in the Labrador and Irminger Basins of the sub polar gyre, and to a lesser extent in the Subtropical Gyre. With evidence for the supply of macronutrients across the gyre boundary (Palter et al., 2011) there could also be an iron signal related to these transfers of nutrients to the subtropical gyre. Thickening of the mixed layer occurs at the

end of the cooling period, i.e. February to March in the Northern Hemisphere.

To elucidate the reasons for this large variability of subsurface iron concentrations in the northern subtropical gyre, we consider monthly values for this subset, shown in figure 2.8. These plots show that the variability in subsurface iron is created by significantly higher concentrations observed in March relative to any other month of the year. This supply of iron from deep waters to the subsurface layers might result from a winter mixing event or from winter storms causing disturbances to continental-shelf sediments. With hydrothermal sources low and lacking seasonality in this region, and atmospheric sources mainly affecting surface regions, physical processes or sediment supplies are the probable cause of the high concentrations in the subsurface of the subtropical gyre.

The tropical region's proximity to the Sahara results in very large quantities of dust being deposited, specifically dust that may be immature with respect to the atmospheric processing that affects the solubility of iron (Zhu et al., 1992; Zhuang et al., 1992; Sullivan et al., 2007). Although the magnitude of the supply is very large it seems from figure 2.7c that the surface does not exhibit particularly high iron concentrations. Although the proximity to the source of the dust is beneficial, it also results in relatively little atmospheric processing. As a result the solubility of the iron is low. The actual impact on iron concentrations seen in the surface is minimal, with many of the particles falling through the surface mixed-layer without much iron dissolving into the water (Schlosser et al., 2014).

A further problem with excessive dust particle supply is that it results in an increase in particle scavenging, depending on the previous atmospheric deposition history of the region and the resulting response of phytoplankton (Ye et al., 2011). Despite this paradox between the high atmospheric supply and low surface iron concentrations, there is a noticeable impact of the atmospheric source deeper in the water column. The low solubility dust particles continue to fall through the ocean, consequently the timescale over which these particles can be remineralised is more comparable to its residence time in the deep

waters than surface waters. The short residence time in the surface layer is insufficient for dissolution of iron to occur to a great extent. The increased scavenging experienced in the surface and subsurface levels also results in an increase of iron at depth, as these particles are remineralised. This depth dependence adds to a growing reservoir of iron in the deep water masses of the Atlantic.

The high values of iron seen between 120 and 550m are probably sustained by upwelling in the Gulf of Guinea. This process allows iron-rich deep waters to be injected into shallower waters. This signal is lost in the surface layer due to the effect of increased particle scavenging by dust particles. The southern subtropical region also has a supply of dust, that originates from the Patagonian desert, into the Southwest Atlantic Ocean, as well as a significant sedimentary source that originates from South America. The magnitude of the sources in this region are smaller than those seen elsewhere in the Atlantic basin; as a consequence the concentrations of iron seen here are low compared to the other regions. The iron concentrations here show a nutrient-like profile with evidence of subsurface scavenging eroding the gradient of the slope between the surface minimum and thermocline maximum (Figure 2.7d).

The deep water signals seen across the regions hint at a contrasting influence of North Atlantic Deep Water (NADW) and Antarctic Bottom Water (AABW). The difference between the deep water iron concentrations seen in the tropical region and the Southern Subtropical Gyre region show that the relatively iron-rich southward flowing NADW influences the conditions in the tropics. However, in the Southern Subtropical gyre, lower iron concentrations are seen due to the increased influence of the iron-poor AABW relative to the NADW.

2.3.3 Pacific Ocean

With respect to sources there are two major differences between the Pacific and Atlantic oceans. Firstly, the Atlantic receives a much greater amount

of terrigenous dust from the Sahara, Namibian and Patagonian deserts. Contrastingly, the Pacific has a much greater source from hydrothermal vent systems located along the ring of fire that encircles the ocean. Traditionally, the emphasis has been placed on atmospheric sources as the major driver of iron distribution (Bruland et al., 1994; Boyle, 1997; Parekh et al., 2004), which would point towards higher levels in the Atlantic ocean. This first order approximation is seen when comparing figures 2.7 and 2.9, particularly when comparing the Northern Subtropical and Tropical/Equatorial regions.

The Pacific sub polar region, however, shows a contrasting view. The Pacific and Atlantic sub polar regions are both areas of upwelling and deep winter convection, however the Pacific gyre convection is often inhibited by the freshness of the surface waters. This suggests that there could be an influence of nutrient-rich water coming to the end of its journey across the bottom of the world's oceans, via the global scale thermohaline circulation, in the North Pacific. It is likely, however, that the significant amounts of sedimentary sources from the relatively shallow continental shelf of the Bering sea and Sea of Okhotsk, will also provide iron to the Pacific sub polar gyre.

The northern subtropical gyre of the Pacific is a significant circulatory feature, covering a huge area and encompassing different possible processes that will affect the iron distribution. The gyre is separated into an east and west area, using a longitudinal partitioning at 210°E. The Western region has more atmospheric supply from the Asian continent.The Eastern region has significant hydrothermal supplies, where the Pacific Plate contacts the North American Plate near the US west coast. There are upwelling areas in both the west and east, along the Japanese shelf slope and the California upwelling respectively. Figure 2.10 shows that the east of the North Subtropical Gyre has greater concentrations as well as greater variability compared to the west. In the east the California upwelling and hydrothermal supply augment the surface and deep waters, respectively.

The Equatorial Pacific has also been divided longitudinally in the same way as the North Subtropical Gyre, though a limited amount of observations,

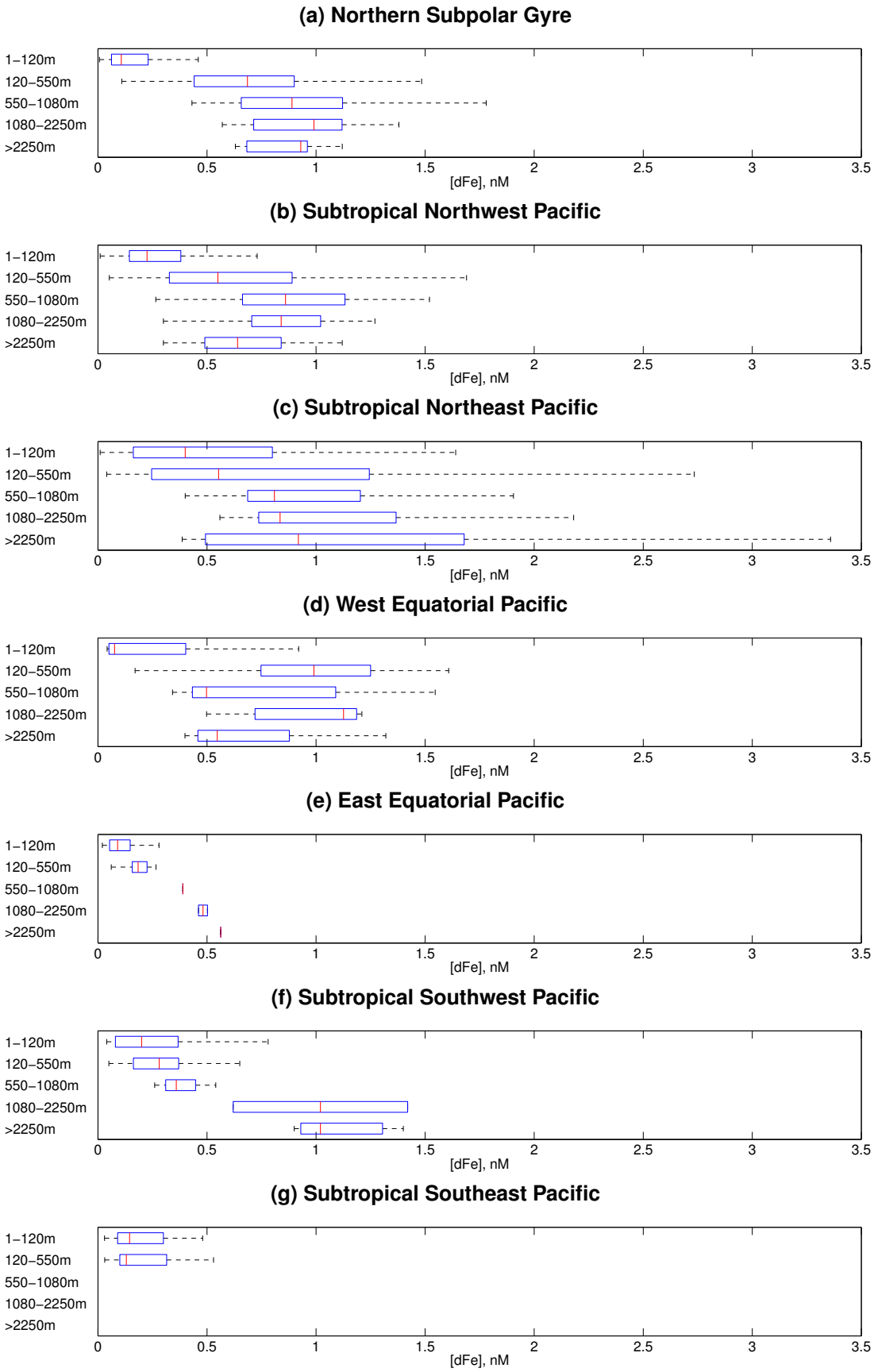

Figure 2.9: Boxplots showing annual mean iron at 120m, 120 to 550m, 550 to 1080m, 1080 to 2250m and >2250m depths for Pacific regions. Red line indicates median value, the box represents upper and lower quartiles and whiskers represent spread of data excepting outliers.

particularly in the eastern region, limits the number of inferences that can be made. Moderately active hydrothermal vents on the boundary between the Cocos Plate and the Nazca Plate (west of the Central American isthmus), as well as circulation bringing nutrient-rich water from the Peruvian upwelling zone to the south of the region, would be shown in elevated iron concentrations to the east. The data in Tagliabue et al. (2012) for this region does not show these signals.

With limited seasonality in the equatorial regions it is harder to observe large variability in nutrient concentrations unless there is a temporal variation in the iron supply. Inter-annual variability in the upwelling regime could provide this variance. There is limited temporal variation in the observations for the East Equatorial Pacific, so the most obvious explanation for the low concentrations of iron in this region is the biological consumption of iron in the surface water. The influx of nutrient rich water from the Peruvian upwelling region might result in significant consumption of all nutrients until one of them becomes limiting. In addition, the upwelled waters in the south of the Peru coastal region are lacking a shelf source, due to the narrow continental shelf in this region. With surface iron concentrations rarely above 0.2 nM this upwelling of iron-depleted water affects the concentrations found in the surface waters of the region (Bruland et al., 2005).

The Pacific Equatorial current transports water from the east of the basin across to the west, which probably transports iron-depleted waters westward. Traditionally, this current is thought to transport excess macro-nutrients from the upwelling zone across the otherwise nutrient poor Pacific. The primary production in this region exceeds that seen for the LNLC subtropical gyres, perhaps as a result of the iron supply from hydrothermal vents. Looking towards the destination of this nutrient-rich, but potentially iron-poor water, one would expect to see similar nutrient patterns; so why do we see higher concentrations of iron?

This key contrast between the west and east Equatorial Pacific is a result of the relative sediment supplies. The West Equatorial Pacific has very large area of

(a) West of the North Pacific subtropical region

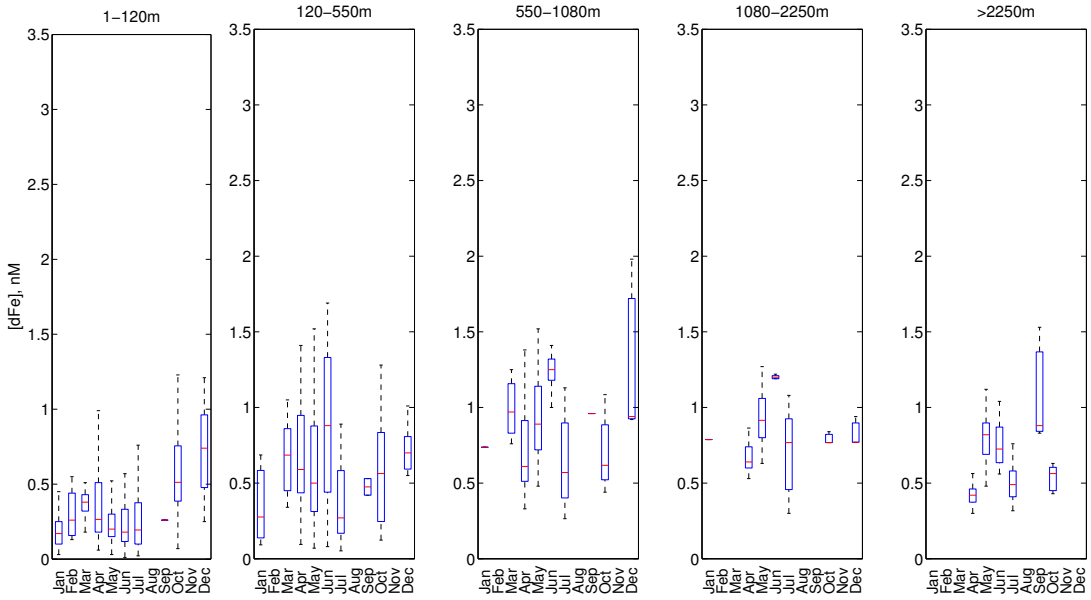

(b) East of the North Pacific subtropical region

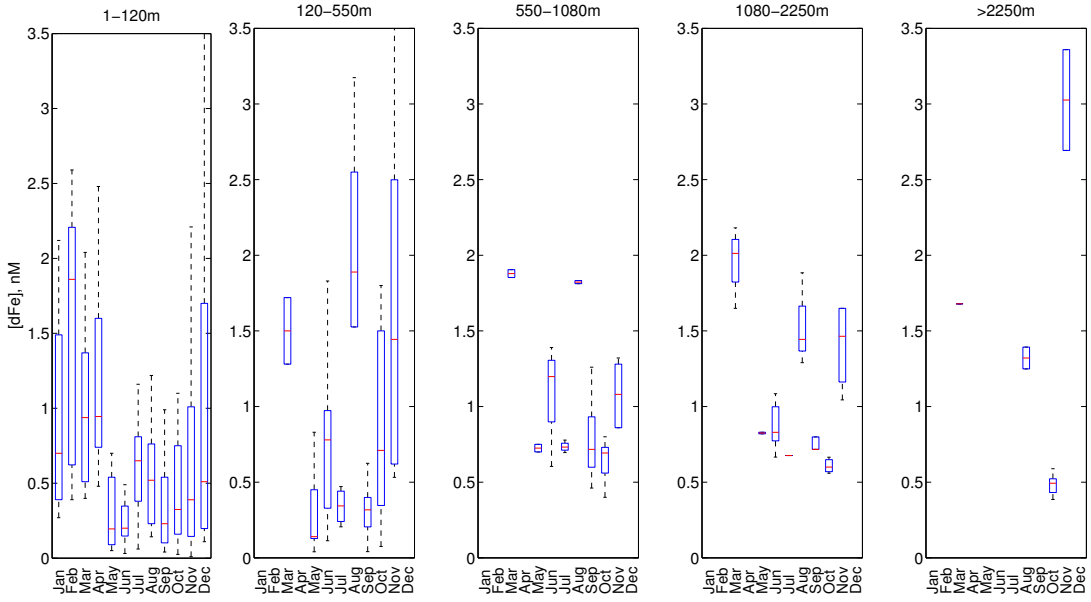

Figure 2.10: Boxplots showing available monthly data ranges for iron at 120m, 120 to 550m, 550 to 1080m, and >2250m in the Pacific North subtropical gyre. Red line indicates median value, the box represents upper and lower quartiles and whiskers represent spread of data excepting outliers.

shelf seas, around Malaysia, the Philippines and Papua New-Guinea etc, the water from which is fluxed into the open ocean by a combination of the New Guinea Coast Current (Kuroda, 2000), Taiwan Current (Yang et al., 1999) and North Equatorial Counter Current, which go in and around the islands gaining sedimentary iron before flowing eastwards back into the open ocean.

The Southern Subtropical Gyre of the Pacific is another oligotrophic region of the world's ocean. This area has the lowest amounts of atmospheric supply across the whole of the globe, with the exception of the remote areas of the Southern Ocean. There is an extremely large contribution at the base of the water column from hydrothermalism. The activity seen on the boundaries of the Nazca Plate, lying beneath the Eastern Subtropical Gyre, is the largest seen in the whole of the vent system. The Western Subtropical Gyre also gets hydrothermal supply from the southern and western boundaries of the Pacific plate. Unfortunately only a handful of data points exist in the East Subtropical Gyre region. However, there are enough data to show the low values of surface iron, which are indicative of many oligotrophic regions.

The West Subtropical Gyre also exhibits these very low surface iron concentrations, but with the existence of observations in the deeper layers, the strong augmentation of iron at these levels by hydrothermalism is very apparent. The concentrations observed here are some of the highest seen across the whole of the Pacific, with concentrations greater than $1nM$. The data for the 1080 to 2250m depth layer should be considered with the knowledge that there are very few observations. In fact, the distribution comes from two observations that fall into the region. The depth layer deeper than 2250m has a more robust subset of data, reenforcing the inference that hydrothermal vent systems have a strong influence in this region.

2.4 The Sub-Polar North Atlantic

2.4.1 Introduction

Using physical tracers the underlying physical system observed in the sub-polar gyre of the North Atlantic is described. The Irminger and Iceland Basins are regions that make up part of the area known as the sub-polar gyre. The circulation in this region is cyclonic; the North Atlantic Drift constituting the southern limb of the gyre before the route of the circulation turns westwards and navigates around the top of the Iceland Basin, down and over the Reykjanes ridge. The flow then circles the Irminger Basin before rounding Cape Farewell and circulating the Labrador Sea returning southwards along the eastern coast of the North American continent.

Two cruises took place during spring, 26th April to 9th May (D350), and summer, 4th July to 11th August (D354), 2010. These cruises were part of the Irminger Basin Iron Study, which aimed to gain understanding of the biogeochemical environment, particularly with respect to iron, in the sub-polar North Atlantic. The data from this cruise is processed and analysed here with respect to the physics of the region. The analysis of the temperature and salinity fields provides evidence of the different water masses that are present and hence the origin of the waters in the study region. Potential temperature-salinity and potential temperature-oxygen plots have been produced to enable identification of water mass end-members. The sections used in the analysis can be seen on figure 2.11, these sections were retrospectively defined from the array of CTDs that were deployed during the cruise.

During D350 and D354 iron and aluminium data were collected by Sebastian Steigenberger and Jessica Klar, nutrient and dissolved oxygen data were collected by Mark Stinchcombe and Debbie Hembury and CTD and navigational data were collected and processed by Stephanie Henson, Stuart Painter and myself. The data presented in this section appear courtesy of

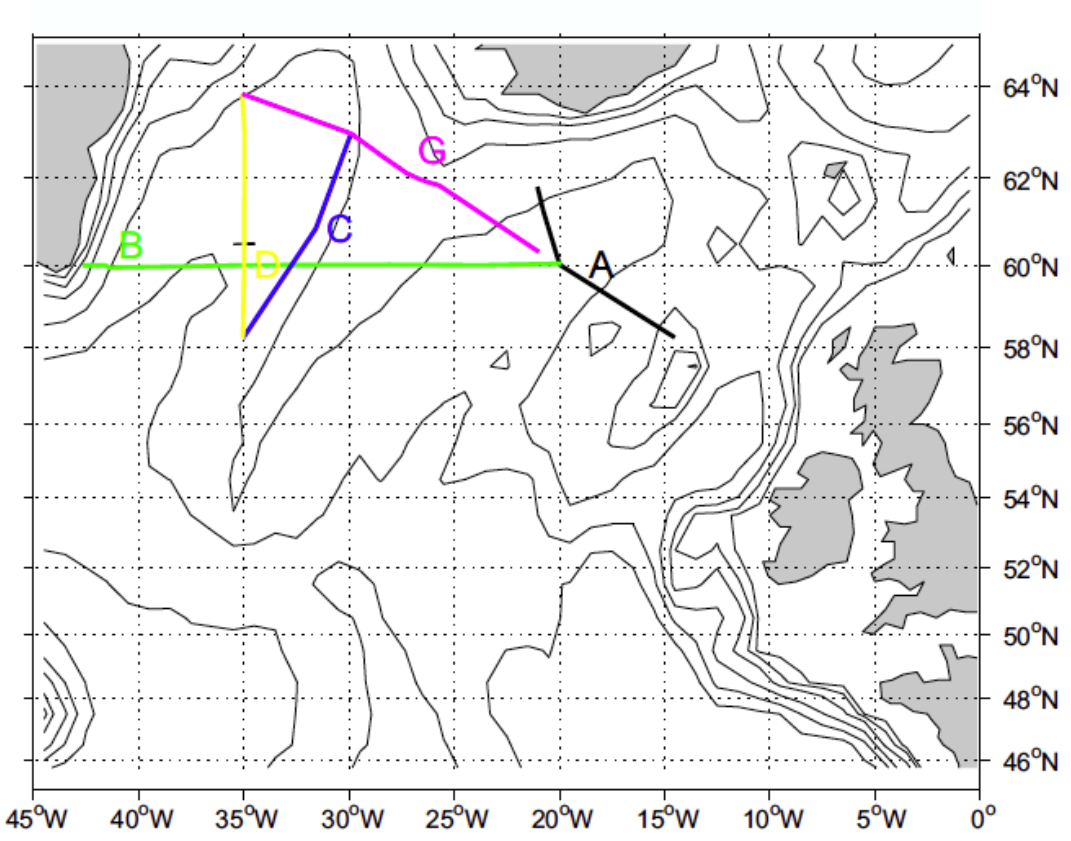

Figure 2.11: Showing the section locations used in this study. The map shows the North Atlantic. Greenland is in the top left and the UK mid-right.

those above.

2.4.2 Water masses of the region

It is worth providing information relating to water masses in the area to provide a basis for the discussions that follow regarding the potential temperature-salinity (T/S) and potential temperature-oxygen (T/O) plots. Table 2.2 provides information on water masses in the North Atlantic and Arctic Ocean regions and used in conjunction with annotated T/S and T/O plots can indicate the locations of specific water masses in T/S and T/O space, Figures 2.12 and 2.13. All abbreviations used for the water masses are included here and will be used throughout the rest of this chapter.

Table 2.2: Table detailing Water Mass Characteristics for North Atlantic

Water Mass, $Abbr.$	Potential Temperature Θ	Salinity (PSS)	Depth m	Oxygen, $\mu mol\ L^{-1}$	Notes
North Atlantic Central Water, $NACW$	6.9 to 13.9	34.9 to 35.8		252 to 291	
Modified North Atlantic Water, $MNAW$	7 to 8.5	35.1 to 35.5			
Labrador Sea Water, LSW	3 to 3.6	34.86 to 34.96		$>$ 275	
North Atlantic Deep Water, $NADW$	2.2 to 3.5	$>$ 34.9	1000 to 4000	$>$ 240	
Iceland-Scotland Overflow Water, $ISOW$	$>$2	$>$ 35			
Denmark Strait Overflow Water, $DSOW$	0 to 1	$\sim$ 34.9			
Arctic Intermediate Water, AIW	0 to 2	34.8 to 35			
Polar Intermediate Water, PIW	$\sim$ 0	34.4 to 34.7			
Norwegian Sea Deep Water, $NSDW$	$<$ 0	34.9 to 34.94			

Potential temperature-salinity and potential temperature-oxygen plots have particular features that can be used to identify water masses. The scatter of the data allows definition of end-members at the points where lines of data meet. These end-members represent the ideal characteristics of a known water mass. Often the line in between these represent the interface between two water masses; in this instance commonly in the vertical plane due to the fact the data was collected from CTDs and therefore has a high resolution in the vertical as opposed to the horizontal.

Of the two property-property plots the most frequently used is the T/S plots. The entirety of the T/S data from the sub polar gyre summer cruise are presented here in combination with pressure data to indicate the water-mass distribution of the region, Figure 2.12. All CTD cast profiles are presented here, and as the data shows there is evidence of Modified North Atlantic Water (MNAW) throughout all of the CTD casts in the sub polar gyre. MNAW is a highly variable water mass, particularly with respect to salinity, due to its proximity to the surface. Surface freshening of water by evaporation and precipitation causes the salinity of MNAW to vary between 35.1 and 35.5 PSS. MNAW has potential temperature values of between 7 and 8.5 Θ, with any water warmer or saltier than MNAW generally classified as surface water. The one exception to this generalisation being the evidence of North Atlantic Central Water (NACW) seen in a station to the far east of the study region.

A Labrador Sea Water (LSW) end-member, named due to its region of origin, is present beneath MNAW in the majority of stations, excepting shallow CTD casts. The transition between these two water masses is clear with a gradual decrease in salinity and temperature from MNAW to LSW at between 3 and 3.6 Θ and 34.86 and 34.96 PSS. A further end-member is evident at depths greater than LSW with similar temperature, but higher salinity. This water mass is North Atlantic Deep Water (NADW), which ordinarily is observed at potential temperatures of 2.2 to 3.5 Θ, salinities of $>$ 34.9 PSS and depths between 1000 and 4000m. NADW is formed by deep winter convection of water in the surface of the North Atlantic. This water mass then flows southwards

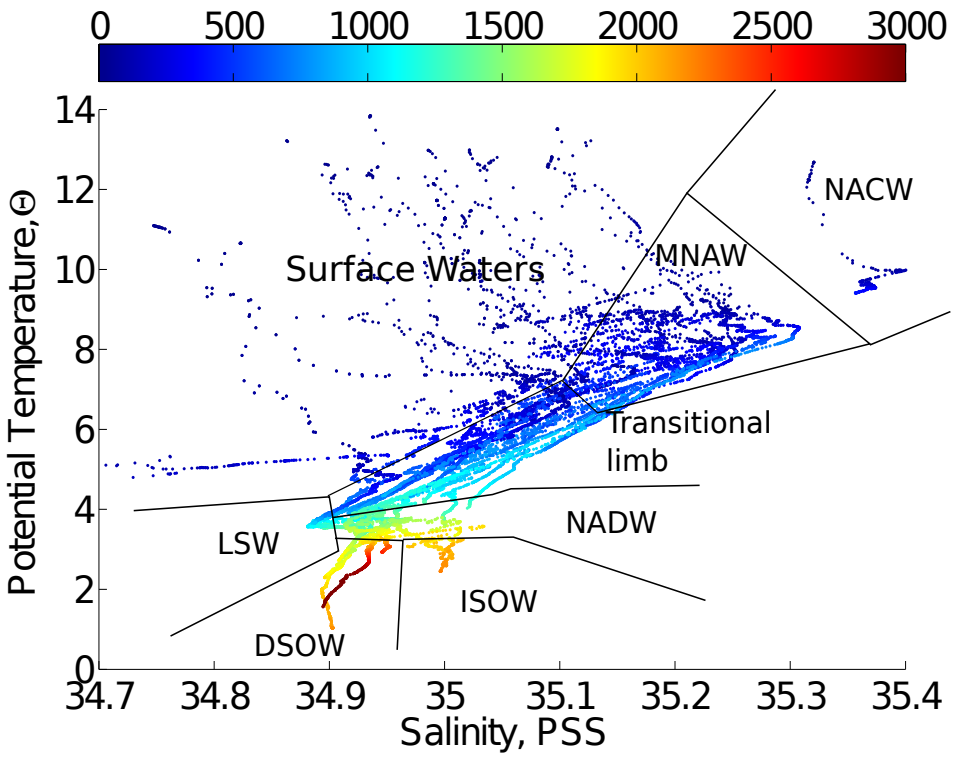

Figure 2.12: T/S plot coloured with pressure for D354 labelled with water mass information

throughout the entire Atlantic. NADW is less salty in the west due to the proximity to the relatively fresh LSW source region, the East Greenland Current (EGC), which brings fresh water of polar origin southwards, and the surface run-off from the Greenland shelf. Very deep water masses can be found in waters beneath NADW, and this is the case in the sub polar North Atlantic. There is evidence of two distinct overflow waters originating from the Arctic Ocean and differentiated between by their varying routes into the Atlantic Basin. Beneath NADW in the Irminger Basin tends to be Denmark Strait Overflow Water (DSOW), which has a salinity of 34.9 PSS and is the coldest water mass found in the region at between 0 and 1 Θ. Contrastingly there is Iceland Scotland Overflow Water (ISOW) present in the Iceland Basin, which is warmer, $>$ 2 Θ, and saltier, $>$ 35 PSS, than DSOW.

These two overflow waters both originate from the Arctic Ocean, but derive from different water masses. DSOW emerges from the the transport of Arctic Intermediate Water in to the Atlantic, resulting in a fresher profile compared to

the ISOW, which derives from Nordic Sea Deep Water and mixes with warm and salty NACW-derived water in the east of the basin.

T/O plots, here presented with longitude information, provide a different perspective relative to T/S plots and can show further variation within the traditional T/S-defined water mass classifications, Figure 2.13. The variation in oxygen, particularly in the MNAW-LSW transitional limb and the LSW end-member is evidence of the consumption of oxygen as LSW flows eastwards from its source region. The consumption of oxygen is strongest within the transitional limb as differences of 50 $\mu mol\ l^{-1}$ are seen between water of similar depth, salinity and potential temperature. The longitude differences illustrate the consumption of oxygen in the east relative to the west of the sub polar North Atlantic. Due to the absence of salinity data within the T/O plots, there is some difficulty in differentiating Iceland Basin (east) LSW and NADW because of the consumption of oxygen; approximately 20 $\mu mol\, l^{-1}$ is respired within LSW as it travels from west to east. The two overflow waters are similar with respect to oxygen and are almost indistinguishable when excepting the longitude of the data. The western overflow water, DSOW, has more oxygen present within it, though this is perhaps an artefact of the deeper casts, made in the Irminger Basin relative to the Iceland Basin.

2.4.3 Nutrient distributions

In this section the general nutrient distribution is described. Focus remains on sections A, B and D, providing information for each of the Irminger and Iceland Basins as well as a look at the inter-basin distribution. Plots of NO_2+NO_3, SiO_3 and PO_4 are included as well as an illustration of the N:P ratio.

$Iceland\ Basin : Section\ A$

The contour plots of these nutrients from section A are shown in figure 2.14. The nutricline depth is very similar between NO_2^-+NO_3^-, figure 2.14a, phosphate, figure 2.14c, with almost a total depletion of these nutrients at the very surface. The strongest gradient in nutrient concentrations lies at

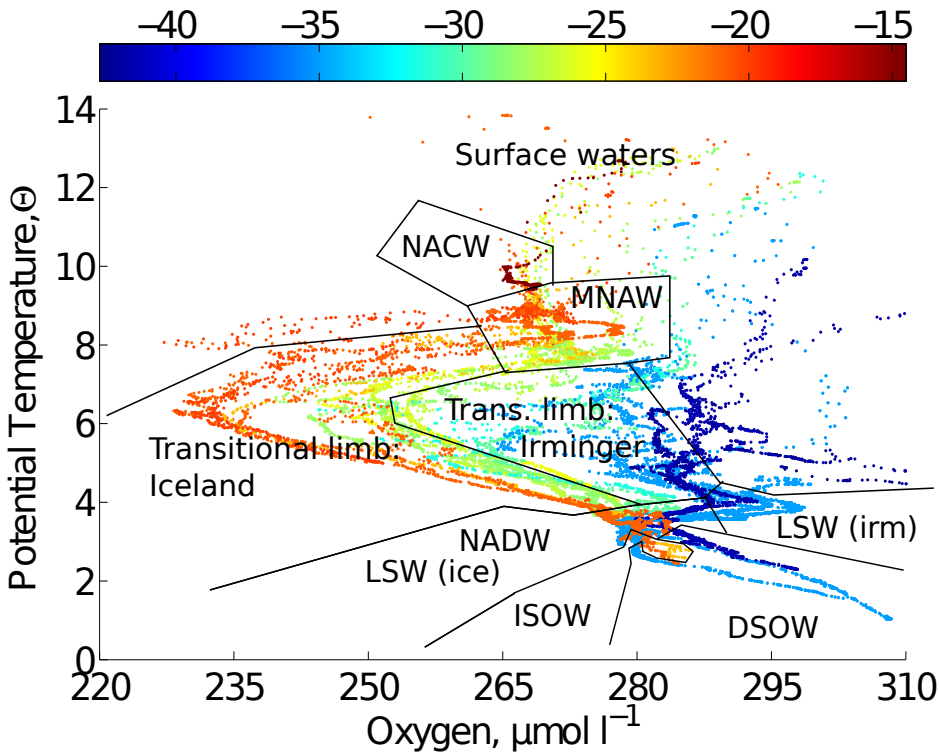

Figure 2.13: T/O plot coloured with pressure for D354 labelled with water mass information

about 30m depth. The depth at which these two nutrients are at the highest concentrations correspond; both have maximum concentrations between 500m and 1000m depths. The deep concentrations appear to have a minimum at the midpoint of the section. This signal is apparent in both the NO_2^-+NO_3^- and phosphate sections.

The nutricline is significantly deeper for silicate, figure 2.14b, with the steep gradient in silicate concentrations lying at ∼300m in the southernmost region of the section, 60°N, and ∼500m in the northern region of the domain, 62°N. The mid-depth maximum apparent in the other nutrients also appears in the silicate at the same depths between 500m and 1000m. However, this band of high silicate concentration is interrupted by the region of deep water with low nutrient concentrations that is also observed in the other nutrients. This region of low nutrient concentration, seen in the three nutrient sections presented here, is likely to be a result of ocean circulation transporting relatively nutrient depleted waters into the region. The position of Section A suggests that

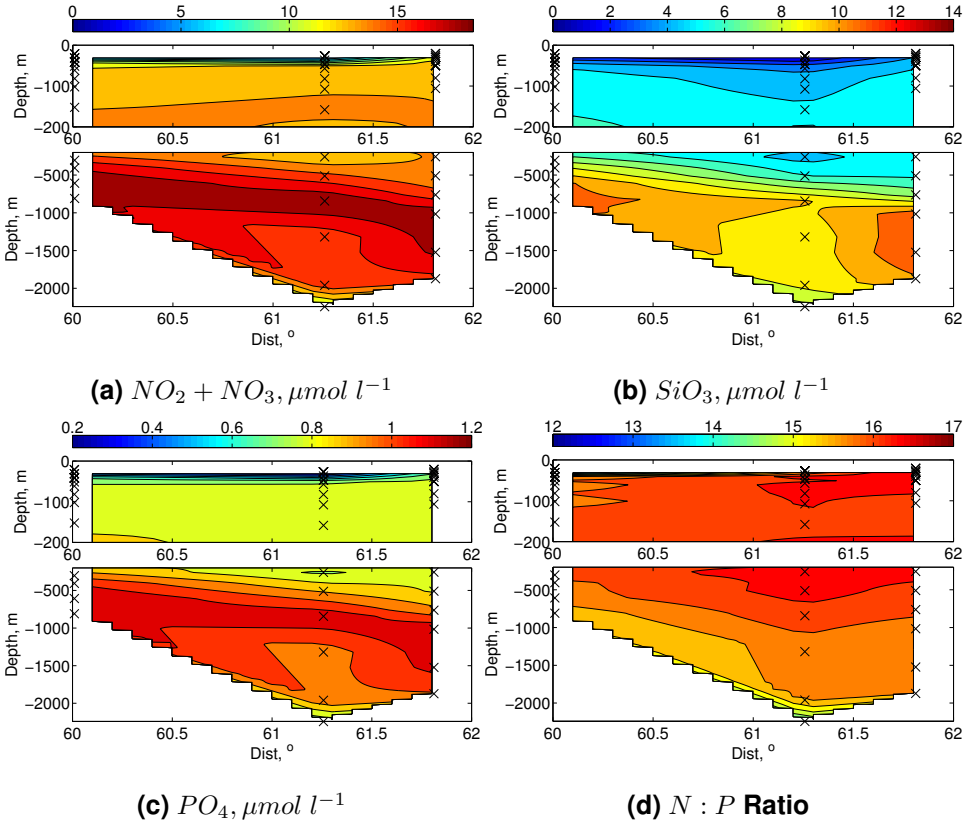

Figure 2.14: Section A Nutrient Sections. Black crosses represent bottle positions.

currents flowing from the south or east of the basin could be influencing the biogeochemistry of the Iceland Basin.

Figure 2.14d shows the relationship between NO_2^-+NO_3^- and phosphate. The ratio between the two does vary across the domain. In general the quantity of NO_2^-+NO_3^- is greater relative to phosphate in the northern region at depths of 10 to 100m and 200 to 500m where the N:P ratio is $\sim$16.5. At the very surface in the northern region the quantity is still $\sim$16.5 whereas there appears to be a very slight N/S surface gradient as it decreases to $\sim$16 in the middle of the section and down as low as $\sim$15.5 in the south of the region. The quantities in the southern region are lower than those for the respective depths in the middle and northern sections with the quantities being just in excess of 16. N:P of between 15.5 and 16.5 are consistent with the typical Redfield ratios and suggest the nutrients are consumed and regenerated in consistent quantities. Ratios consistent with Redfield suggest there may not be a depletion of one of the macronutrients with respect to another, i.e. that the

limitation of phytoplankton by either NO_2^-+NO_3^- or phosphate is uncommon, and that a general co-limitation is more likely to occur. This does not preclude the potential for iron limitation, which as suggested previously has been shown to occur in the Iceland Basin, (Nielsdóttir et al., 2009).

$60°N : Section\ B$

Like Section A the distributions of NO_2^-+NO_3^-, figure 2.15a, and phosphate, figure 2.15c, in particular are very similar. The nutricline for all the nutrients lies at an approximate depth of 50 to 80m across the majority of the section; the exception being the far west of the section where station locations approach the coast of Greenland where the terrestrial and circulatory characteristics related to the east coast of Greenland exert their influence. With respect to NO_2^-+NO_3^- and phosphate, mid-depth to deep waters ($>$500m) are relatively replete with nutrients, $>$14 $\mu mol\ l^{-1}$ and $>$ 1 $\mu mol\ l^{-1}$ respectively, with a very slight decrease in quantities at the base of the water column in deeper stations. There is also an apparent upwelling/non-utilisation of nutrients in waters west of $\sim$30°W; the Irminger Basin. At depths of 100 to 500m in the Irminger Basin concentrations are $\sim$14 to 15 $\mu mol\ l^{-1}$ and $\sim$0.9 to 1 $\mu mol\ l^{-1}$ respectively compared with $\sim$12 to 14 $\mu mol\ l^{-1}$ and $\sim$0.7 to 0.9 $\mu mol\ l^{-1}$ in the Iceland Basin. The distribution of silicate, figure 2.15b, follows a very similar pattern to the other two nutrients. However the contrast between high and low concentrations of silicate is greater compared to the other two nutrients. The deep waters of the silicate section do not demonstrate the same homogeneity as the other nutrients with the maximum, $\sim$14 $\mu mol\ l^{-1}$, lying at a depth of 2500m at 35°W. There is a greater gradient in the nutrient from this point up to 200m depth when compared with NO_2^-+NO_3^- and phosphate.

These observations show there is a definite contrast in the macronutrient environment between the Irminger and Iceland Basins. The surface concentrations are very similar, but there is a striking difference in the concentrations found between 100m and 1000m depth. The Irminger Basin has much higher concentrations relative to the Iceland Basin. The waters beneath 1000m are more homogenous showing that conditions in the two

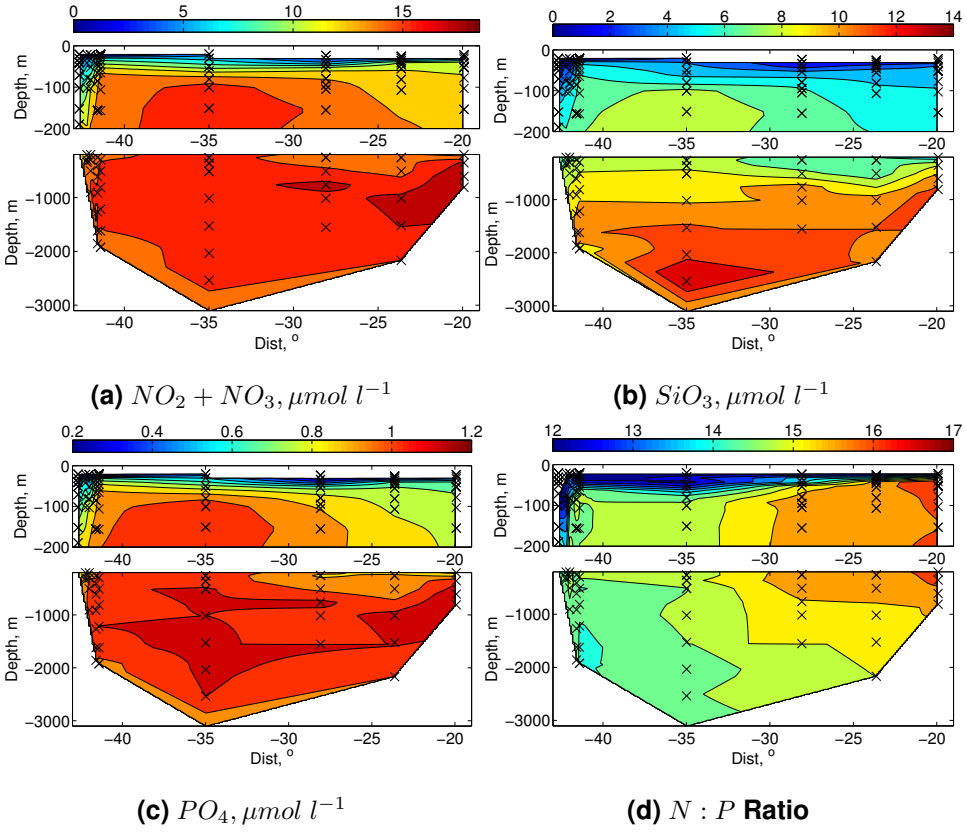

Figure 2.15: Section B Nutrient Sections. Black crosses represent bottle positions.

basins at this depth are similar. The region acts as a downwelling region in winter due to the surface cooling of the ocean in the sub polar North Atlantic. This results in very deep mixed layers and a well-mixed water column at the beginning of summer. The contrast between the basins suggests that the utilisation of nutrients in the Iceland Basin is quicker, resulting in depletion at mid-depths due to phytoplankton blooms in the spring when the mixed-layer can still be deep enough to tap into the subsurface nutrient reservoirs.

Figure 2.15d shows the N:P ratios for the domain and highlights a general pattern of higher N:P in the Iceland Basin when compared to the Irminger Basin. In addition to this there is evidence of surface-deep gradient in N:P in the Irminger Basin with the near-surface waters having lower values than the deep. The region under influence from the Greenland landmass and the EGC may be a factor in this surface phenomenon. In contrast the value of N:P in the Iceland Basin is not depth varying. The variation between the two basins is estimated at approximately 14.5 in the Irminger Basin and 16 in the Iceland

Basin. Considering the surface flows in the region there should be a supply of waters from the east (Iceland Basin) towards the west (Irminger Basin).

The North Atlantic is one of the globe's major regions for nitrogen-fixation, and as a result it would be unsurprising for waters to increase in nitrate and decrease in phosphate; i.e. an increase in N:P. What is evident here is the converse and so there must be another circulatory feature we can use to explain this variation. Yamamoto-Kawai et al. (2006) talk about the importance of the influx of phosphate rich waters from the Pacific Ocean via the Arctic Ocean as a fuel for the nitrogen-fixation that occurs in the North Atlantic. The LSW is one of the vehicles this process uses to distribute phosphate into the North Atlantic. The section supports the hypothesis that this N:P variation could be as a result of LSW waters traversing the basins, in the opposite direction to the surface waters, with nitrogen-fixation altering the N:P signal across the domain.

Section B highlights the importance of the physics in providing the conditions for two important characteristics of the nutrient regime in the sub polar North Atlantic. Firstly, the winter mixing provides a platform of homogeneity of macronutrient distributions upon which the biogeochemical regimes are imprinted. This highlights the veracity of spring growth in the Iceland basin relative to the Irminger Basin. Secondly, the supply and dissipation of Labrador Sea Water from west to east across the basins is characterised by a variation in the N:P ratios seen between the Irminger and Iceland Basins. This water, originating from the Polar regions, via the Canadian Archipelago, has lower values of N:P than the water masses native to the Iceland and Irminger basins. Thus, the influence of the LSW can be clearly seen in the N:P signal.

$Irminger\ Basin : Section\ D$

Like sections A and B, section D demonstrates striking similarities between the nutrient distribution patterns. As can be seen in the contour plots of NO_2^-+NO_3^-, silicate and phosphate in figures 2.16a, 2.16b and 2.16c respectively. NO_2^-+NO_3^- and PO_4 again have similar distributions. The deep

water concentrations are similar to those for section B, and like section B, there is a mid-section, 60°N 35°W, incursion of relatively nutrient-rich waters into the upper 500m of the water column. The nutricline lies at 50 to 80m depth throughout the section. Above this, in the surface waters, concentrations approach zero. The northern waters between 100m and 300m have a relatively low concentration of both of the nutrients when compared with the rest of the section.

The silicate section does not demonstrate the same homogeneity in the deep waters as the other nutrients. The maximum, $\sim$14 $\mu mol\ l^{-1}$, appears at 2500m depth but covers a larger area, stretching from 58°-60°N. Further north than this the concentrations are lower with a layer of water with a concentration of $\sim$10 $\mu mol\ l^{-1}$ reaching all the way along the section at a depth of 1500m. A mid-section region of elevated silicate concentration leads to a region further north with lower values. The contrast between the high and low concentrations at depths of 100m to 300m is not as great as in section B. The surface waters in the south of section D have concentrations close to 0 $\mu mol\ l^{-1}$; this region is that which is shared by the section B domain. In contrast the northern surface waters still have silicate present. In some areas concentrations approach 4 $\mu mol\ l^{-1}$.

The N:P ratio has an interesting pattern in Section D with a region of relatively low N:P covering the entire water column from the surface to the bottom. This region at 60°N separates two regions with higher values to the north and south. The surface at 60°N also has significantly low values of N:P which seems to spread outwards at the surface to a greater extent than the waters underneath, indicative of a surface source. This may result from continental surface run-off or the importance of the glacial melt-influenced surface currents flowing southwards along the Greenland Coast. Both of these phenomenon would provide a source of phosphate resulting in negative N:P anomalies like those that are seen. There is also an interesting patch of low N:P in the north of the region at $\sim$80m depth. This is contained within an area with a particularly high value of N:P. This is due to a relatively high level of PO_4, which upon

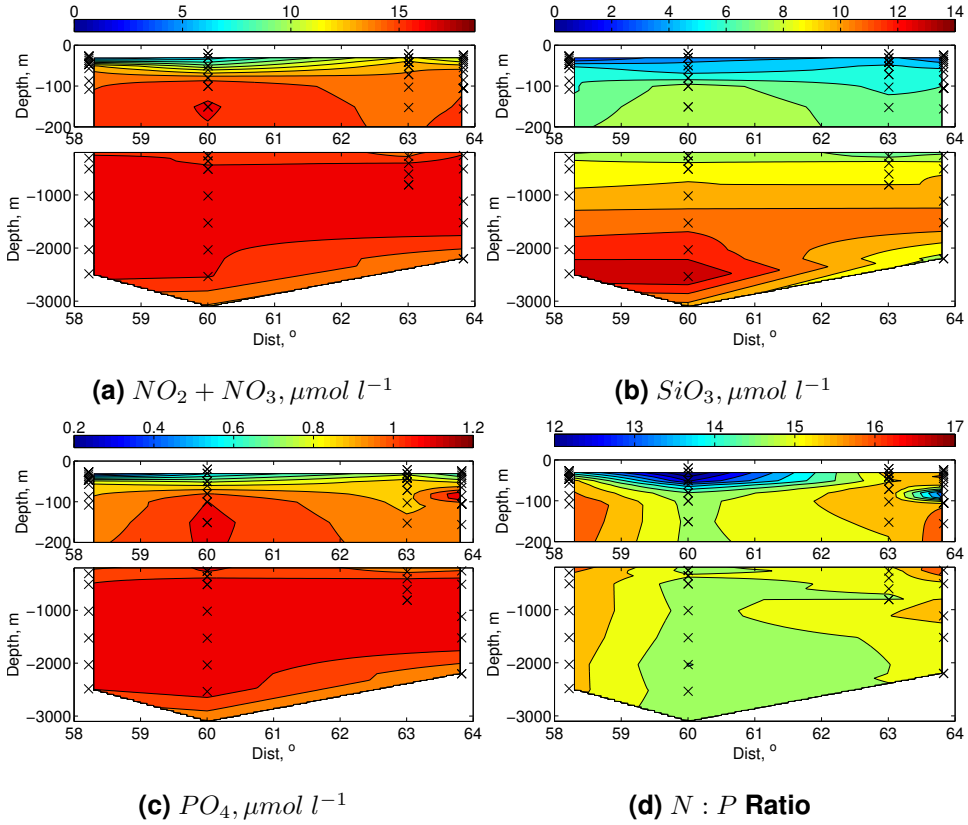

Figure 2.16: Section D Nutrient Sections. Black crosses represent bottle positions.

consultation with the raw data is not found to be anomalous. Considering the hypothesis that the low N:P signal is a tracer of LSW it is evident that the spread of LSW is concentrated at around 60°N. It is possible that this signal is altered by nitrogen-fixers to the north and south of this latitude or that they are further influenced by other processes to modify the N:P signal. The N:P signal seen in the LSW may be further influenced by surface run-off or glacial melt processes at the surface, which will produce water column variations between surface and deep water during spring and summer, but will be homogenised during deep winter convection processes.

2.4.4 Phosphate derivatives

Preformed and regenerated phosphate framework

Macronutrients can be decomposed into several derivatives that demonstrate the characteristics of particular biogeochemical regimes. The distribution of the

nutrient derivatives, specifically those applied to PO_4, are key for determining the spatial variability of the biogeochemistry. The concentration of an inorganic nutrient below the euphotic zone, for example PO_4, can be separated into two different components, the preformed PO_4^{pre} and regenerated PO_4^{reg} pools. The preformed nutrient is that which was in the water parcel at the time of subduction, whereas the regenerated nutrient is the result of the accumulated regeneration of organic matter since the water was subducted. The total PO_4 concentration is the sum of these two components. Nutrient utilisation in a particular water parcel can then be defined using P^*, the ratio between the regenerated PO_4 and the total PO_4 concentration,

$$P^* = \frac{PO_4^{reg}}{PO_4}. \tag{2.1}$$

The fraction of the subsurface PO_4 reservoir that is regenerated indicates what fraction of the nutrient has been recycled from organic material. In effect, this represents the efficiency of nutrient utilisation within a particular water parcel. If the concentration of PO_4^{reg} is the same as the concentration of total PO_4, then all of the nutrient in that water parcel has been regenerated, thus there was no PO_4 present in the water parcel when it left the surface. In effect, all of the surface nutrient pool was utilised and a 100 % nutrient utilisation efficiency was achieved. In this scenario the entirety of the reservoir has accumulated from respiration of organic material beneath the surface; P^* = 1. The opposite extreme is that there has been no utilisation of surface PO_4 prior to the water parcel being subducted. Due to the lack of nutrient utilisation there will be little or no organic matter that can be regenerated, thus $PO_4^{reg} \approx 0$, and $P^* \approx 0$. P^* should always lie between 0 and 1, and can be used as an indicate of the percentage nutrient utilisation within a subducted water parcel.

To estimate the regenerated component of PO_4 we need to consult the oxygen data. Regeneration of inorganic nutrients is accompanied by consumption of dissolved oxygen. The relationship between dissolved oxygen and dissolved inorganic nutrients means that we can estimate regenerated nutrient using the quantity of regenerated oxygen and an estimation of the redfield ratio of P:O_2. Total dissolved oxygen, like macronutrient, is composed of preformed

and regenerated pools. Oxygen concentrations at the surface are at saturation point as a result of the rapid equilibration of O_2 between the surface ocean and the atmosphere. Therefore, assuming $O_2^{pre} \approx O_2^{sat}$, the regenerated component of the dissolved oxygen is simply this quantity subtracted from the total dissolved oxygen concentration, $O_2^{reg} = O_2^{total} - O_2^{pre}$.

When these derivatives are calculated for PO_4, they aid understanding of the nutrient environment in the region and can provide a measure of the efficiency of nutrient utilisation in different nutrient regimes. Using these quantities, particularly P^*, we can easily plot the values onto T/S or T/O plots to investigate the influence of particular water masses on the nutrient environment and phytoplankton growth.

Entire Domain

T/S and T/O plots of the whole domain coloured by P^* are presented here, Figures 2.17a and 2.17b. The differences between the different water masses and the Irminger and Iceland Basin, with regards to the efficiency of nutrient utilisation and biological activity, are shown.

The relationship of P^* to the water masses is best shown using a T/S plot, Figure 2.17a. The highest values of P^* occur in LSW to MNAW transitional waters as well as occurring in the potential ISOW transitional water. These top values are present in the Iceland Basin and not observed to the same extent in the transitional waters of the Irminger Basin. The DSOW end-member has a P^* value of$\sim$0.25 to 0.27; evidence of this exists in numerous stations. The NADW has a very consistent P^* across the whole domain. The end-member apparent on the T/S diagram suggests P^* values of a similar, but slightly greater, magnitude to the DSOW at $\sim$0.26 to 0.29. The value for P^* varies in the end-member that denotes LSW. The variation follows the observed general pattern of Irminger to Iceland Basin variation. P^* in LSW is approximately 0.27 to 0.3 in the Iceland Basin compared with 0.2 in the Irminger Basin. The MNAW end-member seems to display inter-basin similarity with a P^* value of $\sim$0.15 to 0.17 evident throughout the whole domain.

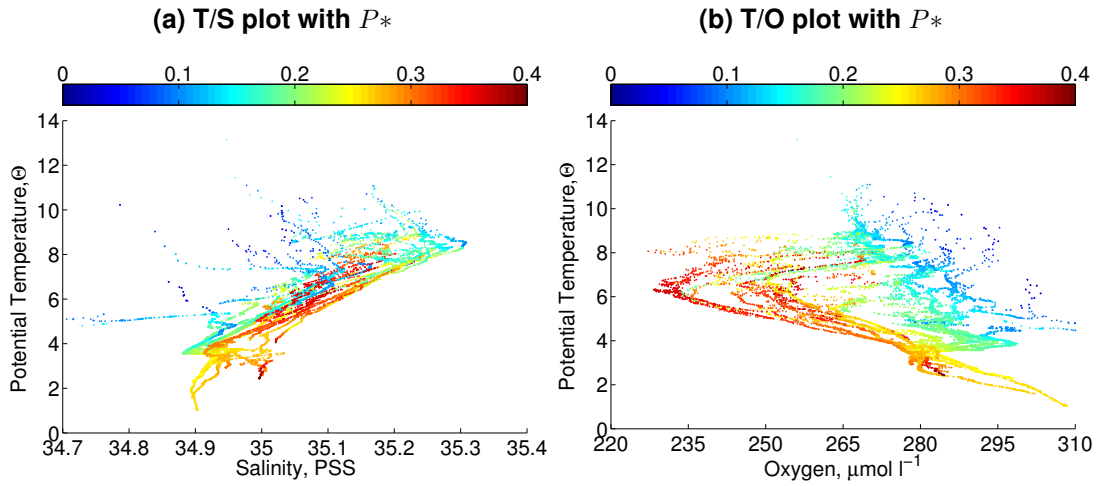

Figure 2.17: Temperature-salinity and temperature-oxygen plots with $P*$ for the whole domain

When comparing the differences between the two basins it is best to consult Figure 2.17b as the split between the oxygen concentrations is a good indicator of the location of the data. Firstly, looking at the waters that are in the region from 0 to 1200m depth, roughly the part of the plot above 4 Θ and $\sim$280 $\mu mol\ l^{-1}$, the waters to the right-hand-side show high oxygen data from the Irminger Basin. The values for P^* in this region do not exceed 0.2 whereas the corresponding region for the Iceland Basin has P^* values frequently reaching 0.35. The divergence between the Irminger and Iceland Basin LSW to MNAW transitional limb, as detailed in section 2.4.2 and Figure 2.13, and their resulting P^* values is clear. This region lies geographically around the Rejkjanes Ridge. The ridge acts as a defining boundary between the regimes seen in the Irminger and Iceland Basins.

$Iceland\ Basin : Section\ A$

Section A's distribution of P^*, geographically and hydrographically, is described along with discussion of PO_4^{reg}. In the Iceland Basin P^* values range from $\sim$0.1 to 0.4. From south-north in the Iceland Basin P^* has very low values, 0.1 to 0.15, in the upper waters between 0 and 200m depth, Figure 2.18a. There is a variation in P^* from north to south between 200m and 500m, with a higher fraction of PO_4 made up of PO_4^{reg} in the south of the basin. Beneath 1000m P^* is more consistent north to south with values of 0.3 to 0.35 from 500 to 1500m

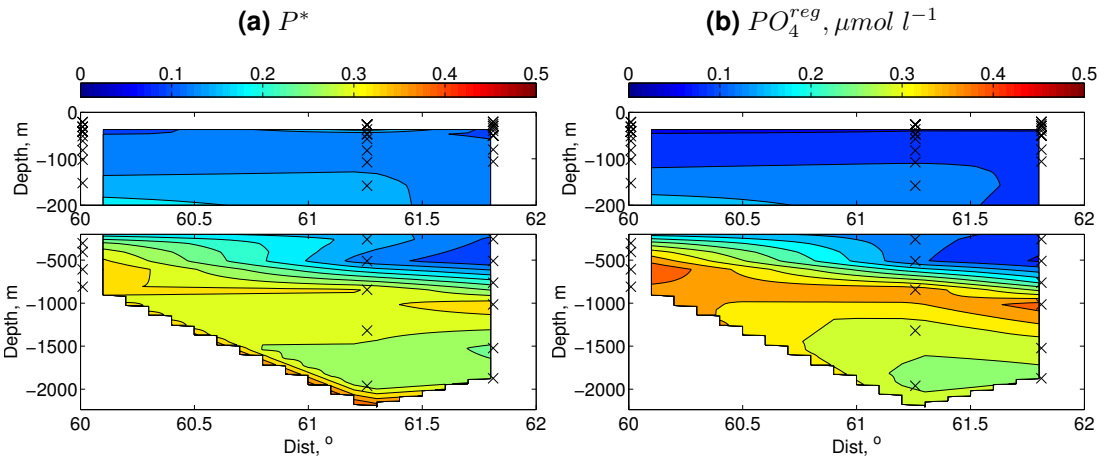

Figure 2.18: P^* **and** PO_4^{reg} **for section A.**

and approximately 0.27 beneath 1500m. At the very base of the water column, throughout the section, the P^* values peak at 0.4. The main driver behind this variation of P^* is the distribution of respiration, and thus PO_4^{reg}. This can be shown in the variability of PO_4^{reg} distributions, Figure 2.18b, and the lack of significant variability in PO_4, Figure 2.14c.

The water masses identified in section 2.4.2 are attributed P^* values. The transition to ISOW has a high value of P^*, $\sim$0.4, Figure 2.19a. This is close to the maximum value experienced throughout the whole domain. NADW has a value of 0.26 to 0.27, which is maintained during the transition to LSW before an abrupt gradient raises the P^* value at the end-member to $\sim$0.29. During the transition from LSW to MNAW the P^* values increase up to a maximum of between 0.32 and 0.35 in the middle part of the transition limb; comparison with figure 2.12 suggests these waters lie between 400 to 1200m. The values then decline again as the transition limb approaches the MNAW end-member, where the values become a consistent 0.15. The filaments that denote the surface waters do not change hugely from the MNAW end-member but do continue the decline, reaching P^* values of 0.06 to 0.07 at the very surface, but generally falling within the 0.1 to 0.15 range.

The water masses with the largest regeneration signals occur within the LSW to MNAW transitional limb. This water mass will have influences from the surface waters, via the formation of MNAW, and the highly oxygenated waters

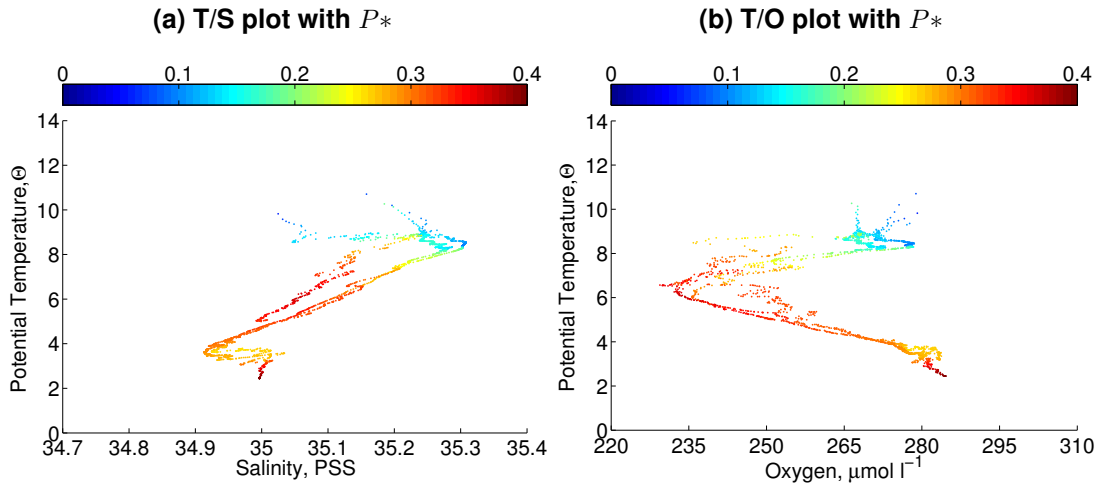

Figure 2.19: Temperature-salinity and temperature-oxygen plots with $P*$ for section A.

of LSW. This combination results in a strong signal of regeneration of organic material in the mid-depths of the Iceland Basin. Thus, mixing within the basin and the far field effects of subsurface water masses are important when determining the biogeochemistry of the Iceland Basin.

$60°N : Section\ B$

The values of P^* across the Irminger and Iceland Basins, using section B, vary throughout much of the water column. The values in the surface of the Irminger Basin are lower than the Iceland basin, > 0.05 and 0.1 respectively, Figure 2.20a. The mid-depth water, between 100m and 800m, is conversely higher in the Iceland Basin relative to the same depths in the Irminger Basin, 0.15 and 0.1 respectively. Higher values of P^* in the Iceland Basin are also seen in deeper water with values of around 0.25 to 0.35 in patches. The deep water in the Irminger Basin has values rarely higher than 0.25. The driver of this variation, as was seen for section A, was the distribution of PO_4^{reg}, Figure 2.20b. The higher P^* values seen in the Iceland Basin imply that nutrient utilisation is stronger in the Iceland Basin.

The water mass P^* attributes are described working from the base of the water column to the surface. DSOW, the limb of the plot reaching into waters colder than 2 Θ at a salinity of 34.9, has a P^* value of 0.25 to 0.27. NADW has P^* values of 0.25 to 0.27, Figure 2.21a. This is consistent with evidence observed

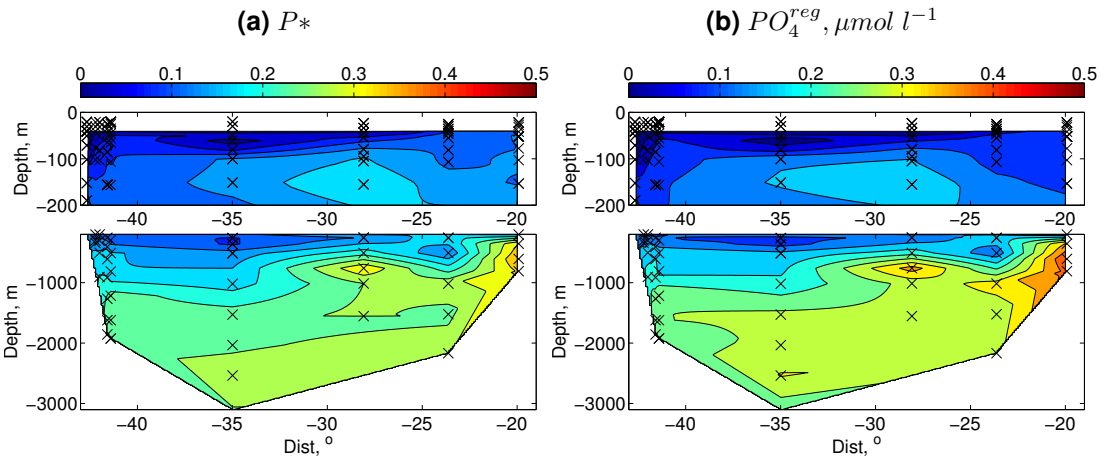

Figure 2.20: $P*$ **and** PO_4^{reg} **for section B.**

in the Iceland Basin. In the Irminger Basin, the transition from this water mass to LSW has a much greater gradient than that for the Iceland Basin, resulting in P^* values for the LSW that are significantly lower, $\sim$0.2. Some higher values are seen for LSW, 0.27, corresponding to data from the Iceland Basin. The stations with lower P^* values are from the Irminger Basin and the Reykjanes Ridge. This difference between the characteristics of the water masses continues when examining the transition between LSW and MNAW. There is a definite split between the transition limbs, some displaying characteristics described in the previous section and some displaying a gradual gradient throughout the limb from the LSW values of 0.2 to the MNAW end-member value of 0.12. These two different regimes appear to depend on the location of the station; either the Iceland Basin, the former, or the Irminger Basin, the latter. As in the previous section the MNAW end-member value for P^* appears to be consistent at all stations, between 0.12 and 0.15. The filaments branching from the LSW to MNAW transition again display similar characteristics, with respect to P^*, across the whole section. These values range from 0.07 to 0.15, a spread very similar to that observed for section A.

The evidence presented using the section B data highlights the variation in regimes between the Irminger and Iceland basins. The regeneration of nutrients occurs more strongly in the Iceland Basin water masses compared to the Irminger Basin. The contrast in the oxygen data is intuitively reflected in the P^* differences.

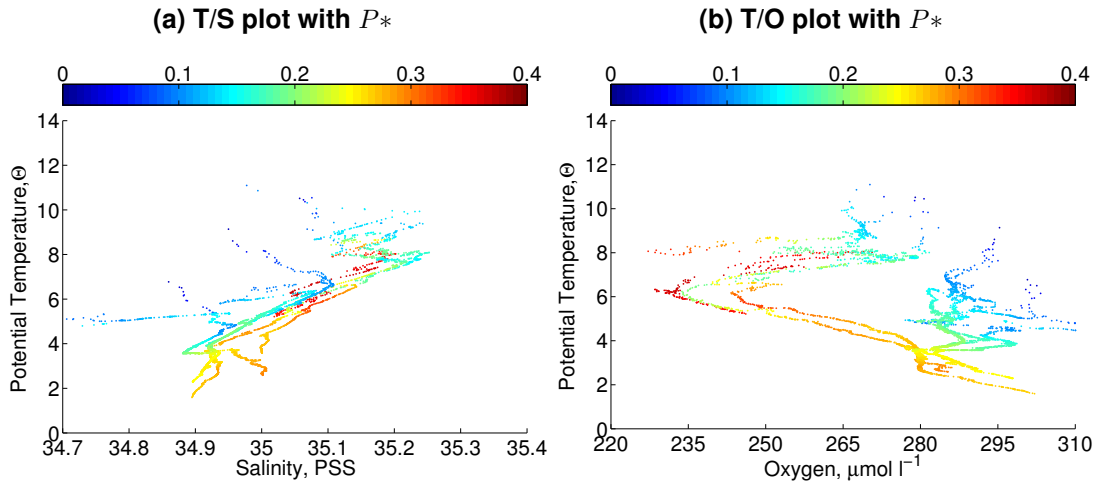

Figure 2.21: Temperature-salinity and temperature-oxygen plots with $P*$ for section B

Irminger Basin : Section D

The meridional distribution of P^* throughout the Irminger Basin is fairly consistent at most depths, Figure 2.22a. The upper 100m has values less than 0.05 for the region between 58N to 64N. P^* then increases from 0.15 at 500m to 0.25 at depths greater than 1500m. This pattern is consistent at all latitudes of the Irminger Basin. The pattern of nutrient utilisation percentage demonstrated by P^* is mirrored in the PO_4^{reg} distributions, Figure 2.22b. The variation in PO_4^{reg} dominates over the variations in PO_4, Figure 2.16c, to affect a strong similarity between P^* and PO_4^{reg}.

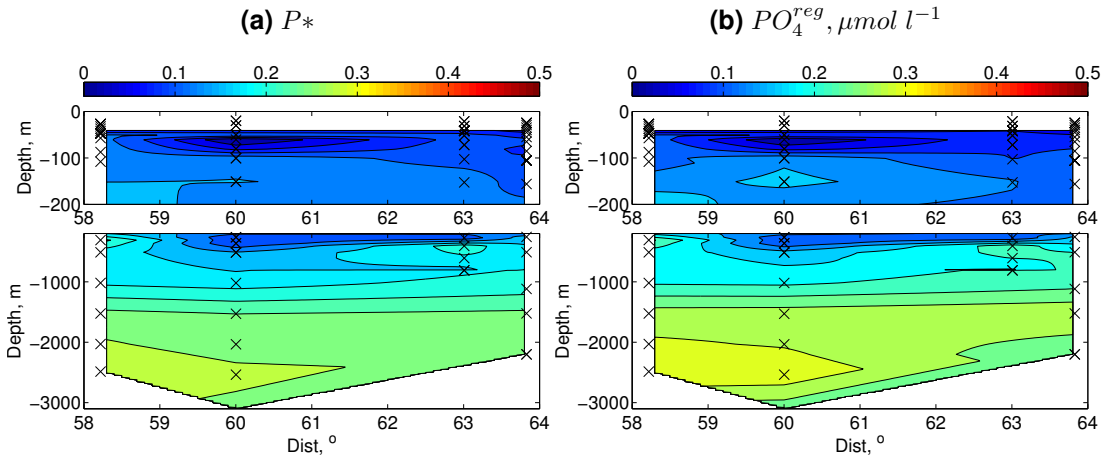

Figure 2.22: $P*$ and PO_4^{reg} for section D.

The T/S distribution of P^* is presented and the water masses are attributed values of P^*. The deepest water corresponds to the DSOW, lying on the

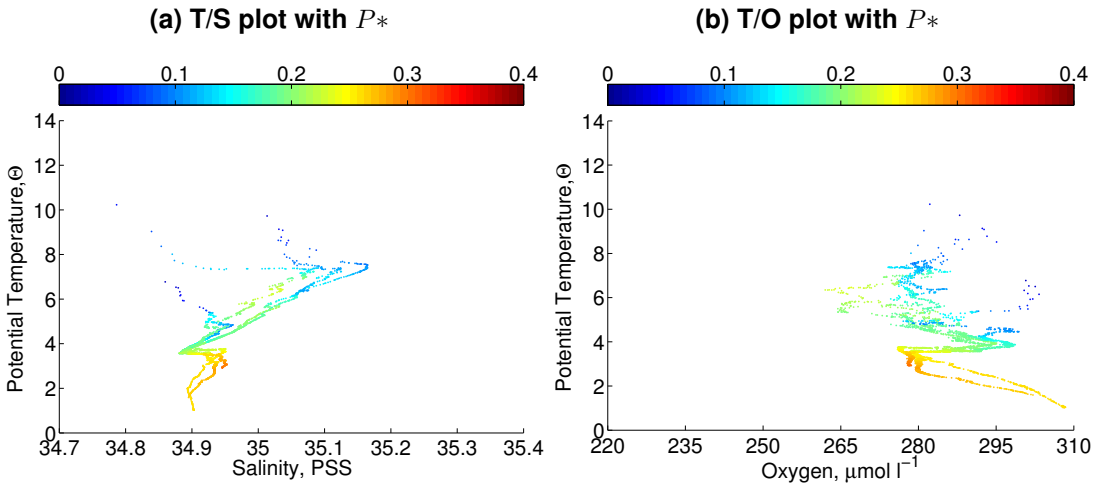

Figure 2.23: Temperature-salinity and temperature-oxygen plots with $P*$ for section D

coldest region of the figures, and this water mass has P^* values of 0.25 to 0.27, Figure 2.23a. The transition from DSOW to NADW holds a consistent P^* value of 0.25 to 0.27 with a small part reaching values of 0.28. There is evidence of a more elevated value in the deep waters of 0.31, this corresponds to the most southerly station, 58°N. This station does not display the previously described definitive evidence of DSOW, merely having the beginning of the transition limb towards the DSOW end-member from NADW. The NADW end-member in this section remains consistent with the evidence consulted previously holding a P^* value of $\sim$0.25. The transition from NADW to LSW has a relatively strong gradient in P^* values compared to section A, but similar to section B. The LSW end-member displays a P^* value of 0.2, reflecting evidence seen in section B. For much of the region the transition from LSW to MNAW mirrors previous evidence, seen in section B, with a steady decrease in P^* values from 0.2 towards the MNAW end-member value of $\sim$ 0.12 to 0.15.

2.4.5 Micronutrients in the sub-polar North Atlantic

Introduction

This chapter describes the distribution of iron and aluminium, especially with respect to the water masses. The analysis of seawater samples in order to ascertain trace metal concentrations is difficult in comparison to

other nutrients. As a result the data obtained is often sparse due to the time-consuming nature of the analysis and also liable to inaccuracies and anomalous data-points requiring removal. The hydrographical distribution of micronutrients is analysed in order to ascertain how important physical processes are in determining their distribution. Unfortunately the spread of the micronutrient data precludes assimilation of a suitable contoured section from CTD stations. Thus, in this section there is no dedicated section for the Iceland Basin. Contrasts between the two basins are examined using the entire dataset.

Entire domain

The two sub basins of the subpolar gyre have significantly different iron concentrations (Figure 2.24a). The Iceland Basin sections tend to have between 0.6 and 0.9 nM of Fe within the LSW to MNAW limb. There are also high concentrations in the ISOW signal from the Iceland basin. A similar signal is seen in the Al concentrations with the largest concentrations seen in the LSW to MNAW transitional limb above the Reykjanes Ridge, Figure 2.24b (and Figure 2.13 for water mass reference).

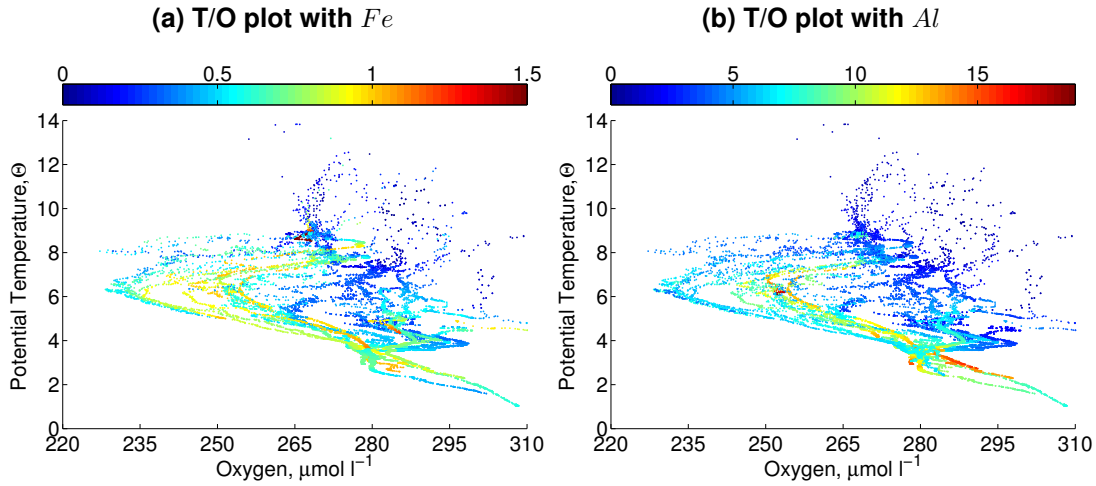

Figure 2.24: Temperature-oxygen plots with Fe and Al (nM) for the Entire domain.

$60°N$: Section B

T/S and T/O plots showing iron and aluminium concentrations from across $60°N$ are presented here to help identify physical processes that impact on

micronutrient concentration and cycling, Figure 2.26. There is a clear contrast with respect to iron between the Irminger and Iceland Basins, Figure 2.26. The relatively oxygen depleted Iceland Basin water has higher concentrations of iron, 0.7 to 1 nM, than the oxygenated water found in the Irminger basin, 0.2 to 0.6 nM. High concentrations of iron, 0.9 to 1.1 nM, in the deep waters of the Iceland Basin can also be seen in the region close to ISOW. These concentrations far exceed concentrations seen in the DSOW, suggesting that despite their similar origins in the Arctic ocean there are clear differences that result in opposing characteristics between the two overflow waters.

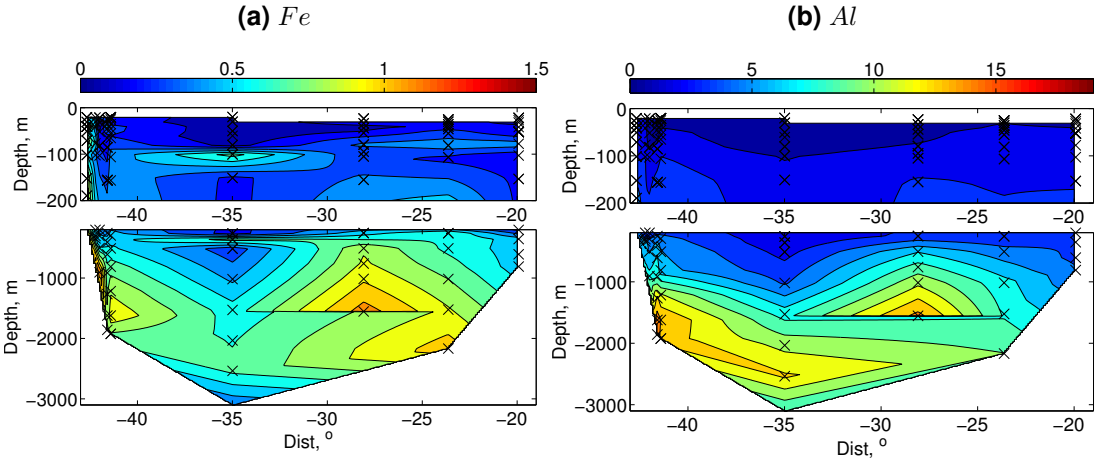

Figure 2.25: Fe and Al for section B.

Aluminium displays a particularly strong signal in the DSOW limb. For this peak in aluminium to have been transported into the region at some point the DSOW water mass must have been augmented with Aluminium, and most likely this process would supply iron too. The possibility of this signal is evident in Figure 2.28c, where concentrations of trace metals upstream are of a smaller magnitude compared with concentrations downstream in the south of the section. There is evidence of the DSOW diverging in the north of the Irminger Basin and followng two distinct paths. The most common path is that which falls down the continental slope into the very bottom of the Irminger Basin, becoming the deepest water mass present. The second path, results from interaction of DSOW with NADW as it flows over the Denmark Strait sill and descends the continental shelf into the Irminger Basin. The interaction with NADW can lead to a slight warming of the DSOW and resulting in neutral

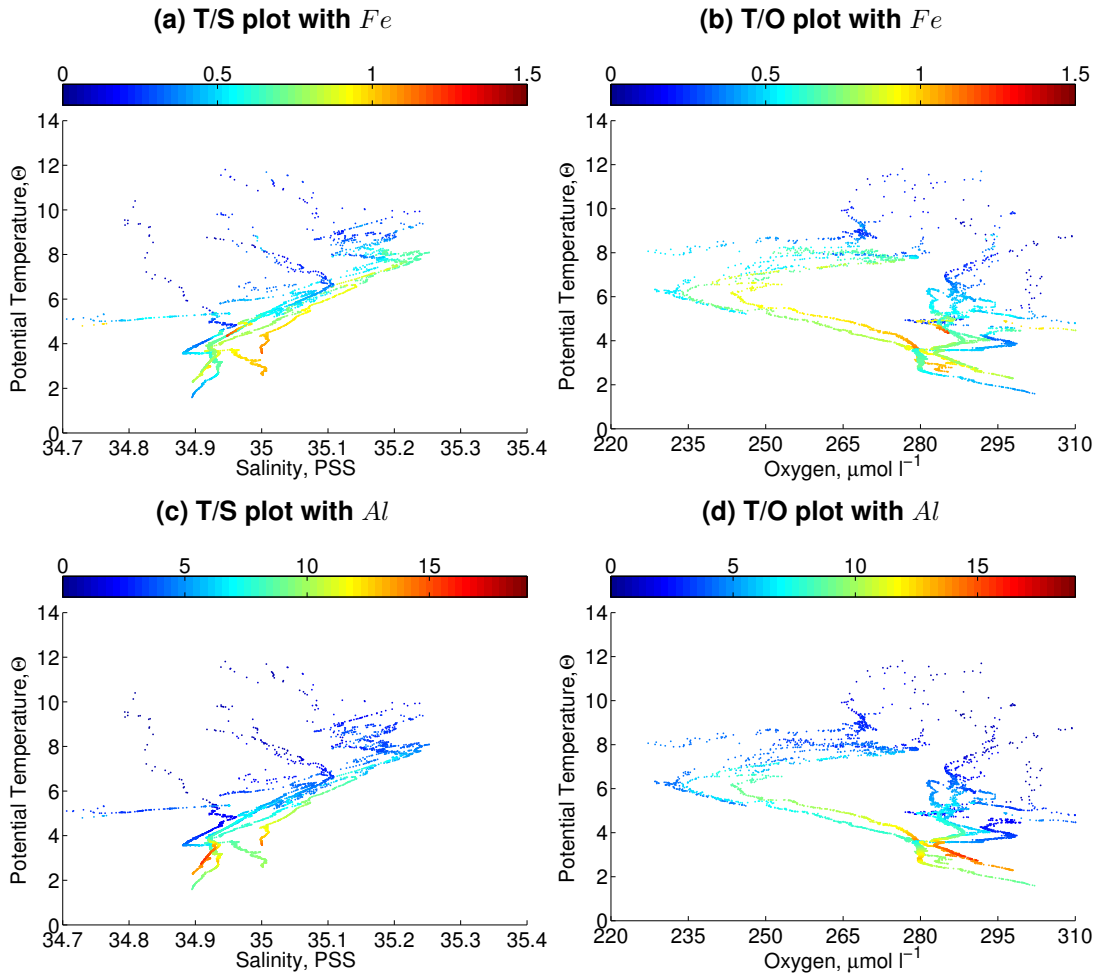

Figure 2.26: Temperature-salinity and temperature-oxygen plots with Fe and Al (nM)for the $60°$N Section: B.

buoyancy occurring at a shallower depth, approximately 2000m. When this occurs the DSOW is carried cyclonically in the sub polar gyre circulation and begins to flow along the continental shelf of the Greenland Coast, beneath the shallower East Greenland Current (Swift, 1984). It is this secondary path which is showing evidence of augmentation of the water mass with trace metals. The DSOW in the north of the Irminger Basin has lower concentrations of iron and aluminium compared to the DSOW found further south near the Greenland Coast at $60°N$.

Irminger Basin : Section D

Water masses in the Irminger BAsin seem to have consistent iron concentrations associated with them, Figure 2.28a. The deep waters between

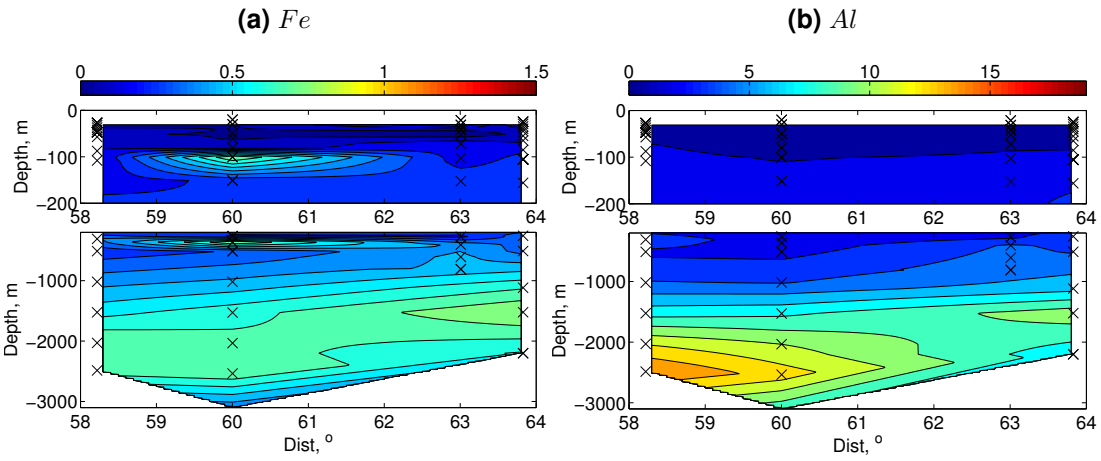

Figure 2.27: Fe **and** Al **for section D.**

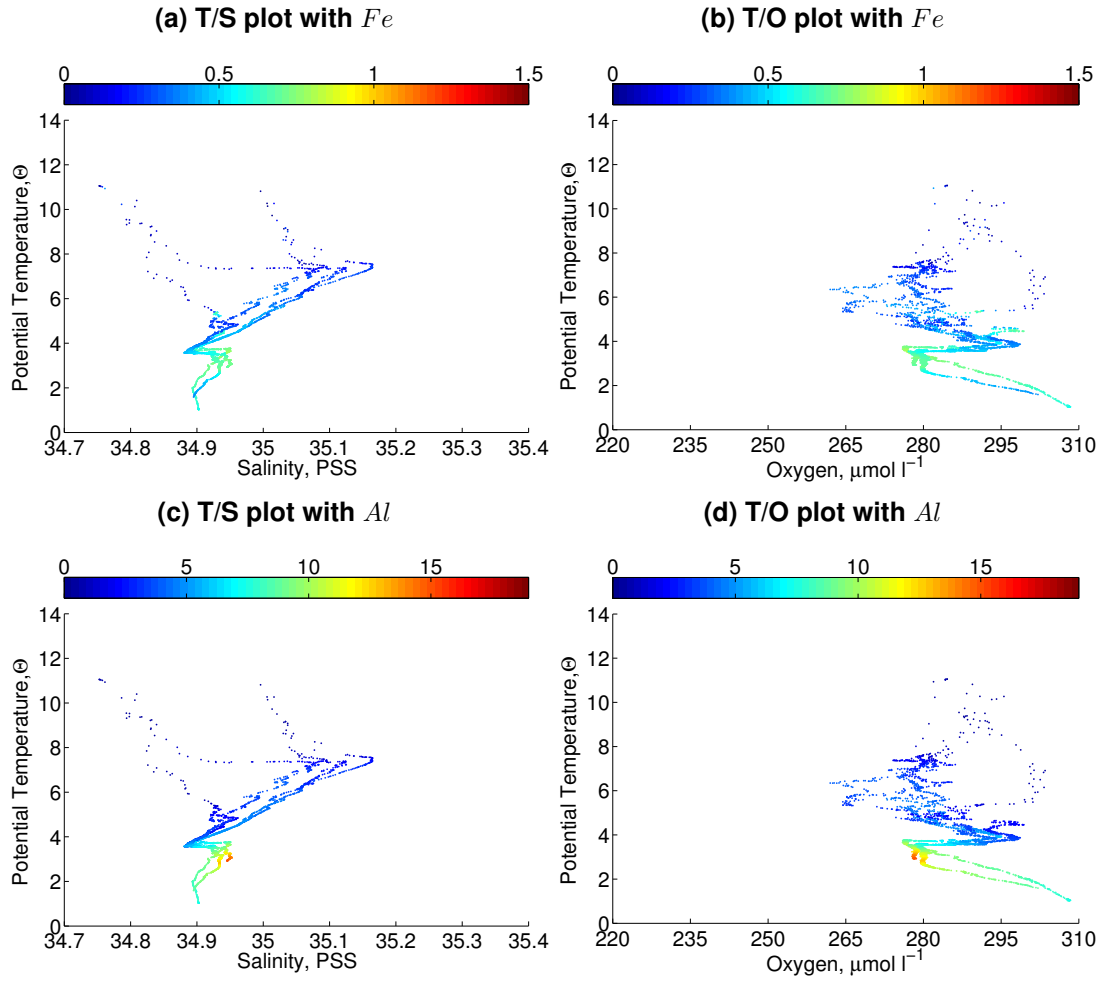

Figure 2.28: Temperature-salinity and temperature-oxygen plots with Fe **and** Al **(**nM**) for the Irminger Basin: Section D.**

23°W and 30°W correspond to the two filaments in the TS plot with DSOW characteristics. This region lies in the Irminger Basin just to the west of the

Reykjanes Ridge. The DSOW has concentrations of around 0.6 nM. NADW has Fe concentrations of around 0.7 nM, while LSW is relatively lacking in iron with 0.3 to 0.4nM, Figure 2.28b. There is very little iron in the waters shallower than the LSW, though some of the shallower MNAW has some isolated signals of slightly higher iron concentrations within it.

The aluminium has a very strong signal associated with the the NADW end-member and seeping in towards some of the DSOW. Concentrations of around 12 nM are seen in the NADW with the DSOW also augmented with Al having 10 to 12 nM (Figures 2.26c and 2.26d). This aluminium signal has a similar pattern to the observed iron concentrations. The maxima of both the Fe and Al signals are seen in the NADW. This aluminium signal is indicative of a lithogenic source of iron, due to the use of aluminium as a proxy for sedimentary or atmospheric supply of trace metals. The aluminium signal persists more than iron as it is not as particle reactive. This implies that this signal is from a lithogenic source, which can be either a source of sediments or atmospheric dust supplied to the NADW upstream from its current location. The slight shift of the high-Al NADW signal to a colder temperature implies this water mass could be closer to its formation zone, thus in the north of the Basin. This station further north is close to the seabed sediments and could also be a consequence of sediment interaction of the DSOW with sediment as it cascades over the sill between Greenland and Iceland. This is interesting evidence of a potential sediment interaction.

2.4.6 The importance of physical processes and biogeochemical regimes in the sub polar North Atlantic

The sub polar North Atlantic has a range of physical processes that influence or determine the biogeochemcial regimes present in the region. The supply and distribution of macro and micro nutrients are affected by circulation, mixing and diffusion. A deep knowledge and understanding of these processes and regimes helps when trying to validate theoretical work and numerical models.

Circulatory features throughout the region have very differing effects. In the east of the region evidence is seen that demonstrates the supply of nutrient depleted waters into the basin. Whereas in the west of the basin, close to the Greenland coast, there is strong surface run-off and glacial melt processes that incorporate freshwater into the surface ocean. These terrigenous supplies also contain signals of phosphate, resulting in a shift in observed N:P ratios in the Irminger Basin. A supply of phosphate that flows through from the Arctic Ocean via the Canadian Archipelago into the Irminger Basin is also apparent in the physical data. These two low N:P signals are combined in the central Irminger Basin within evidence of deep winter mixing, where the freshwater and elevated phosphate signals are mixed throughout the water column.

The winter mixing events serve to highlight the difference in biogeochemical regimes between the Iceland and Irminger Basins. During winter, the sub polar North Atlantic experiences strong mixing events, which result in well mixed water columns. These homogenous distributions provide a platform for the differences in biogeochemical regimes of the two basins to imprint. The biology of the Iceland Basin is able to respond to the improving conditions for growth experienced at the end of winter relatively quickly, which is reflected in the depleted subsurface nutrient pool seen in the Iceland basin. spring blooms in the Iceland Basin must occur prior to the link between the surface mixed layer and the nutricline being broken as the mixed layer shallows following winter. There are many more subsurface nutrients observed in the Irminger Basin. The stronger growth regime in the Iceland Basin is further strengthened by the strong regeneration signals seen in the Labrador Sea Water and Modified North Atlantic Water of the Iceland Basin. There are also strong signals seen in the Iceland-Scotland Overflow Water of this region, indicative of the larger amounts of organic material descending from the surface water of the Iceland Basin.

The distribution of iron in the sub polar North Atlantic is also influenced by physical processes. Though there is redistribution of iron supply signals by circulation, there is diffusive component that transports these iron supply

signals towards the centre of the basins, though the magnitude of this diffusion is poorly known with current estimates suggesting the diffusive flux can be quite low relative to the iron residence time (Painter et al., 2014). The most profound iron redistribution signal is found within the Denmark Strait Overflow Water, which upon entering the Atlantic Basin splits along two different pathways. The first route descends the continental shelf and travels down the centre of the basin with a signal of sedimentary iron gained from its turbulent descent of the shelf. The second route, more interestingly, clings to the continental shelf and traverses the Irminger Basin at 2000m depth. This water mass becomes augmented with iron and aluminium from sediments or hydrothermal vents as it travels southwards as a deep component of the East Greenland Current. This benthic source of micronutrients is then available for further redistribution into the central Irminger Basin downstream. Similar to this there is evidence of micronutrient supply from the Reykjanes Ridge, which is incorporated into the sub polar gyre circulation. These iron and aluminium signals are then also diffused into the centre of the Irminger Basin at depth. These processes do effect the iron distribution, but have very limited immediate impact on the biogeochemical regimes due to their supply into intermediate waters instead of surface waters, where they can be utilised by biology to consume persistent macronutrients.

2.5 The Tropical Atlantic

The Tropical Atlantic receives large amounts of aeolian dust. The atmospheric circulation frequently transports terrigenous dust from the Sahara and Sahel and disperses it across the tropical latitudes of the Atlantic. The most abundant supply falls between 15°N and the Equator. This section analyses data from D361, a cruise which took place in this region in February 2011. The station locations, shown in figure 2.29, provide a long transect down the tropical Atlantic as well as a transect coming away from the African continent into the centre of the Atlantic. Similar analyses to section 2.4 are carried out to compare the two regions with respect to the iron regimes that are present and the sources that are important.

During D361 iron and aluminium data were collected by Christian Schlosser and Jessica Klar, nutrient and dissolved oxygen data were collected by Anouska Bailey, Malcolm Woodward and Francois-Eric Legiret and CTD and navigational data were collected and processed by Alex Forryan and Jonathan Lauderdale. The data presented in this section appear courtesy of those above.

2.5.1 Physics of the tropical Atlantic

The physical properties of the regions are explored here in the same way as for the subpolar gyre region. The data are separated into four sections determined by preliminary analysis of the hydrographic properties of the data and geographical location, Figure 2.30, providing four distinct contoured sections and biogeochmical regimes.

The tropical region of the Atlantic is a key area of water-mass interaction. There are several water masses that spread eastwards or westwards across the Atlantic Basin at different depths and latitudes, in addition to the more traditional large-scale water masses that originate at high latitudes. Beginning with deep water interactions there are three major basin-scale water masses

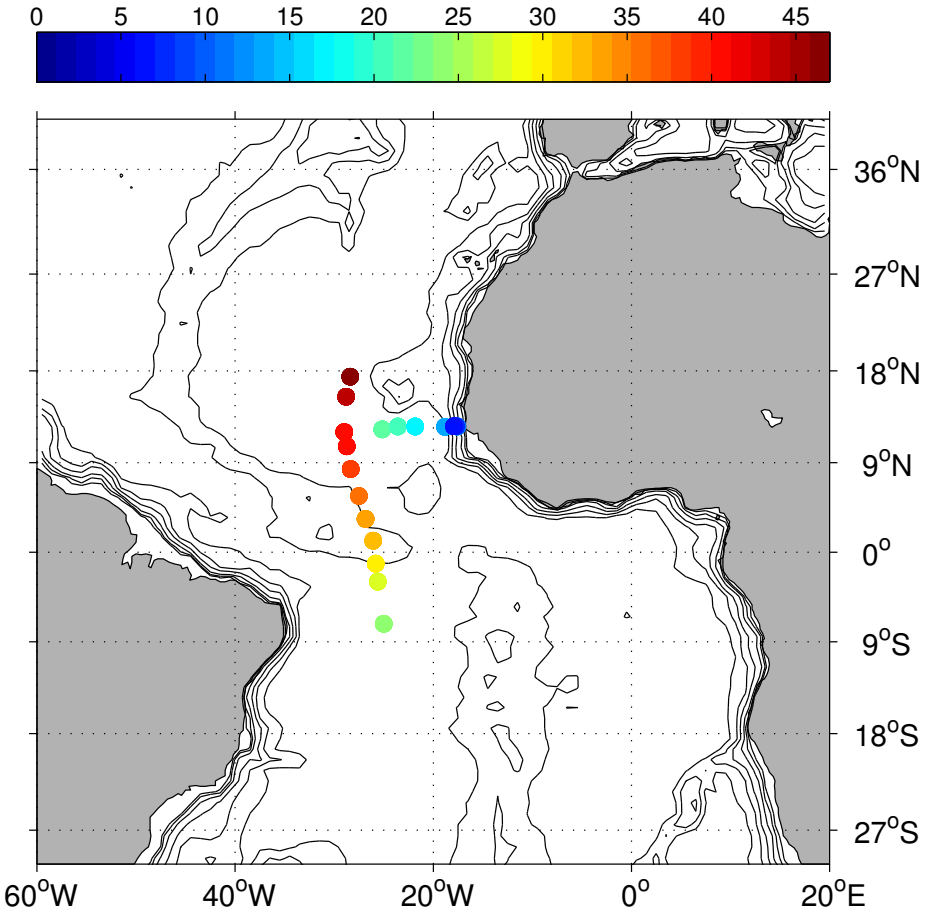

Figure 2.29: D361 Station Locations, colours represent cast number

separated vertically in the water column due to the different temperature and salinity, and therefore density, characteristics. The deepest water mass is Antarctic Bottom Water (AABW), formed in the surface of the Southern Ocean before subducting and travelling northwards. It is cold and relatively fresh, and is the densest of the water masses in the region lying at the bottom of the ocean. Typical T/S values for this water mass are between to 0.8 to 2° C and a salinity of 34.6 to 34.7 (PSS) (Stramma and Schott, 1999). AABW is typically found at depths greater than 4000m, as indicated in Figure 2.31c, where the data points coloured deep red correspond to this water mass.

Above AABW lies North Atlantic Deep Water (NADW). This water mass was discussed in some detail for the Sub-polar Gyre of the North Atlantic. It is found between 1200 and 4000m depth and occupies the same T/S space in the tropics as further north. This water is formed by a combination of overflow waters in the North Atlantic. The angle in the T/S plots above the AABW signal

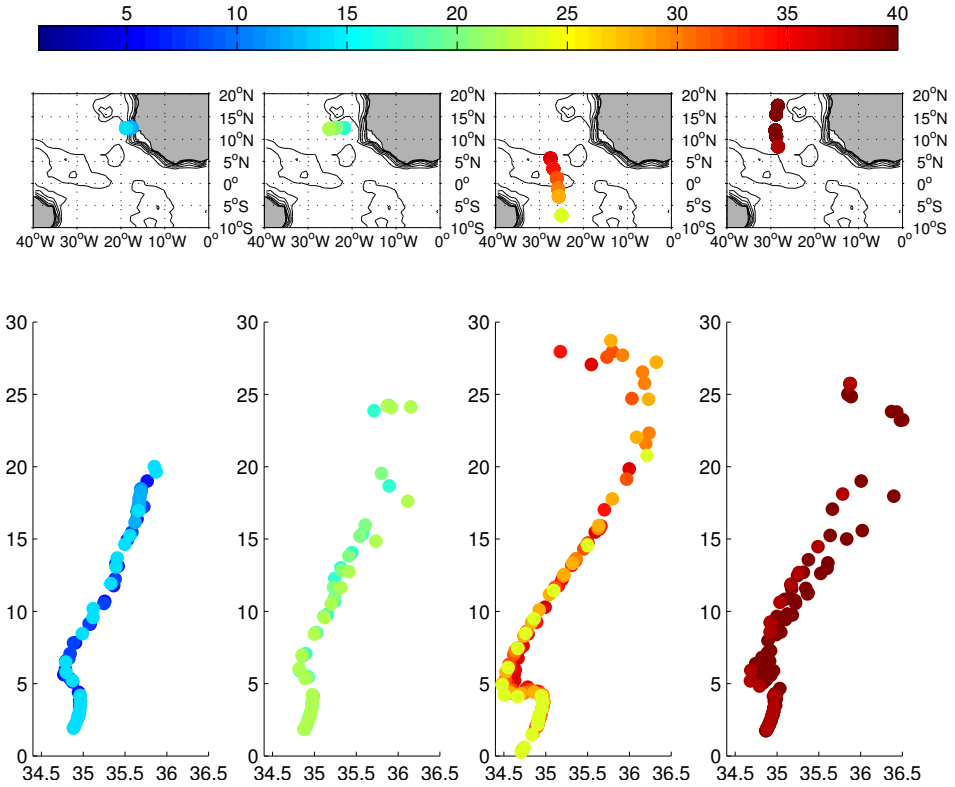

Figure 2.30: D361 Station Locations and T/S plots, colours represent cast number. From left to right the regions are: coastal, central, southern and northern

indicates NADW, Figure 2.31c. These first two water masses are homogenous and persistent in all of the stations in this study, Figure 2.31a. They both exhibit high levels of oxygen due to their cold polar source regions, Figure 2.31d.

The water mass that is situated above NADW is AAIW occupying a depth range of water between 500 and 1200m depth. AAIW is cold and fresh due to its origin near the Antarctic Circumpolar Current, having a temperature of 5 Θ and a salinity of 34.2 to 34.4 in its formation region (Suga and Talley, 1995). This water mass is more variable than the deeper ones due to its tendency to interact with other water masses in the intermediate Southern Ocean, which results in an increase of salinity as the water mass travels northwards. Hence, in Figures 2.31c and 2.31a the AAIW gradually warms and becomes more saline, lying in the region of 5 Θ and salinity of 34.5 to 34.8, higher values than at the formation site. Suga and Talley (1995) observe AAIW at these ranges.

The surface Tropical Atlantic has a very complex and variable circulation pattern, with the Northern Equatorial Current (NEC), Southern Equatorial

Current (SEC), the Northern Equatorial Counter-Current (NECC) and the North Equatorial Under-Current (NEUC) all acting to transport the surface and subsurface water masses. The NEC and SEC are westward flowing surface currents that sandwich the NECC, which flows eastward (Weisberg and Weingartner, 1988). The NEUC is a very strong feature that flows eastward beneath the surface at $\sim$ 150m (Giarolla, 2005), bringing elevated oxygen levels from the west of the basin (Stramma et al., 2005).

The physical transport features are revealed in the water-mass directly above the AAIW. This Atlantic Central Water is split into two water-masses of similar properties, the North (NACW) and South (SACW). While these water masses occupy the same density space, NACW has higher temperature and salinity values. NACW also has higher oxygen levels compared to SACW due to its proximity to the well-ventilated North Atlantic Subtropical Gyre. The separation between the two water-masses, and the boundary between well-ventilated subtropical waters and the tropical ”shadow-zone” with its low oxygen content (Zenk et al., 1991) is the Cape Verde Frontal Zone (CVFZ). This front usually lies at around 20°N, but this can vary within the study region.

In this tropical dataset there is no signal of NACW, which might have been present in the most northerly stations. The low oxygen levels seen in the temperature range of 8 to 20 Θ in figure 2.31f confirm that SACW is present in this region. Surprisingly, the SACW further south, indicated by the blue colours in figure 2.31f, contains higher oxygen levels. The reason for this is the impact of the NEUC current, which brings oxygen rich waters from the west at the same depths as SACW (Stramma et al., 2005). Within the surface mixed layer there is the Tropical Surface Water (TSW), which has temperatures higher than 20 Θ and exhibits freshening from a sub-suface salinity maximum as a result of strong precipitation.

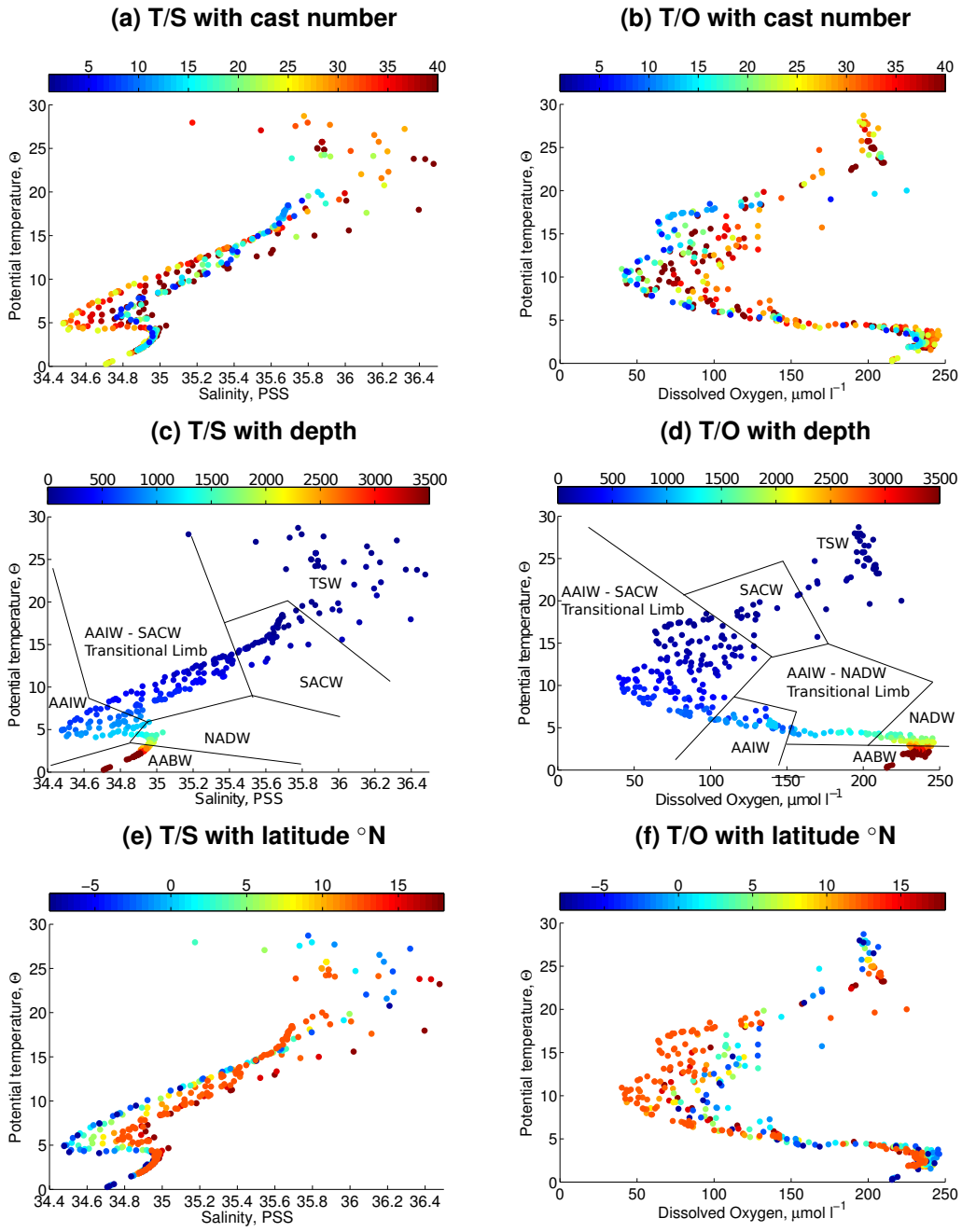

Figure 2.31: D361 T/S and T/O plots coloured by cast depth and latitude, The depth plots include an indication of water masses

2.5.2 Macronutrient distributions and hydrography

The distributions of NO_2^-+NO_3^-, SiO_3 and PO_4, Figure 2.32, in the Tropical Atlantic are different to those seen in the sub polar North Atlantic. The physical processes that occur in the Equatorial Atlantic may influence the biogeochemical regimes. An analysis of contoured sections of these nutrients

will provide an initial assessment of the characteristics of the region.

Central Atlantic, $-28°E$ Section

The northern and southern sections, which when combined run meridionally up the Atlantic from -8°N to 18°N along 25° to 28°W, have a depletion of both NO_2^-+NO_3^- and PO_4 in the upper 150m of the water column throughout the section, $>$10 μM and $>$ 0.6 μM respectively, Figures 2.32a and 2.32c. The nutrient concentrations increase between 150m and 1500m depth up to values of 30 μM of NO_2^-+NO_3^-,and 2 μM of phosphate, before decreasing to 17 and 1.2 μM respectively between 1500m and 3000m. The nutrient concentrations in the deepest water, beneath 3000m, show the first evidence of latitudinal variation in concentrations of nutrients. South of 5°N the concentrations are 25 and 1.8 μM respectively. North of 5°N the concentrations are 17 and 1.3 μM respectively. The distribution of NO_2^-+NO_3^- and PO_4 are similar, as shown by the homogeneity in N:P ratio, Figure 2.32d. The distribution of

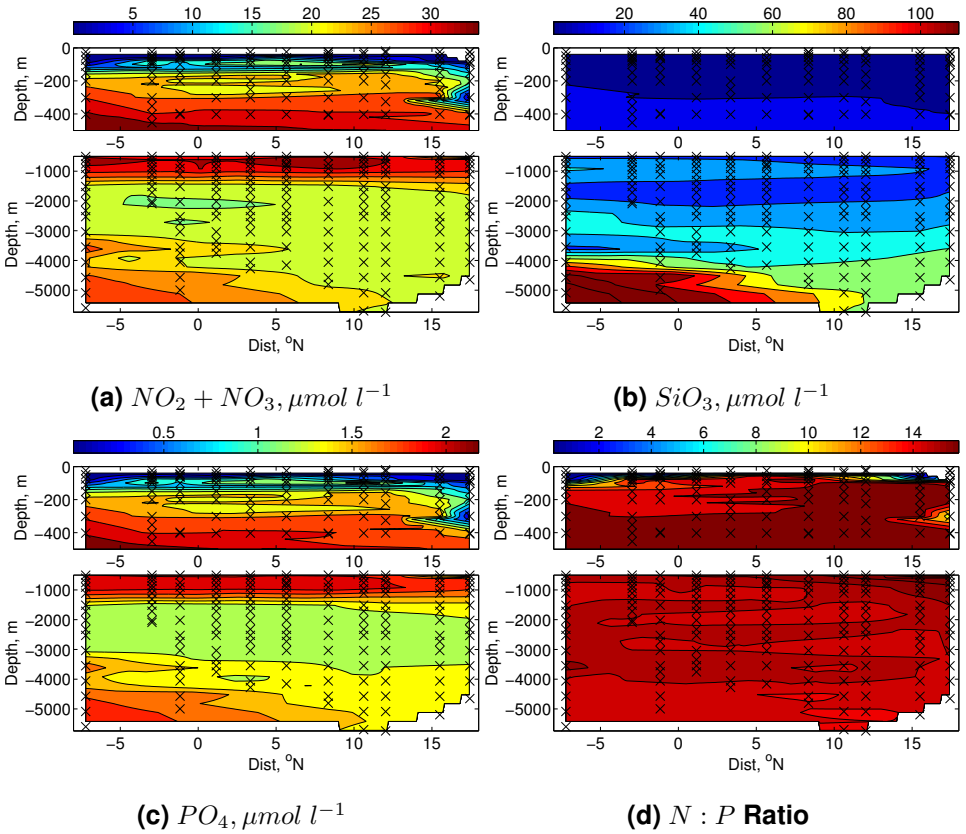

(a) $NO_2 + NO_3, \mu mol\ l^{-1}$ **(b)** $SiO_3, \mu mol\ l^{-1}$

(c) $PO_4, \mu mol\ l^{-1}$ **(d)** $N : P$ **Ratio**

Figure 2.32: Tropical Atlantic south-north ($\sim$ 28°W) nutrient sections. Black crosses represent bottle positions.

silicate is not consistent with the distribution of the other two macronutrients. Concentrations of SiO_3 are low, less than 10 μM, from the surface down to 400m depth throughout the section, Figure 2.32b. There is then a peak of 35 μM at 1000m before decreasing again to 20 μM between 1500m and 2500m. Similarly to the other two macronutrients there is a latitudinal variation in the nutrient concentrations beneath 4000m, where the highest concentrations are found south of 5°N, $>$100μM, and lower concentrations of 60μM are found to the north of 5°N.

Despite the differences between SiO_3 and the other two macronutrients there are some qualitative similarities between them. The latitudinal variation in deep water nutrient concentrations and subsurface increase in concentration between 200m and 1500m are similar, but quantitatively different, suggesting differing biogeochemical regimes for the different nutrients.

$Zonal\ Section,\ 13°N$

The pattern of nutrient distribution for each of the nutrients in the west-east section that runs along 13°W between -26 and -17°E has very little variation horizontally, Figure 2.33. The surface minimum down to 100m depth is seen in all three nutrients. NO_2^-+NO_3^- and PO_4 increase to the same mid-depth maxima as seen for the south-north section. Beneath 1500m the concentrations are homogeneous through out the section. SiO_3 is slightly different in that there is a constant gradient of concentration increase from the surface down to 5000m, from 5 μM to 28 μM. This continuous gradient in concentration is disturbed by some patchiness in the section close to the coast, mainly east of -20°E, where some patches of concentration of 30-35 μM are seen.

$Property - property\ plots\ of\ phosphate\ and\ derivatives$

Figure 2.34 shows the distribution of phosphate across T/S and T/O space for the two sections. The coastal section is a set of stations close to the African Continent at 10°N spreading out into the central Atlantic Ocean as far as -26°E. These stations are closest to the source of the atmospheric iron deposition,

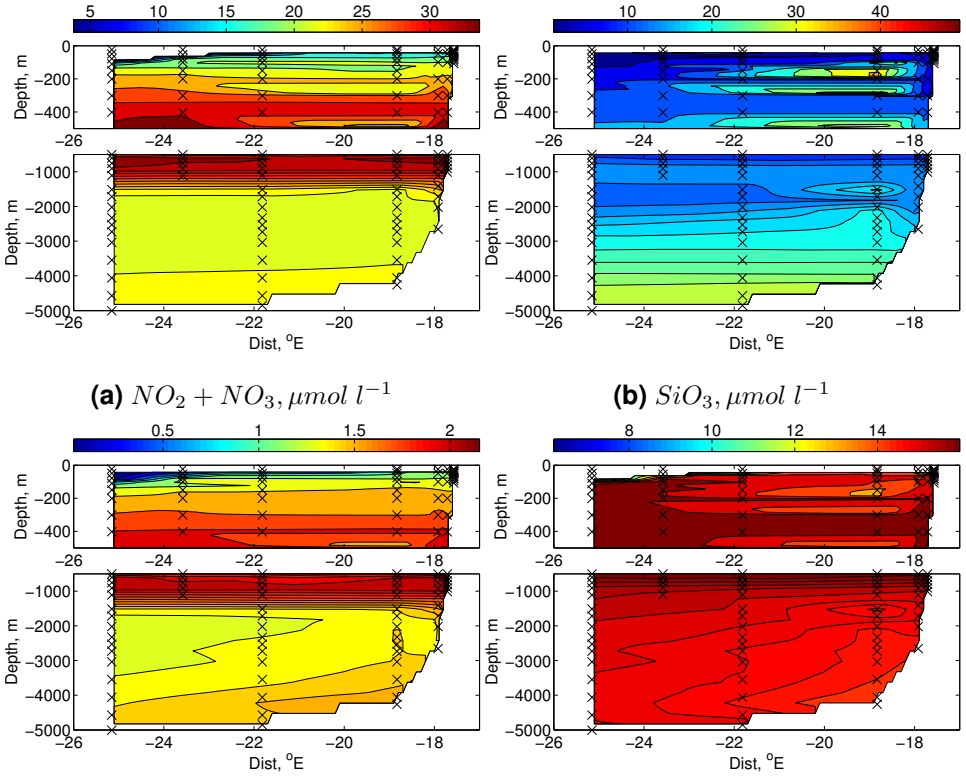

(a) $NO_2 + NO_3, \mu mol\ l^{-1}$ **(b)** $SiO_3, \mu mol\ l^{-1}$

(c) $PO_4, \mu mol\ l^{-1}$ **(d)** $N : P$ **Ratio**

Figure 2.33: Tropical Atlantic west-east (13°N) nutrient sections. Black crosses represent bottle positions.

with the deposition plume strongest, close to the continent. This region has the lowest concentrations of phosphate of all of the stations, see figures 2.34a and 2.34b. The SACW phosphate concentrations are particularly low, with a range of 1.6 to 2.4 μM compared with a range of 2.2 to 2.5 for the other regions. The larger range of observed concentrations relative to the other regions extends into the AAIW where values again get as low as 1.6 μM. The AAIW does not have PO_4 concentrations lower than 2.2 μM in any other region. Another distinguishing feature of the coastal Section is the lack of a NADW phosphate minimum, which is seen in the other section. The south-north transect displays NADW phosphate concentrations of 1.3 to 1.4 μM. The coastal section has values of 1.6 and 1.5 μM respectively, suggesting a west-east gradient in NADW phosphate concentrations. The water masses of Antarctic origin tend to have higher concentrations compared to the North Atlantic sourced NADW. The AABW seen in the southern section and AAIW in all of the other regions both have phosphate concentrations exceeding 2.2 μM. The NADW in contrast

has phosphate concentrations ranging from 1.3 to 1.6 μM.

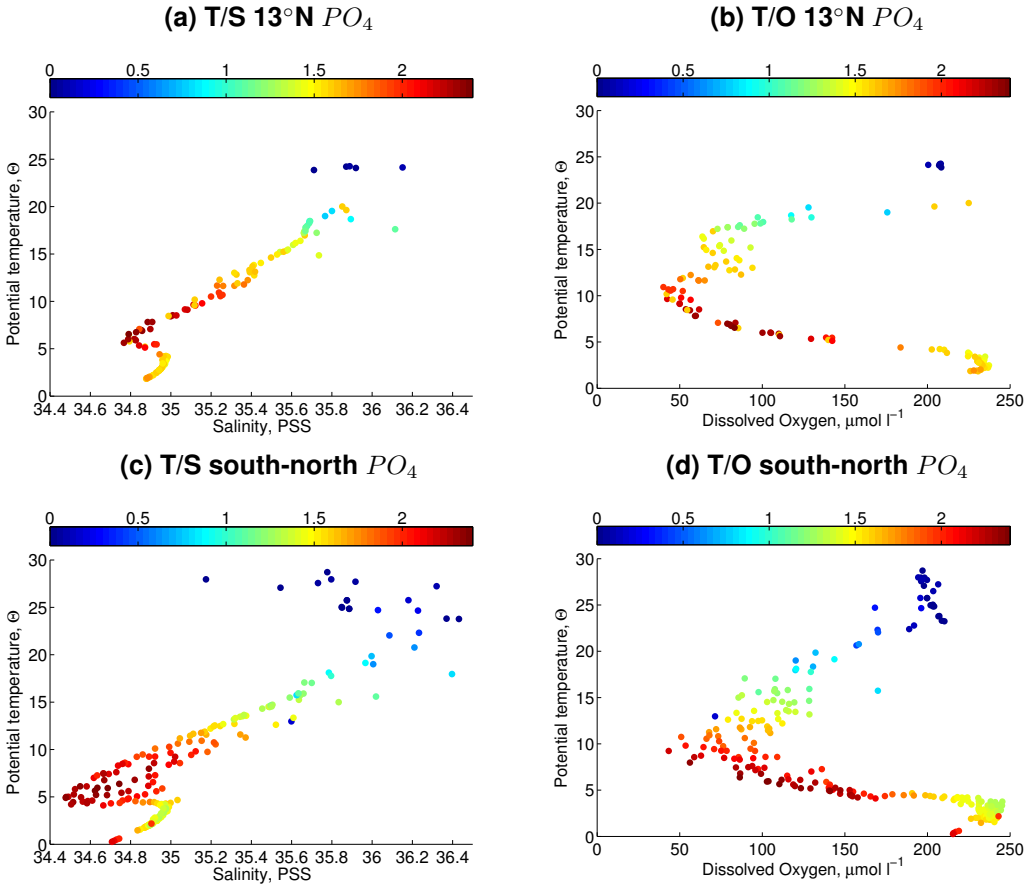

Figure 2.34: D361 T/S and T/O plots coloured by PO_4, $\mu mol\ l^{-1}$

The $P*$ quantity indicates the fraction of the total inorganic phosphate pool that has been regenerated from organic matter. For a review of the theory return to section 2.4.4. The hydrographic distributions of $P*$ are shown in figure 2.35. For coastal and south-north regions, figures 2.35a and 2.35c, there is a very coherent relationship that transcends the subsurface water masses. $P*$ increases from close to 0 in the deepest water, i.e. AABW water, up to around 0.6 to 0.8 in the SACW. TSW has some strange signals with some very high and some very low values, these can be ignored as instability in the framework is inherent when considering waters close to the surface. The relatively high values of $P*$ in the SACW means that there is considerable subsurface regeneration of nutrients in all regions. Figure 2.35a shows that this regeneration is particularly active in the coastal region, where some stations show $P*$ values of 0.8; in effect 80% of the inorganic phosphate here has been

recycled from organic matter.

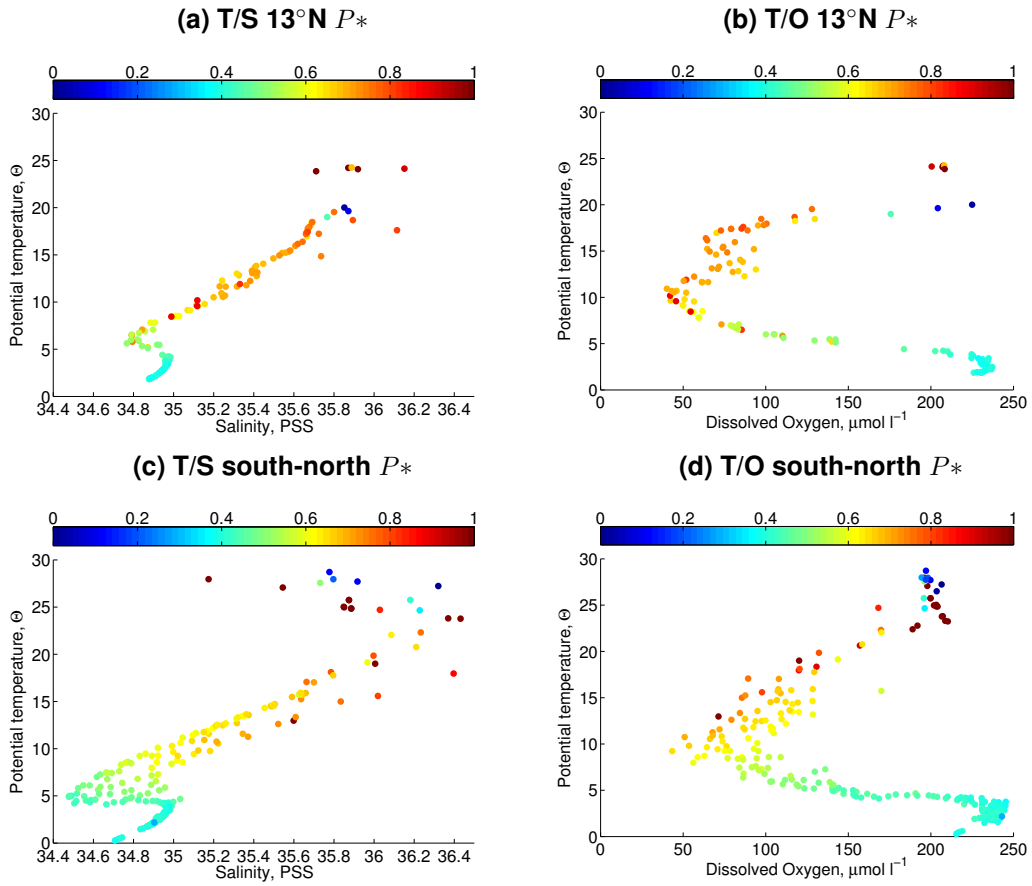

Figure 2.35: D361 T/S and T/O plots coloured by $P*$

2.5.3 Iron in the tropical Atlantic

Contoured iron sections

The iron distribution meridionally up the Central Atlantic, from -8°N to 18°N, shows low concentrations of iron relative from the maxima seen throughout the Tropical Atlantic region. The section is several hundred miles from the coast of Africa. The upper 50m are low throughout the section, $>$ 0.3 nM, Figure 2.36a. The pattern seen throughout the rest of the section is dominated by the location of the atmospheric dust deposition plume, which reaches out from the coast of Africa over the central Atlantic. There are patches just beneath the mixed layer depth with concentrations at approximately 1 nM. The existence of these reservoirs of nutrients just beneath the seasonal

mixed layer depth is indicative of the isolation of the mixed layer from the nutrients in the nutricline. From 150m to 1000m, between 0°N and 18°N, the concentrations are between 0.8 and 1.2 nM. The peak for the section, 1.3 nM, is seen between 500m and 1000m between 5°N and 10°N. The deeper waters in the Northern Hemisphere are then relatively consistent at 0.6 to 0.8 nM. South of the equator there are values of 0.5 to 0.8 nM throughout the entire water column, with some waters with elevated iron concentration seen flowing from north of the equator. Generally, there are few detectable physical effects when analysing the meridional section. The distribution is dominated by the intermittent nature of the atmospheric dust deposition plume, reflected in the striped appearance of the iron concentrations throughout the section. This stripe appearance is a combination of the timing of dust deposition and resulting blooms triggered by nutrient supply.

(a) Contoured south-north section of Fe **(b) Contoured Fe section along 13°W**

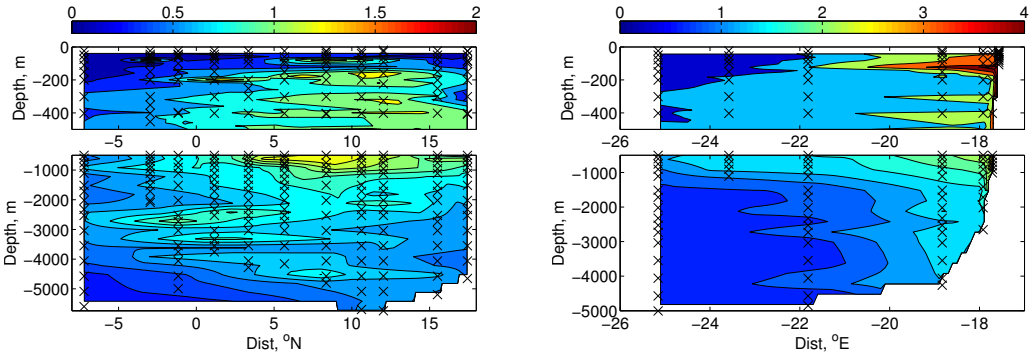

Figure 2.36: D361 contoured sections of Fe (nM), note differing axes.

The west-east section dissects the expected region of maximum atmospheric dust deposition, running zonally from the central Atlantic towards the coast of Africa along 13°W. The section has as strong dependence on proximity to the coast, Figure 2.36b. The closest stations to the coast have high concentrations of iron, between 3 and 6 nM from the surface to 1000m. Further off the coast, at around 19°W, there is a similar striped appearance that was seen in the south-north section. The surface, 0 to 1000m, iron concentrations are between 2 and 3 nM, with concentrations around 1 nM beneath this elevated surface layer, interspersed with patches of higher concentrations, 2 nM. Waters deeper than 400m are more consistent with concentrations from 1.2 to 1.5

nM. The surface waters between 26°W and 22°W are relatively depleted in iron, $<$ 0.5 nM. Between 200 and 500m depth the iron concentration is 1 nM before very low levels, $<$ 0.5 nM are seen beneath 1000m.

$Property - property\ plots\ of\ iron$

The property-property plots allow a clearer connection between the physics and the biogeochemistry of the region. The south-north section was shown to have some influence from the atmospheric dust deposition plume, where a small increase in iron concentrations coincided with the latitudes of high dust deposition. The influence of the plume seems to be the major driving factor behind the iron distribution. The T/S plot shows there is very little relationship between the water mass distribution and the iron distribution, Figure 2.37a, with the exception of the majority of higher iron concentrations lying within the AAIW to SACW transitional limb. There is a hint of higher concentrations in NADW end-member, which suggests that there is some persistent iron concentrations originating in the sub polar North Atlantic present in NADW. This signal can be seen more clearly in the T/O plot, where NADW is clearly indicated by high oxygen concentrations, Figure 2.37b. The decomposition of the AAIW to SACW limb by the variation in oxygen concentration demonstrates how the elevated iron concentrations in this is region is likely to be due to regeneration of organic matter beneath the surface. The correlation between the lower oxygen concentrations and the high iron concentration suggest that the respiration of organic matter causes a return of iron to the inorganic form in the intermediate water masses.

The 13°N section shows similar qualitative patterns to the south-north section. In general, high concentrations of iron are found in the AAIW to SACW transitional limb, Figure 2.37c. There are also some high concentrations found in the TSW, due to the delivery of atmospheric dust into the surface water. The NADW demonstrates higher concentrations relative to the south-north section, suggesting that the iron found in this water mass may no be solely due to persistent nutrients reaching the region from the high latitude North Atlantic. The T/O plots again shows the highest iron concentrations are found in the

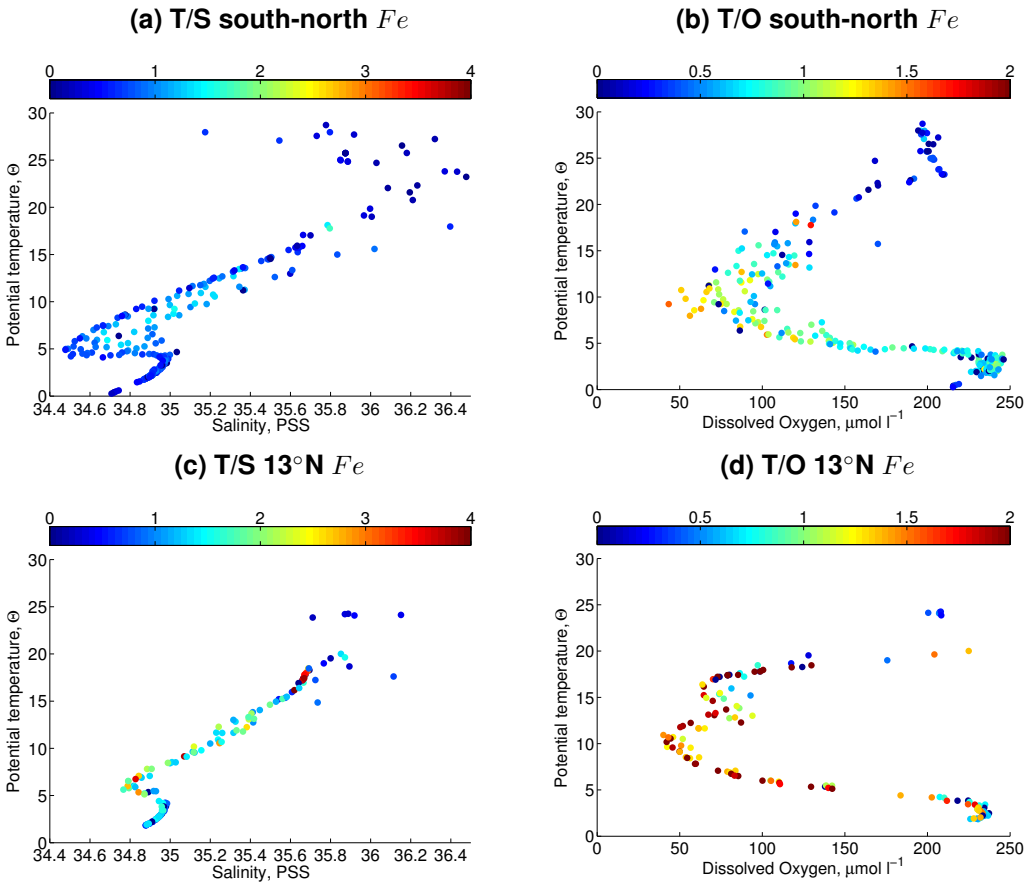

Figure 2.37: D361 T/S and T/O plots coloured by Fe (nM), note differing axes between T/S and T/O plots.

waters with the strongest depletion of oxygen concentrations, Figure 2.37d. The incidence of iron in the interior of the ocean is strongly dependent on the respiration of organic matter at depth. The consumption of oxygen in this region is higher than was seen for the south-north section, suggesting that the increase of atmospheric dust deposition towards the coast leads to an increase in consumption of oxygen, and consequently an increase in regeneration of organic matter. However, the high concentrations of iron seen in NADW without the consumption of oxygen suggests that there are processes in addition to biological processes such as respiration, that enable iron to penetrate into the deeper waters. The subsurface supply of iron by sediments and hydrothermal vents or the remineralisation of inorganic iron from particles, either as a result of the initial dust deposition or the adsorption on to particles, can provide a mechanism for this augmentation of deep waters with iron.

2.5.4 Importance of physical processes and biogeochemical regimes in the Tropical Atlantic

In contrast to the sub polar North Atlantic there are relatively few influences from the physics of the region on the nutrient distributions. There are significant differences between macro and micronutrient distributions. Macronutrients are relatively depleted in the surface but with high concentrations between 200m and 1500m. There are also high concentrations in the very deep waters. These two signals are connected to the waters of the Antarctic, which are often characterised by their persistent macronutrients following the growth season. The N:P ratios suggest that NO_2^-+NO_3^- and PO_4 are both similarly cycled. The regeneration signals are strongest within the South Atlantic Central Water with regeneration in Antarctic Intermediate Water, North Atlantic Deep Water and Antarctic Bottom Water also strong.

The distribution of iron is determined by the atmospheric dust deposition, both directly and indirectly. The direct deposition of dust into the surface water of the Tropical Water provides a direct supply of iron into the region. This direct supply diminishes with distance from the coast, but has a lasting impact on the waters beneath the surface further afield. There are two processes acting to redistribute the deposited iron in the dust: remineralisation of inorganic particles, via initial atmospheric deposition and particles partaking in the scavenging processes, and regeneration of organic material descending from the surface. The oxygen data suggests both of these processes are important. The latter is particularly important in the North Atlantic Deep Water, which is significantly augmented with iron beneath the dust plume. There is also evidence of persistent iron in the NADW in the stations further afield, where the dust plume has a much smaller influence and the oxygen data suggests there is no regeneration. The signal suggesting persisting iron in NADW suggests that iron can be transported significant distances without being completely stripped out of the water column by particle scavenging.

2.6 What Drives the Variation in Iron Regimes?

A discussion of the global and regional iron distributions is useful to establish a view of how the distribution of iron compares to its sources. The importance of the iron sources is apparent from the predictions that were possible based purely on source fields. An order of magnitude scaling based upon the iron source field and the physical circulation of a region can give a reasonable estimate of the relative magnitudes of iron when they are compared with a global database.

- Atmospheric sources (Mahowald et al., 2009) provide a strong imprint on the oceans. The Tropical Atlantic has the highest concentrations of all regions in the Atlantic due to the increased export and regeneration resulting from fertilisation of the phytoplankton community by atmospheric deposition.

- The areas of highest hydrothermal sources (Tagliabue et al., 2010) in the southeast Pacific are associated with the highest observed deep ocean concentrations of either the Pacific or Atlantic.

The subpolar North Atlantic exhibits a variety of biogeochemical characteristics. The Irminger and Iceland basins exhibit differing regimes. There is much more phosphate remaining in the upper 200m. The Iceland basin has less phosphate but more iron. The Iceland Basin displays elevated iron concentrations in waters around 500m deep. The higher concentrations of iron within the basin imply that the macronutrients in the Iceland basin could have been consumed due to the higher concentrations of iron.

The only major signals of iron in the Irminger Basin are those seen in the Denmark Strait Overflow Water and the North Atlantic Deep Water. Between two stations in the north and south of the basin there is some evidence for the augmentation of deep water by sediment supply. The consistency of T/S measurements and the existence of more buoyant plumes associated with the

DSOW circulating around the Irminger Basin close to the coast support this inference.

The Tropical Atlantic case study is a fantastic example of the complexities of the iron system (Schlosser et al., 2014). The atmospheric deposition of dust has a significant effect on the region. The deposition occurs in a more southerly region than expected resulting in a subtle change to the regime. Schlosser et al. (2014) indicated the importance of the precipitation patterns in determining the specific impacts that are seen from the atmospheric deposition. High concentrations of iron were observed close to the coast. The signal did not project very far showing the negative feedback of particle scavenging caused by atmospheric fertilisation by iron.

The processes that have not been widely covered in this introductory discussion play key roles on regional scales. The variability in processes such as scavenging, organic ligand concentrations and regeneration of organic material can cause localised variations. The unknown is whether they control the global-scale distribution of iron or just modify local iron cycling features. The complexity of the system on smaller scales is variable so there is a need to try to better understand some of the processes, such as scavenging.

When considering using the outcomes of this chapter to validate numerical models there are several important points that should be considered. The sub polar North Atlantic has a distinct difference in the two sub basins in the region. The Irminger Basin has several signals of iron supply on the basin fringes that are incorporated into cyclonic circulatory factors to redistribute iron throughout the basin. There significant supplies of phosphate replete water from surface run-off and glacial melt from the Greenland Coast, and from the Arctic Ocean via the Canadian Archipelago. The Iceland Basin is relatively depleted in macronutrients and is influenced by a supply of nutrient depleted water from the east and south of the sub polar North Atlantic. The strongest regeneration of nutrients occurs in the Iceland Basin, reflecting the stronger growth conditions apparent in the basin.

The Tropical Atlantic has strong far-field signals from the Antarctic, with intermediate and bottom waters very important for supplying macronutrients into the region. Upon this backdrop of subsurface nutrient supply there are strong signals of regeneration seen in the intermediate waters. These regeneration signals are possible due to the strong influx of terrigenous iron allowing strong utilisation of nutrients in the region. The presence of persistent nutrients in the North Atlantic Deep Water arriving at these low waters is also a key observation, suggesting that iron can persist in the ocean interior throughout the long journey from the sub polar region to the South Atlantic. The data also points to important regeneration of organic iron, and remineralisation of scavenged iron and dust particles at depth. These processes are important in simulating the iron cycle within models and can be seen as robust guidelines when it comes to validating and analysing numerical model results.

Chapter 3

Quantifying Trace Metal Scavenging Rates

3.1 Introduction

Particle scavenging is an important component of the iron cycle. Following detailed discussions of the supplies of iron and some net scavenging effects in chapter 2 a more in-depth look at our knowledge of particle scavenging is included here. Scavenging of trace metals by particles was a long-held hypothesis because of thermodynamical undersaturation (Goldberg, 1954; Krauskopf, 1956) and an inability to explain observed dissolved metal distributions with physical mixing processes. Krauskopf (1956) and Turekian (1977) formulated the hypothesis that scavenging was a result of the chemical surface reactions (adsorption, absorption and surface precipitation) associated with the presence of marine particles. Development of models to include the mechanics of these processes improved the accuracy of predictions for the vertical profile of scavenged trace metals. The observational challenges connected with verifying these molecular scale interactions was a major stumbling block for these early modellers. Significant development was made by Honeyman et al. (1988)

who detailed the calculation of particle concentration dependent scavenging rates. They exploited the discrepancy between dissolved and particulate pools of radionuclides of a suitable daughter-parent nuclide pairing. Assuming a chemical equilibrium, the partitioning of the radioisotope is diagnosed from observational measurements. The pairing they used was ^{234}Th / ^{238}U. These radioactive elements were useful due to the fact that the parent nuclide, ^{238}U, has a very long half life, 4.468 billion years, and is not particle reactive. The daughter nuclide, ^{234}Th, has a half-life of 24.1 days and is particle reactive with a much shorter residence time. There is a strong positive correlation of ^{238}U with salinity in the ocean, due to the element's very low reactivity and long residence time. This correlation reflects the dilution of terrestrial-derived inputs in the surface ocean (Chen and Millero, 1986).

The initial identification of partitioning between particulate and dissolved trace metals helped explain some of the observational data. However, Wu et al. (2001) found that for dissolved iron, the dissolved fraction had further subtle partitioning. They identified that there was less iron in the soluble and soluble-ligand-bound iron pool than previously assumed. Ultrafiltration techniques identified a large fraction of iron incorporated within the organic dissolved colloid pool. These colloids had previously been hypothesised as an intermediate phase within scavenging models, and an important catalyst for the removal of iron within the particulate phase (Honeyman and Santschi, 1989). The method of using radioisotope activity to measure the partitioning of ^{234}Th between the dissolved and particulate phase has been extensively used to estimate particle fluxes from the surface mixed layer as a proxy for biological carbon export. The biological carbon export calculations entail several steps: making estimates for the rate of adsorption to particles and subsequent fallout of particles, and then applying the observed $C :^{234} Th$ ratios of particles to estimate the export of carbon from the mixed layer.

We aim here to focus on the adsorption and fallout rates themselves and apply them to the iron cycle to calculate scavenging rates of dissolved iron and provide robust error estimates. We test the assumption that the system is

at equilibrium via a prognostic one-dimensional model. These model estimates can be applied to net adsorption rates and vertical removal rates of trace metals from the mixed layer following Honeyman et al. (1988). The calculations used here result in an integrated estimate of all sorption processes, including surface coordination and colloidal aggregation. The term adsorption is from here on used to refer to the net effect of these sorption processes. The method has been applied to a dataset in the Sub-polar North Atlantic to provide an indication of scavenging rates in this region. There is also an emphasis on determining the dominant drivers of scavenging rates. Combining observations within the water column, as well as potential causes for the variability of the observed scavenging rates, will be discussed. The data presented here appear courtesy of Dr. Frederic Le Moigne and Dr. Chris Marsay as well as model output courtesy of Stohl et al. (2011).

3.2 Method

3.2.1 ^{234}Th / ^{238}U Scavenging Models

The methods utilising the partitioning of ^{234}Th species rely on scavenging models to estimate various rate constants in order to reveal how the system behaves. There are numerous models that have been used that vary in the number of processes and element pools represented. There are two categories of these models: (a) Sorption and (b) Export models (Savoye et al., 2006).

(a) Sorption models represent the processes of adsorption to, and desorption from, particles. They take the form of a complexation reaction between dissolved metals and particle surface sites (Balistrieri et al., 1981), such as

$$\underbrace{PH_2}_{Particle} + \underbrace{Me^{2+}}_{Free\ metal} \rightleftharpoons \underbrace{PMe}_{Metal\ complex} + \underbrace{2H^+}_{Free\ ions}, \tag{3.1}$$

where P represents a particle, H represents a hydrogen ion and Me^{2+} represents a generic particle reactive metal ion. Different adsorption

models assume different mechanisms control this relationship, including: the organic content of particles (Balistrieri et al., 1981; Guo et al., 2002), reversibility of adsorption, the proportionality of desorption to particulate thorium concentration (Nozaki et al., 1981) and the dependence of adsorption rate on particle concentration (Bacon and Anderson, 1982). Early modelling based on these mechanisms resulted in improvements in predicting observed partitioning of radionuclide species. However, subsequent work (Santschi et al., 1986; Honeyman and Santschi, 1989; Burd et al., 2000) has suggested a higher complexity system with colloidal material behaving as an intermediary. These colloids are small particles (1nm to 1μm), not collected using standard filtration techniques, which aggregate to form larger particles. The importance of the colloidal fraction and the consequent aggregation and disaggregation between numerous size classes has been highlighted (Burd, 2013). The lack of observational partitioning of numerous size classes makes validation of these more complex colloid inclusive models difficult. There is still no consensus about the specifics of the sorption of ^{234}Th, with the different models mentioned above still in use.

(b) Export models deal with the removal of particulate ^{234}Th by fallout/settling. There are different levels of complexity to represent particle removal depending on the number of species or pools of ^{234}Th. In this study a two-pool model is employed (Figure 3.1), including partitioning between dissolved and particulate ^{234}Th with no further breakdown of the particulate pool into varying classes. A three-pool model is often also employed including small and large particles. The two-pool model is easier to constrain and provides a more integrated view of the system.

Sorption and export combine to provide the scavenging process, involving the integrated effect of transfer of a dissolved metal into particulate form, and its subsequent removal from a particular depth layer.

The scavenging model used in this study combines a sorption model with reversible sorption processes and no intermediate reactions, with a two-pool export model. The adsorption rates are dependent on particulate organic

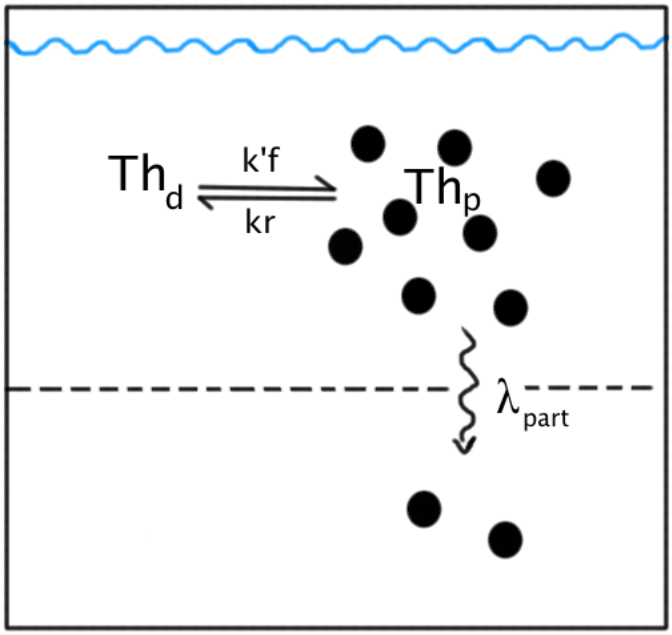

Figure 3.1: Schematic of a two-box export model. Dissolved (Th_d) and particulate (Th_p) thorium are controlled by forward ($k'f$) and reverse (kr) sorption processes and the physical fallout (λ_{part}) of particles.

carbon (POC) concentration and desorption rates are independent of particles. We use POC because of the wide availability of these data in conjunction with ^{234}Th / ^{238}U measurements. Calculations of the net rates are independent of particle concentration. There is a wide range of ^{234}Th / ^{238}U measurements and POC data, which have not been exploited to their full potential. We aim to exploit this abundant resource, alongside a novel approach to quantifying adsorption and removal rates, to map spatial variation of scavenging rates across the subpolar gyre of the North Atlantic.

3.2.2 Calculation of the Rate Constants

The partitioning of ^{234}Th is calculated using the equations first presented by Honeyman et al. (1988). The derivation of these equations is shown here. Following on from (3.1) we can substitute in the two species of our metal of interest, ^{234}Th, which we have decided to represent in our model:

$$\underbrace{SX_{\chi}}_{Particle} + \underbrace{[Th_{diss}]}_{Dissolved\ metal} \overset{K_{ThD}}{\rightleftharpoons} \underbrace{[Th_{part}]}_{Metal\ complex} + \underbrace{\chi X}_{Free\ ions} . \tag{3.2}$$

We have also generalised the other aspects of the equation for simplicity; S represents the particle surface site, χ is the number of exchangeable ion sites available per particle (i.e. replaces the 2 in H_2 and $2H$ from (3.1)) and X represents "other exchangeable ions" that compete with ^{234}Th for the surface sites. K_{ThD} is the thorium distribution coefficient, which defines how ^{234}Th is partitioned between dissolved and particulate forms.

We can stipulate the rate of change of a dissolved metal pool, in this case $[Th_{diss}]$, in terms of overall system variables. The change of dissolved thorium concentration is determined by two processes: the "forward" net adsorption rate, which is reliant upon $[Th_{diss}]$ and particle concentration $[SX_\chi]$, and the "backward" desorption reaction rate, which involves reactions between the particle-metal complex $[Th_{part}]$ and other exchangeable ions, $[\chi X]$,

$$\frac{\partial[Th_{diss}]}{\partial t} = \underbrace{-k_f[Th_{diss}][SX_\chi]}_{Net\ adsorption} + \underbrace{k_r[Th_{part}][\chi X]}_{Desorption}, \tag{3.3}$$

and likewise for the particulate phase,

$$\frac{\partial[Th_{part}]}{\partial t} = \underbrace{k_f[Th_{diss}][SX_\chi]}_{Net\ adsorption} - \underbrace{k_r[Th_{part}][\chi X]}_{Desorption}. \tag{3.4}$$

where k_f and k_r rates are the net expression of the forward and reverse reactions including coagulation and adsorption.

We make the assumption that the change in exchangeable ion pool, $\Delta[\chi X]$, is unimportant and substitute k'_f in for the term $k_f[SX_\chi]$. With the latter substitution, adsorption rates are assumed dependent on particle, or POC, concentration. We can now include source and sink terms for the ^{234}Th species. The source of $[Th_{diss}]$ results from radioactive decay of ^{238}U, the rate of this supply is determined by the decay constant, λ_U, of ^{238}U. Th_{diss} is lost as a consequence of its own decay into ^{234}Pa, the rate of which is determined by its decay constant, λ_{Th},

$$\frac{\partial[Th_{diss}]}{\partial t} = \underbrace{\lambda_U[U]}_{Supply\ of\ ^{234}Th} - \underbrace{\lambda_{Th}[Th_{diss}]}_{Decay\ of\ ^{234}Th} - k'_f[Th_{diss}] + k_r[Th_{part}]'. \tag{3.5}$$

$[Th_{part}]$ is itself modified by radioactive decay of ^{234}Th as well as the physical fallout of $[Th_{part}]$ associated with particles,

$$\frac{\partial[Th_{part}]}{\partial t} = k'_f[Th_{diss}] - \underbrace{\lambda_{Th}[Th_{part}]}_{Decay\ of\ ^{234}Th} - k_r[Th_{part}] - \underbrace{\lambda_{part}[Th_{part}]}_{Particle\ fallout}. \tag{3.6}$$

The final step before being able to apply these equations to the available data is to convert the quantities from change in concentration to change in activity (A). Activity is by definition a rate of change of a radioisotope concentration, where for example,

$$A_{Th_{diss}} \equiv \frac{\partial[Th_{diss}]}{\partial t} \equiv \lambda_{Th}[Th_{diss}], \tag{3.7}$$

$$A_{Th_{part}} \equiv \frac{\partial[Th_{part}]}{\partial t} \equiv \lambda_{Th}[Th_{part}], \tag{3.8}$$

and

$$A_U \equiv \frac{\partial[U]}{\partial t} \equiv \lambda_U[U]. \tag{3.9}$$

For the dissolved phase,

$$\frac{\partial A_{Th_{diss}}}{\partial t} = \lambda_{Th}A_U - \lambda_{Th}A_{Th_{diss}} - k'_f A_{Th_{diss}} + k_r A_{Th_{part}}, \tag{3.10}$$

provides a balance for dissolved ^{234}Th; the supply from ^{238}U decay, λA_U, the decay of Th_{diss}, $\lambda_{Th}A_{Th_{diss}}$, the adsorption of Th_{diss} onto particles, $k'_f A_{Th_{diss}}$, and the desorption from particles, $k_r A_{Th_{part}}$. For the particulate phase,

$$\frac{\partial A_{Th_{part}}}{\partial t} = k'_f A_{Th_{diss}} - \lambda_{Th}A_{Th_{part}} - k_r A_{Th_{part}} - \lambda_{part}A_{Th_{part}}, \tag{3.11}$$

which further takes into account the decay of Th_{part}, $\lambda_{Th}A_{Th_{part}}$, and the fallout of Th_{part}, $\lambda_{part}A_{Th_{part}}$ to provide a balance for particulate ^{234}Th.

Bacon and Anderson (1982) found that the desorption rate (k_r) was independent of particle concentration and was equal to 0.007 $\pm$ 0.003 day^{-1}. With this desorption rate as a known constant and the decay constants and activities known there remain two unknowns if we assume equilibrium.

Rearranging (3.10) and (3.11) we find the adsorption rate (k'_f) and fallout rate (λ_{part}) respectively,

$$k'_f = \frac{\lambda_{Th}A_U - \lambda_{Th}A_{Th_{diss}} + k_r A_{Th_{part}}}{A_{Th_{diss}}}, \tag{3.12}$$

$$\lambda_{part} = \frac{k'_f A_{Th_{diss}} - \lambda_{Th}A_{Th_{part}} - k_r A_{Th_{part}}}{A_{Th_{part}}}. \tag{3.13}$$

Instead of assuming equilibrium, we can retain the tendency terms,

$$k'_f = \underbrace{\frac{\lambda_{Th}A_U - \lambda_{Th}A_{Th_{diss}} + k_r A_{Th_{part}}}{A_{Th_{diss}}}}_{equilibrium\ estimation} - \underbrace{\frac{\frac{\partial A_{Th_{diss}}}{\partial t}}{A_{Th_{diss}}}}_{error}, \tag{3.14}$$

$$\lambda_{part} = \frac{\overbrace{k'_f A_{Th_{diss}} - \lambda_{Th}A_{Th_{part}} - k_r A_{Th_{part}}}}{A_{Th_{part}}} - \frac{\overbrace{\frac{\partial A_{Th_{part}}}{\partial t}}}{A_{Th_{part}}}. \tag{3.15}$$

With our modelling approach we provide estimates of the tendency and therefore provide an error associated with the equilibrium assumption.

3.2.3 Error quantification model

Once the rate constants have been calculated from the observations we then experimented with quantifying the errors in the calculations. The model uses the rate constants k'_f and λ_{part} that were calculated using (3.12) and (3.13), along with a hypothetical time series of POC concentration to test the assumption of equilibrium. k_f is diagnosed, where $k_f[POC] \approx k'_f$, in order to test the importance of changing particle concentration, and k'_f in (3.10) and (3.11) is substituted for $k_f[POC]$ in order to introduce the dependence of adsorption rate on the temporal variability of $[POC]$;

$$\frac{\partial A_{Th_{diss}}}{\partial t} = \lambda_{Th}A_U - \lambda_{Th}A_{Th_{diss}} - k_f[POC]A_{Th_{diss}} + k_r A_{Th_{part}} \tag{3.16}$$

and

$$\frac{\partial A_{Th_{part}}}{\partial t} = k_f[POC]A_{Th_{diss}} - \lambda_{Th}A_{Th_{part}} - k_r A_{Th_{part}} - \lambda_{part}A_{Th_{part}}. \tag{3.17}$$

The errors are quantified by building a model from these prognostic equations for the change in activity of dissolved and particulate ^{234}Th, (3.16) and (3.17). The tendency terms on the left hand side of these equations can be used in conjunction with the respective activities to calculate the error term illustrated in (3.14) and (3.15), thus obtaining an estimate for the error in the equilibrium assumption.

The hypothetical time series formulated have daily values for POC concentration, which can evolve depending on certain components. We use three components, the background residual POC concentration level, $[POC]_R$ and single (annual) and double (biannual) phytoplankton bloom seasonal variation in $[POC]$, S_1 and S_2 respectively. These three components are summed to create an annual cycle of hypothetical POC concentrations,

$$[POC] = [POC]_R + S_1 + S_2. \tag{3.18}$$

The seasonal variation terms are formed from a sine with two types of seasonal variation. Type 1 scenarios are dominated by the annual seasonal cycle,

$$S_1 = A_1 sin\left(\frac{2\pi t_{day}}{\tau_1} - \varphi_S\right), \tag{3.19}$$

and type 2 scenarios are dominated by the biannual seasonal cycle,

$$S_2 = A_2 sin\left(\frac{2\pi t_{day}}{\tau_2} - \varphi_S\right). \tag{3.20}$$

The different parameters, and the range of values used to generate the time series, are detailed in table 3.1, and a sample of the range of seasonal cycles produced is shown in Figure 3.2. Type 1 represents a ”single bloom” scenario where primary production increases throughout the year to peak at day 180 before steadily declining again. Type 2 represents a ”double bloom” scenario, where primary production increases from day 1 to day 90, then a decline until reaching a mid-year minimum on day 180, before peaking again at day 270 and finally declining back to the yearly low at day 360.

Table 3.1: Values used for Time series component parameters

Symbol	Description	Units	Values
$\overline{POC}$	Mean [POC]	μM	[0.4 0.6 0.8]
A_1	Amplitude of signal 1	μM	[0.4 0.6 0.8]
A_2	Amplitude of signal 2	μM	[0 0.2 0.3 0.4]
τ_1	Period of seasonal signal 1	days	365
τ_2	Period of seasonal signal 2	days	182.5
φ_S	Phase shift of seasonal signals	-	$\pi/2$
t_{day}	Day of the year	-	1 - 365

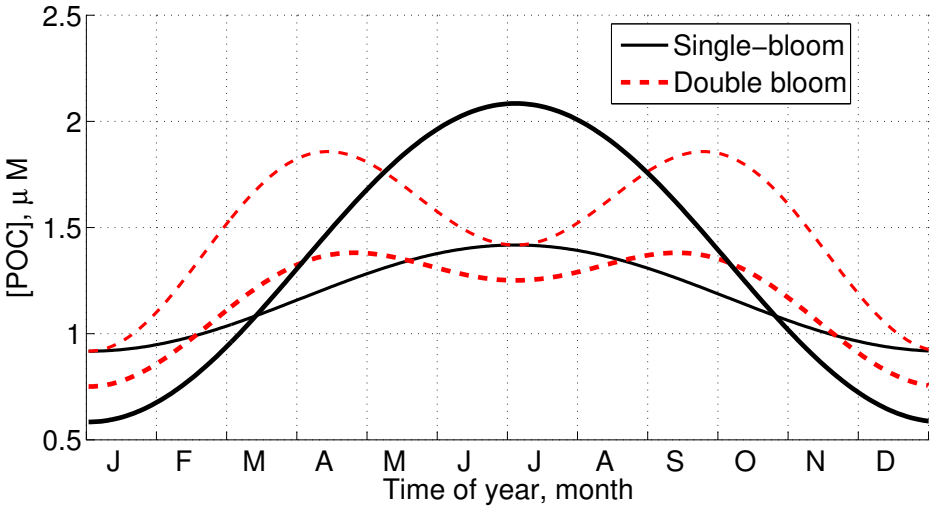

Figure 3.2: Examples of simulated [POC] time-series

To recap, the model is built from the activity prognostic relations (3.16) and (3.17). The model is forced with the theoretical seasonal $[POC]$ cycles and a single pair of observationally derived adsorption (k_f) and fallout (λ_{part}), rates in addition to the observed activities and known decay constants, then integrated in a 1-dimensional configuration. The normalised error for both the adsorption and fallout rates is diagnosed from the dynamic tendency that emerges from the model iteration. For each observation the model is integrated with each of the 128 hypothetical $[POC]$ time series generated from the three temporal components, resulting in a large ensemble of model runs per datapoint. These runs are collated and analysed to provide minimum, maximum and mean error estimates for each individual pair of rates calculated from the cruise dataset.

3.3 Results and Discussion

The methods detailed above are applied to datasets for the subpolar gyre of the North Atlantic. A range of stations were sampled at different times of the year. D350 took place in early-May 2010 and D354 in July-August 2010. The station locations for the cruises are shown in Figure 3.3. The results from this analysis are presented within three main sections.

1. The findings from the scavenging rate error quantification model;
2. The calculation of the adsorption and fallout rate constants from the data;
3. Application of the scavenging rates to quantify magnitudes of iron fluxes in the subpolar gyre of the North Atlantic.

The error estimates are presented first to avoid repetition and provide context to adsorption and fallout rate calculations.

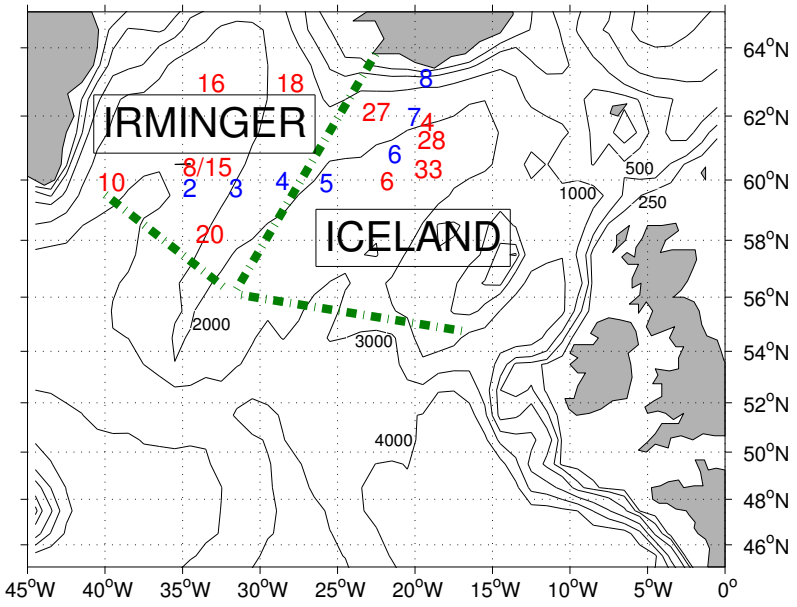

Figure 3.3: Station location and Irminger and Iceland basin partitioning plot for D350 (blue) and D354 (red), with bathymetric contours at 250m, 500m, 1000m, 2000m, 3000m and 4000m

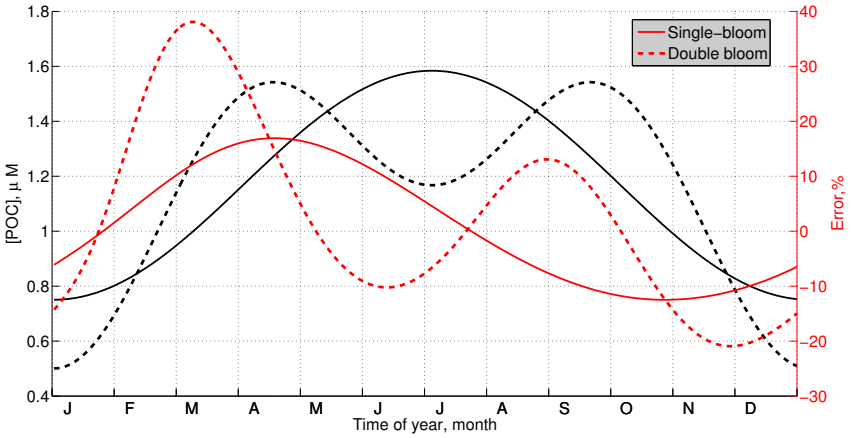

Figure 3.4: Plot showing examples of idealised single and double bloom [POC] seasonal cycles (Black, left y-axis). Quantified errors in diagnosed adsorption rates associated with these [POC] time series are also shown (Red right-hand y-axis)

3.3.1 Model error quantification

General assessment of errors

To provide some context to the implications of the model results, the effect of two different growth regimes on the error over the seasonal cycle is presented. An idealised boreal $[POC]$ seasonal cycle for each of the growth regimes, single-bloom and double-bloom, are shown alongside the temporal variation in adsorption rate error resulting from the equilibrium assumption (Figure 3.4). The single-bloom scenario generally results in lower errors in the diagnosed adsorption rates, with maximum errors around 15% compared with 35% for the double-bloom scenario. This difference is due to the greater rate of change of $[POC]$ during the double-bloom scenario, as revealed by the slope in Figure 3.4. When the $[POC]$ is changing quickly the disequilibrium between the adsorption, desorption and fallout is greatest. The times of largest $\frac{\partial[POC]}{\partial t}$ coincide with the largest errors for both of the scenarios; at the end of March for the single-bloom scenario and the end of February for the double-bloom scenario. This effect is modified by the prior history of the system, as seen most clearly in the difference in the errors between the double-bloom February and November absolute maxima in $\frac{\partial[POC]}{\partial t}$. The February maximum produces errors of 35%, whereas the November maximum produces errors of 20%.

This initial analysis shows that the gradient in $[POC]$ affects the magnitude of the error. This is modified by the prior history of the system, meaning the increase in $[POC]$ during Spring of the seasonal cycle produces the largest error. Periods following the Spring bloom are less affected by errors resulting from the equilibrium assumption.

Rate error assessments for cruise data

For relevant errors to be applied to each pair of diagnosed data-derived rates, the seasonal variation in the errors needs to be put into the context of the time at which the data was sampled. The D350 cruise took place in early May 2010 (Julian day 122 to 129) and the D354 cruise took place in July-August 2010 (Julian day 197 to 221). The errors associated with the respective cruises were taken from days 110 to 140 for D350 and 185 to 235 for D354. When extracting errors for the data points these time periods are used to determine the appropriate choice, including a temporal mismatch in the seasonal cycles of approximately two weeks.

These errors are extracted from the model ensembles by taking the maximum absolute error that is found within the time period defined above and denoted by the dotted lines on the plots. The minimum and maximum errors in adsorption and fallout rates diagnosed from the suite of model ensembles run for each dataset are presented here as an example of the results found with this method.

The minimum error for adsorption rates during D350 was 18% (Figure 3.5a) and the maximum adsorption rate error was 50% (Figure 3.5b). These minimum and maximum adsorption rate errors emerge from different adsorption-fallout rate pairings calculated at a specific station from the cruise. These errors are then applied to the diagnosed adsorption rates to give minimum and maximum errors for D350 data as 0.068 $\pm$ 18% d^{-1} and 0.0018 $\pm$ 58% d^{-1} respectively. Similarly, minimum and maximum errors in the fallout rate (Figure 3.6) are 0.64 $\pm$ 1% d^{-1} and 0.063 $\pm$ 25% d^{-1}. The adsorption

and fallout rate results are presented more completely in the following section, but to avoid repetition the error quantification results are presented first, even though their calculation relies on the calculated adsorption and fallout rates.

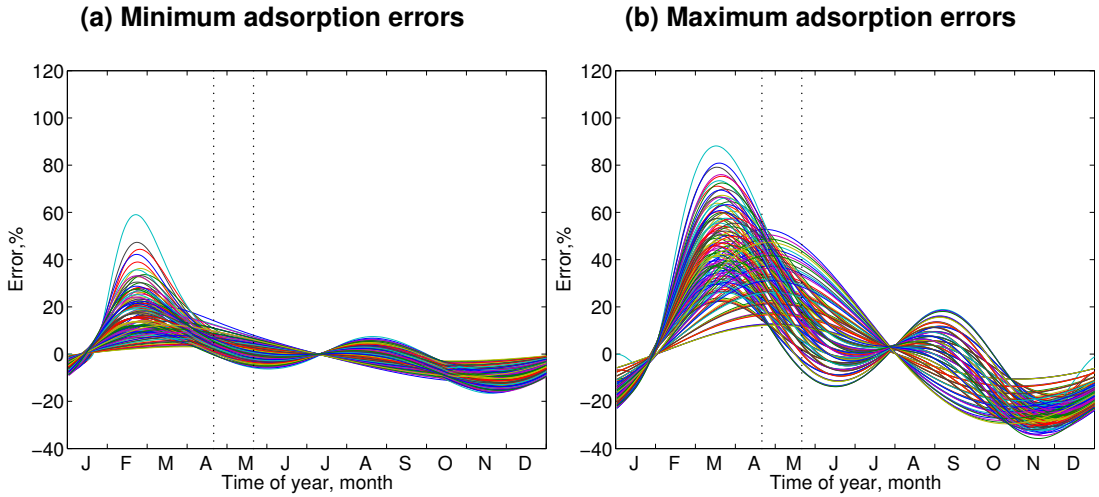

Figure 3.5: Plots of normalised adsorption error over the seasonal cycle for D350, dotted line shows timing of in situ measurements $\pm$ 10 days.

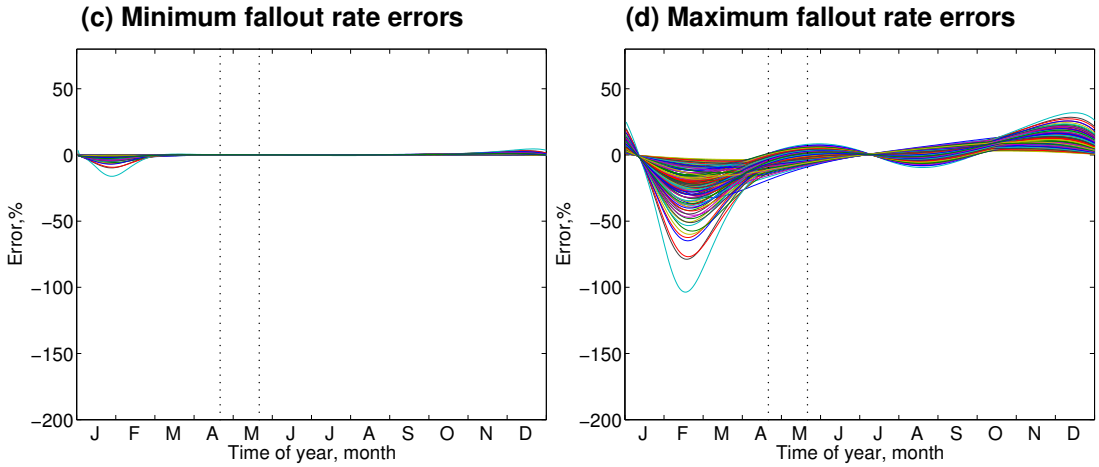

Figure 3.6: Plots of normalised fallout rate error over the seasonal cycle for D350, dotted line shows timing of in situ measurements $\pm$ 10 days.

The D354 dataset was gathered in the summer of 2010 a few months following the spring bloom and later in the year than D350. Consistent with the model inferences the errors in the adsorption and fallout rates are much lower in this later dataset than for D350. The minimum and maximum errors in adsorption rates (Figure 3.7) were 0.095 $\pm$ 8% d^{-1} and 0.0055 $\pm$ 19% d^{-1} respectively, whereas the minimum and maximum errors in fallout rates (Figure 3.8) were

0.40 $\pm$ 1% d^{-1} and 0.03 $\pm$ 20% d^{-1} respectively.

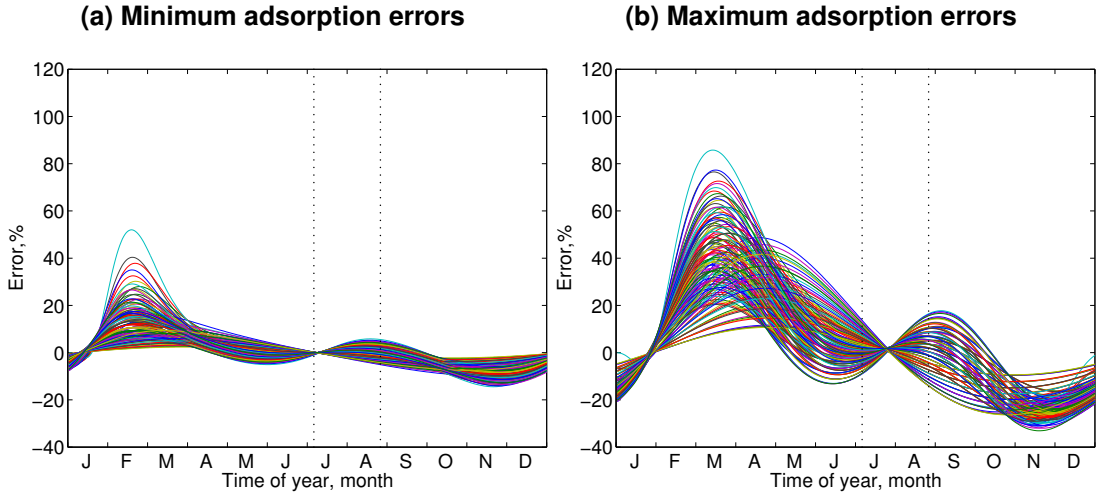

Figure 3.7: Plots of normalised adsorption error over the seasonal cycle for D354, dotted line shows timing of in situ measurements $\pm$ 10 days.

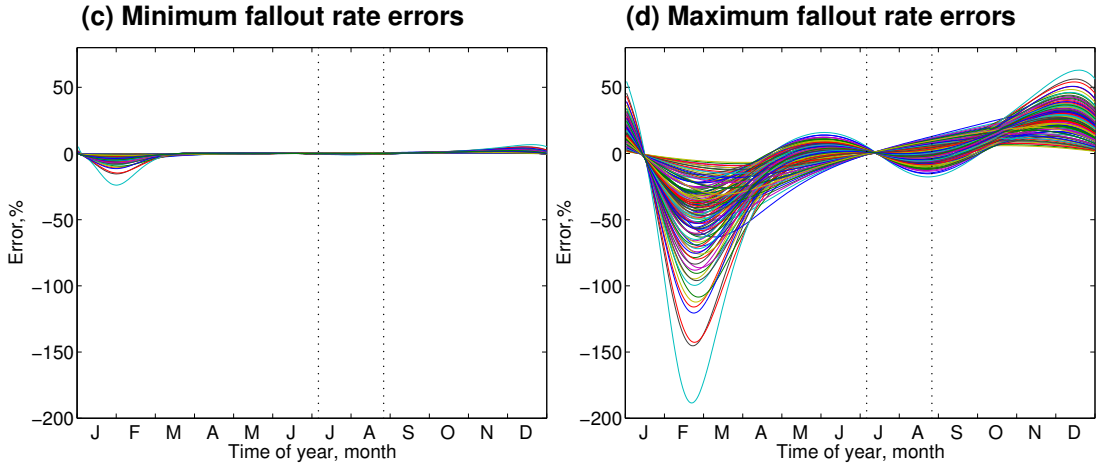

Figure 3.8: Plots of normalised fallout rate error over the seasonal cycle for D354, dotted line shows timing of in situ measurements $\pm$ 10 days.

3.3.2 Adsorption and fallout rates in the subpolar North Atlantic

3.3.2.1 Calculation of net rates

We present our results as a particle concentration dependent adsorption rate and net adsorption rate. Both of these rates provide a net representation of all sorptive processes, such as surface coordination and colloidal aggregation. The particle dependent rates assume a relationship between forward sorption

processes and particles in the water column. We calculated the rate constants for data from two cruises investigating the biogeochemistry of the North Atlantic subpolar gyre, D350 and D354 (Tables 3.2 and 3.3). Comparisons are made between the estimates in this study and other studies encompassing calculations of adsorption and colloidal aggregation rates of ^{234}Th and Fe.

Table 3.2: Table showing rates derived from ^{234}Th for D350 data at depths of 150m and 50m. (*Bold-italicized numbers are from 150m*)

Station	Adsorption Rate d^{-1}	Particle Dependent Adsorption Rate $\mu mol^{-1} L\ d^{-1}$	Error %	Fallout Rate d^{-1}	Error %
2	0.00946	0.0215	$\pm$ 34 %	0.26344	$\pm$ 2 %
3	0.00509	0.0117	$\pm$ 42 %	0.19261	$\pm$ 3 %
4	0.00219	0.0066	$\pm$ 47 %	0.06304	$\pm$ 8 %
5	0.00215	0.01	$\pm$ 44 %	0.16151	$\pm$ 3 %
6	0.00179	0.0095	$\pm$ 43 %	0.0869	$\pm$ 6 %
7	0.00445	0.0217	$\pm$ 33 %	0.20359	$\pm$ 2 %
8	0.00338	0.0298	$\pm$ 28 %	0.53702	$\pm$ 1 %
2	0.00919	0.017	$\pm$ 37 %	0.26253	$\pm$ 2 %
3	0.0143	0.0235	$\pm$ 32 %	0.3662	$\pm$ 1 %
4	0.00248	0.0019	$\pm$ - %	-	$\pm$ - %
5	0.00426	0.0018	$\pm$ 58 %	0.12414	$\pm$ 5 %
6	0.00598	0.0115	$\pm$ 42 %	0.18994	$\pm$ 3 %
7	0.00364	0.0064	$\pm$ 49 %	0.1176	$\pm$ 5 %
8	0.00433	0.069	$\pm$ 14 %	0.6366	$\pm$ 0 %
Min	0.00179	0.0018	-	0.06304	-
Max	0.0143	0.069	-	0.6366	-
Mean	0.00519$\pm$0.0035	0.0173$\pm$0.017	-	0.24655$\pm$0.17	-

The mean values of the particle dependent adsorption rates for the two cruises are of similar magnitude, 0.017 $\pm$0.017 $\mu mol^{-1}\ L\ d^{-1}$ for D350 and 0.022 $\pm$0.02 $\mu mol^{-1}\ L\ d^{-1}$ for D354. Direct surface adsorption onto particles cannot produce rates as high as are found in this study. Previous estimates of surface adsorption (Nyffeler et al., 1984) are much lower, 1.8 to 4.2 x $10^{-4} \mu mol^{-1}\ L\ d^{-1}$ (For full synthesis of observational and model estimates of rates see Table 3.4). Our findings are much more consistent with a system where colloidal

Table 3.3: Table showing rates derived from ^{234}Th for D354 data at depths of 150m and 50m. (*Bold-italicized numbers are from 150m*)

Station	Adsorption Rate d^{-1}	Particle Dependent Adsorption Rate $\mu mol^{-1}L\ d^{-1}$	Error %	Fallout Rate d^{-1}	Error %
4	0.00581	0.0195	± 14 %	0.11942	± 3 %
6	0.00381	0.0147	± 14 %	0.04578	± 8 %
8	0.00248	0.0055	± 16 %	0.14853	± 3 %
10	0.00131	0.0024	± - %	-	± - %
15	0.00882	0.0123	± 15 %	0.03517	± 10 %
16	0.00417	0.0045	± 16 %	0.03939	± 11 %
18	0.06064	0.0949	± 6 %	0.27245	± 1 %
20	0.00509	0.0132	± 15 %	0.09335	± 4 %
27	0.00672	0.007	± 16 %	0.05127	± 8 %
28	0.00081	0.0009	± - %	-	± - %
33	0.00254	0.0079	± 15 %	0.0305	± 13 %
4	0.00061	0.0022	± - %	-	± - %
6	0.03271	0.0347	± 11 %	0.16883	± 2 %
8	0.0217	0.0191	± 14 %	0.0867	± 4 %
10	0.02999	0.0269	± 12 %	0.10453	± 3 %
15	0.02333	0.0215	± 13 %	0.09414	± 4 %
16	0.02399	0.0391	± 10 %	0.10689	± 2 %
18	0.05519	0.0453	± 10 %	0.39568	± 1 %
20	0.00771	0.0063	± 16 %	0.05677	± 8 %
24	0.08753	0.0824	± 6 %	0.14698	± 1 %
27	0.02588	0.0218	± 13 %	0.27826	± 1 %
28	0.02037	0.0208	± 14 %	0.17553	± 2 %
33	0.00796	0.0117	± 15 %	0.07932	± 5 %
Min	0.00061	0.0009	-	0.0305	-
Max	0.08753	0.0949	-	0.39568	-
Mean	0.01909±0.02	0.0224±0.02	-	0.12648±0.09	-

aggregation is important, as our rates are comparable to those found by Wen et al. (1997) for colloidal aggregation of iron. Our estimates of net adsorption rates are also consistent with a study by Baskaran et al. (1992) who took into account the colloidal aggregation of ^{234}Th. Baskaran et al. (1992) surveyed adsorption rates from coastal regions to the open ocean, with their lower estimates being from open ocean regions analogous to the regions sampled in our study. Our estimates of net adsorption rates are 5.2 x 10^{-3} and 16 x 10^{-3} d^{-1} for D350 and D354 respectively, consistent with the lower end of the estimates by Baskaran et al. (1992) of 7 x 10^{-3} to 164 x 10^{-3} d^{-1}.

Table 3.4: Table showing comparison of rates from other studies,[a] NEMO-PISCES model as Aumont and Bopp (2006); Tagliabue et al. (2010), [b] MITgcm as described in Chapter 4. Numerical model studies are italicised.

Processes diagnosed and Authors	Adsorption Rate d^{-1}	Particle Dependent Adsorption rate $\mu mol^{-1}\ L\ d^{-1}$	Fallout rate d^{-1}
Fe Adsorption only Nyffeler et al. (1984)		0.18 to 0.42 x 10^{-3}	
Fe Colloidal Wen et al. (1997)		3 to 150 x 10^{-3}	
^{234}Th Colloidal Baskaran et al. (1992)	7 to 164 x 10^{-3}		
Fe Adsorption only Ye et al. (2011)		0.3 to 9 x 10^{-3}	
Fe Scavenging NEMO-PISCES[a]	5 x 10^{-3}		
Fe Scavenging MITgcm[b]	4.9 $\pm$1.5 x 10^{-3}	22$\pm$17 x 10^{-3}	
This study			
D350$_{MAX}$	14.3 x 10^{-3}	69 x 10^{-3}	0.64
D350$_{MIN}$	1.8x 10^{-3}	1.8 x 10^{-3}	0.063
D350$_{MEAN}$	5.2 x 10^{-3}	17 x 10^{-3}	0.25
D354$_{MAX}$	87 x 10^{-3}	95 x 10^{-3}	0.4
D354$_{MIN}$	0.61 x 10^{-3}	0.09 x 10^{-3}	0.03
D354$_{MEAN}$	19 x 10^{-3}	22 x 10^{-3}	0.12

Ye et al. (2011)'s modelled adsorption rates, excluding coagulation, during a mesocosm study further support the inference that colloidal aggregation is important. Their suggested rates only reconcile the lower end of our particle dependent adsorption rate estimates. The calculated rates from this study are consistent with the rates that are applied to current general circulation models: NEMO-PISCES and the MITgcm. Atlantic basin mean net and particle dependent rates from the MITgcm (as described in Chapter 4) are diagnosed and presented here to illustrate the variability represented within these models (Table 3.4).

The rates diagnosed during D350 and D354 are comparable to previous estimates of colloidal aggregation and coagulation. The processes contributing to particle scavenging in the North Atlantic subpolar gyre are a combination of direct scavenging and colloidal aggregation, consistent with the framework set out by Honeyman et al. (1988).

The respective mean fallout rates derived from ^{234}Th are 0.25 and 0.13 d^{-1}, for D350 and D354. Thus while the particle sorption dynamics are a similar order of magnitude between the two periods, the fallout rates during D350 are twice as large as those for D354. The timing of the Eyjafjallajokull volcanic eruption in Iceland coincides with the D350 cruise. The volcanic eruption deposited significant amounts of volcanic tephra across the subpolar gyre and stimulated biological productivity (Achterberg et al., 2013). This deposition is likely to drive the variation in fallout rates between the cruises.

Table 3.5: Table showing the basin mean net adsorption and fallout rates for D350 and D354

Basin	Cruise	Net adsorption rate (K), d^{-1}	Fallout rate(λ), d^{-1}
Irminger	D350	0.0073	0.228
Iceland	D350	0.0020	0.124
Irminger	D354	0.0138	0.118
Iceland	D354	0.0039	0.062

The variability in the adsorption and fallout rates appears to be relatively large, but does this variability dominate on regional scales or is there the potential for

consistent inter-basin contrasts? To explore this question the ratios between Irminger and Iceland basin stations (Figure 3.3) are used, where for example the net adsorption rates (K) for the two basins during D350 are represented as K^{irm}_{D350} and K^{ice}_{D350} (Table 3.5). The ratios between the basins are very similar,

$$\frac{K^{irm}_{D350}}{K^{ice}_{D350}} \approx \frac{K^{irm}_{D354}}{K^{ice}_{D354}} \approx 3.6. \tag{3.21}$$

Thus, we find that for both cruises the mean net adsorption rates in the Iceland Basin are approximately 3.6 times larger than those in the Irminger Basin. Similarly, for fallout (λ) rates:

$$\frac{\lambda^{irm}_{D350}}{\lambda^{ice}_{D350}} \approx \frac{\lambda^{irm}_{D354}}{\lambda^{ice}_{D354}} \approx 1.87. \tag{3.22}$$

The difference in magnitude of the mean adsorption and fallout rates for the two basins suggests that there is regional-scale variation in trace metal scavenging rates. However, the consistency in the ratios of the rates between the basins suggests that the underlying drivers of the particle scavenging system are broadly similar.

3.3.2.2 Iron fluxes

To apply the adsorption and fallout rates to iron we make the assumption that the rate constants applicable for ^{234}Th are equivalent to those that drive the adsorption, desorption and removal of iron. Comparisons with other work in the previous section suggest our rates are comparable to Ye et al. (2011); Wen et al. (1997). Using this assumption it is possible to estimate the respective iron fluxes for each of the two datasets (Tables 3.6 and 3.7). The derived iron fluxes ($pM\ Fe\ d^{-1}$) are calculated as a product of the dissolved iron concentration and net adsorption,

$$Fe^{sorp}_{T} = k'_f[Fe_T], \tag{3.23}$$

and the particulate iron concentration and fallout rate,

$$Fe^{fal}_{P} = \lambda_{fal}[Fe_P]. \tag{3.24}$$

Further fluxes can be estimated for additional dissolved iron species, such as free inorganic iron, Fe', and colloidal iron, Fe_{coll}. To estimate free and

ligand-bound iron the ligand-bound iron is calculated by using an equilibrium assumption,

$$K_{FeL}^{cond} = \frac{[FeL]}{[Fe'][L']}, \tag{3.25}$$

where,

$$[Fe_T] = \underbrace{[Fe']}_{Free\ iron} + \underbrace{[FeL]}_{Complex}, \tag{3.26}$$

Table 3.6: Table showing derived iron fluxes for D350 data from "free", "colloidal" and "Total" iron pools at depths of 150m and 50m. (*Bold-italicized numbers are from 150m*)

Station	Adsorption Fe'^{sorp} $pMFed^{-1}$	Fe_{coll}^{sorp} $pMFed^{-1}$	Fe_T^{sorp} $pMFed^{-1}$	Error %	Fallout Fe_P^{fal} $pMFed^{-1}$	Error %
3	2.17 x 10^{-6}	0.91	0.913	$\pm$ 42 %	5	$\pm$ 3 %
4	1.14 x 10^{-6}	0.45	0.451	$\pm$ 47 %	5.1	$\pm$ 8 %
5	1.4 x 10^{-6}	0.51	0.509	$\pm$ 44 %	7.9	$\pm$ 3 %
6	1.69 x 10^{-6}	0.52	0.521	$\pm$ 43 %	9.3	$\pm$ 6 %
3	6.9 x 10^{-7}	0.4	0.395	$\pm$ 32 %	7.7	$\pm$ 1 %
4	5.16 x 10^{-6}	1.01	1.006	$\pm$ - %	-	$\pm$ - %
5	1.28 x 10^{-6}	0.59	0.591	$\pm$ 58 %	3.6	$\pm$ 5 %
7	1.957 x 10^{-5}	1.84	1.841	$\pm$ 49 %	35.3	$\pm$ 5 %
8	0.086619	2.6	3.075	$\pm$ 14 %	188.4	$\pm$ 0 %
Min	6.9 x 10^{-7}	0.4	0.395	-	3.2	-
Max	0.086619	2.6	3.075	-	188.4	-
Mean	0.0096281$\pm$0.029	0.98$\pm$0.76	1.034$\pm$0.89	-	26.9$\pm$63	-

and,

$$[L_T] = \underbrace{[L']}_{Free\ ligand} + \underbrace{[FeL]}_{Complex}. \tag{3.27}$$

The value of total ligand, $[L_T] = [FeL] + [L']$, is approximated to $0.6\ nM$ covering a range of observed ligand concentrations, 0.4 to 0.8 nM (Wu and Luther, 1995; Wu et al., 2001; Mohamed et al., 2011). K_{FeL}^{cond} represents the ligand conditional stability constant, which determines the partitioning of complexed iron, FeL, free iron, Fe', and free ligand, L'. Here we use a value of $10^{12}\ M\ M^{-1}$ for K_{FeL}^{cond} following ++++++++. Total ligand concentration and

Table 3.7: Table showing derived iron fluxes for D354 data from "free", "colloidal" and "Total" iron pools at depths of 150m and 50m. (*Bold-italicized numbers are from 150m*)

Station	Adsorption Fe'^{sorp} $pMFed^{-1}$	Fe_{coll}^{sorp} $pMFed^{-1}$	Fe_{T}^{sorp} $pMFed^{-1}$	Error %	Fallout Fe_{P}^{fal} $pMFed^{-1}$	Error %
4	0.00413	1.45	1.452	$\pm$ 14 %	0.5	$\pm$ 3 %
8	0.0023	0.72	0.718	$\pm$ 16 %	0.9	$\pm$ 3 %
15	0.17632	5.28	14.811	$\pm$ 15 %	0.5	$\pm$ 10 %
16	0.08344	2.48	2.92	$\pm$ 16 %	3	$\pm$ 11 %
18	0.01512	7.26	7.277	$\pm$ 6 %	4.9	$\pm$ 1 %
15	0.46669	13.84	15.867	$\pm$ 13 %	0.4	$\pm$ 4 %
16	0.00797	3.59	3.599	$\pm$ 10 %	0.7	$\pm$ 2 %
18	0.02549	10.46	10.487	$\pm$ 10 %	3.2	$\pm$ 1 %
Min	0.0023	0.72	0.718	-	0.1	-
Max	0.46669	13.84	15.867	-	4.9	-
Mean	0.09768$\pm$0.16	5.64$\pm$4.6	7.141$\pm$5.9	-	1.3$\pm$1.7	-

conditional stability constant are used in combination with equations (3.25), (3.26) and (3.27) to calculate the ligand-bound iron concentration, $[FeL]$, from which the other quantities can be diagnosed. We simplify the system so that the colloidal iron is represented by the ligand-bound pool ($FeL \approx Fe_{coll}$). The "free" iron is then assumed to be the difference between the total dissolved iron and the ligand-bound iron. These assumptions are a simplification, but are employed in order to estimate the importance of the partitioning of iron. The data available from the cruises precludes further detailed analysis into the specifics of the partitioning.

The partitioning of the iron pool further illustrates the importance of colloidal aggregation in order to reconcile the observations with other studies. The colloidal iron fluxes contribute largely to the overall adsorption of iron onto particles. The implied fluxes as a result of direct adsorption of free inorganic iron onto particle sources are 0.009$\pm$ 0.029 and 0.09$\pm$0.16 $pMFed^{-1}$. When the derived fluxes are compared with the Atlantic mean scavenging and coagulation rates (these processes crudely represent the direct adsorption and

colloidal aggregation processes, respectively) from the MITgcm (Table 3.8), the model fluxes are an order of magnitude greater than the observations. The colloidal fraction contributes significantly to the overall adsorption of iron and the net adsorption rate is certainly a net representation of all sorptive processes, including surface coordination, and coagulation and aggregation of organic colloidal material.

For D350 and D354 respectively, the fluxes of iron from a dissolved to particulate state are 0.007 and 0.009 $nMFed^{-1}$; similarly the fluxes of iron removed by particle transport are 0.026 and 0.0013 $nMFed^{-1}$. The effect of a 50% reduction in fallout rates between D350 (Table 3.2) and D354 (Table 3.3) is augmented by a reduction in observed particulate iron concentrations for D354, resulting in removal fluxes that reduce by greater than an order of magnitude from spring to summer. The large difference in iron fluxes between the two cruises suggests that the volcanic eruption is important in determining the magnitudes of scavenging and fallout rates, as well as total iron concentrations (Achterberg et al., 2013).

To provide context to the net fluxes of iron out of the dissolved pool, our estimates are compared with modelled iron source contributions and removal rates (Table 3.8). Each of the iron processes have been diagnosed from the MITgcm using a basin integral of each source and assuming instantaneous mixing throughout the upper 500m to approximate the potential basin mean flux of each source.

The mean adsorptive flux of iron for D350 is similar to the MITgcm scavenging rates, but 3 x larger than any of the estimated sources. The fallout flux for D350 is two orders of magnitude larger than any of the processes diagnosed from the model. This particular process has a possible large anomalous impact as a result of the volcanic eruption. A difference of such magnitude implies that there may be a process, such as atmospheric deposition from volcanism, that the model cannot resolve.

The integrated model values provide an annual average, spatially

Table 3.8: Table showing approximations of iron supply rates and fluxes from observations or diagnosed within the MITgcm (Italicized), see Chapter 4. The model utilises input fields from Mahowald et al. (2006); Aumont and Bopp (2006); Tagliabue et al. (2010).

Iron source	Basin Mean flux $pM\ Fe\ d^{-1}$
Atmospheric Dust Deposition	+0.08
Sedimentary Supply	+0.3
Hydrothermal Vent Emissions	+0.03
Basin Mean Scavenging	-0.40$\pm$0.75
Basin Maximum Scavenging	-54.7
Basin Mean Coagulation	-0.34$\pm$0.18
Basin Maximum Coagulation	-1.5
D350 Mean Iron Adsorptive flux	-1.0$\pm$0.89
D354 Mean Iron Adsorptive flux	-7.1$\pm$5.9
D350 Mean Iron Fallout flux	-26.9$\pm$63
D354 Mean Iron Fallout flux	-1.3$\pm$1.7

homogenised representation of the iron system within the MITgcm. These mean rates are mostly an order of magnitude smaller than any of the rates derived from the ^{234}Th and ^{238}U framework. The maximum scavenging rate diagnosed from the model is significantly greater than the observed adsorptive fluxes and the maximum coagulation rate is of a similar order to the D350 adsorptive flux.

The calculated adsorption and fallout rates are high relative to the basin-mean source and scavenging terms, but are smaller than the maximum rates of scavenging seen in the MITgcm. The consistency of the net adsorption rates with previous work supports using this framework to estimate trace metal scavenging rates. The application of the specific rates to iron produces adsorption and fallout rates that are of the same order as analogous processes within the MITgcm. The occurrence of the volcanic eruption complicates the situation as it is not clear whether the conditions during the D350 and D354 surveys were representative of the region.

3.3.3 Determining the drivers behind scavenging rate variability

Scavenging of trace metals onto particles and their removal from the mixed layer has been a key biogeochemical issue over the last two decades. Many studies have identified various drivers for this process. Honeyman et al. (1988) identified a strong relationship between particle concentration and the transfer of ^{234}Th from the dissolved phase to the particulate phase. Ye et al. (2011) identified atmospheric supply of lithogenic dust as driving removal of dissolved iron in a mesocosm experiment in the Mediterranean Sea. Biological activity in the surface waters, particularly new production, has also been identified as a driver of scavenging of trace metals. The creation of organic molecules through primary production and uptake provides particulate material for dissolved iron to interact with. The adsorption and subsequent fallout of particles drives the scavenging regime in these circumstances (Coale and Bruland, 1987).

Accompanied with the measurements of ^{234}Th and ^{238}U during the cruise a filtration of the sampled water also provided measurements of POC. Following Honeyman et al. (1988) a comparison between the forward adsorption rate and particle concentration is made. In this case POC is used instead of total particle concentration, effectively restricting this study to biogenic particle relationships. For all size classes of POC during D350, there was no significant relationship found between POC and adsorption rates (Figures 3.9a, 3.9b and 3.9c). Adsorption rates at 150m depth, from D354 were found to be significantly correlated with POC concentration, particularly POC within small particles (1 to 53μm). Variation in POC concentrations, explained 34% of the variability, implying an important link between primary production and other biological activity and adsorption rates of trace metals in the water column beneath.

The lack of a relationship between POC concentration and the adsorption and fallout rates during D350 raises further questions about the driving factors behind the variability and magnitudes of these processes.

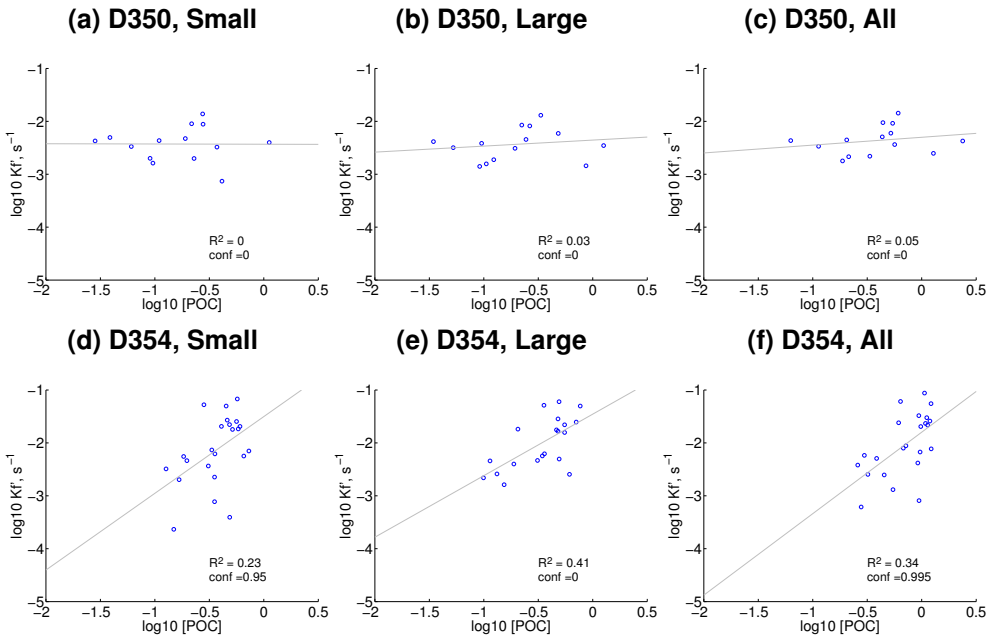

Figure 3.9: Relationship between $\log_{10}$ adsorption rate and $\log_{10}$ POC concentration for 'Small' (1-53 μm), 'Large' ($>$53 μm) and 'All' ($>$1 μm) particles

3.3.4 Is volcanic ash deposition a potential sink of iron?

The eruption of the Eyjafjalljokull volcano in Iceland in April and May 2010 provided an anomaly of particle and iron supply to the Subpolar North Atlantic; a potential driver of variability in particle scavenging rates for the region. During this period there were total emissions of 11.9$\pm$5.9 Tg of ash (Stohl et al., 2011) deposited into the North Atlantic. Using a priori source information in tandem with an atmospheric Lagrangian dispersion model and satellite data, Stohl et al. (2011) estimated volcanic ash deposition for the duration of the eruption, which lasted for approximately two months between 20 March and 23 May 2010. Deposition fields on 1st May and 8th May are shown in figure 3.11.

Achterberg et al. (2013) showed that this deposition of volcanic material caused a large perturbation to the biogeochemistry of the region, stimulating phytoplankton and increasing major nutrient drawdown when compared with historical records for this time of the year. There was only a minor increase in annually integrated observed satellite chlorophyll measurements suggesting that there was a large-scale response in biological activity during

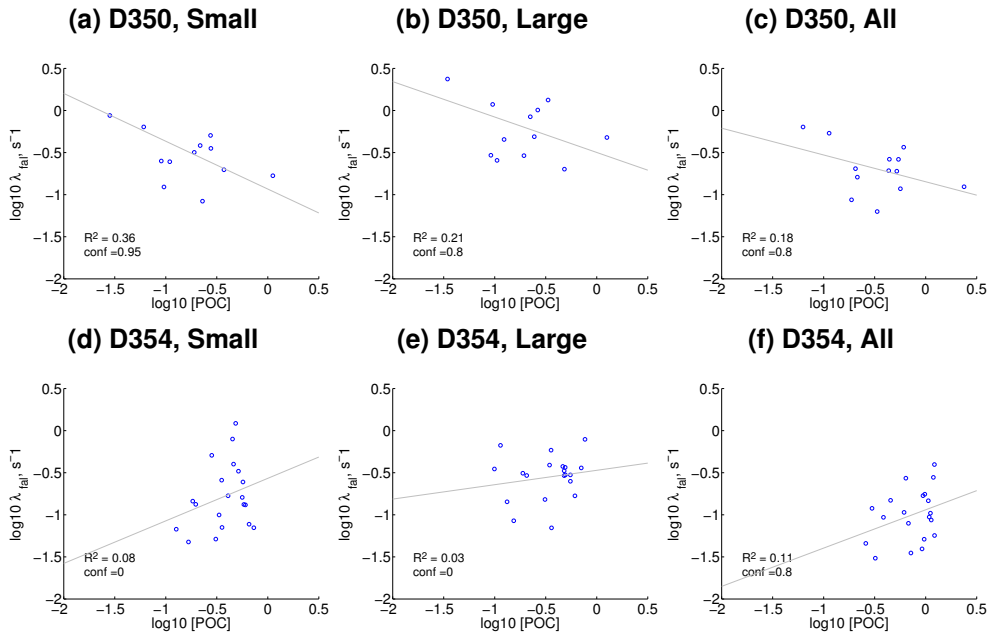

Figure 3.10: Relationship between $\log_{10}$ fallout rate and $\log_{10}$ POC concentration for 'Small' (1-53 μm), 'Large' ($>$53 μm) and 'All' ($>$1 μm) particles

the eruption, which consequently resulted in exhaustion of macronutrient stock and subsequent colimitation by nitrate and iron in the months following the ash deposition event. There are clearly complexities to this process of iron supply from volcanic ash, supported by the fact that Achterberg et al. (2013) failed to identify elevated DFe concentrations relative to previous years' measurements.

Complementary to this work a comparison between observed adsorption and fallout rates and the volcanic ash deposition was carried out. Characterising the ash is difficult due to the chemistry of the ash suggesting varying size classes, iron percentages and iron solubility (Gislason et al., 2011; Achterberg et al., 2013). Stohl et al. (2011) examined the size of the ash particles from airborne samples as well as collection at a station on the ground 60km from the volcano. For their inverse modelling study they produce a near-normal particle size distribution over a log range of 1 to 100 μm centred at 9 to 10μm. Achterberg et al. (2013), following Soulsby (1997), estimated the settling velocity of two particle size-classes from ship-board samples taken very close to the eruption directly underneath the plume: the first size class, $<$63μm, made up 1.5% of the total ash deposition and exhibited a settling velocity of 0.2 $mm\ s^{-1}$ or 17.3 $m\ d^{-1}$; while the larger particle size class, 63 to 123 μm,

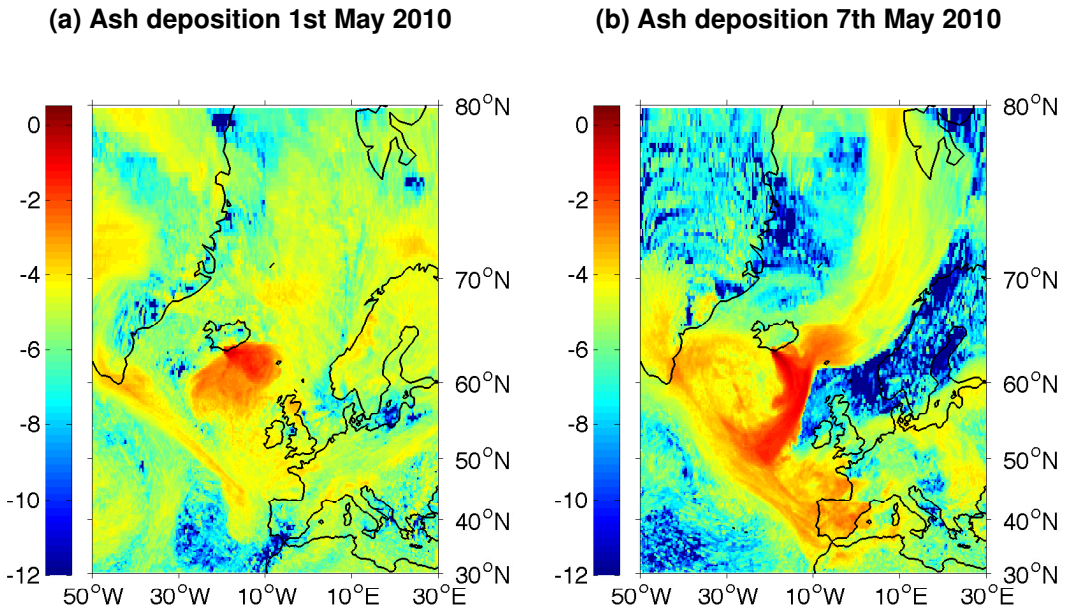

Figure 3.11: Maps showing the deposition of volcanic ash from the Eyjafjallajokull Eruption, units are $log(g\ m^{-2}\ d^{-1})$. Greenland can be seen in the top left of the maps and mainland Europe in the bottom right, (Stohl et al., 2011)

made up a larger fraction of the deposited ash and with a settling velocity of 400 $m\ d^{-1}$. The ash sample taken beneath the plume is not characteristic of the wider basin-scale deposition as the proximity to the volcano favours elevated quantities of larger particles. The distances the different size particles travel varied significantly; the finer particles are more likely to exhibit long term atmospheric residence times, enabling the circulation and deposition of ash throughout the Sub-polar North Atlantic region (Gislason et al., 2011).

Using the mass deposition fields of Stohl et al. (2011), it is possible to estimate arrival times for deposited ash at different depths. The most abundant particle sizes modelled range from 10-60μm, thus settling velocities lie approximately between 17 and 200 md^{-1}. If there is any impact by the volcanic ash particles on the adsorption and fallout rates, a signal at 150m depth would be seen with a lag of 1 to 9 days since the deposition of the material at the surface. Using this time-lag, significant relationships are found between adsorption rates at 150m depth and the deposition of volcanic ash 2 to 3 days prior to the Th/U observations (Figure 3.12). The R^2 values for both days suggest a large portion of the variability, $>$80%, can be explained by the deposition of volcanic

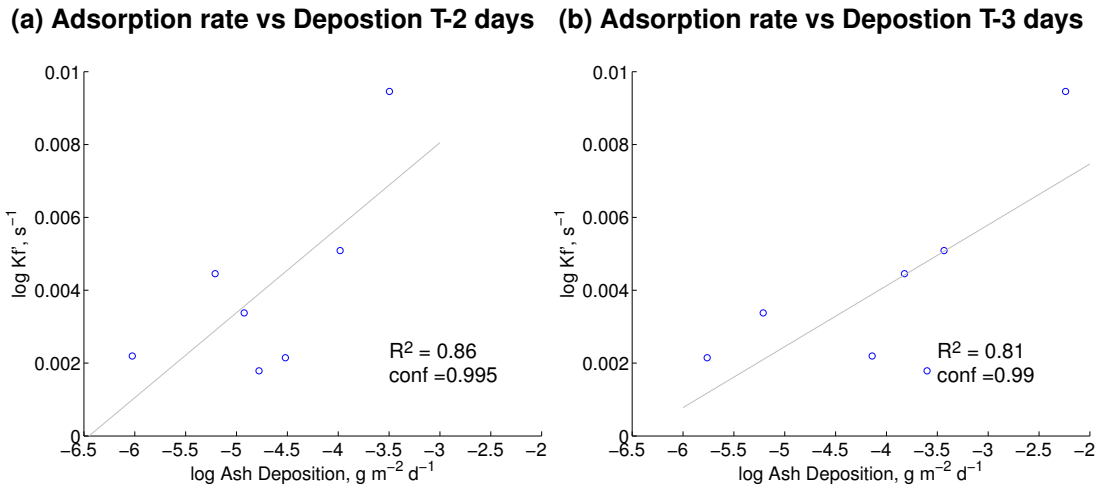

Figure 3.12: Scatter plots showing the relationship between volcanic ash deposition, $log(g\ m^{-2}\ d^{-1})$, and adsorption rates, d^{-1}, at 150m

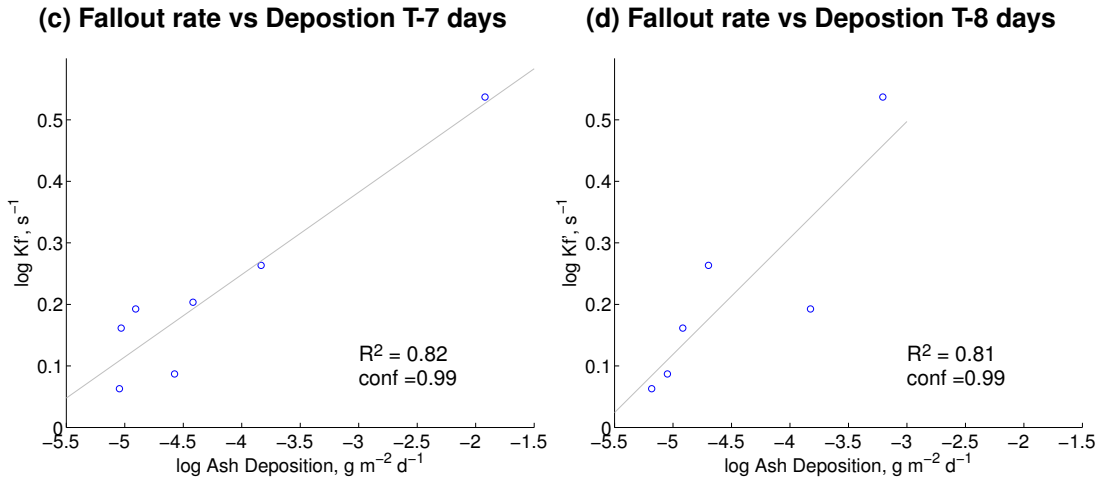

Figure 3.13: Scatter plots showing the relationship between volcanic ash deposition, $log(g\ m^{-2}\ d^{-1})$, and fallout rates, d^{-1}, at 150m

ash in the days prior to the adsorption rate observations. The particles that reached a depth of 150m in 3 or 4 days have a settling velocity of 37 to 50 md^{-1}, representing a moderate size class. These correlations are significant to greater than 99% confidence.

A further relationship between the particle removal rates and volcanic ash deposition 7 to 8 days prior to the observations is also identified, explaining $>$80% of the variability in the fallout rates (Figure 3.13). This study raises intriguing questions as to the impacts of the Eyjafjallajokull volcanic eruption, complementing evidence pointing towards a limited net impact on

phytoplankton abundance over the course of the year (Henson et al., 2013) and a negligible effect of the ash deposition on observed iron stock in the Sub-polar North Atlantic surface waters (Achterberg et al., 2013). The potential for the volcanic ash particles to deliver soluble iron to, and remove dissolved iron from, the water column may well have affected these observations and contributed to the exhaustion of nitrate in the Iceland Basin. These two conflicting processes could ultimately lead to no net iron supply to the ocean as a consequence of volcanic ash supply. Similarly, Ye et al. (2011) found opposing net effects of dust particle supply, which depended on the prior history of deposition and phytoplankton physiological state. Analogous processes and balances may well exist for the deposition of volcanic ash into surface waters.

3.3.5 Implications of volcanic ash control on particle scavenging

The impact of volcanic ash on the climate has been widely reported. The increase in aerosols as a result of volcanic eruptions results in a cooling of the climate due to diffraction of incoming solar radiation (Langmann, 2014). More recently there have been studies examining the potential fertilisation of ocean regions resulting from volcanic ash deposition (Frogner et al., 2001). The use of flow-through experiments on unhydrated volcanic ash has demonstrated leaching of iron and other nutrients into de-ionised water and ocean surface water samples, (Jones and Gislason, 2008). In addition to the study of Achterberg et al. (2013) in the sub polar North Atlantic, which used bioassay experiments to identify iron fertilisation, a study that took place in the North-East Pacific also identified the potential for nutrient release, including iron, from volcanic ash by establishing a causal link between volcanic ash dispersal data and satellite chlorophyll data (Langmann et al., 2010).

The evidence shown here supporting the influence of volcanic ash on the particle scavenging of trace metals demonstrates that there are further processes previously unreported that affect the net effect of ash deposition on the biogeochemistry. The evidence supporting natural iron fertilisation comes from experiments that took place either in the laboratory or in shipboard

vessels where flow-through leaching or bioassay experiments pointed towards the potential for iron to be released, and thus induce a biological response. These experiments take place in vitro and preclude processes that require larger temporal or spatial scales, such as particle scavenging, from having an impact on the system. Despite the experimentally determined iron fertilisation, Achterberg et al. (2013) noted that the observed dissolved iron concentrations during the natural iron fertilisation event resulting from the volcano did not differ from prior observations made in the region. The absence of the particle scavenging effect during shipboard bioassay experiments could be responsible for this paradox. Future natural iron fertilisation studies should take into account the potential for particle scavenging resulting from ash deposition before making inferences from in vitro experiments.

3.4 Summary and Conclusions

Diagnosis of scavenging rates from ^{234}Th and ^{238}U measurements is relatively straightforward, particularly in this era of GEOTRACES, where multi-disciplinary datasets are widely available. There is great potential if the ^{234}Th and ^{238}U measurements are augmented with associated iron partitioning measurements. Sampling of free inorganic, organically complexed and particle associated iron will help quantify the relative contributions of scavenging by the various species of iron.

Evidence for a significant contribution to scavenging by lithogenic ash supply implies that measurement of a range of particle types are needed when ^{234}Th and ^{238}U measurements are made in order to elucidate the driving factors behind any observed relationships.

Consistent inter-basin variation between the Irminger and Iceland basins of the North Atlantic suggest that there is a clear difference in biogeochemistry between the two regions. However, the consistency in the relative variation of the two basins over time imply that the underlying drivers behind scavenging rate variability are broadly similar.

Scavenging rates calculated in the North Atlantic are highly variable and exceed diagnosed iron source rates. These scavenging rates are of the same order as modelled scavenging and coagulation rates from the MITgcm. The model suggests significant variability within the scavenging rate fields equivalent to that seen in the observational data. The rates are broadly consistent with a range of other studies.

The equilibrium relationship between ^{234}Th and ^{238}U is used for calculation of scavenging rates. The errors associated with equilibrium were tested and found to be less than 60% for the diagnosed adsorption rates and less than 20% for the diagnosed particle fallout rates.

There is evidence that deposition of volcanic ash had a controlling effect on the magnitudes of iron supplied to the subpolar gyre of the North Atlantic. There is also evidence of biological growth resulting from the fertilisation of the basin by iron (Achterberg et al., 2013; Henson et al., 2012). The evidence from this study suggests that the paradox between demonstrated iron fertilisation effects and no discernible increase in observed oceanic iron concentrations presented by Achterberg et al. (2013) can be explained by the effect of particle scavenging, which requires larger temporal and spatial scales than those provided by shipboard bioassay experiments. The response to volcanic ash deposition is complex with volcanic ash deposition acting as a source and sink of trace metals through dissolution of metal salts and particle scavenging respectively.

Chapter 4

Developing the MITgcm Iron Closures

4.1 Motivation for modelling work

In chapters 2 and 3 the importance of iron supply and scavenging within the global ocean has been emphasised. A range of iron regimes, dependent on the balance of iron sources around the globe and the rates of particle scavenging of iron, have been inferred from observational data, both globally and regionally. The seasonal variability and magnitude of particle scavenging has also been explored. The potential for particle scavenging to significantly alter local dissolved iron balances has been suggested. The key question arising from these data-driven conclusions is: how do iron source regimes and particle scavenging affect the global distribution and transport of iron? Short of a long-term global high-resolution survey of hydrography and nutrients it is very difficult to address this question with existing observational data. An Ocean General Circulation Model can be used to understand how the observational distributions are controlled. There are a range of OGCMs and model closures to represent the physics and biogeochemistry. The specific purpose of this chapter is to determine the best tool, i.e. OGCM, to be used to understand the iron distribution.

4.2 Iron in General Circulation Models

Iron has been present in many OGCMs since its identification as a key limiting nutrient throughout the oceans (Martin and Fitzwater, 1988; Martin, 1990; Coale et al., 1996). Its presence is vital in order to reconcile observed distributions of nutrient regimes, e.g. Low Nutrient Low Chlorophyll (LNLC) regions found in the subtropical gyres and High Nutrient Low Chlorophyll (HNLC) regions such as the North and Equatorial Pacific and Southern Ocean. Early attempts to model the observed iron distributions in the Pacific Ocean (Johnson et al., 1997), used a station by station method of predicting dissolved iron profiles. This early model used a highly idealised view of the iron system, assuming that the only source of iron within the water column is remineralisation of iron from particles. The model used the observed carbon export fluxes as a source of particulate organic matter. This remineralised iron was exposed to particle scavenging, but only when concentrations exceeded a particular apparent solubility of iron. This apparent solubility of iron is a simplistic representation of the complexation of iron with organic ligands. This implicit use of ligands produced reasonable results, allowing adequate prediction of dissolved iron profiles at each station as a function of the production of particulate organic matter. With sparse data coverage, modelling then represented an approach to improve our knowledge of the iron cycle.

Lefèvre and Watson (1999) followed on from the work of Johnson et al. (1997) and developed a box-model for the global ocean. They supported the introduction of iron-binding ligands into models (Johnson et al., 1997) as a key process to balance the aeolian source of iron at the surface and the remineralisation and scavenging of iron within the water column. Assuming a constant ligand concentration across the globe of 0.6 nM they tested different rates of scavenging, which applied to the dissolved iron in excess of the ligand concentration. Based on the existing data coverage, Johnson et al. (1997) suggested that there was no inter-ocean fractionation of deep iron concentrations. However, Lefèvre and Watson (1999) suggested that

a consistent dissolved iron concentration could not be achieved throughout the global ocean with the parameter regime Johnson et al. (1997) had utilised.Archer and Johnson (2000) developed their suite of models, integrating an iron seawater chemistry regime into a global biogeochemical model. The basis of their model is that concentration of iron-binding organic ligands controls the distribution of subsurface dissolved iron. The results from their model study suggested that the global biological production is strongly linked with the iron cycle,on timescales of several hundred years for the global iron concentration to several thousand for the timescale of ligand distribution. They predicted that 70-80% of global export production is sustained by the upwelling of iron from the deep waters, and not as reliant upon the atmospheric deposition as Lefèvre and Watson (1999) had suggested. The models of Archer and Johnson (2000) began to resolve the High Nutrient Low Chlorophyll regions more accurately within GCMs, utilising iron as a limiting nutrient in these parts of the ocean to better represent the basin-scale macronutrient distribution.

The increasing complexity of the iron closures continued with the inclusion of an equilibrium balance between the dissolved iron and dissolved ligand species into, first, a box-model by Parekh et al. (2004) and then subsequent GCM work by Parekh et al. (2005) and Dutkiewicz et al. (2005). These equilibrium balances were applied to reproduce the more recent measurements of dissolved iron across the globe, capturing the inter-ocean fractionation evident in the observations. The key outcomes showed that without the organic complexation of iron by ligands, the deep water concentrations become heavily controlled by particle scavenging and atmospheric supply. The damping of the variability in atmospheric supply and scavenging by the complexation by organic ligands provides the relatively stable deep-ocean iron concentrations that are evident in the measurements.

With the increasing amount of observations of iron came increased insights into the variations of the iron cycle in different regions. The Sub-polar North Atlantic, for example, has also been identified as an area in which

phytoplankton are experiencing physiological stress as a consequence of iron limitation (Nielsdóttir et al., 2009). These more recently identified regions of iron limitation are not resolved as successfully as the traditional HNLC regimes; evidence of this is discussed later (section 4.6.1).

More recently much of the modelling using iron cycling closures has been carried out on one of the major GCM platforms. Perhaps the two most influential platforms are the MITgcm and NEMO. The work done by Parekh et al. (2005) and Dutkiewicz et al. (2005) was done using the MITgcm. A further development of the MITgcm with respect to iron was done by Lauderdale (2010), who improved the representation of particles within the model and coupled the scavenging process to these particles. The MITgcm is ideal for carrying out experiments with respect to global transport and palaeo-timescale experiments, such as glacial-interglacial differences in biogeochemical cycles. There are a number of different packages available to augment the basic physical-biogeochemical models. Ecosystem interactions have been extensively investigated using the MITgcm, including original stochastic generation of multiple-species phytoplankton communities (Dutkiewicz et al., 2009). The MITgcm is a broad and flexible tool that has a large range of applications and is widely used for carrying out ocean modelling experiments. It has 6 tracers; alkalinity, dissolved inorganic carbon, dissolved organic phosphorous, iron, oxygen and phosphate, with iron and phosphate limiting biological community production. There is no explicit biology in this model, it uses an integrated biological community growth rate. Implicit in this coefficient is all the primary production by bacteria and phytoplankton, mortality of these primary producers and also grazing, excretion and mortality of zooplankton.

NEMO is an alternative platform used for similar experiments to the MITgcm (Madec, 2008) and (Foujols et al., 2000). Aumont and Bopp (2006) used NEMO combined with a complex biogeochemical package, PISCES, to investigate the efficacy of iron fertilisation experiments to drawdown atmospheric CO_2. This biogeochemical package had 24 tracers with 5

explicitly limiting nutrients; nitrate, ammonia, phosphate, silicate and iron. In addition to this there were two phytoplankton groups and two zooplankton groups. Interactions between the living groups and the explicit tracer regime for C, N and P were assumed to be the same as proposed by Takahashi et al. (1985), but the utilisation, excretion and regeneration of Fe and Si varied as a function of external nutrient concentrations and light levels. This model has a much greater complexity when comparing to the MITgcm model in use by Lauderdale (2010). The difference in complexity is reflected in the difference in the computing efficiency of the two models. The complexity of the NEMO-PISCES regime precludes it from being used to carry out large numbers of long-term simulations at high resolution in order to investigate basin-scale transport and the impact of different processes on the overturning and residence times of iron within the ocean. NEMO-PISCES has been used widely for numerous iron-related studies suggesting that the iron scheme is a successful one (Aumont and Bopp, 2006; Aumont et al., 2008; Tagliabue et al., 2009; Resplandy et al., 2009; Masotti et al., 2011; Tagliabue et al., 2012).

4.3 The MITgcm

Chapter 2 emphasised the importance of local iron supply as well as the uncertainties related to the subsurface physical transport of iron throughout the ocean. Further, in chapter 3 the magnitude, distribution and variability of particle scavenging processes was discussed. The spatial variation of this process can impact the interior ocean dynamics of the iron cycle. In order to explore the importance of transport within the iron cycle, and the impact of subsurface removal processes, it is highly desirable that long-term model simulations are run. Due to our limited knowledge on the driving factors behind transport of iron, as well as the complexity of the iron system, it is likely that a large number of simulations will be required to fully explore the impact of iron cycle processes on the transport, and subsequent downstream impacts, of iron. For these reasons the MITgcm is the most suitable tool to use to explore

the aims of this thesis.

4.3.1 Iron in the MITgcm

The focus of this thesis is to improve scientific understanding of the oceanic iron cycle. Here a detailed description of the representation of iron chemistry within the MITgcm is provided and a discussion of the processes explicitly omitted from this closure is given. The original model setup from Lauderdale (2010), a development of the work of Dutkiewicz et al. (2005), is a relatively simplistic representation of the processes that dissolved iron undergoes in the global ocean. The traditional balance of a tracer in an OGCM incorporates three key components: sources, processes and sinks. Within the MITgcm there is only one source of iron to the ocean, the atmospheric deposition of dust to the surface ocean, and one ultimate sink, particle scavenging. A portion of the iron cycle is coupled to the cycling of generic macronutrients as well as the inclusion of processes that affect iron solely. In the chosen configuration of the MITgcm phosphate is the sole macronutrient carried. Below are the equations showing the processes that impact on inorganic phosphate, $\frac{\partial PO_4}{\partial t}$ (4.1) and total dissolved iron, $\frac{\partial Fe}{\partial t}$ (4.3), as well as explicitly showing the POP flux, F_P, closure (4.4). The main focus of this section is on the factors affecting the evolution and speciation of iron in the water column. However, the partial coupling of iron to phosphate implies a relationship between the two nutrients, scaled by an assumed ratio, $R_{Fe:P} = 4.68 \times 10^{-4}\ mol\ mol^{-1}$, seen in the first term on the right-handside of equation 4.3, $R_{Fe:P}\frac{\partial PO_4}{\partial t}$.

$$\frac{\partial PO_4}{\partial t} + \underline{\mathbf{u}}.\nabla PO_4 = -\gamma\Gamma - \frac{\partial F_P}{\partial z} + \lambda_{remin}[DOP] \tag{4.1}$$

$$\frac{\partial DOP}{\partial t} + \underline{\mathbf{u}}.\nabla DOP = \gamma\Gamma - \lambda_{remin}[DOP] \tag{4.2}$$

$$\frac{\partial Fe}{\partial t} + \underline{\mathbf{u}}.\nabla Fe = R_{Fe:P}\frac{\partial PO_4}{\partial t} - \lambda Fe' + \alpha_{Fe}F_{dust} \tag{4.3}$$

$$F_P = (1-\gamma)\Gamma\Delta z\left(\frac{z}{z_c}\right)^{-\alpha_{remin}} \tag{4.4}$$

Table 4.1: MITgcm Parameter table

Symbol	Description	Units
γ	Fraction of production assigned to DOP	
Γ	Biological community consumption	$mM\ s^{-1}$
F_P	POP Flux	$mM\ m^{-2}\ s^{-1}$
λ_{remin}	DOP Remineralisation rate	s^{-1}
$\delta\ z$	Thickness of Γ-originating layer	m
z	Depth of destination layer	m
z_c	Depth of base of Γ-originating layer	m
α_{remin}	POP remineralisation power law coefficient	-
$R_{Fe:P}$	Ratio of iron to phosphate	$mM\ mM^{-1}$
λ	Iron Scavenging rate	s^{-1}
α_{Fe}	Solubility of atmospheric iron supply	%

The factors affecting phosphate, shown on the right-handside of equation 4.1, are, from left to right: Biological consumption (Γ), the particulate organic phosphate (POP) fallout flux ($\frac{\partial F_P}{\partial z}$), (more explicitly described in equation 4.4) and the remineralisation of dissolved organic phosphorous ($\lambda_{remin}[DOP]$).

In addition to the phosphate coupling of the iron system mentioned above, the initial closure describes two further key components that alter the dissolved iron concentrations (4.3). Scavenging of "free" iron, ($\lambda[Fe']$), and the supply of aeolian dust from the atmosphere, ($\alpha_{Fe}F_{dust}$) also modify iron concentrations. The atmospheric supply has 3.5% of total weight of deposited dust being iron and also has a solubility factor representing the percentage of incoming iron that dissolves ($\alpha_{Fe} = 1\%$). The processes affecting iron in (4.3) alter total dissolved iron concentrations ($[Fe_T]$), except for scavenging, which removes "free" iron $[Fe']$ in particular. This $[Fe']$ also undergoes a precipitation process if its concentration exceeds a fixed limit (Fe_{max} = 0.3nM), representing the effect of iron solubility in seawater. The inclusion of Fe_{max} limits the maximum dissolved iron concentration to $[L_T] + [Fe_{max}]$.

The speciation of iron is derived using a series of balances (Equations 4.5 and 4.6) and an equilibrium relationship (4.7). $[Fe_T]$ is conservative with respect to transport and Total ligand concentration is an imposed quantity, $[L_T] = 1nM$. The conditional stability constant ($K^{cond}_{FeL} = 10^8\ mol\ mol^{-1}$) determines how strongly the ligands interact with dissolved iron, and hence, the fraction of iron available for scavenging.

$$[Fe_T] = [Fe'] + [FeL] \tag{4.5}$$

$$[L_T] = [L'] + [FeL] \tag{4.6}$$

$$K^{cond}_{FeL} = \frac{[FeL]}{[Fe'][L']} \tag{4.7}$$

Within the model these equations are solved so that $[FeL]$ is calculated. Firstly, substitute rearranged versions of (4.5) and (4.6) into (4.7),

$$K_{FeL} = \frac{[FeL]}{([Fe_T] - [FeL])([L_T] - [FeL])}, \tag{4.8}$$

take the reciprocal,

$$\frac{1}{K_{FeL}} = \frac{([Fe_T] - [FeL])([L_T] - [FeL])}{[FeL]}, \tag{4.9}$$

then multiply through by $[FeL]$ and multiply out the brackets,

$$\frac{1}{K_{FeL}}[FeL] = [FeT][L_T] - [Fe_T][FeL] - [L_T][FeL] + [FeL]^2, \tag{4.10}$$

subtract $\frac{1}{K_{FeL}}[FeL]$ from both sides and partially factorise to give a quadratic expression of the form $ax^2 + bx + c$,

$$[FeL]^2 - ([Fe_T] + [L_T] + \frac{1}{K_{FeL}})[FeL] + [FeT][L_T] = 0. \tag{4.11}$$

A solution for x can be derived from the quadratic equation,

$$x = \frac{-b \pm \sqrt{b^2 - 4ac}}{2a}, \tag{4.12}$$

thus for our quadratic,

$$[FeL] = \frac{-([Fe_T] + [L_T] + \frac{1}{K_{FeL}}) \pm \sqrt{([Fe_T] + [L_T] + \frac{1}{K_{FeL}})^2 - 4[FeT][L_T]}}{2}. \tag{4.13}$$

This formula provides two solutions as a result of the $\pm$, resulting from the positive and negative solutions from the square root. One can quickly establish which solution is correct, the other is usually unreasonable.

4.3.2 Limitations

4.3.2.1 Sub-polar North Atlantic

When applying the default setup of the MITgcm and analysing the model output, initially relative to data obtained on the Summer 2010 Discovery cruise D354, there were clear problems with the predicted iron distributions in the subpolar North Atlantic. When comparisons are made between the data and the model output the concentrations of dissolved iron are significantly overestimated by the MITgcm, particularly in the surface waters of the subpolar North Atlantic. A zonal section across 60°N allows comparison between the model and the data. With observational data plotted over the top of the model distributions it is clear that the model dramatically overestimates iron concentration across the entire section (Figure 4.1).

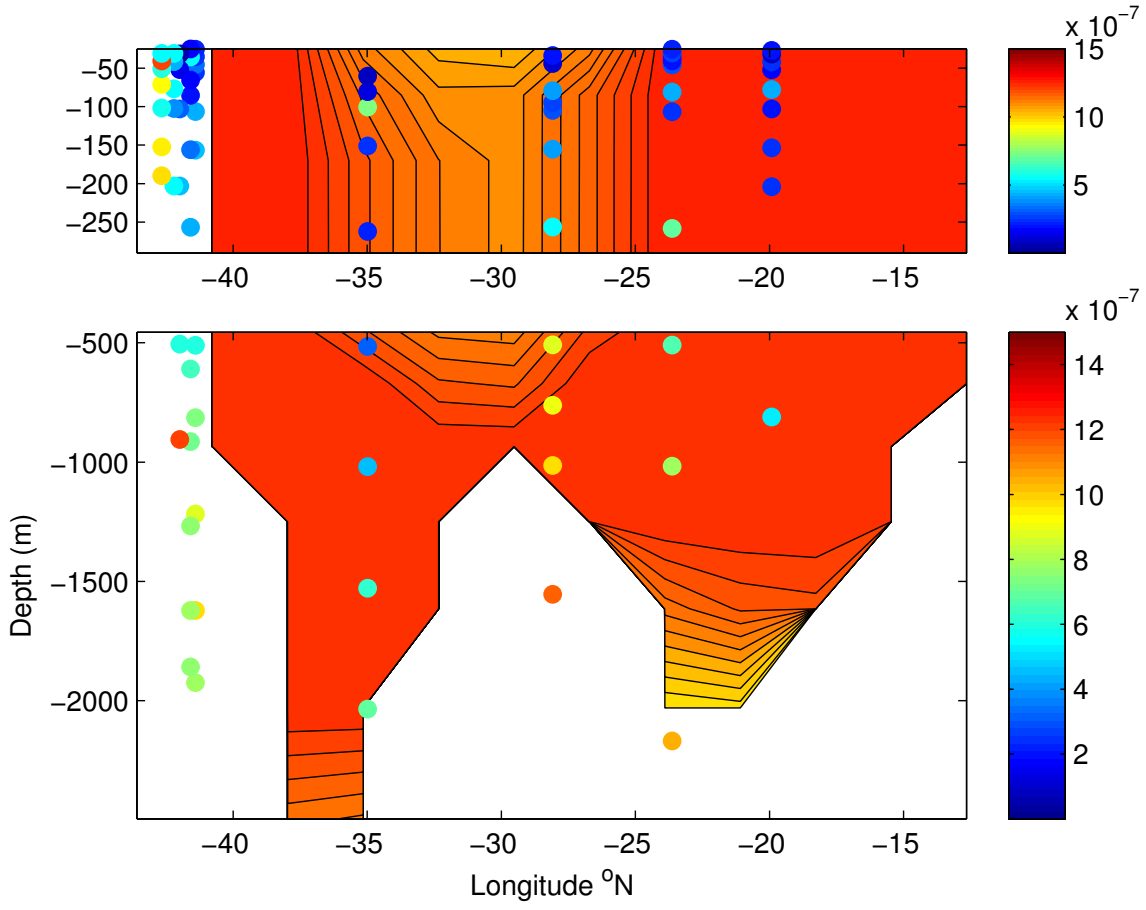

Figure 4.1: Subpolar North Atlantic data scattered onto MITgcm 60°N July average dissolved iron distributions, $mol\ m^{-3}$

The general distribution for the data shows low values in the open ocean surface waters (0.1-0.4nM), increasing (0.6-1nM) towards the greenland shelf (-42°E). There are elevated concentrations at depths between 1000 and 2500m (0.7-1.1nM), with an inversion (0.6-0.3nM) in the deepest part of the central Irminger basin (-35°E). The MITgcm control run predicts concentrations of between 1.1 and 1.3nM throughout the whole upper 1500m of the section with values of 0.9nM at 2000m in the East (-30 to -20°E) of the section. The high concentrations across much of the sub polar gyre represent a pseudo-maximum concentration of total dissolved iron, $[Fe_T] \approx [L_T] + Fe_{max}$. Without this limiting factor the concentrations of iron in the sub polar region would reach concentrations too high to be plausible. This limiting factor represents dissolved iron being saturated in the water column causing precipitation followed by fallout. This saturation of the potential iron inventory suggests that the iron 'turnover' by the model's biogeochemical processes in the subpolar North Atlantic is inadequate, resulting in very little local incorporation of atmospheric iron, and unrealistically high concentrations of dissolved iron persisting throughout the year. An experimental study by Nielsdóttir et al. (2009) showed that the phytoplankton community is nutrient limited post-summer despite the system being replete in macro-nutrients. The iron concentrations were found to be low enough to inhibit the growth in the Iceland Basin, with a similar situation hypothesised for the Irminger Basin.

This condition is not reflected in the model's current iron regime. In addition to the iron distributions it is also important to consider the model's ability to reproduce observed macronutrient concentrations, in this case phosphate (Figure 4.2), observations show that there are depleted surface concentrations with a clear dipole between the two basins, 1.1 μM in the Irminger Basin and 0.7-0.9 μM in the Iceland Basin, at depths between 100 and 500m. Waters below this depth level are more homogenous with concentrations of 1.1-1.2 μM across the whole section. The model predicts a uniform concentration of 0.85 μM across the whole section, with the exception of a slight decrease at the surface (0.8 μM).

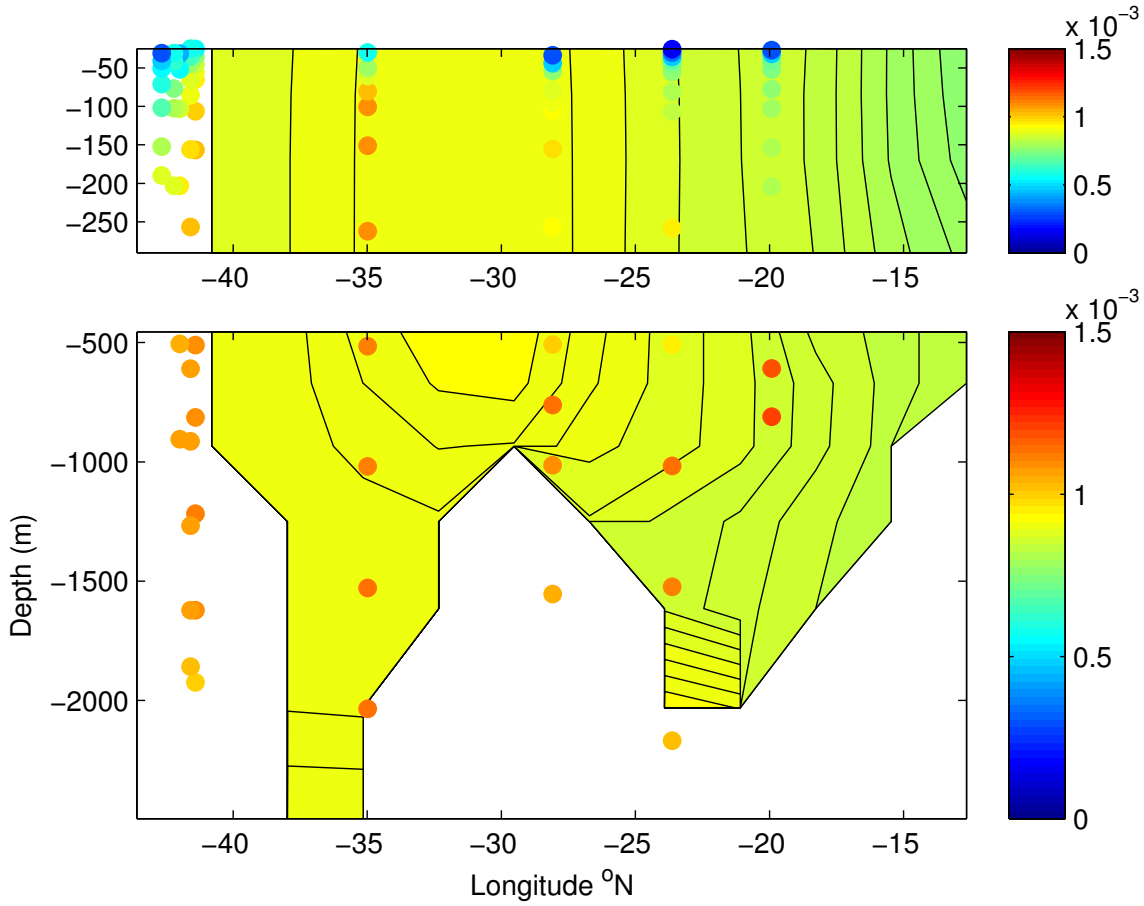

Figure 4.2: Subpolar North Atlantic phosphate data scattered onto MITgcm 60°N July average phosphate distributions, $mol\ m^{-3}$

4.3.2.2 Atlantic basin

Plots of the original MITgcm iron closure's surface distribution of iron indicate the significant flaws in the model's simulation of observed iron concentrations (Tagliabue et al., 2012) (Figure 4.3). It is apparent that the iron concentrations across the majority of the North Atlantic are at the saturated level prescribed by the model, i.e. $Fe_T = [L_T] + Fe_{max} \approx 1.3\ nM$. With the exception of the small patch in the sub polar gyre that exhibits concentrations slightly lower (1.1 nM) due to the region of deep winter convection that mixes the iron-rich surface waters with deep waters of lower concentration. The mismatch between this iron saturated region and the observational data is profound. With the exception of isolated measurements of greater than 1.4 nM on the Bay of Biscay continental shelf and values of 0.8 nM in parts of the subtropical gyre, the observational dataset indicates that iron concentrations rarely exceed 0.3

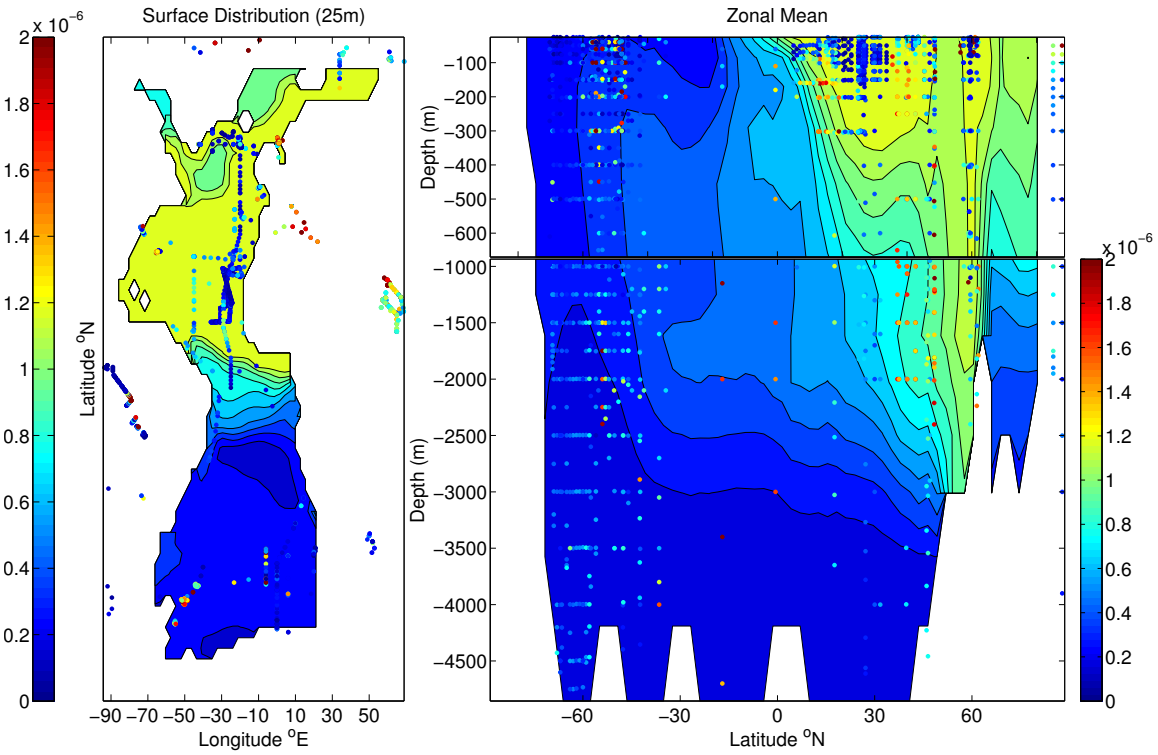

Figure 4.3: MITgcm surface Atlantic dissolved iron ($left$) and MITgcm Atlantic basin zonal mean dissolved iron ($right$), with observational iron concentrations (Tagliabue et al., 2012) scattered over the modelled iron distributions.

nM north of 10 °N. The low iron measurements found in the South Atlantic are captured within the model but the regions of high benthic sources, such as the South Georgia Islands and the Southeast african continent, are not well represented at all due to the lack of subsurface iron sources.

The Atlantic zonal mean iron concentration highlights the flawed mechanism by which the model is able to mix and transport iron from the high latitude North Atlantic into the ocean interior and further on to the Southern Ocean. The model ultimately demonstrates a saturated state with respect to iron, both organically complexed and inorganic. Without this large saturation of iron, and low scavenging rates, there would be very little, if any, iron supplied to the Southern Ocean via the NADW. In fact, even with this mechanism for supplying the Southern hemisphere the model struggles to match the iron concentrations at the depths of NADW in the Tropical Atlantic (Figure 4.4a). The data in this 1000 to 2500m depth range shows concentrations of 0.7 to

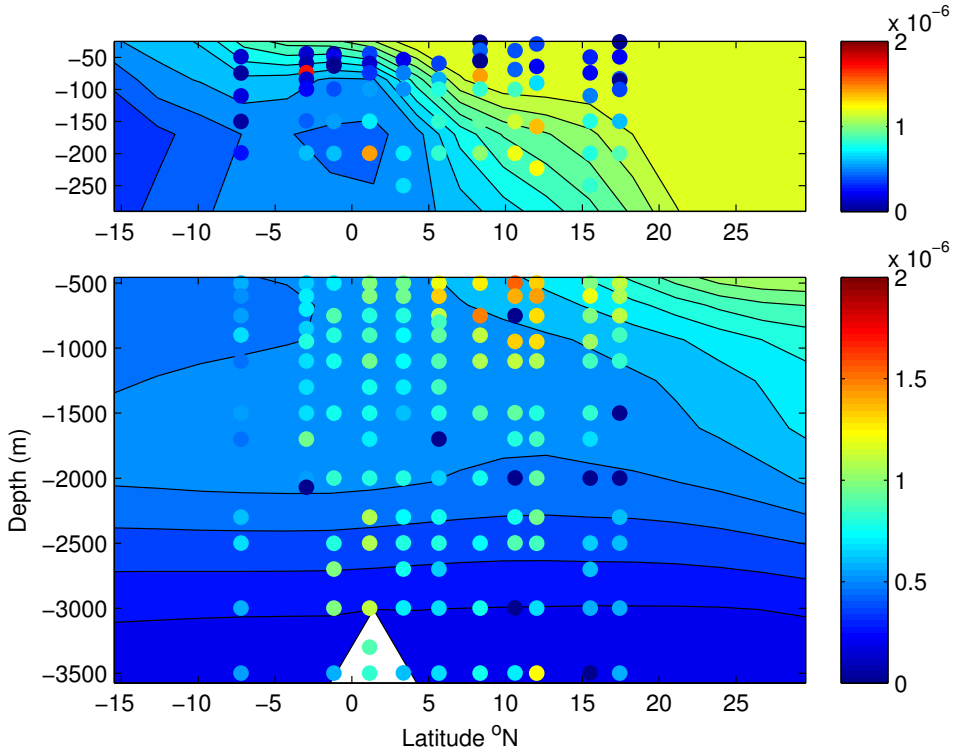

(a) Observational iron concentrations scattered over MITgcm old closure 28°W March Average dissolved iron distributions, $mol\ m^{-3}$

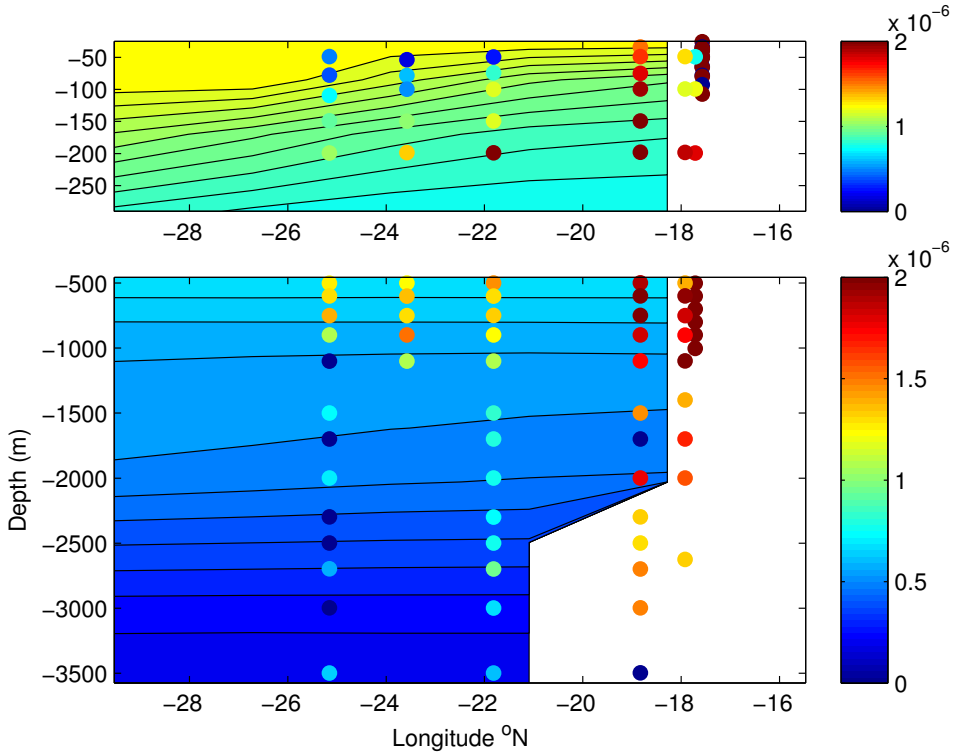

(b) Observational iron concentrations scattered over MITgcm old closure 11°N March Average dissolved iron distributions, $mol\ m^{-3}$

Figure 4.4: Figure showing Tropical Atlantic iron data comparison

1.2 nM of dissolved iron, whereas the iron concentrations from the model are approximately 0.4 to 0.5 nM. The model also fails to resolve the horizontal gradient in the iron distributions in the Tropical regions, underestimating (0.4 nM) the concentrations of iron found between 250 and 1000m (1 to 1.5 nM) at 11 °N (Figure 4.4b).

The phosphate distribution within the model qualitatively matches the observed phosphate distribution reasonably well in the Tropical Atlantic. The subsurface maxima between 250m and 2000m depth is captured within the model, Figure 4.5. The depletion of phosphate at the surface is also replicated well. The model predicts a layer between 2000m an 3000m that is slightly depleted relative to the water beneath it, which is not seen in the observations. In general, the model under-predicts the concentrations of phosphate throughout the domain, but captures well the characteristics of the regime in the region.

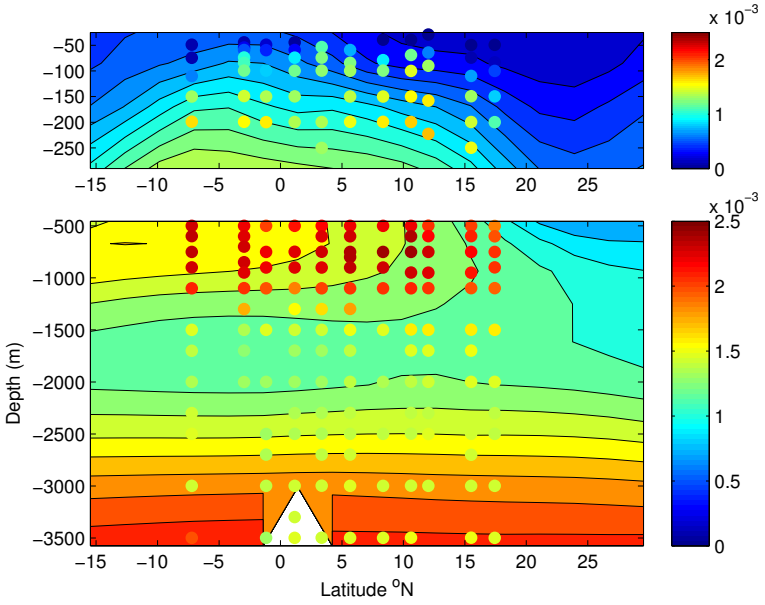

Figure 4.5: Figure showing Tropical Atlantic phosphate data comparison, $mol\ m^{-3}$. The contoured section is model output; data values are scattered onto the model field.

4.3.2.3 Nutrient limitation distribution

As well as aiming to represent the dissolved iron distributions as effectively as possible it is also key to maintain realistic biological growth patterns, and thus a suitable macronutrient and micronutrient limitation balance. A global distribution of nutrient limitation was compiled by Moore et al. (2013)

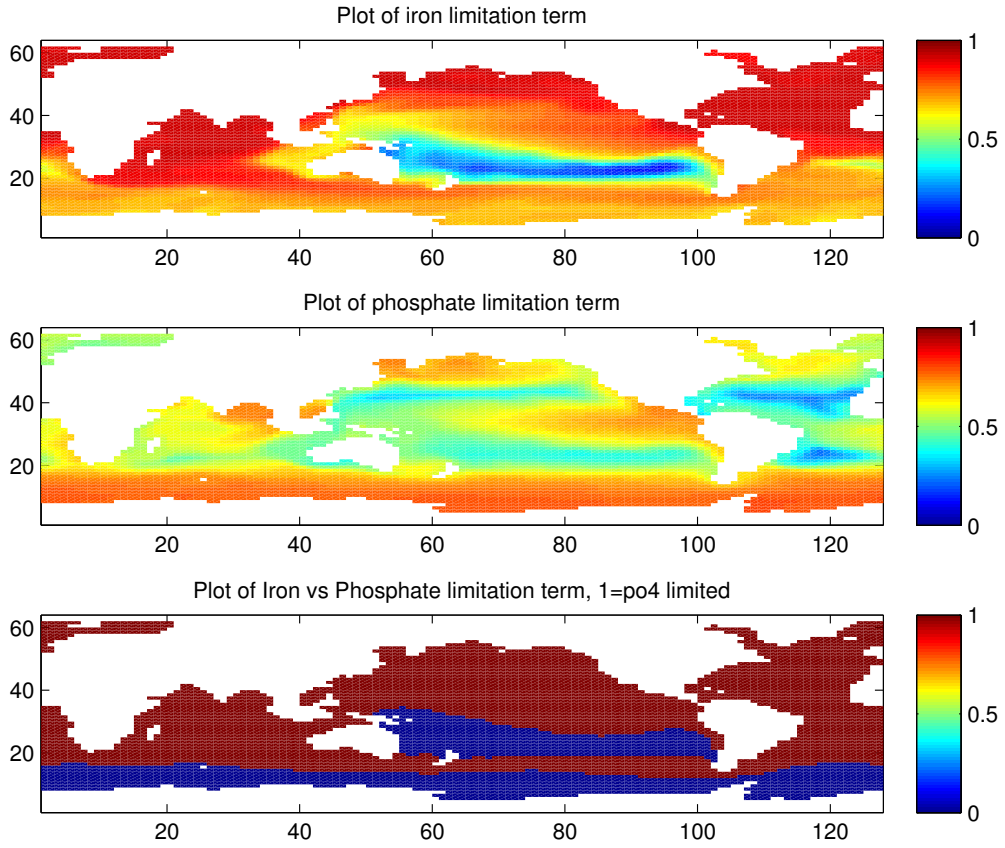

(a) Plots showing the annual mean limitation terms found with the MITgcm old closure, bottom panel indicates whether iron (0) or phosphate (1) is the limiting nutrient.

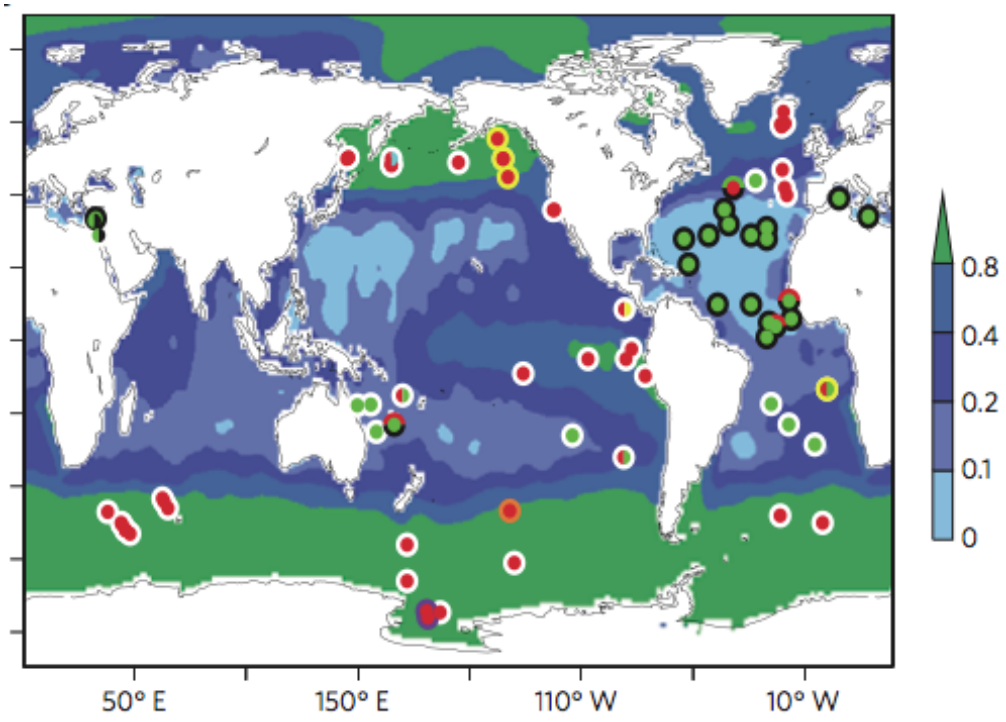

(b) Plot from Moore et al. (2013) showing global distribution of nutrient limitation. Background is global phosphate distribution in $\mu molkg^{-1}$ and circles indicate primary (centre) and secondary (outer) limitation: N (green), P (black), Fe (red), Si (orange), Co (yellow), Zn (cyan), vitamin B12 (purple) and no secondary limitation (White).

Figure 4.6: Nutrient limitation characteristics

and enables a comparison between the observed nutrient limitation and the pattern which emerges from the MITgcm iron closure. The MITgcm limitation is dominated by macronutrient limitation (Figure 4.6a). The majority of the Southern Ocean and the South Pacific Subtropical gyre are the only regions where iron is limiting. Compared with the findings of Moore et al. (2013) there are some key regions within the model that are in the wrong nutrient limitation regime. The North Pacific, Tropical East Pacific and high-latitude North Atlantic are all regions limited by iron (Figure 4.6b). However, the MITgcm fails to capture these regimes due to its dependence on atmospheric supply of iron and the subsequent transport of this source. Consequently, the regions mentioned above are replete in iron in the model because iron is maintained in surface waters for relatively long timescales, allowing a sustained supply of iron to regions that in observations demonstrate frequent iron-limitation.

4.3.3 Attempts to reconcile the model $[Fe_T]$ with data values

A range of tuning procedures were carried out to try and get the model output closer to the data. The key parameters altered in this initial tuning were biological growth rate (γ), the scavenging coefficient (λ) and the conditional stability constant (K^{cond}_{FeL}). These tunings were then compared to a 'control run', this was the original model setup, which was run alongside these initial model regime alterations. Increasing γ threefold had very little effect on the $[Fe_T]$ with only some minor migration of $[Fe_T]$ contours. The phosphate distribution pattern remains very similar to the control run, however the concentrations are lower, in the range of 0.55 to 0.65 μM. The surface minimum is more pronounced than the control, in line with the observed distribution, but the concentrations across the rest of the section are unrealistic. Increasing the scavenging coefficient to achieve the desired iron concentrations in the high latitude North Atlantic resulted in almost complete removal of iron everywhere else in the model, with the exception of the areas directly below the strong dust deposition plumes. Altering K^{cond}_{FeL} also had only limited benefits, adversely affecting the distribution elsewhere in the model in order to achieve good

correlations in the subpolar North Atlantic. With the MITgcm set up as it is there is no way of reconciling the observations from the subpolar North Atlantic while avoiding detrimental effects occurring to the iron concentrations elsewhere. The inherent problem with the MITgcm is the limited source of iron. A source restricted to the surface layer means that iron deposited here needs to survive any subsequent transport to the deep waters in order for the model to be able to resolve observed data from the deep ocean. In order for this to be achieved the scavenging rates need to be low to avoid large amounts of iron being stripped from the system. The absence of remineralisation of scavenged iron from particles amplifies the importance of a low scavenging rate. A consequence of the low scavenging rate is that some regions will become extremely saturated with iron. The subpolar North Atlantic is one of these regions, and in order to keep iron concentrations reasonable a free iron maximum is necessary, effectively scrubbing any iron that creeps above a predetermined concentration. The iron closure is effectively hamstrung by its lack of subsurface sources; many of the potential parameter choices are limited depending on the iron distribution priorities at the outset.

4.4 Comparisons with NEMO-PISCES

4.4.1 Introduction

Following attempts to tune the MITgcm, it became apparent that the initial model setup and closures are too restrictive. The model is able to simulate global ocean nutrient distributions, but is unable to reconcile sub-basin distributions, particularly in this instance the subpolar North Atlantic. The initial alterations fail to reduce the surface concentrations in the subpolar North Atlantic. The MITgcm cannot resolve intra-basin variability with its simplistic biogeochemical closures for iron, thus the iron closure is a primary target for improvement. Comparing the MITgcm's performance against other Ocean General Circulation Models should elucidate the key differences in iron

closures. One such OGCM is the PISCES biogeochemical scheme applied alongside the OPA physical model within NEMO (Aumont and Bopp, 2006). The NEMO-PISCES model is better able to replicate the observed surface iron distributions in the North Atlantic (4.7). The distributions at 1000m are very similar to those seen in the MITgcm. Reducing the surface iron concentrations to levels below 0.3 nM in regions with moderate, or even low, atmospheric dust supply, is something the MITgcm struggles to do.

Consequently, a comparison with the NEMO-PISCES closures is useful in order to identify which processes are not represented in the simpler MITgcm. Identifying aspects of the more sophisticated iron closure that can be integrated into the MITgcm, without compromising the efficiency and simplicity, is a good step towards improving the model results and make the most of the more realistic physical characteristics for effective basin-scale effects on iron distributions.

4.4.2 The NEMO-PISCES iron closure

The NEMO-PISCES iron closure is more complex than the MITgcm closure. The scavenging package alone has several different components, leading to a larger number of tracers carried by NEMO-PISCES, 24 compared to 6 in the MITgcm. There are three explicit processes within the closure representing scavenging-type processes: scavenging onto particles, coagulation and aggregation. The scavenging process (4.14) is quantified using $[Fe']$ and a rate that consists of a background rate (S_{min}) and a particle dependent rate (S_{part}). It uses four particle tracers, particulate organic carbon ($[POC]$), larger particulate organic carbon ($[GOC]$), calcium carbonate ($[CaCO_3]$) and biogenic silica ($[BSi]$), and also a surface constrained dust deposition dependent rate ($S_{dust}Fe_{in}$).

$$S_{Fe} = \underbrace{Fe'(S_{min}}_{Background} + \underbrace{S_{part}([POC] + [GOC] + [CaCO^3] + [BSi])}_{Biogenic\ particles} + \underbrace{S_{dust}Fe_{in})}_{Dust} \tag{4.14}$$

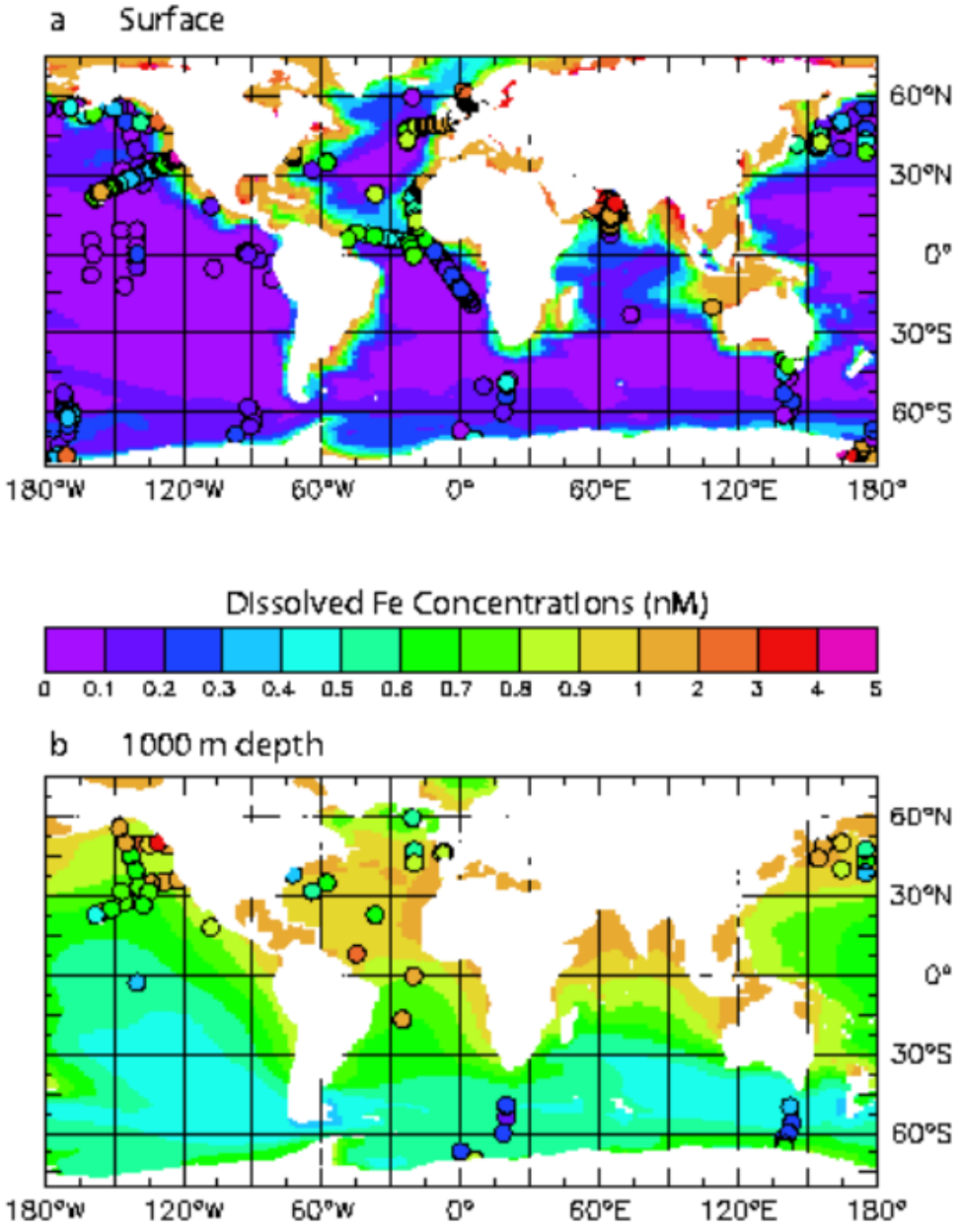

Figure 4.7: Modelled NEMO-PISCES iron distributions at the surface and 1000m depth, taken from Aumont and Bopp (2006)

$$Coag_1 = Fe_{coll}(\underbrace{\sigma(a1[DOC] + a2[POC])}_{Shear\ turbulence\ coagulation} + \underbrace{a3[POC] + a4[DOC]}_{Brownian\ coagulation}) \tag{4.15}$$

$$Coag_2 = \underbrace{Fe_{coll}\sigma(a3[GOC])}_{Large\ particle\ coagulation} \tag{4.16}$$

$$Fe_{coll} = 0.5FeL \tag{4.17}$$

$$Agg_{Fe} = (100 \times S_{Fe})max(0, Fe_T - L_T)Fe' \tag{4.18}$$

The coagulation process (4.15 and 4.16) is dependent on various size grades of organic carbon, including the dissolved pool ($[DOC]$). It is the colloidal fraction of iron (Fe_{coll}) that is reactive in these processes. There is also a dependence upon the shear (σ) which scales the rate of coagulation by an order of magnitude according to whether the process is occurring within the mixed-layer ($\sigma = 1$), or below it ($\sigma = 0.1$). Aggregation (4.18) occurs as a function of S_{Fe} and Fe'. The only term from the NEMO-PISCES closures that has an analogue in the MITgcm closure is S_{min}, which is represented by λ. The other processes are not explicitly represented in the MITgcm, effectively they are bundled up into λ. An additional factor is that NEMO-PISCES transfers these losses of Fe_T into a particulate iron pool. This pool is tracked in the model, which enables reintroduction of iron from the particulate pool back to the dissolved form. This reintroduction does not occur explicitly in the MITgcm, thus λ represents an implicit balance of these higher order 'loss' and 'source' terms, including particulate remineralisation.

4.4.3 Comparison of model parameters in MITgcm and NEMO-PISCES

There are certain limitations when comparing the iron closures of the two models, specifically trying to determine whether a process that is lacking from one of the closures is implicit or ignored with respect to the other. Generally it is the MITgcm closure that does not explicitly represent some of the higher order processes present in NEMO-PISCES. For the purposes of this section any processes not explicitly represented are taken to be ignored, enabling direct comparison, Table 4.2.

Table 4.2: Comparison of parameters for the MITgcm and NEMO-PISCES iron closures

Symbol MIT / NEMO-P	Description	MITgcm	NEMO-PISCES
S_{min} / λ	Background scavenging rate, s^{-1}	6.1 x 10^{-9}	3.6 x 10^{-8}
K_{FeL}^{cond}	Ligand conditional stability constant	10^8	10^{12}
L_T	Total ligand concentration, nM	1	0.6
$R_{Fe:P}$	Redfield ratio Fe:P, mol_{Fe}/mol_{PO^4}	4.7 x 10^{-4}	variable
α	Atmospheric Fe solubility, %	1	2

There are significant differences between the background scavenging rates and stability constants of the two closures. The scavenging rate in the MITgcm is a fifth of the value for NEMO-PISCES; the NEMO-PISCES closure strips out $[Fe']$ much faster than the MITgcm as well as enabling spatial variation in scavenging rates. When the NEMO-PISCES rate is implemented using the MITgcm (Figure 4.8) the iron distribution across 60°N improves relative to the data, but still lies some way short of the target. This parameter regime also causes intense removal of $[Fe_T]$ from the southern portion of the Atlantic, and Southern Ocean, taking the modelled distribution further from accepted values in this region.

The conditional stability constant is four orders of magnitude larger in NEMO-PISCES than the MITgcm. Higher values of this parameter mean that the ligand interactions act to maintain a higher proportion of $[Fe_T]$ in the ligand-bound form, $[Fe_L]$. If this change were also to be implemented into the MITgcm closure, it would cause a return of higher concentrations due to the fact a smaller amount of the $[Fe_T]$ would be 'accessible' to the scavenging process. The value for the ligand stability constant in NEMO-PISCES is consistent with observed data values (Rue and Bruland, 1997), so in addition to potential improvements of the iron distributions using the NEMO-PISCES value for this parameter would bring the MITgcm in line with observational data.

Implementing the NEMO-PISCES parameter values in the MITgcm does not immediately replicate the observed data values. Consequently, we can assume the MITgcm closure is too simplistic to be able to recreate iron distributions on local scales purely by using the NEMO-PISCES parameters. The net effect of adding the increased complexity of the NEMO-PISCES closure into the MITgcm is that the total scavenging rate increases even more than using the NEMO-PISCES background scavenging rate. In addition there is the added factor of the coagulation and aggregation processes, which both act on $[FeL]$; a fraction of the $[Fe_T]$ previously inaccessible to the geochemical removal processes. This ability for removal of the complexed iron highlights the importance of the larger, and more realistic, ligand stability constant that is present in NEMO-PISCES. The NEMO-PISCES closure has a faster turnover of $[Fe_T]$ in the water column so the system needs retain a portion of the iron in order to simulate the situation in the real world. In truth, it is no longer possible to hide iron from the removal processes, however it avoids rapid removal by forming organic complexes with ligands.

The NEMO-PISCES closure has several characteristics, in addition to the parameter differences, that will be extremely useful within the MITgcm. The spatially varying, and process dependent, scavenging rate is an important difference. Variable $R_Fe : P$ is also a very important process, representing the ability of the biological community to adjust to iron-limiting and iron-replete conditions. The two benthic iron sources, sedimentary and hydrothermal, included in NEMO-PISCES are also necessary in order to represent natural sub-surface supplies of iron. The dependence of the MITgcm on atmospheric dust deposition to supply iron to the system has effectively confined the MITgcm to a particular parameter regime. Inclusion of subsurface sources reduces the reliance on surface source and physical transport of iron to replicate deep iron concentrations.

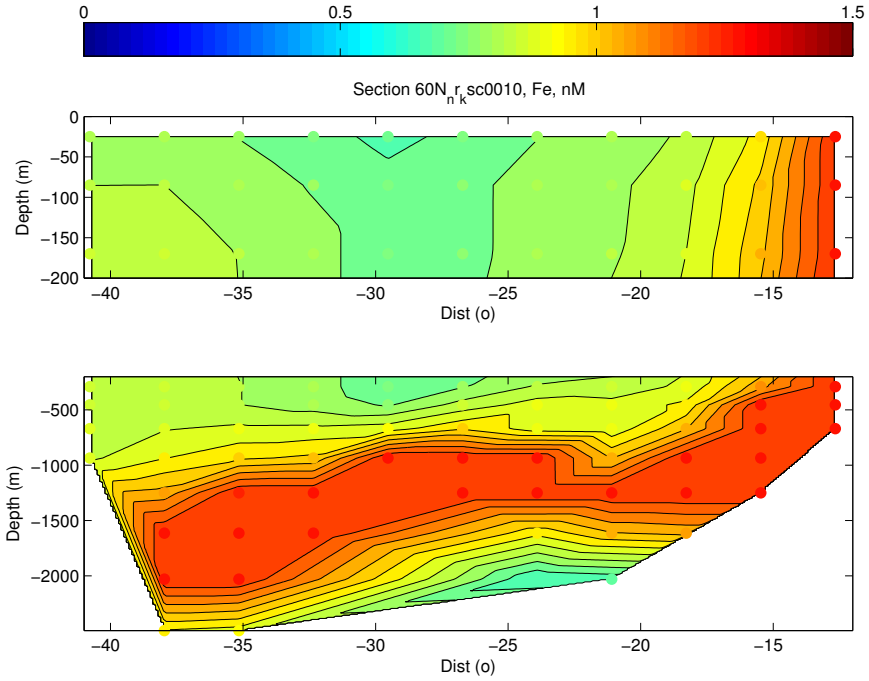

Figure 4.8: MITgcm, λ = 1.14 yr^{-1}, Iron distribution (nM) for 60N

4.5 Improvements to the MITgcm

The MITgcm has one iron source, the atmospheric deposition of dust to the surface ocean. In order to be able to best explore the impacts of scavenging rates and transport it is vital that the two subsurface iron supplies, sedimentary and hydrothermal, are incorporated into the iron closure as for NEMO-PISCES.

4.5.1 Inclusion of sedimentary sources

Sedimentary iron supply is parameterised with the use of a high resolution bathymetry field and an imposed dependence of sedimentary iron flux on depth. Due to the coarse resolution of the MITgcm configuration, large amounts of sedimentary supply are smoothed out causing inaccuracies in the integrated global magnitude of iron sourced from the sediments, as well as biasing against isolated sediment supply hotspots, such as mid-ocean features like the Kerguelen Islands. A method of binning the high-resolution ETOPO 1 arc-minute ocean bathymetry data field (Amante and Eakins, 2009) was

developed and applied following Aumont and Bopp (2006). For each grid box, the total bathymetric area of sediments was calculated as a fraction of the total grid box area, sed_{frac}. A calculation of the mean depth of the seafloor fraction is also made. This inclusion allowed a representation of mid-ocean islands, for which otherwise the sediment supply would have been omitted because of the lack of such bathymetric features in the chosen resolution of the seafloor. The total supply of iron to the water column in a particular grid box is the product of a prescribed sedimentary iron flux, grid cell base area and fraction of grid cell that is seafloor. The prescribed sedimentary iron flux is constrained by observational data from Elrod et al. (2004) and Homoky et al. (2013). Elrod et al. (2004) provide flux estimates of 4.3 to 8.9 $nMFem^{-2}d^{-1}$ compared to estimates of between 0.1 and 2.4 $nMFem^{-2}d^{-1}$ from (Homoky et al., 2013). Elrod et al. (2004) also identified an important relationship between observed iron fluxes and the depth of the sediment, ultimately tied to the diminishing levels of oxygen available to oxidise iron deep within the sediments. Fluxes become minimal at 650m and negligible below 1000m, therefore here we prescribe a sedimentary iron supply rate, sed_{sup}, of 2 $nMFem^{-2}d^{-1}$, which diminishes to zero at depths greater than 550m, z^{sed}_{max}, by the relation $\frac{z^{sed}_{max}-z}{z^{sed}_{max}}$. This sedimentary iron flux parameterisation is shown explicitly in (4.19) and as a function of depth in figure 4.9. The flux of iron, F^z_{sed}, at each depth level is then calculated as a fraction of the grid box, sed_{frac}, that is a sediment-ocean interface (4.20).

$$sed_{sup} = max\left(0, sed_{in}\frac{z^{sed}_{max} - z}{z^{sed}_{max}}\right) \tag{4.19}$$

$$F^z_{sed} = sed_{frac}sed_{sup} \tag{4.20}$$

4.5.2 Hydrothermal vent supplies of iron

Hydrothermal sources of iron are similarly parameterised as a flux into grid boxes adjacent to a hydrothermal source. These hydrothermal sources have been largely overlooked by OGCMs, however recently a number of observational studies (Bennett et al., 2008; Mackey et al., 2002; Statham et al.,

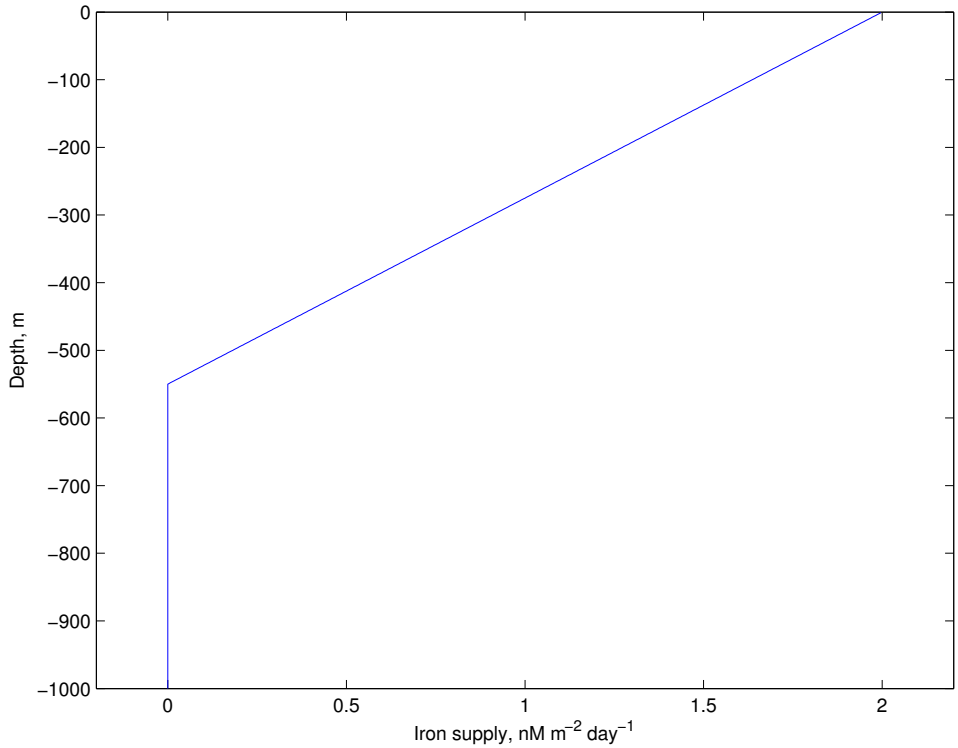

Figure 4.9: Figure showing iron supply rate dependence on depth

2005) have emphasised the importance of hydrothermal iron supply affecting the dissolved iron distributions, particularly in the deep ocean. The observed relationship between ^3He and dFe (Boyle et al., 2005; Boyle and Jenkins, 2008) combined with modelling on the injection of ^3He from the mantle into the deep ocean via hydrothermal vents (Dutay et al., 2004; Farley et al., 1995) allows robust parameterisation of a previously unqualified source of iron. The flux of iron to a grid box adjacent to a hydrothermal vent is therefore quantified using modelled ^3He emissions, $^3He_{in}$, and an observationally derived ratio of dissolved iron to ^3He, $R_{Fe:\,^3He}$ (4.21) following Tagliabue et al. (2010)..

$$F^z_{hyd} = R_{Fe:^3He}\ {}^3He_{in} \tag{4.21}$$

4.5.3 Scavenging regime

The first steps to improving the performance of the MITgcm are to begin to introduce some of the processes that are represented in NEMO-PISCES, but not in the MITgcm. These processes include particle dependent scavenging (biogenic and dust) and coagulation. There are some problems with

implementing these processes as they are implemented in NEMO-PISCES. There are a number of tracers that NEMO-PISCES uses for these closures that are not explicitly represented in the MITgcm, for these closures $[POC]$ is specifically required. It is possible to calculate an implicit $[POC]$ from the biological export fluxes in the model. Biological activity occurs in the uppermost 6 layers of the MITgcm. Biological production in these boxes transfers inorganic phosphate into dissolved and particulate organic phosphate pools. $[DOP]$ is carried by the model, but $[POP]$ is assumed to sink with a specific velocity and is distributed down the water column using a martin curve. A biological export flux can be calculated by accumulating the losses from each depth level, hence, providing a flux of particulate phosphate at each z-layer interface. By using the inverse of the sinking velocity this flux can be converted to an in situ pseudo-concentration of particles, then converted to carbon units using the Redfield ratio,$R_{P:C}$ (4.22). Ignoring the other particle pools we can therefore adapt, and simplify the NEMO-PISCES scavenging regime (4.14) to the MITgcm (4.23).

$$[POC] = \frac{1}{R_{P:C}} \frac{\partial [POP]}{\partial t} \partial z \frac{1}{w_s} \tag{4.22}$$

$$S_{Fe} = Fe'(S_{min} + S_{part}([POC]) + S_{dust} Fe_{in}) \tag{4.23}$$

$$Coag = Fe_{coll}(\sigma(a1[DOC] + a2[POC]) + a4[POC] + a5[DOC]) \tag{4.24}$$

The process of coagulation represents the Brownian and turbulent accumulation of particles within the water column. This process mainly operates with the colloidal fraction of the iron species, approximated as half of organically complexed iron: $Fe_{coll} = 0.5 \times FeL$. Chapter 3 highlighted the importance of the colloidal fraction in the overall transfer of iron from the dissolved to the particulate phase, thus it is important to represent it within the MITgcm. Without the explicit representation of large particulate organic matter ($[GOC]$) there is a limit to the number of these coagulation and aggregation processes that can be included. Implementing the first coagulation closure has the same issue with regard to $[DOC]$ and $[POC]$. We can again use $R_{P:C}$ to estimate $[DOC]$ from $[DOP]$ and use the estimate for $[POC]$ from above. These process can be included as for NEMO-PISCES (4.15).

Explicit representation of additional particle size fractions was omitted, due to computational costs, leaving a single equation representing coagulation within the MITgcm, (4.24) see summary box (Figure 4.11).

4.5.4 Remineralisation of scavenged iron

Remineralisation of scavenged iron is a key process in redistributing dissolved iron from the surface waters. Previously the MITgcm used an implicit desorption term within the net scavenging rate. Following the reformulation of the scavenging closure and the explicit representation of particle dependent scavenging rates, as well as the inclusion of coagulation of colloidal iron within the ligand-bound pool, it is important to ensure that the representation of desorption from particulate material is maintained. NEMO-PISCES tracks particles, allowing explicit representation of adsorption and desorption of dissolved iron, as well as other processes related to the formation and breakup of particulate material. This can be computationally expensive so as a compromise an instantaneous redistribution of scavenged particulate iron, complete with a desorption timescale is applied. This process is directly analogous to the remineralisation of $[POP]$ within the phosphate closure. It is assumed that the particles formed by the process of scavenging onto particle surfaces, as well as the coagulation of colloidal material, behave in a similar way as those formed via biological activity. The biological production of particles is a key driver of oceanic iron scavenging so this assumption is robust. The distribution of the particles is governed by a new parameter, $K^{Fe}_{remin} = 0.9$, similar to the power law function used to govern the remineralisation curve of $[POP]$, $K^{POP}_{remin} = 1.1$. As for the implicit calculation of $[POP]$ above, particulate iron concentration is calculated from the export flux of particulate iron and the fallout rate of particles,

$$[Fe_P]_{(n)} = F_{(n)} \frac{1}{w_s}. \tag{4.25}$$

The export flux of scavenged particulate iron is calculated using the same closure as for the redistribution of organic particles, except instead of biological activity supplying particles it is the scavenging process and a different

remineralisation rate is used, $K^{Fe}_{remin} = 0.9$,

$$F_{(n)} = Sc^{tot}_{Fe(n)} h_{(n)} + \sum_{i=n-1:1} Sc^{tot}_{Fe(i)} h_{(i)} \left(\frac{z_{(n)} + h_{(n)}}{z_{(i+1)}} \right)^{-K^{Fe}_{remin}} . \tag{4.26}$$

This particulate concentration, $[Fe_p]$, can then be transferred back to the dissolved pool by the remineralisation rate of particulate iron , $\lambda^{Fe}_{remin} = 0.003\ d^{-1}$. In addition to this remineralisation rate a scaling of a factor of 12 is applied in the surface mixed layer. This scaling factor is introduced following the work of Boyd et al. (2010) who found much greater levels of remineralisation of particles in the upper ocean, $\approx\ 25\%\ d^{-1}$, compared to the deep, $<\ 2\%\ d^{-1}$.

4.5.5 Variable iron to phosphate uptake ratios

The inclusion of an expanded particle scavenging scheme is necessary to enable the iron system to react to excessively high concentrations of dissolved iron. The coagulation process also enables removal of dissolved iron from the previously protected ligand-bound iron concentration ($[FeL]$). It is important to consider the biological processes that also act to drawdown excessive concentrations of iron in the water column. A study by Sunda and Huntsman (1995) found the ratio of iron to carbon found in phytoplankton, both a coccolithophore and a diatom, increased with dissolved iron concentrations. This variation in assimilated Fe:C must be sourced from the surrounding water, hence when there is excessive iron concentrations phytoplankton will exhibit luxury uptake; this is the uptake of excess iron in preparation for times when iron is less abundant. Conversely, when iron concentrations are low phytoplankton are forced to make do with replacement nutrients that allow them to synthesise sub-optimal alternative enzymes (Raven et al., 1999). The current MITgcm configuration prescribes an $R_{Fe:P}$ ratio of $4.468 \times 10^{-4} mol\ mol^{-1}$. Converting to carbon units via a Redfield ratio of $R_{C:P} = 106$ this equates to $4.2\ \mu molFe\ molC^{-1}$. Comparing with ranges of $R_{Fe:C}$ found by Twining et al. (2004), Strzepek et al. (2005) and Sunda and Huntsman (1995) of 6 to 36, 2 to 19 and 1 to $50\ \mu molFe\ molC^{-1}$ respectively for ocean

concentrations of $[Fe_T]$, there is a substantial lack of high $R_{Fe:C}$ uptake rates within the model. A variable rate of iron uptake is applied to the MITgcm iron closure via a parameterised relationship with $[Fe_T]$. The $R_{Fe:C}$ has lower, FP_{min}, and upper, FP_{max}, bounds of 1.11 and 44.2 $\mu molFe\ molC^{-1}$, representing 0.2 and 10 times the existing $R_{Fe:C}$. With the partial coupling of phosphate and iron it is useful to calculate these uptake rates with respect to phosphate, so within the model $R_{Fe:P}$ is calculated. This relationship is assumed to vary linearly between the concentrations of 0.05 and 1 nM of iron ($Fe_{max}^{Fe:P}$), where a plateau produces a maximum $R_{Fe:P}$, which is parameterised as,

$$R_{Fe:P} = max\left(FP_{min}, FP_{max} min\left(\frac{dFe}{Fe_{max}^{Fe:P}}, 1\right)\right), \tag{4.27}$$

and visually represented in Figure 4.10.

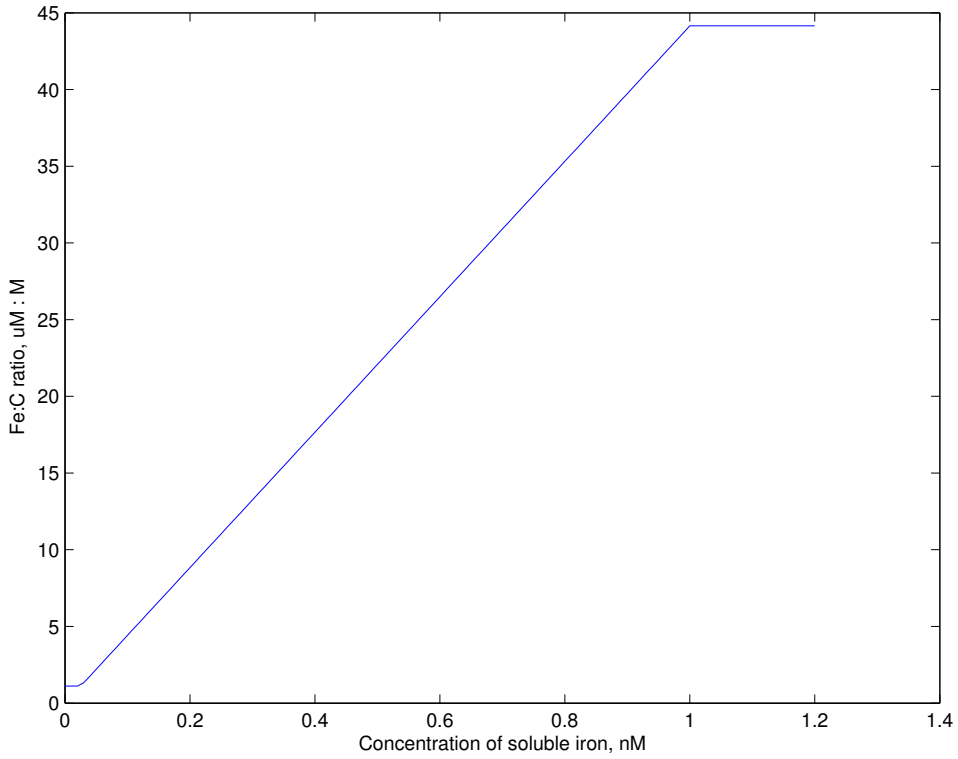

Figure 4.10: Figure showing $R_{Fe:P}$ dependence on Fe_T

4.5.6 Other processes included in the new MITgcm closure

There is one further aspect of the NEMO-PISCES closure that has not yet been discussed; particulate iron as a tracer. NEMO-PISCES carries $[Fe_P]$ as a tracer. This pool is supplied by biological fallout as well as the scavenging, coagulation and aggregation terms of the iron closure. The particulate iron pool also resupplies iron into the dissolved form. This is a process analogous to remineralisation and desorption from particles. At this current time there is no $[Fe_P]$ in the MITgcm and as a result no resupply of scavenged/coagulated iron. Implicit representation of this process will avoid excessive computational cost resulting from explicit inclusion of particle tracers. The initial method of simulating the $[Fe_P]$ to $[Fe_t]$ transfer is to mimic the method used to calculate $[POC]$ from the biological export flux. Using this implicit calculation a pseudo-particulate iron concentration can be calculated from the losses of $[Fe_T]$ by scavenging and coagulation. The entire MITgcm iron closure used in this study is provided as a summary box in Figure 4.11.

4.6 New Model Distributions and Processes

In order to best qualify the model, two regional comparisons are made with data from the Sub-polar North Atlantic and the Tropical Atlantic, as well as an overall Atlantic/Global comparison made using the global database of Tagliabue et al. (2012). Examination of tracer distributions as well as some discussion of key processes affecting iron cycling is then carried out. In addition to these data-led discussions a quantitative comparison between the old and new MITgcm control runs is made to put into context the effect of the developments on the MITgcm model output.

The tendency of total dissolved iron concentration is calculated as the sum of several processes:

$$\frac{\partial Fe_T}{\partial t} = R_{Fe:P}\frac{\partial PO_4}{\partial t} - Sc^{tot}_{Fe(n)} + \lambda^{Fe}_{remin}[Fe_P] + \alpha_{Fe}F_{dust} + F_{sed} + F_{hyd}. \tag{4.28}$$

The ratio of iron to phosphate is a function of total dissolved iron concentration:

$$R_{Fe:P} = max\left(FP_{min}, FP_{max}min\left(\frac{Fe_T}{Fe^{Fe:P}_{max}}, 1\right)\right). \tag{4.29}$$

The removal of iron from the dissolved to the particulate phase is a sum of scavenging and coagulation processes,

$$Sc^{tot}_{Fe(n)} = (S_{Fe(n)} + Coag_{(n)}), \tag{4.30}$$

where particle scavenging is a combination of "background", "organic particle" and "atmospheric dust" scavenging,

$$S_{Fe} = Fe'(S_{min} + S_{part}([POC]) + S_{dust}Fe_{in}), \tag{4.31}$$

and coagulation is dependent on colloidal iron concentration and dissolved and particulate organic carbon,

$$Coag = Fe_{coll}(\sigma(a1[DOC] + a2[POC]) + a4[POC] + a5[DOC]). \tag{4.32}$$

A scavenged iron export flux calculated using a remineralisation curve,

$$F_{(n)} = Sc^{tot}_{Fe(n)}h_{(n)} + \sum_{i=n-1:1} Sc^{tot}_{Fe(i)}h_{(i)}\left(\frac{z_{(n)} + h_{(n)}}{z_{(i+1)}}\right)^{-K^{Fe}_{remin}}, \tag{4.33}$$

is used to implicitly remineralise particulate iron into the water column below using an assumed sinking rate of particles,

$$[Fe_P]_{(n)} = F_{(n)}\frac{1}{w_s}. \tag{4.34}$$

Sedimentary iron supply is parameterised as a linear function of the depth at which the continental shelf is found, bounded by a maximum sedimentary supply depth and limited by a maximum flux of sedimentary supply,

$$sed_{sup} = max(0, sed_{in}\frac{z^{sed}_{max} - z}{z^{sed}_{max}}). \tag{4.35}$$

This supply flux is weighted by the area of continental shelf in a given model grid box using etopo bathymetry data,

$$F^z_{sed} = sed_{frac}sed_{sup}. \tag{4.36}$$

Hydrothermal supply of iron is calculated by scaling the ^3He flux at continental shelf boundaries by the ratio of iron to ^{3}Helium,

$$F^z_{hyd} = R_{Fe:^3He}\ {}^3He_{in}. \tag{4.37}$$

Particulate organic carbon is used to calculate a fraction of the coagulation process, this is calculated implicitly from the phosphate to carbon ratio and the export flux of particulate phosphate,

$$[POC] = \frac{1}{R_{P:C}}\frac{\partial [POP]}{\partial t}\partial z\frac{1}{w_s}. \tag{4.38}$$

Figure 4.11: Summary of the new iron closure developed for the MITgcm

4.6.1 Subpolar North Atlantic

The observation data from cruise D354 (for more information see chapter 2) provides a subpolar North Atlantic perspective of the model's capability. The model bathymetry at latitudes higher than 55°N becomes very basic, particularly when considered relative to the width and depth of the ocean in that region. As a consequence, some of the peripheral regions from the data are masked out in the model. Despite this a good indication of the comparison is given in figure 4.12. The variability in the observations is not

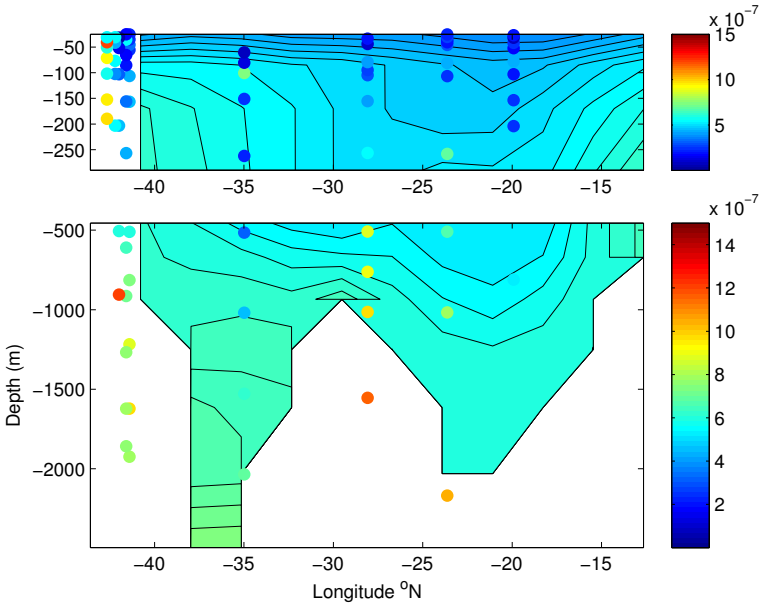

Figure 4.12: MITgcm new closure 60°N dissolved iron distributions, $mol\ m^{-3}$. The contoured section is model output; data values are scattered onto the model field.

present in the model field, in part due to the fact that 4.12 is a modelled annual mean. The model captures the subsurface minimum in the Iceland Basin region (-30 to -15°E), but the analogous feature in the Irminger Basin is not resolved. A gradient in iron concentration emanating from the Greenland continent in the west implies an effect of implementation of sedimentary supply. The high concentrations seen centred on the Reykjanes Ridge in the data (at approximately -28°E) is not seen in the model. This subsurface supply of iron falls below the threshold for sedimentary sources in the model. This is a feature that could not be resolved by the model without an overhaul of the benthic sediment interaction closures. This level of detail was something that

was always going to be difficult to capture while targeting long-term transport experiment capability. The elevated iron concentrations seen in the data to the West of the model boundary display similar concentration levels to the model region between -38 and -35°E. This is an indication that the observed deep sedimentary iron in the data can be resolved using subsurface sediment sources and a transport mechanism. The high spikes of iron concentration seen in the data represent features that are unresolvable in an annual mean field.

The phosphate distribution produced by the new model closure is generally of equal quality to the old model closure. The concentrations of phosphate have increased markedly across the domain, Figure 4.13. The old iron closure under-predicted phosphate concentrations by 0.5 μM in the west of the domain, but matched quite well in the intermediate waters in the west, Figure 4.2. Now the model, over-predicts phosphate concentrations by around 0.2 μM throughout the domain. The surface phosphate concentrations are much higher than compared to the plotted snapshot of summer phosphate concentrations from D354. The net effect of the changes is to maintain a similar level of correlation with a bias towards over-predicting phosphate concentrations.

The key characteristics of the sub polar North Atlantic biogeochemical regime were described in section 2.4.6. The model set-up chosen here performs reasonably well when compared to this regional regime definition. However, there are significant limitations too. The model performs better are replicating observed iron distributions, and is able to moderately resolve the effect of circulation bringing nutrient depleted water into the east of the section. The magnitude difference between the west and east is very small relative to the observations. The model fails to resolve the surface depletion of phosphate due to biological consumption. This failure to consume surface macronutrients is indicative of iron limitation, a phenomenon which did not occur in the original setup and which this development specifically set out to achieve. The supply of nutrients from surface run-off and glacial melt is also not resolved due to the

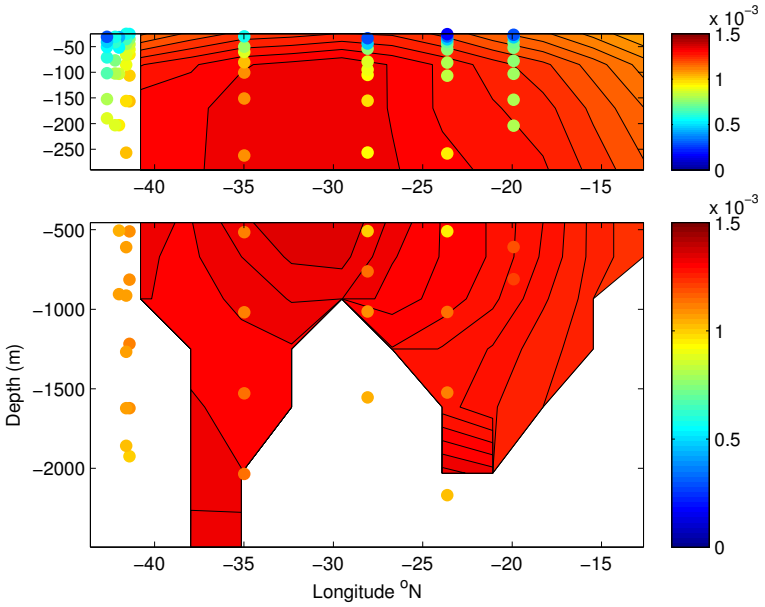

Figure 4.13: MITgcm new closure 60°N phosphate distributions, $mol\ m^{-3}$. The contoured section is model output; data values are scattered onto the model field.

lack of these processes explicitly within the model. The mixing of the nutricline is very strong within the model, which compares well with the observations made from the data, however the lack of biological consumption fails to imprint the basin-scale variations in nutrient regimes onto the macronutrient distributions.

Due to the chosen grid for the model, there are several physical processes which are not resolved within the model. The supply of phosphate from the Arctic Ocean via the Canadian Archipelago cannot occur, nor can the physical influence of the Arctic water masses on the inter-basin distribution of iron. The lack of an Arctic Ocean, in addition to the high resolution chosen for this study, causes difficulties for the model with regards to resolving the inter-basin physical interactions on the relatively small spatial scales of the high latitude North Atlantic.

4.6.2 Tropical Atlantic

The variability observed in the D354 dataset is very small compared to that seen in the D361 Tropical Atlantic, data. This data was collected in the region

of ocean adjacent to the plume of atmospheric dust that originates from the Sahel region of Africa. This atmospheric source is one which varies hugely depending on meteorological and terrestrial conditions across North Africa. Within the model the process of atmospheric supply of dust is provided with monthly average modelled deposition fields. The process of averaging monthly fields removes the deposition model's ability to resolve variations on shorter timescales. Consequently, large sporadic depositions caused by large weather systems may be missed by the MITgcm. The zonal section at 11°N from the Tropical Atlantic data, figure 4.14, shows the magnitude of this atmospheric deposition being particularly strong close to the African Continent.

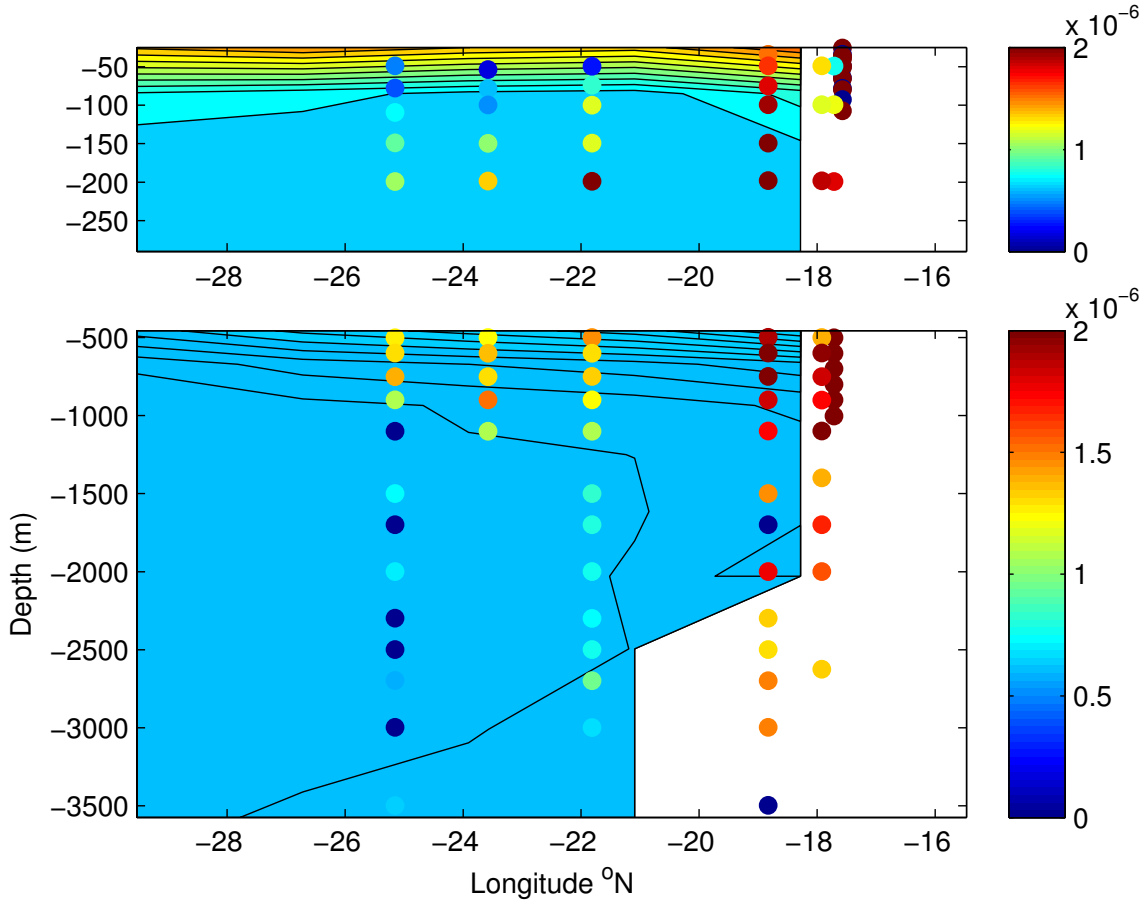

Figure 4.14: MITgcm new closure 11°N dissolved iron distributions, $mol\ m^{-3}$. The contoured section is model output; data values are scattered onto the model field.

This region at the surface is reasonably well captured by the model, however the model's surface layer performance worsens with distance from Africa. The data suggest a low iron surface layer, whereas the model predicts that the

surface layer is the only depth which concentrations greater than 0.6nM are seen. This statement also highlights the failing of the model to capture a plume of iron emanating from the continent westwards at 500 to 1000m depth. This may be the model lacking the suitable structure to resolve some small circulatory features or, more likely, suggests that local extremes of supply can cause significant variations from the annual average iron concentrations, particularly when considering the work of Ye et al. (2011) who highlight the vitality of timing in determining the exact response of the system to an iron source perturbation. The modelled deep water away from the continental shelf is well matched to the observations with concentrations below 0.8nM replicated in the model. A patch of particularly low iron in the west most station below 1500m is not seen in the model. This minimum could be a second order response of the system to the high deposition of particles. A section taken

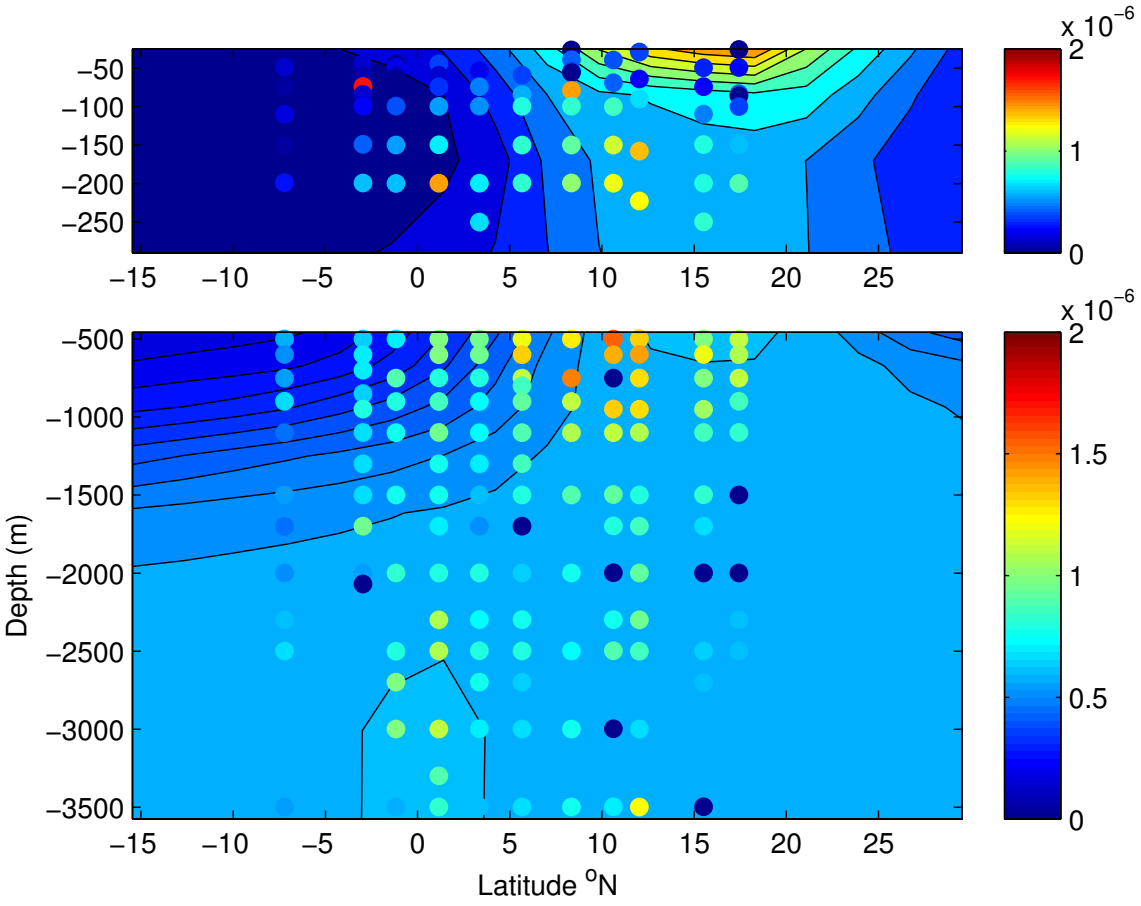

Figure 4.15: MITgcm new closure 28°W dissolved iron distributions, $mol\ m^{-3}$. The contoured section is model output; data values are scattered onto the model field.

through the tropical region of the Atlantic at approximately 28°W shows how the model's meridional distribution fares through the dust deposition plume of the mid-Atlantic. The problem of the model failing to capture the low surface iron concentrations continues into this section. Despite the model identifying the latitudes between 10 and 20°N as a region of strong iron supply, and resultant iron concentration, these high concentrations are not seen in the observations. As mentioned previously, Ye et al. (2011) talk about the ability of atmospheric dust supply acting as a sink of iron due to particle scavenging and a lack of iron-binding ligands. This mechanism for deposition instigating removal involving variable ligand concentrations is not in the MITgcm iron closure. Alternatively, the natural variability of deposition, that is lacking in the MITgcm, could provide an explanation for the low concentrations of iron in the observations from the surface. If the deposition was particularly short-ranged, or anomalously deposited at higher or lower latitudes to those shown here, the surface supply of iron could be missed by the geographical range of the observations. The region to the south of the deposition plume in the model is well replicated, both the data and model concentrations are particularly low, from 0.1 to 0.3 nM. This region represents the South Subtropical Gyre of the Atlantic. The deeper waters in this section show strong similarities. With the exception of the patch of high iron, 1.2 to 1.5 nM at 500 to 1000m, between 5 and 15°N, the deep iron concentrations consistent, observational data tends to be slightly higher, but the homogeneity and magnitude of these measurements support the model's representation of the deep water.

The phosphate distributions produced by the original iron closure were reasonable and it was important to avoid perturbing this regime. However, the distributions of phosphate in the Tropical Atlantic resulting from the new iron closure have improved the phosphate concentrations quite considerably, Figure 4.16. The new iron closure maintained the qualitative skill of the model and improved the phosphate concentrations within the model to match the data observations. The surface depletion and subsurface nutrient maximum of phosphate concentrations were maintained and the gradient of phosphate at depths greater than 2000m was reduced in line with the observed distribution.

Although the aim was to try and maintain the phosphate distributions as they were prior to adjusting the iron closure, the changes made have improved the skill of the model at resolving phosphate distributions in the Tropical Atlantic.

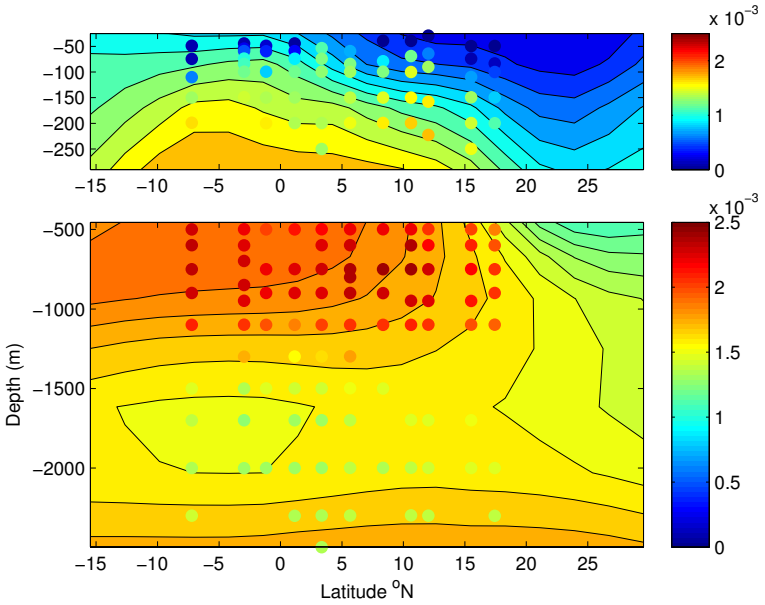

Figure 4.16: MITgcm new closure 28°W phosphate distributions, $mol\ m^{-3}$. The contoured section is model output; data values are scattered onto the model field.

The biogeochemical regimes present in the Tropical Atlantic dataset were described in section 2.5.4. The iron closure has qualitatively replicated the macronutrient and micronutrient regimes. The supply of iron to the surface of the Tropical Atlantic is able to encourage biological activity, which allows the regeneration of organic material and the remineralisation of scavenged iron to resupply iron into the subsurface waters. The plume of iron resulting from these processes augments the intermediate and deep water masses with iron. The supply of iron within the North Atlantic Deep Water, is resolved well in the model. There are still aspects of the regimes that are not well simulated. The concentrations of iron in the surface water of the model are far too high. The model is still unable to rapidly remove this strong atmospheric source. The capacity for the model to retain iron in the water column is also lower than seen in the data. The constant total ligand concentration effectively sets a limit to the amount of iron the model can retain in the subsurface ocean. This parameter precludes any higher concentrations of iron being maintained by a supply of organic ligands from the atmosphere or another source.

The steps forward made in the resolution of the biogeochemical regimes of the Tropical Atlantic will help to provide meaningful and reliable inferences from the model output. It is clear the processes important in this region are simulated qualitatively within the new iron closure, in contrast to the limited range of processes previously resolved.

4.6.3 Atlantic and Global comparison

On a basin scale the distribution of iron within the model has been compared against the regional studies from the North Sub-polar and Tropical Atlantic in combination with the global dissolved iron database of Tagliabue et al. (2012). A combination of surface distributions and integrated subsurface concentrations are used to test the ability of the model to resolve the observational datasets. Comparisons are initially made against a model annual average dissolved iron field and using observational data taken at various times of the year.

The new iron closures result in a much improved surface distribution. The saturation of the upper waters of the Atlantic north of 10°N that was characteristic of the old MITgcm iron closure is no longer seen. The tropical region directly beneath the atmospheric supply plume still exhibits very high concentrations of iron (1.5nM), driven by the atmospheric model used to determine aeolian deposition. This region of high iron concentrations has a mixed correlation with the observational data in that region, matching well with some and overestimating with respect to the other data (Figure 4.17). Other than the region close to the West African continent where observational data suggests low iron concentrations, the tropical regions are relatively well resolved. The Central Tropical Atlantic matches well with observed measurements of 0.7nM. The Eastern coastal waters of South America, from 10 °N to 30 °S also correspond well with observed iron values. The high latitude North Atlantic, no longer saturated, shows good correspondence with measurements taken during the subpolar North Atlantic cruise, D354, as well as historical data in other regions of the North Atlantic. The model predicts

concentrations from 0.1 to 0.4nM. These match well with the observations but are unable to capture the variability seen in the data, with measurements of 0.8 nM taken in several locations across the region. The modelled iron distributions in the South Atlantic also show good correspondence with observations. The model captures the low iron concentrations seen in the south subtropical gyre of the Atlantic. In the Southern Ocean sector of the Atlantic there are isolated observations of iron exceeding 1.5nM. The region of ocean close to the South Georgia islands and Antarctic peninsula has measurements $>$1.8nM. The new closure is able to increase the dissolved iron in this region relative to the surroundings, as a result of the inclusion of benthic sources, but can not replicate these individual data points.

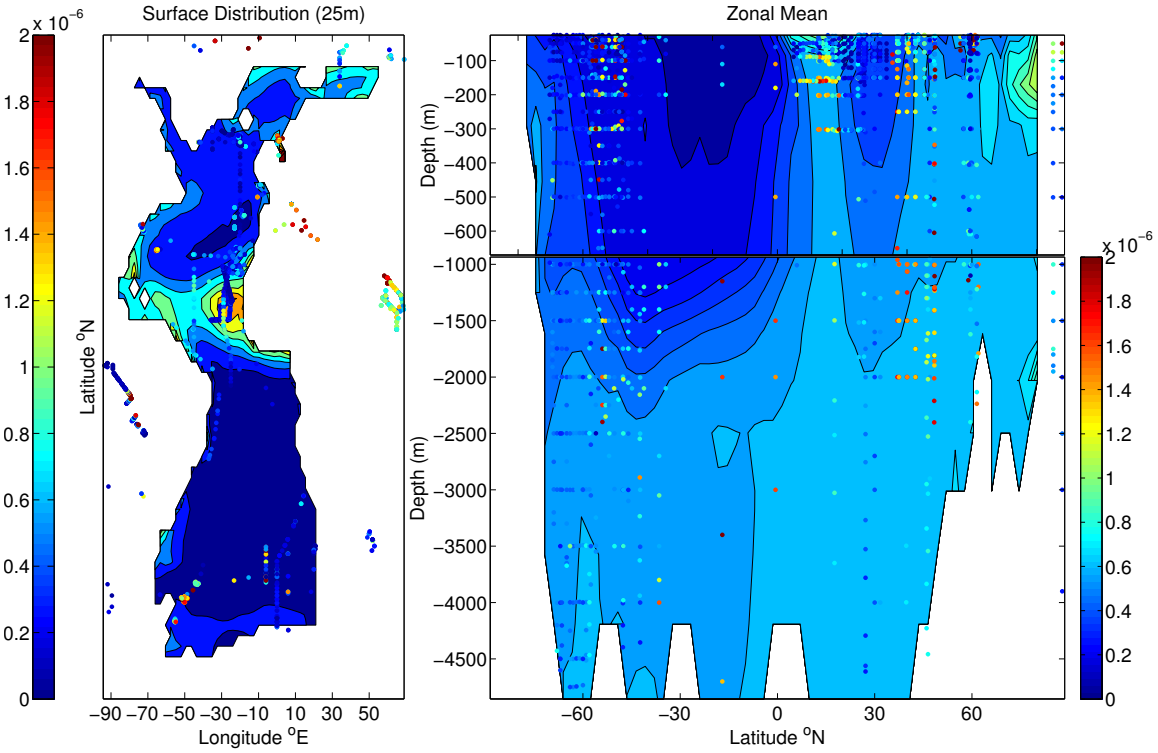

Figure 4.17: Observational iron data scattered over new closure MITgcm dissolved iron distributions for the Atlantic, $mol\ m^{-3}$

Box and whisker plots provide an opportunity to compare the distribution and variability of a dataset. Here, observational data and model output are presented side by side to provide an insight into the performance of the model. Instead of comparing point by point values a method of binning the dataset

into specific depth layers and latitude bands provides the datasets required in order to provide the box and whisker plots (Figure 4.18). The upper 125m of the water column comparison shows that the new iron closure is able to replicate the absolute values for the sub polar regions in both the North and South, but is unable to produce the observed variability. In the Tropics the model captures the the whole range of the observational data. The subtropical gyre iron concentrations are overestimated (0.8nM) relative to the observations (0.4nM) in the north and underestimated (0.1nM against 0.3nM) in the south. This inability to capture variability across the equator is likely to do with the rigid atmospheric iron distribution prescribed in the model. In reality there is much greater variability in deposition than is resolved within the fields used by the model (Schlosser et al., 2014). The iron concentrations in the northern polar region from the model have a reasonable range (0.4 to 0.6nM), but overestimate the average concentrations seen in the observations (0.25 to 0.65nM). The Southern Ocean sector (SP on the figure) shows how the model fails to capture the extreme concentrations of iron that are found in the observations. The model predicts a range of 0.15 to 0.25nM, but the observations show a range of 0.1 to 1nM. The dataset is biassed towards higher concentrations as many of the iron studies, used as a source of data by Tagliabue et al. (2012), took place downstream of island chains and subsurface sea mounts, both known to supply sedimentary iron into the Southern Ocean. The new benthic source scheme included in the MITgcm allows the model to resolve surface iron concentrations in excess of 0.5nM in the Southern Ocean, previously unattainable within the old MITgcm iron closure scheme.

Modelled iron concentrations for depths between 125 and 1000m capture the observed iron concentrations well for the entire North Atlantic. Again the model is unable to provide the variability seen in the data with a modelled range of $\pm$ 0.2 nM compared with observed ranges of the order of $\pm$ 0.7 nM. The high modelled concentrations in the Tropical Atlantic are not translated to depth as the model can not replicate the increase in observed dissolved iron. A difference of 0.6nM is seen between the modelled and observed average iron concentrations (0.5 and 1.1 nM respectively). The average iron concentrations

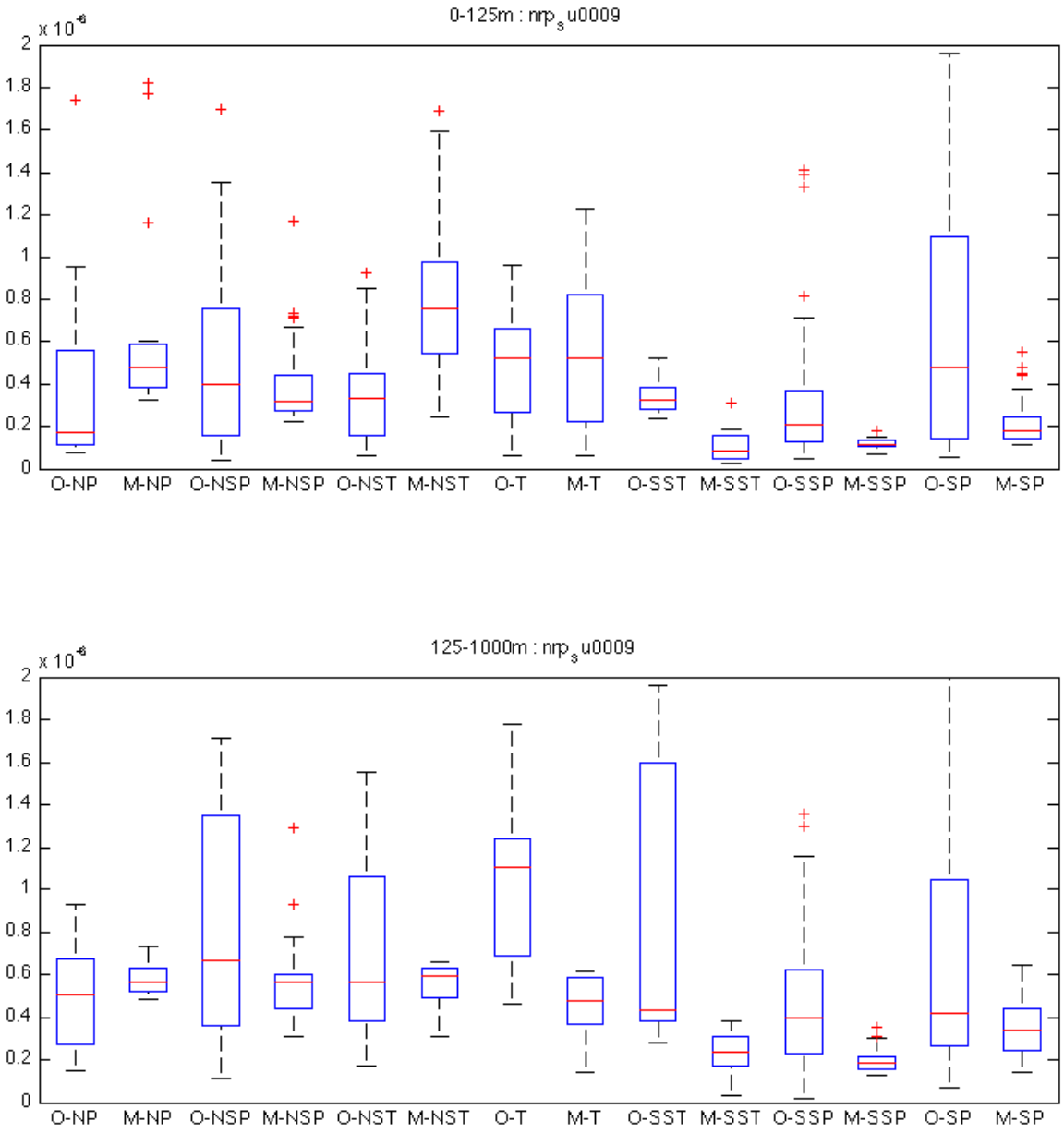

Figure 4.18: MITgcm new closure Atlantic dissolved iron box and whisker plots, $mol\ m^{-3}$. O and M refer to observations and model values. The first letter following the hyphen then designates North or South followed by either one or two letters referring to "Polar-P", "Subpolar-SP", "Subtropical-ST" and "Tropical-T" regions. The red lines represent the median value, box limits represent the upper and lower quartiles and the whiskers then indicate extreme values not considered outliers (effectively $\pm$ 2.7σ or 99.4% of the data).

observed in the South subtropical region are better resolved with average model iron concentrations falling within 0.2 nM of the observed average (0.25 and 0.45 nM respectively). However, the variability at the higher end of the scale is not represented within the modelled distributions. A similar relationship

is seen in the South Subtropical region with the model underestimating average iron concentrations by 0.2 nM and failing to capture the large variability of the observations. The Southern Ocean iron concentrations are better resolved by the model at these depths with modelled and observed averages of 0.35 and 0.4 nM respectively and a modelled range of 0.1 to 0.7 nM reflecting the increased influence of the benthic source regimes at this depth level. The observed range is 0.1 to in excess of 2 nM, further emphasising the difficulty of resolving the variability of observational iron data.

The model skill of the new iron closure has improved the dissolved iron concentrations and represents the latitudinal variation in iron concentrations in the Atlantic. A comparison of the correlation of the original and improved MITgcm iron distributions with the global iron database yields a strong improvement in the reconciliation of observations. The original MITgcm iron closure yielded a Global correlation of $R^2 = 0.05$, demonstrating the limitations of the original parameter choices. Following the improvements made here the MITgcm has a correlation coefficient of $R^2 = 0.4$. The MITgcm can resolve global iron observations as well as other, more complex, biogeochemical general circulation models.

4.6.4 Old and new model comparison

To aid a quantitative understand of the changes made to the MITgcm iron closure a table of metrics has been compiled including many of the key processes, which have been either altered or included for the first time, Table 4.3. This table contains two scales of metrics, the first being a view of the changes at small scales, i.e. at the spatial scale of a m^{-3} box over the period of a second. These metrics include average nutrient concentrations and rates of removal or supply of iron. The second scale of metric is on the basin scale and over the period of a year, these metrics provide an integrated view of the size of the nutrient inventory and the quantity of iron being supplied, or removed, from the ocean.

The new iron closure has significantly increased the average scavenging removal rate of iron by 2.5 times across the globe. In addition to this, a mechanism for the removal of organically bound iron by coagulation has also increased the rates of removal of iron from the water column. To balance this increased removal of iron the solubility of atmospheric dust has increased and two new benthic sources have been added to the model. The two news sources are much slower than the atmospheric supply, but are able to supply iron into subsurface regions and are present across a wider geographical range than the atmospheric dust supply.

The mean iron concentration has increased across the globe by over 25%. Average global phosphate concentrations have remained the same, however more of the phosphate is being retained within the Atlantic basin, reducing concentrations in the Pacific and Indian Oceans. The subsurface respiration of organic material has been reduced by the increased stress placed on the biology as a result of the new iron regime. This demonstrates that despite an increase in the average iron concentrations there have been significant shifts in the distribution. These shifts have pushed some environments towards iron limitation and increased the possibility of persistent macronutrients following the growth season. The reduction in Apparent Oxygen Utilisation is not ideal, but the main focus of this study was to improve the distribution of the iron.

The basin scale metrics give a more holistic view of the global system. The quantity of iron scavenged by particles within the model has increased significantly, from 2.4 x10^{15} $nmol\ Fe\ yr^{-1}$ to 1.9 x10^{16} $nmol\ Fe\ yr^{-1}$, with an even greater relative increase taking place in the Atlantic Ocean specifically. This increase is before the consideration of the extra removal process of coagulation, which removes a further 8.8 x10^{15} $nmol\ Fe\ yr^{-1}$. There is an opposing increase in the quantity of iron supplied to the model, with 6.6 x10^{15}, 4.5 x10^{15} and 3.8 x10^{15} $nmol\ Fe\ yr^{-1}$ supplied globally from atmospheric, sedimentary and hydrothermal sources, respectively. The shortfall between removal and supply of iron is made up for by the implicit remineralisation of scavenged iron from particles back into the water column, this is clearly a very

Table 4.3: Comparison of old and new MITgcm closures

Model Metric	Old		New	
	$Global$	$Atlantic$	$Global$	$Atlantic$
Mean scavenging rate of Fe_{free}, s^{-1}	6.1 x 10^{-9}	6.1 x 10^{-9}	1.7 x 10^{-8}	3.8 x 10^{-8}
Mean coagulation rate of $\frac{1}{2}[FeL]$, s^{-1}	-	-	3.6 x 10^{-10}	1.2 x 10^{-9}
Atmospheric supply rate, $nM\ m^{-2}\ s^{-1}$	3.2 x10^{-7}	6.5 x10^{-7}	6.4 x10^{-7}	1.3 x10^{-6}
$Old\ and\ new\ solubility:\ 1\%\ and\ 2\%$				
Sedimentary supply rate, $nM\ m^{-2}\ s^{-1}$	-	-	3.6 x10^{-8}	5.8 x10^{-8}
Hydrothermal supply rate, $nM\ m^{-2}\ s^{-1}$	-	-	3.2 x10^{-8}	1.9 x10^{-8}
Mean Iron concentration, nM	0.15	0.46	0.19	0.52
Mean phosphate concentration, μM	0.95	1.6	0.95	1.8
Mean AOU concentration, μM	58	75.5	38	60
Scavenging removal, $nmol\ yr^{-1}$	2.4 x10^{15}	1.4 x10^{15}	1.9 x10^{16}	7.2 x10^{15}
Coagulation removal, $nmol\ yr^{-1}$	-	-	8.8 x10^{15}	3.4 x10^{15}
Net atmospheric input, $nmol\ yr^{-1}$	3.3 x10^{15}	1.8 x10^{15}	6.6 x10^{15}	3.5 x10^{15}
Net sedimentary input, $nmol\ yr^{-1}$	-	-	4.5 x 10^{15}	1.8 x 10^{15}
Net hydrothermal input, $nmol\ yr^{-1}$	-	-	3.9 x 10^{15}	6 x 10 ^{14}
Iron inventory, $nmol$	4 x10^{17}	1.4 x10^{17}	5.2 x 10^{17}	1.53 x 10^{17}
Phosphate inventory, μmol	2.5 x10^{18}	4.8 x10^{17}	2.5 x 10^{18}	5.5 x 10^{17}
AOU inventory, μmol	1.5 x 10^{20}	2.24 x10^{19}	1 x 10^{20}	1.8 x 10^{19}

important process within the new model closure.

The nutrient inventories have been perturbed significantly by the iron closure changes with the quantity of iron increasing from 4 x10^{17} $nmol$ to 5.2 x10^{17} $nmol$. The inventory of phosphate within the Atlantic has also increased by a similar magnitude. An increase in both phosphate and iron in the Atlantic Ocean seems counter-intuitive as one would expect an increase in total iron to lead to an increase in drawdown of macronutrients into the interior of the ocean. Once drawn down these nutrients would be transported away from the Atlantic via the global thermohaline circulation. However, as mentioned previously, the increase in iron supply comes along with a stronger surface removal of iron by scavenging and coagulation, this in turn leads to increased limitation and a reduction in the export of macronutrients from the surface layer. This reduction in export of organic material has lead to a decrease in Apparent

Oxygen Utilisation within the ocean interior by a third from 1.5 x10^{20} to 1 x10^{20}.

4.7 Summary

The MITgcm is one of several GCMs that are in use modelling iron. We chose to use, and develop, the MITgcm as its representation of physical processes is very strong. This is important in order to achieve the aims of this thesis with respect to testing the basin-scale partitioning of iron and the effects of iron processes and sources on the distribution of total iron.

The inclusion of sedimentary and hydrothermal sources is important as subsurface benthic sources are important for the global iron cycle (Elrod et al., 2004; Tagliabue et al., 2010, 2014).With respect to the subsurface transport and effect on total dissolved iron the benthic sources are very important.

Additional removal processes of iron were also added to represent the effects of biogenic and lithogenic particles. The Brownian and turbulent coagulation of organic ligands and colloidal material is parameterised using a range of rates. Implicit representation of the particle fallout as a result of scavenging is included as a driver of subsurface remineralisation processes returning iron to its inorganic form in the deep ocean.

Variable $Fe : P$ ratios allow the biological community to exhibit luxury uptake and increases potential export of iron in regions with surface iron concentrations. The removal of excess dissolved iron transports more beneath the surface potentially increasing signals of regeneration.

The new iron closure has resulted in a significant increase in the magnitude of removal and supply processes for iron. This has led to an increase in the iron inventory and a reduction in the global average AOU, in addition to a retention of more phosphate in the Atlantic Basin. However, for a coarse resolution GCM with a relatively simple biological model, 6 tracers and a moderate complexity iron closure the model skill for reconciling observational data is high. The model correlates with global iron measurements with an R^2 coefficient of 0.4,

this is a significant improvement on the values of 0.05 for the original MITgcm closures. This compares well with other state-of-the-art models, which are also unable to improve much beyond this strength of correlation. The current version of NEMO-PISCES demonstrates an R^2 coefficient of 0.5.

The computationally cheap and well-represented physical model provides a good platform for initiating a suite of investigations into basin-wide drivers of iron concentration.

Chapter 5

Developing a Preformed, Regenerated and Scavenged Iron Model Framework

5.1 Introduction

Much work has been performed on the mechanisms of organic carbon production and its transfer from the surface ocean to the abyssal waters of the global ocean. An estimated 45 Pg of organic carbon is produced in the euphotic zone each year (Field et al., 1998). Estimates of carbon being exported from the surface mixed layer range from 16 Pg (Longhurst et al., 1995) to 5 Pg (Henson et al., 2011). The difference in magnitude between Longhurst et al. (1995)'s and Henson et al. (2011)'s estimates demonstrate how our knowledge of the global flux carbon to the deep ocean is incomplete. Different drivers for the variation in efficiency of carbon export have been found; assemblages of marine organisms with varying nutrient uptake ratios (Brix et al., 2006), seasonality of growth periods and physical supply of nutrients (Berger and Wefer, 1990) and the utilisation of dissolved organic nutrients (Roussenov et al., 2006). Primary production is low in

the subtropical gyres, where wind-driven downwelling occurs (Williams and Follows, 2003) precluding local biological communities from accessing large amounts of nutrients from the thermocline. The magnitude of the growth of phytoplankton can increase greatly in upwelling regions, such as along the continental shelf and in the subpolar gyres, as well as being associated with mesoscale circulatory features providing eddy-induced pumping (Falkowski et al., 1991; McGillicuddy and Robinson, 1997). The supply of nutrients from the thermocline into the mixed-layer affects the flux of carbon from surface waters to the deep. This quantity of primary production that is subsequently removed from the surface layer is referred to as export production.

On geological timescales, CO_2 from the atmosphere is transported into the deep waters and sediments that lie beneath the world's ocean, driving deep ocean carbon storage. This transfer of carbon from the surface mixed layer to the interior of the ocean is carried out via physical, and biological transfer (Volk and Hoffert, 1985). These transfers are known as "pumps. The physical transfer of carbon into the ocean interior occurs mainly via a process known as the solubility pump. The density structure of the global ocean is determined by temperature, thus in regions where ocean temperatures are low carbon dioxide solubility is high. This results in the subduction of cold, carbon-rich waters underneath warm, relatively carbon-depleted waters. The transfer of organic carbon and calcium carboante from the surface to the deep waters occurs due to biological activity fixing carbon into organic molecules or into calcium carbonate shells. These soft tissue and carbonate pumps both transfer carbon from surface water to the deep. Respiration of organic carbon and remineralisation of calcium carbonate at depth returns carbon to the dissolved inorganic pool. These biological enhancements of carbon stored at depth are together known as the biological pump. Of all the inorganic carbon stored within the ocean interior, approximately 90% is due to the solubility pump and 10% is due to the biological pump.

The biological pump is fuelled by primary production carried out by photosynthetic organisms in the surface ocean. The process of photosynthesis

ties up carbon into organic molecules and releases oxygen; this removal of CO_2 then allows further drawdown of atmospheric CO_2 into the ocean (Sarmiento and Gruber, 2006). This productivity ultimately converts carbon from inorganic into dissolved and particulate organic carbon (DOC/POC). These pools of carbon are mainly recycled in situ, but the gravitational fallout of particles can result in the transport of carbon to the ocean interior where it is remineralised through respiration (Dugdale and Goering, 1967). This respiration consumes oxygen and returns carbon back to an inorganic form. The efficiency of this process, known as the biological pump, is dependent on the utilisation of nutrients in the surface water (Coale et al., 1996).

The physical pathway is the transport of nutrients and organic material from the surface to the ocean interior via physical processes such as ocean circulation and deep winter convection. This transport involves inorganic macronutrients, such as nitrate, phosphate, silicate, and micronutrients like iron, cobalt and zinc. However, where waters that are replete in inorganic macronutrients are subducted and transported to depth the biological pump is not working at full efficiency. The remaining macronutrients can be seen as an unrealised driver of atmospheric CO_2 drawdown (Ito and Follows, 2005). A key method used to explore the efficiency of the biological pump has been the partitioning of macronutrient inventories into ”preformed” and ”regenerated” components, (5.1) where N refers to a generic macronutrient (Broecker, 1974; Broecker et al., 1985; Toggweiler et al., 2003).

$$N = N_{pre} + N_{reg} \tag{5.1}$$

The nutrients that are present in surface water masses when they are subducted are termed the preformed nutrients, N_{pre}. As N_{pre} is transported in the deep waters it is augmented with regenerated nutrient, N_{reg}, along the way, which comes from the remineralisation of exported organic material. This framework, despite its simplicity, is able to provide a good first estimate of the shortfall between the maximum and observed efficiency of the biological pump. So much so that Ito and Follows (2005) argued that atmospheric pCO_2 and the efficiency of the soft tissue pump of CO_2 were related and

could be predicted using the global average fraction of organic matter that was exported and remineralised. If the biological pump were working at full efficiency the concentration of macronutrients at the surface would be equal to zero, $N_{pre} = 0$, consequently macronutrient concentrations below the surface mixed layer would be dominated by $N = N_{reg}$. Conversely if there was no utilisation of macronutrients in the surface waters then there would be no biological export, and therefore $N_{reg} = 0$ and $N = N_{pre}$. Understanding the reasons for the variation in biological efficiency may help us to understand long-term past and future climate change (Stocker et al., 2013).

In this chapter a new framework for the application of the preformed and regenerated nutrient theory to the micronutrient iron is presented. This extension is aimed at elucidating the balances between the traditional nutrient-type cycling, the subsurface supplies of iron and particle scavenging. Previously, impact of iron sources has been investigated using model sensitivity studies by removing and perturbing particular sources (Tagliabue et al., 2009, 2010, 2014). This framework represents a next step in trying to understand the interactions between iron sources and identify distinguishable iron regimes that rely on a particular iron source. The importance of transport of these subsurface iron sources and resulting proximity of the regimes is naturally explored with the preformed framework. In addition, via application of the framework, quantification of the net scavenging effect can be extracted from the balances. The iron regime identification can be further augmented with information about local scavenging variations. Consequently questions about the importance of subsurface iron sources and the magnitude of particle scavenging of iron can be addressed.

Due to the numerous processes acting to supply and remove iron from the ocean, the framework is more complex than for a macronutrient such as phosphate. The different contributions to the framework are diagnosed using a General Circulation Model, specifically in this case the MITGCM. The definition of the framework is described here and the initial implications of the derived distributions are discussed.

5.2 Iron Framework

5.2.1 Framework definition

Application of the preformed and regenerated framework to iron is challenging because of the various processes that affect iron distributions in the ocean. The cycling of phosphate is predominantly a circulation of nutrient from surface mixed layer to ocean interior and a subsequent return of the nutrient back to the surface. Though there is burial and external supply of phosphate, these processes have a small contribution to the balances compared to the physical transport and biological utilisation that occurs in the water column. Consequently phosphate has a long ocean residence time of 20 to 100 Kyr (Paytan and McLaughlin, 2007). In contrast, iron has numerous sources (Tagliabue et al., 2010; Duce and Tindale, 1991) that are important, and clearly evident in the oceanic distribution of iron (Laes et al., 2007; Moore and Braucher, 2008; Bennett et al., 2008), because of the rapid removal of the trace metal from the water column by a range of processes. Particle scavenging (Yuan-Hui, 1981; Honeyman et al., 1988); surface adsorption, brownian and turbulent aggregation and colloidal association (Wen et al., 1997) are the major processes acting to move iron from the dissolved phase into a sinking particulate phase. When taking into consideration the various sources of iron, it becomes clear that the method of determining N_{pre} in observations, using oxygen-derived N_{reg} concentration becomes uncertain.

In the traditional framework N_{reg} is calculated from the Apparent Oxygen Utilisation (AOU) within a subsurface water parcel and an assumed ratio of nutrient to oxygen, $N : O$. AOU is a measure of the net change in oxygen concentration as a result of biological activity, both primary production and respiration, since the water parcel was last in contact with the surface. The presence of subsurface sources and sink processes within the iron cycle make this residual estimate of preformed iron from AOU redundant.

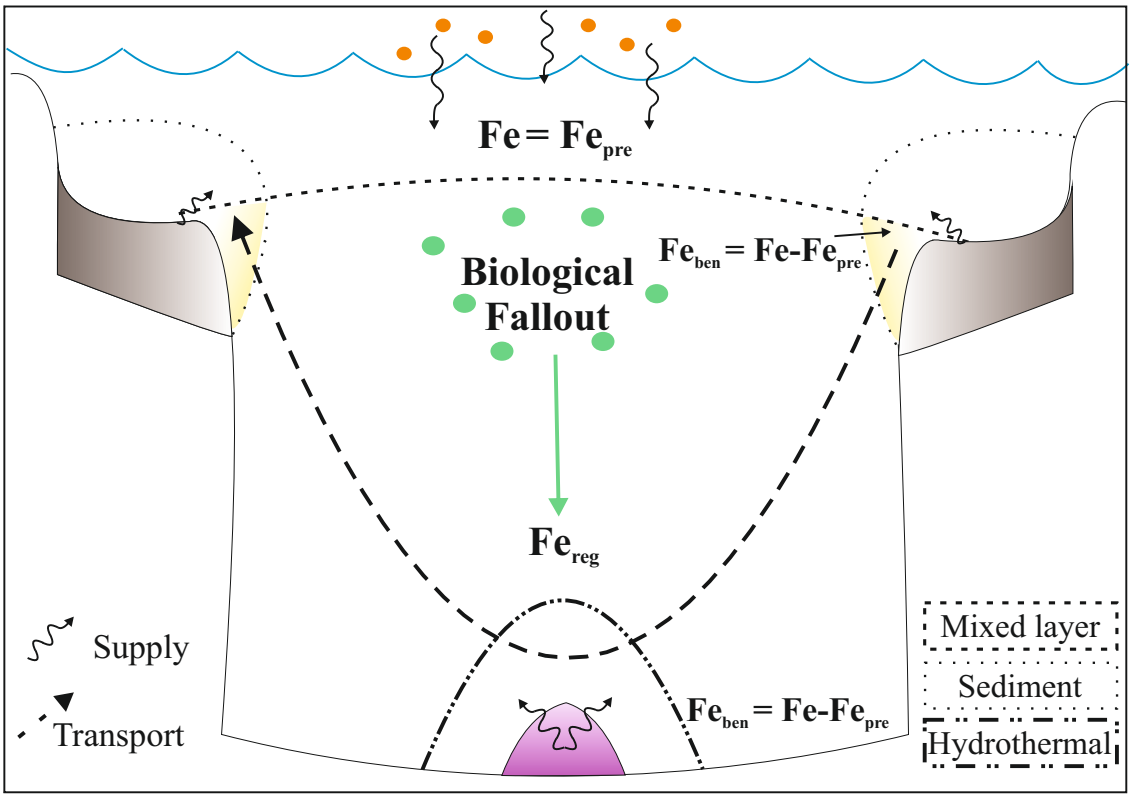

Figure 5.1: Schematic of a generic ocean basin illustrating the framework for investigating preformed iron

In this study we employ two new tracers that can be used to define the partitioning of iron into preformed and regenerated pools (figure 5.1). The framework for iron has five terms in (5.2), compared with two for a generic macronutrient (5.1). In addition to the traditional surface mixed layer preformed tracer, Fe_{pre} and the regenerated tracer, Fe_{reg}, there are the two known subsurface iron sources, Fe_{sed} and Fe_{hyd}, as well as the effect of particle scavenging, Fe_{scav}, which generally diminishes dissolved iron concentrations at all depths.

$$Fe = Fe_{pre} + \underbrace{Fe_{sed} + Fe_{hyd}}_{Fe_{ben}} + Fe_{reg} + Fe_{scav} \tag{5.2}$$

5.2.1.1 Mixed layer preformed iron

The preformed iron tracer, Fe_{pre}, is directly analogous to the traditional N_{pre}, and is defined as iron present in the surface mixed layer of the ocean. We assume that dissolved total iron (Fe_T) present in the surface mixed layer is

equivalent to Fe_{pre},

$$Fe_T = Fe_{pre}. \tag{5.3}$$

This tracer is the one truly passive tracer set out in this framework. The original theory of N_{pre} is built on the assumption that any nutrient that is present in the surface mixed layer is preformed. By definition any N_{reg} that returns to the surface mixed layer is instantly redefined as N_{pre}. Thus, Fe_{pre} depends on a number of processes. It consists of all iron sources to the surface mixed layer, including atmospheric, sedimentary and hydrothermal sources. Any regeneration of organic iron within the surface mixed layer is also labelled as Fe_{pre}. The tracer is therefore an indication of surface mixed layer iron concentrations, not indicative of a specific iron process or source.

5.2.1.2 Benthic source preformed iron

Two new quanities, the preformed sedimentary and hydrothermal tracers, Fe_{sed} and Fe_{hyd}, are implemented in a similar manner, but instead of the surface mixed layer acting as a trigger to define the preformed tracer we use localities where a subsurface or benthic iron source is encountered. The way that these sources are implemented in the model are similar and as a result it is convenient to consider them as a single pool, benthic-supply iron, Fe_{ben}. The preformed iron in the mixed layer has already been defined (5.2), so that automatically the preformed benthic iron is zero within the mixed layer, Fe_{ben} = 0. The benthic sources of iron are included at grid boxes below the mixed layer where either sediment or hydrothermal sources are present. If the sedimentary or hydrothermal supply of iron is greater than 0 then we define a benthic iron source (5.4), based on the difference between total dissolved iron, Fe_T, and Fe_{pre},

$$Fe_{ben} = Fe_T - Fe_{pre}. \tag{5.4}$$

The sum of the two subsurface source tracers must equal the net benthic iron at the source region (5.5):

$$Fe_{sed} + Fe_{hyd} = Fe_{ben}. \tag{5.5}$$

At these source regions, the partitioning of Fe_{ben} between the sedimentary and hydrothermal tracers is determined. The tracers are then transported in a conserved manner unless they come into contact with another benthic source or they return to the surface mixed layer. To calculate the partitioning of the two benthic sources we utilise the tendencies of the two tracers based on the iron sources in the model. This partitioning is done by assuming that these benthic tracers are independent of Fe_{pre}. Tendencies are defined and derived below, firstly differentiating (5.5) in time

$$\frac{\partial Fe_{sed}}{\partial t} + \frac{\partial Fe_{hyd}}{\partial t} = \frac{\partial Fe_{ben}}{\partial t}, \tag{5.6}$$

which are affected by transport and source regions,

$$\frac{\partial Fe_{sed}}{\partial t} = u.\nabla Fe_{sed} + S_{sed} \tag{5.7}$$

$$\frac{\partial Fe_{hyd}}{\partial t} = u.\nabla Fe_{hyd} + S_{hyd} \tag{5.8}$$

where S_{sed} and S_{hyd} are sedimentary and hydrothermal sources, and $u.\nabla Fe_{pre}$ is the divergence of advective fluxes for the iron tracer. This partitioning of Fe_{ben} is estimated from the rate at which each of the benthic sources, as defined in Chapter 4 Section 4.5, evolves if they were independent of each other. We assume that there is a proportional relationship between tracer concentration and tendency ($\frac{\partial}{\partial t}$), such that

$$Fe_{sed} \propto \frac{\partial Fe_{sed}}{\partial t}. \tag{5.9}$$

Thus, combining (5.6) to (5.9) gives

$$\frac{Fe_{sed}}{Fe_{ben}} = \frac{u.\nabla Fe_{sed} + S_{sed}}{u.\nabla Fe_{sed} + S_{sed} + u.\nabla Fe_{hyd} + S_{hyd}}, \tag{5.10}$$

which is used to calculated the fraction of Fe_{ben} that is sedimentary. Fe_{hyd} is inferred from 5.6,

$$Fe_{hyd} = Fe_{ben} - Fe_{sed}. \tag{5.11}$$

In this framework the definition of the surface preformed tracer supersedes all other tracer definitions. This choice means that in the surface mixed layer $Fe_{ben} = 0$, despite there being grid points where sedimentary and hydrothermal iron enters the mixed layer. This source of benthic iron is effectively lost to the Fe_{ben} tracer, and consequently Fe_{pre} is a tracer of resident surface iron.

5.2.1.3 Regenerated iron

The regenerated iron, Fe_{reg}, is analogous to regenerated macronutrient, N_{reg}, which is derived from AOU and the stoichiometric ratio between dissolved oxygen and the relevant nutrient. For N_{pre} this ratio is often assumed to be constant across the global ocean. The major problem here for iron is that the biological uptake ratio of iron to phosphate can vary significantly across different nutrient regimes. Sunda and Huntsman (1995); Twining et al. (2004); Strzepek et al. (2005) found observed iron to carbon ratios in phytoplankton ranging from 6 to 36, 2 to 19 and 1 to 50 $\mu molFe\ molC^{-1}$ respectively. This variance makes it very difficult to reliably calculate regenerated iron from observed AOU, because of the requirement for an accompanying Fe:P ratio of the organic matter. Within the model it is possible to diagnose an Fe:P ratio accompanying the traditionally diagnosed regenerated phosphate. The regenerated iron is diagnosed using the in situ ratios of iron to phosphate,$R_{Fe:P}$ and oxygen to phosphate, $R_{O:P}$, and AOU. Biological processes within the MITgcm are processed using phosphate before being scaled with $R_{Fe:P}$ to ascertain the effect on iron:

$$Fe_{reg} = AOU\ R_{P:O}\ R_{Fe:P}. \tag{5.12}$$

5.2.1.4 Scavenged iron

Scavenged iron, Fe_{scav}, is diagnosed as the difference between all of the other terms,

$$Fe_{scav} = Fe - (Fe_{pre} + Fe_{sed} + Fe_{hyd} + Fe_{reg}). \tag{5.13}$$

This quantity represents the amount of iron that has been transferred from the dissolved iron pool in to the particulate iron pool and lost to the system. Fe_{scav} represents a clear sink, acting to counterbalance the extra subsurface sources that are added to the iron pool.

The aim of quantifying scavenged iron is a key driver behind this work, enabling an insight into the role of scavenging between iron source and iron regeneration regimes. The explicit definition of the different preformed and regenerated pools will highlight the key drivers of the global iron distribution.

5.3 Initial Tracer fields

A new framework for the cycling of iron within ocean models has been formulated. This framework aims to improve our understanding of the balances of different iron sources and sinks within the ocean. Iron sources and their respective importance to the global iron cycle has been a topic that iron biogeochemists and modellers have strived to understand (Tagliabue et al., 2010; Elrod et al., 2004; Ye et al., 2011). Developing this iron partitioning framework provides additional information as to how the balance of transport, sources, regeneration and scavenging interact to produce the observed global iron distributions. The MITgcm is a model that is ideal for exploring the balance between these processes. The representation of the iron cycling and sources has been improved, see chapter 4, and is now ideal for testing the framework on decadal and millennial timescales. Initial comparison is made between the iron framework and its analogous tracers in the traditional preformed macronutrient framework (Figure 5.2) of Broecker (1974); Broecker et al. (1985).

5.3.1 Comparison between macronutrient and iron frameworks

The distribution of the two dissolved nutrients, iron and phosphate, are very different. The phosphate is dominated by phosphate-rich Antarctic

waters flowing northwards at intermediate and deep levels (figure 5.2b) within Antarctic Intermediate and Bottom Waters (AAIW and AABW). There is a stark contrast between the high concentrations in these water masses originating from the Southern Ocean, and the relatively nutrient-poor North Atlantic Deep Water (NADW). The North Subtropical Gyres exhibit low phosphate concentrations in the surface and down to 100m depth (Mather et al., 2008) compared to the South Atlantic subtropical gyre. The dissolved iron distribution, however, does not have the same structural differences as phosphate by water mass in the ocean interior. The one key exception is the very deep iron minimum in the South Atlantic that extends from the surface down to 1500m depth (Figure 5.2a).

The interior ocean iron concentrations are relatively uniform, at 0.6 to 0.7 nM. Patches of higher iron concentrations occur directly underneath the atmospheric dust plume in the Subtropical North Atlantic and around the sedimentary and hydrothermal sources in the Subpolar North Atlantic. As would be expected from these initial nutrient distributions, the distributions of N_{pre} for the two tracers also differ. The Fe_{pre} is dominated by the NADW signal, transporting unutilised iron from the North Atlantic southwards (Figure 5.2c). There are also elevated concentrations underneath the atmospheric dust plume at 20°N. Interestingly there is also evidence of iron being transported around the Southern Ocean and entering the Atlantic basin at depths between 500 and 1000m, there are subsurface sources of iron in the Southern Ocean upstream of the Atlantic Basin that are transported eastwards into the Atlantic. This suggests that iron supplies outside of the Atlantic Basin may affect on the iron regimes seen in the Atlantic. This NADW dominated transport of Fe_{pre} is in contrast to the Southern Ocean dominated distribution of P_{pre}^{mix} (figure 5.2d).

The starkest contrast between the two nutrients is seen in the distributions of the regenerated fraction. Fe_{reg} exceeds total dissolved iron concentration by 2-3 times in the ocean below regions that have a relative abundance of iron at the surface (figure 5.2e). Fe_{reg} is not an observable iron pool, it is more of a pseudo-concentration that is calculated from the cumulative regeneration

of iron within a particular parcel of water in the period since its subduction, corresponding to the consumption of oxygen. This pseudo-concentration gives a first indication of the magnitude of Fe_{scav}. Any excess of iron above total dissolved iron must be balanced by the removal, or remineralisation, of iron by particle scavenging and fallout. Phosphate in comparison does not have this same removal process, as a consequence the magnitudes of P_{reg} are smaller than for P_{pre}^{mix} (figure 5.2f).

5.3.2 Dominant balances within the iron framework

A more holistic view of the iron partitioning framework provides an estimate of the important factors determining the distribution of total dissolved iron. To first order the distribution seen throughout the Atlantic in the upper 2500m is dominated by Fe_{pre} (figure 5.2c). The majority of the features in dissolved iron are replicated in the traditional preformed tracer, with a few exceptions: the discontinuity of the plume of iron seen underneath the high surface iron concentrations in the Tropical Atlantic, the low preformed iron concentrations in the very deepest water, $>$2500m, and the isolated pockets of very high iron at 100 to 300m and 2000-2500m depth at 80°N.

The preformed sedimentary iron tracer (figure 5.3a) helps to explain the disconnect in the tropical iron plume, suggesting that despite the atmospheric deposition found in the Tropical North Atlantic, there is a significant impact from strong sediment sources to intermediate depths in this region. There is also a significant sedimentary source in the high latitude North Atlantic, which contributes to the high subsurface dissolved iron concentrations found in the model output. Fe_{hyd} is seen to have a significant contribution to deep ocean iron concentrations (figure 5.3c) contributing $\approx 0.4nM$ to the dissolved iron inventory of $\approx 0.6nM$ in much of the deep Atlantic. The isolated high dissolved iron concentrations seen at 2000-2500m at 80 °N is also explained through hydrothermal supply, though the relative concentration of Fe_{hyd} compared to Fe_{pre} is lower than the basin-wide signal seen in the very deepest waters. The distribution of iron in the Atlantic ocean can largely be explained by considering

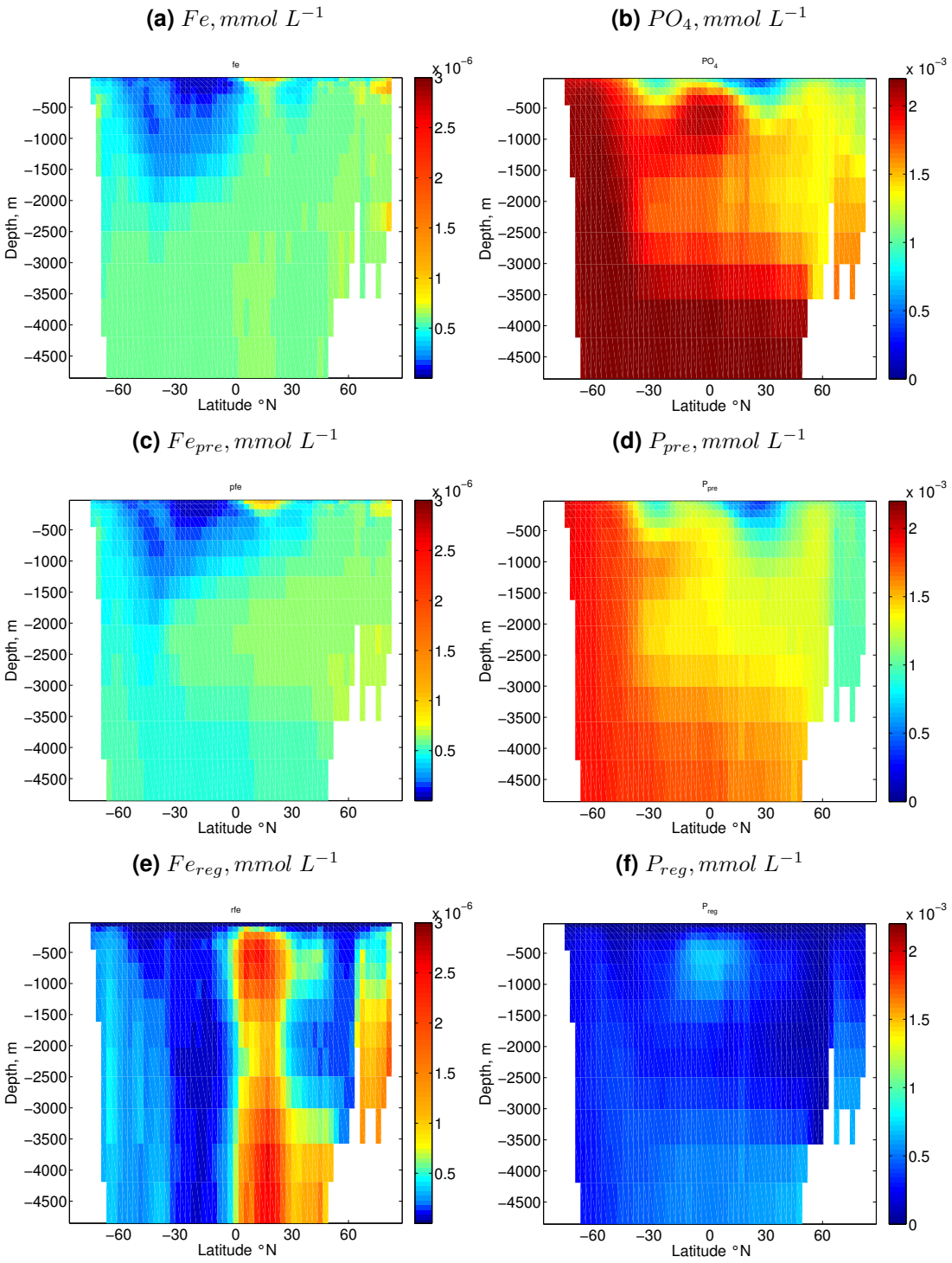

Figure 5.2: Atlantic zonal mean sections for Fe and PO_4 tracers

the distribution of the these iron sources.

However, regeneration and scavenging of iron are almost an order of magnitude greater than the other terms in this framework (figures 5.2e and 5.3d). This highlights the huge amounts of iron that are lost to particle

scavenging in both the deep and intermediate water. The similarity between the distribution of Fe_{reg} and $-Fe_{scav}$ implies a two-tier iron cycling system.

The lowest order balance of this system comprises the opposing processes of regeneration and scavenging. These processes can be large enough to dominate the distribution of dissolved iron concentrations, however these processes appear to cancel out: $Fe_{reg} \approx -Fe_{scav}$. As a result of this near-cancellation the dissolved iron distribution has very little imprint from Fe_{reg} or Fe_{scav}. The regeneration and scavenging of iron are closely linked due to their ultimate reliance on organic particle production. Regenerated iron is derived from this process via its connection to the AOU. AOU is largely determined by the remineralisation of organic particles. The scavenging process also relies on the presence of particulate material and lithogenic dust particles, however these dust particles are only important in the surface mixed layer. The close link between the regenerated and scavenged iron can be seen in plots of the sum of the two terms. A zonal mean shows that on the scales of the partitioned iron tracers the magnitude of the differences are very small (Figure 5.3b). Fe_{reg} is larger beneath the dust plume of the mid-Atlantic, but elsewhere Fe_{scav} is larger.

The next higher order balance involves the sources of iron and the transport from these sources setting the distribution of dissolved iron throughout the ocean basin. The framework shows that $Fe \approx Fe_{pre} + Fe_{sed} + Fe_{hyd}$. These two balances in the iron cycling act on completely different scales with the magnitudes of the tracers in the higher order balance approximately half those in the lower order balance (figures 5.2 and 5.3).

5.3.3 Caveats to the derived iron partitioning framework

The iron partitioning framework presented here is highly idealistic. The theory behind the framework is simply that any iron present in the surface mixed layer or a source region is labelled, and subsequently tracked throughout the model domain until it comes in contact with another source region or returns to the

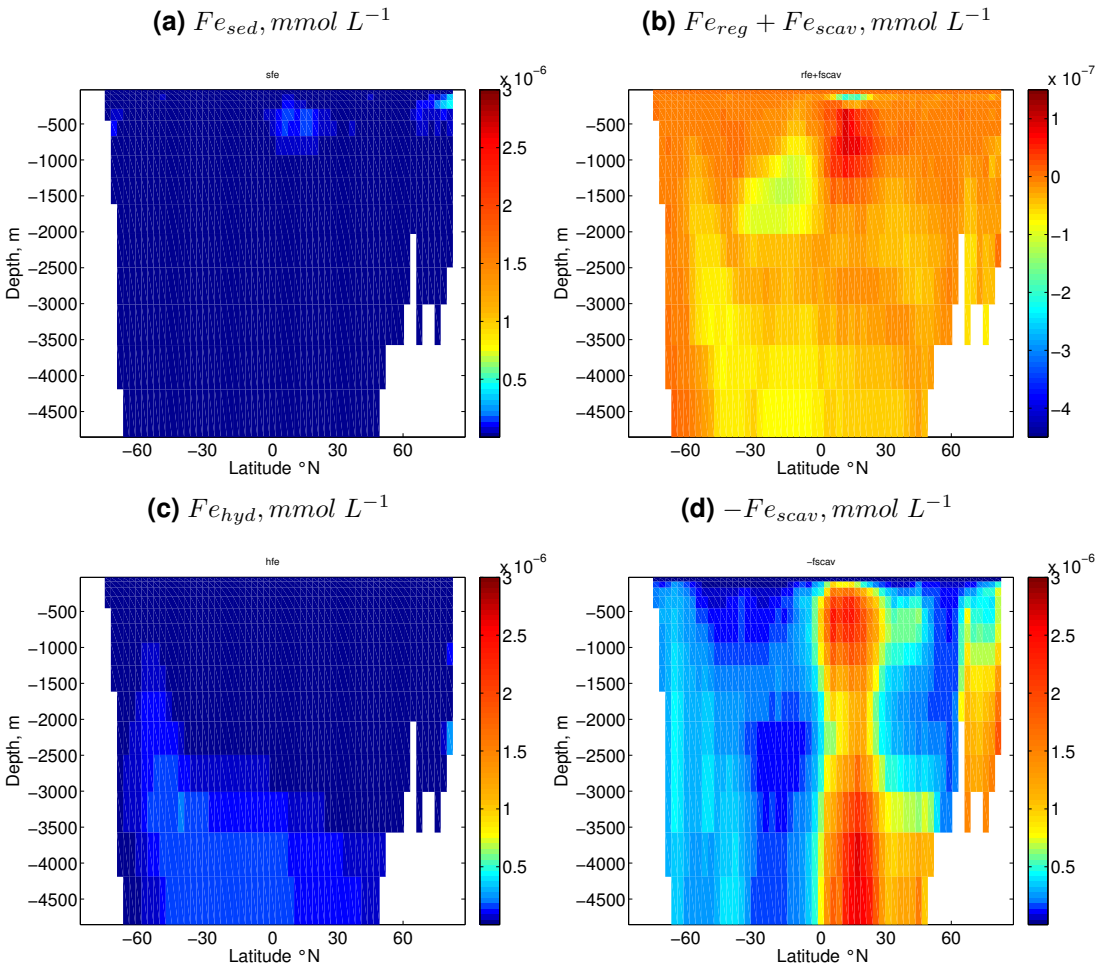

Figure 5.3: Atlantic zonal mean Sections of Benthic tracers and Fe_{scav}

surface mixed layer. The simplicity of the framework instantly creates a number of contradictory definitions. The first being that any benthic sources that enter into the mixed layer are ”lost” from the benthic iron tracers to the preformed iron tracer. This is unfortunate, but is necessary to conserve mass within the framework. The consequence of this is that sedimentary and hydrothermal sources are occasionally pooled into the preformed tracer. A similar problem arises from the balances for regeneration and scavenging, which both occur within the mixed layer and within the grid boxes into which subsurface supplies are made. Again, these quantities are lost from the regenerated and scavenged iron tracers to the preformed, sedimentary and hydrothermal tracers. We assume that the losses are negligible when considering the volume of the entire model domain. However, it is important to bear in mind that there is a bias towards reducing the magnitude of scavenging and regeneration

because of this overlap of the source regions into the biogeochemically active water column.

One of the key limitations of the framework is its reliance on a residual calculation to estimate the size of the scavenged iron tracer. This calculation may lead to an inherent cancellation of the regeneration term by the scavenging term by default. To address this potential weakness of the framework a calculation of the actual remineralisation and scavenging rates produced by the model is made. Total remineralisation rate of 1.4 x 10^{10} $mol\ yr^{-1}$ is nearly balanced by the total scavenging rate of 1.3 x10^{10} $mol\ yr^{-1}$, supporting the validity of the inferences made using the framework.

5.3.4 Implications for the observational community

These initial outcomes of the new iron framework has interesting implications for the observational community. Although the model environment purposely restricts the complexity of the system there are still important points to be made. The distribution of the total dissolved iron is strongly controlled by atmospheric and sedimentary supplies into the mixed layer,(Fe_{pre}) and hydrothermal iron sources into the bottom waters (Fe_{hyd}). Subsurface supplies from sediments are also important (Fe_{sed}). Although there is work stating the importance of remineralisation of organic matter to provide regenerated inorganic iron (Hutchins et al., 1993), this framework suggests that due to the coupling of the biological processes and particle scavenging processes this regeneration is often negated by removal of dissolved iron by scavenging. This cancellation means there must still be an iron source in order to balance the iron budget.

Chapter 3 of this thesis presented some work aiming to quantify the magnitudes of particle scavenging rates in the ocean. The initial results of this framework suggest there is a potential to quantify scavenging removal by using the coupling of regenerated iron and scavenging, $Fe_{reg} \approx -Fe_{scav}$. In comparison to the technical aspects of directly measuring and calculating

specific adsorption, desorption and fallout fluxes for a particular station, the use of the assumption that Fe_{reg} and Fe_{scav} are magnitudinally equivalent can provide a quick estimate of the scavenging regime.

5.4 Summary

The development of the iron partitioning framework illustrates the difference between preformed iron and phosphate. The preformed tracers are a direct response to the concentrations of each respective nutrient in the mixed-layer. In addition to this, the iron preformed tracer is significantly augmented in shallow subsurface water by the supply of iron from continental shelf sediments.

Traditionally the phosphate preformed tracer is strongly controlled by residual phosphate concentrations in the Southern Ocean subduction zones, resulting in high preformed phosphate associated with Antarctic Intermediate Water and Antarctic Bottom Water.

Iron is found to be strongly related to waters subducted in the North Atlantic. The water here is strongly augmented with sediment sources beneath the surface to produce a strong signal of preformed iron in the North Atlantic Deep Water.

The new tracers defined, sedimentary (Fe_{sed}), hydrothermal (Fe_{hyd}) and scavenging (Fe_{scav}), produce two important balances within the framework:

1. The first order basin-wide distribution of iron is strongly determined by iron source supply to the mixed layer, i.e. Fe_{pre}. Hydrothermal and sedimentary subsurface supplies augment Fe_{pre} to diagnose an approximation of Fe; $Fe \approx Fe_{pre} + Fe_{sed} + Fe_{hyd}$.

2. While Fe_{reg} and Fe_{scav} can be 5 x larger than the other tracers, they effectively cancel out, $Fe_{reg} \approx -Fe_{scav}$. The cancellation of these terms means that there is very little imprint of regenerated iron onto the total

dissolved iron distributions. However this is likely to be sensitive to assumptions made regarding Fe_{scav}.

The strong relationship between Fe_{reg} and Fe_{scav} is an important balance. The mismatch between these terms determines whether regenerated iron influences Fe_T and understanding this mismatch is key to elucidating the iron process drivers behind the total iron distribution.

This framework also provides support for using indirect observational methods to determine the magnitude of scavenging in the open ocean. The measurement of regenerated iron in ocean data samples can provide a first order estimate of the magnitude of iron scavenging. This assumption can be true to varying degrees of accuracy, however modelling of Fe_{reg} and Fe_{scav} using the iron partitioning framework can inform observationalists on the suitability and error of their estimates.

Chapter 6

Sensitivity of the Preformed Iron Framework

6.1 Introduction

Following the improvements made to the MITgcm in chapter 4 and development of the preformed framework for iron in chapter 5, this chapter aims to present the sensitivities of the model and framework to a large range of parameter perturbations. This goal represents a key aim of the thesis, to elucidate the driving factors behind the distribution and cycling of iron in the global ocean. Using the outcomes of chapter 5, three key questions are focussed on:

1. How do the different mechanisms of iron supply determine the preformed iron tracer concentrations, which subsequently set the basin-scale distribution of total dissolved iron?
2. Why is the regenerated iron, Fe_{reg}, imprint on the total dissolved iron distribution so small?
3. How does the traditional macronutrient preformed and regenerated framework compare with the new iron framework?

The model control run revealed that $Fe \approx Fe_{pre} + Fe_{sed} + Fe_{hyd}$. The sensitivity studies address how the different processes adjust the relative importance of these three tracers. In particular, the apparent lack of importance attributed to Fe_{sed}, despite the numerous studies emphasising the importance of sediment sources (Elrod et al., 2004; Lam et al., 2012; Tagliabue et al., 2014). The initial model spin-up also revealed a near cancellation of Fe_{reg} and Fe_{scav}, suggesting that recycling and scavenging of iron does not strongly affect the observed interior iron distributions, despite the magnitude of the terms involved being up to 5 x greater than seen for the preformed tracers. Their large magnitudes imply that if these two processes are significantly out of balance the potential for substantial changes to the iron distribution. As a consequence of this partial cancellation, the majority of the ocean does not see an imprint of regenerated iron through opposing contributions from scavenging across the basin. This partial cancellation is explored to reveal why there is an absence of a signal from excess regenerated iron. In addition, differences between the phosphate and iron preformed framework are addressed in order to understand the differences between the two tracers.

6.2 Method and Approach

A total of 44 experiments are integrated, aimed at assessing the sensitivity of the iron closure and new iron partitioning framework, defined in chapter 5, to a range of parameter perturbations. The chosen parameter perturbations were chosen to test the sensitivity of the iron cycle to alterations in the model. These experiments provide insight into the drivers behind the modelled iron distributions and iron framework diagnostics.

The model used for these sensitivity experiments is described in detail in chapter 4. The model runs were integrated for 500 years in order to allow the model to reach a state close to equilibrium in the Atlantic Ocean Basin. After 500 years the maximum yearly drift in atmospheric CO_2 concentration found across the suite of experiments was less than 7.5 ppb, or a percentage

Table 6.1: Table detailing sensitivity experiments carried out, each model run has a positive and negative perturbation, except for runs 4, 5 and 22 which are source turned off and variable Fe:P removed. The symbols represent the groupings of experiments: ◯ = Sources, □ = Scavenging, ▽ = Speciation, ◇ = Biological processes, △ = Stoichiometry, ▷ = Transport via wind speed perturbations and ∗ = Control.

Run	Symbol	Process	Parameter	Units	Default Value	Range of perturbation
1	◯	Aeolian Source	Iron Solubility, $alpfe$	%	1	$\pm 50\%$
2	◯	Sediment	Shelf Flux, $SedIn$	$nMFem^{-2}d^{-1}$	2	$\pm 50\%$
3	◯	Hydrothermal	Fe:^{3}He, $HydIn$	$mol\ mol^{-1}$	4×10^6	$\pm 50\%$
4a	◯	Aeolian Source	$alpfe$	%	1	OFF
4b	◯	Benthic Sources	$SedIn$, $HydIn$	-	-	OFF
5a	◯	Sediment	$SedIn$	$nMFem^{-2}d^{-1}$	2	OFF
5b	◯	Hydrothermal	$HydIn$	$mol\ mol^{-1}$	4×10^6	OFF
6	□	Scavenging	"Background", K_{sc0}	d^{-1}	0.0031	$\pm 50\%$
7	□	Scavenging	Biogenic, K_{scb}	$\mu MPOC^{-1}d^{-1}$	0.005	$\pm 50\%$
8	□	Scavenging	Dust, K_{scd}	$molFe^{-1}m^2$	120	$\pm 50\%$
9	□	Coagulation	Turbulent DOC, $a1$	$mM^{-1}d^{-1}$	3.7×10^{-4}	$\pm 50\%$
10	□	Coagulation	Turbulent POC, $a2$	$\mu M^{-1}d^{-1}$	1.02×10^{-4}	$\pm 50\%$
11	□	Coagulation	Brownian POC,$a3$	$\mu M^{-1}d^{-1}$	5.095×10^{-2}	$\pm 50\%$
12	□	Coagulation	Brownian DOC, $a4$	$mM^{-1}d^{-1}$	0.114	$\pm 50\%$
13	▽	Total Ligand	L_T	nM	0.6	$\pm 50\%$
14	▽	Lig. Stab. Const.	K_{FeL}	$mol\ mol^{-1}$	10^{12}	10^{11}, 10^{13}
16	◇	Phos. Half-Sat	K_{PO_4}	mM	5×10^{-4}	$\pm 50\%$
17	◇	Iron Half-Sat	K_{Fe}	mM	1.2×10^{-7}	$\pm 50\%$
18	▽	Max Fe'	$freefemax$	nM	2	
19	◇	Bio Activity	α	mMd^{-1}	5.5×10^{-4}	
20	△	Fe:P Minimum	FP_{min}	$mMFe\,mMP^{-1}$	1.18$\times 10^{-4}$	$\pm 50\%$
21	△	Fe:P Maximum	FP_{max}	$mMFe\,mMP^{-1}$	47.2 $\times 10^{-4}$	$\pm 50\%$
22a	△	Var. Fe:P OFF	FP_{min}, FP_{max}	$mMFe\,mMP^{-1}$	1.18-47.2 $\times 10^{-4}$	4.68 $\times 10^{-4}$
22b	△	Var. Fe:P OFF	FP_{min}, FP_{max}	$mMFe\,mMP^{-1}$	1.18-47.2 $\times 10^{-4}$	9.36 $\times 10^{-4}$
23	▷	Transport via wind speed	τ_x, τ_y	$m\ s^{-1}$	variable	$\pm 50\%$
15	∗	CONTROL	-	-	-	-

change of 0.026%. Maximum yearly drifts in annual mean PO_4 and Fe concentrations were less than 0.002% and 0.03% respectively. These runs were initialised from a 5000 year control model spin-up. Table 6.1 provides details of the processes and their associated parameters, along with the perturbations and adjustments made for each run. Along with the definition of the sensitivity studies, the individual experiments are grouped with process

parameters that are similar. This results in the creation of 6 groups of experiments addressing the importance of sources, scavenging processes, speciation, biological processes, stoichiometry choices and transport:

- Source experiments involve removal of and $\pm$50% perturbations in the supply of iron from the three sources; atmospheric dust supply, sedimentary supply and hydrothermal vent supply.
- The scavenging experiments involved $\pm$50% perturbations of the rates of background scavenging (K_{sc0}), biogenic particle scavenging (K_{scb}) and lithogenic particle scavenging (K_{scd}), as well as turbulent and brownian coagulation of dissolved and particulate organic matter ($a1, a2, a3, a4$).
- The speciation experiments perturbed the total ligand concentration ($[L_T]$) and the maximum free iron limit ($freefemax$) by $\pm$50%, and increased and decreased the ligand stability constant (K_{FeL}) by an order of magnitude.
- The biological processes perturbed were the iron (K_{Fe}) and phosphate (K_{PO_4}) half-saturation coefficients and biological community consumption rate (α); these processes were adjusted by $\pm$50%.
- Following the inclusion of the variable $Fe : P$ ratio within the model, stoichiometry perturbation experiments were conducted; the maximum (FP_{max}) and minimum (FP_{min}) prescribed limits for $Fe : P$ were perturbed by $\pm$50% and two runs with constant ratios set to the original model default value (4.68$\times 10^{-4}$ $molFe\ molP^{-1}$), and double the default value.
- Transport experiments were run using $\pm$50% perturbations in the global windstress (τ_x, τ_y). These groupings are used to aid identification of key drivers of variation for particular tracer concentrations or model diagnostics.

The model experiments were analysed using a variety of plots. Initial analysis was carried out using variable-variable scatter plots to reveal the experiments which have the greatest effect on the model output. The experiments that were

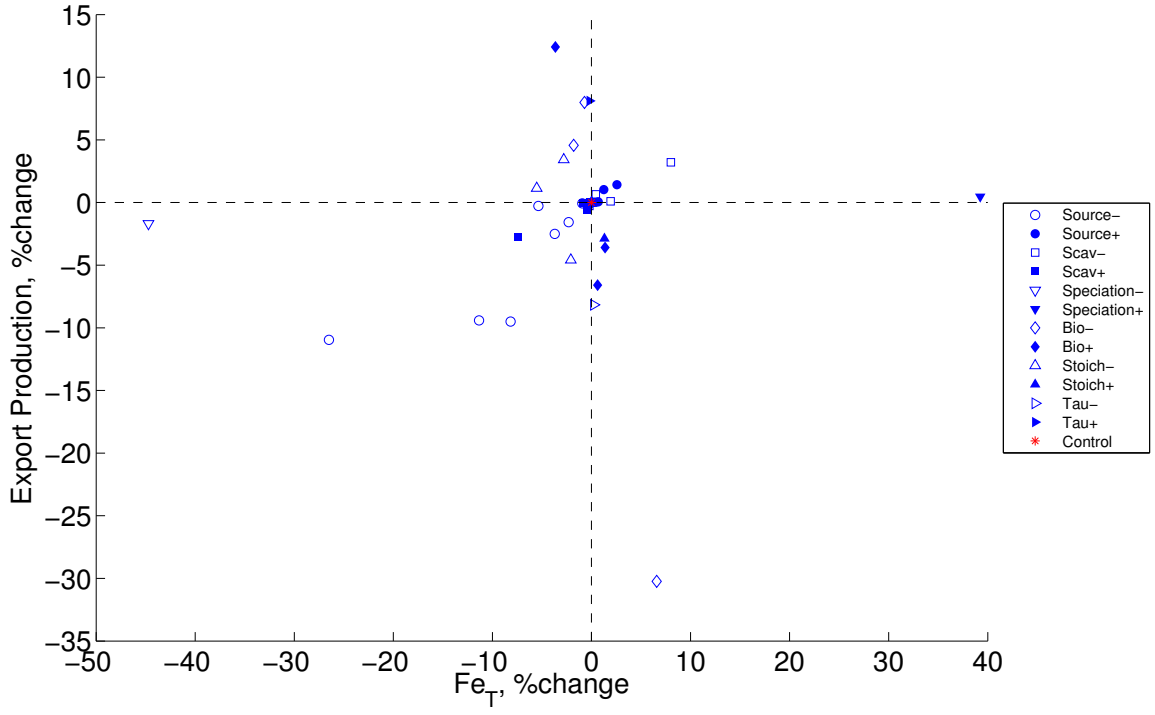

Figure 6.1: Scatter plot of all sensitivity experiments showing percentage change of Fe_T and Atlantic integral export production from the control

deemed as important in order to analyse specific aspects of the model output were selected and examined using zonal depth mean plots to understand latitudinal variation between the control and the experiments. Further, some of the experiments were explored using zonal mean meridional sections of tracer distributions and anomalies from the control run.

For some aspects of the following analysis, comparisons were made of the responses of Fe_{reg} and Fe_{scav} to the experiments. The sum of these two tracers gives an indication of which of the processes is dominant, in effect determining whether the system is in a regime of net regeneration or net scavenging. For this choice we define "Regeneration excess", Reg_{ex}, which represents the mismatch between regeneration and scavenging, thus giving an indication of the imprint of regenerated iron on total dissolved iron concentrations,

$$Reg_{ex} = Fe_{reg} + Fe_{scav}. \tag{6.1}$$

6.3 Results and Discussion

6.3.1 Impact on total dissolved iron

The experiments and their effect on Atlantic mean total dissolved iron concentration and Atlantic-integral export production are shown in Figure 6.1. Source and speciation perturbations have a strong effect on total dissolved iron concentrations, in contrast biological parameters,transport and s source perturbations all have an effect on export production.

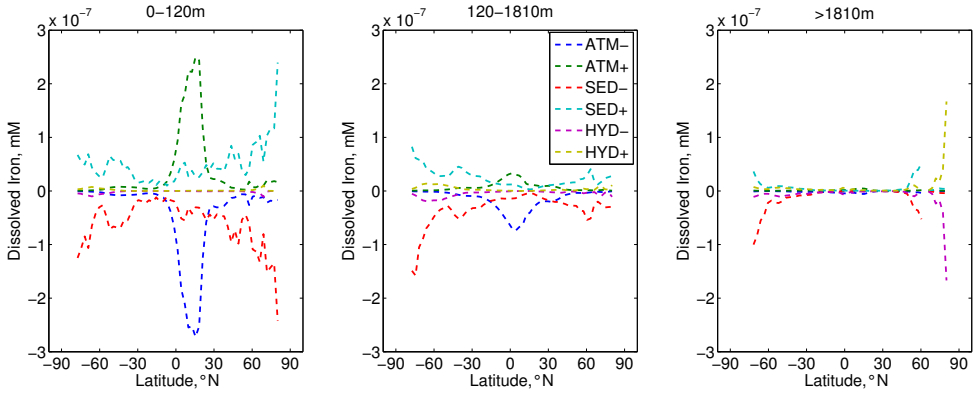

Figure 6.2: Zonal mean plots of Fe_T anomalies from the Control run at three depths for the source experiments. From Left to right plots show zonal mean values for the upper 120m, 120-1800m and $>$1800m. Lines represent -50% and +50% perturbations for the three sources of iron, Atmospheric (ATM), Sedimentary (SED) and Hydrothermal (HYD).

Turning to the key experimental groups, the atmospheric iron supply has a major impact on mean iron concentrations between 0 and 20°N, causing anomalies of $\pm$ 0.25 nM depending on whether the iron solubility is halved or doubled (Figure 6.2). At low latitudes in the surface the benthic sources have little effect. The sedimentary source have greater impact at high latitudes in the surface, as well as at the intermediate depth level. The anomalies in the deep waters are very small with the exception of an isolated hydrothermal source in the far north of the Atlantic add a weak signal in the sedimentary experiments in the Southern Ocean.

The speciation experiments reveal a generally weak response from the 6 experiments, apart from perturbations to $[L_T]$. The surface response of Fe_T

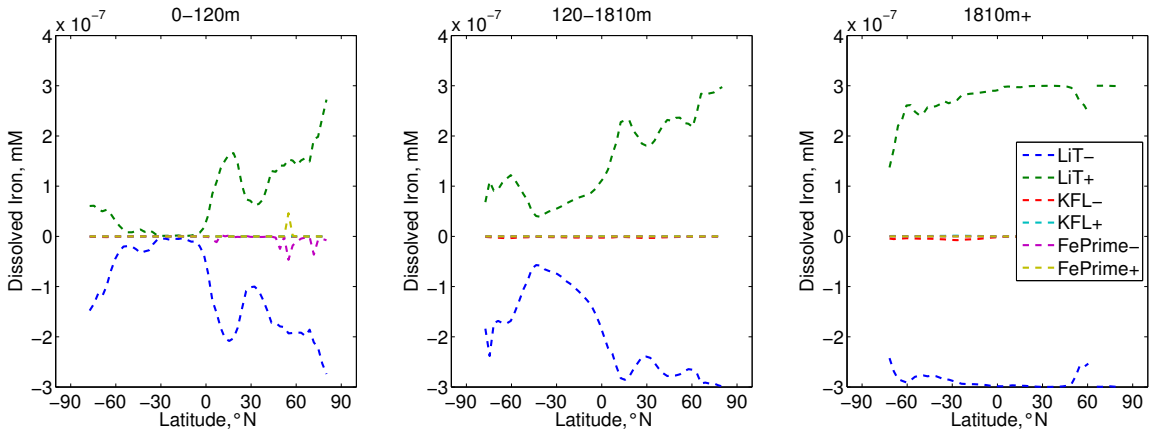

Figure 6.3: Zonal-depth mean plots of Fe_T anomalies from the Control run at three depths for the speciation experiments. From Left to right plots show zonal-depth mean values for the upper 120m,120-1800m and +1800m. Lines represent -50% and +50% perturbations for the $[L_T]$ and .

to changes in $[L_T]$ are strongest in the North Atlantic (Figure 6.3). Increasing $[L_T]$ leads to an increase in Fe_T as the extra ligand interacts with free iron to retain iron in the dissolved form. The opposite occurs for decreasing $[L_T]$. The anomalies for the $[L_T]$ experiments reach maximum absolute values of 0.3 nM in the sub polar region of the North Atlantic. An increase in Fe_T in the Southern ocean is also seen, with anomalies of -0.15 and 0.05 for the decrease and increase in $[L_T]$ respectively (Figure 6.2). A very similar pattern is seen in the intermediate waters with a strong latitudinal response for both experiments. The absolute anomalies are at a minimum in the South Atlantic subtropical gyre, increasing North and South of this region. Absolute anomalies reaching 0.3 nM in the high latitude North Atlantic. The centering of this anomaly about the subtropical gyre of the South Atlantic is due to the very low concentrations of Fe_T. Increasing or decreasing $[L_T]$ has relatively little effect. The response in the deep waters is much more homogenous with absolute anomalies of between 0.25 and 0.3 nM throughout the Atlantic.

The strong latitudinal and depth dependence of response of Fe_T to changes in $[L_T]$ suggests that these changes may be driven by direct effects on the Fe_T in the surface water-mass formation regions. The response in these regions, and their subsequent subduction and transport, leads to a downstream response in Fe_T distributions across the basin (Figure 6.4). It is unclear whether the direct

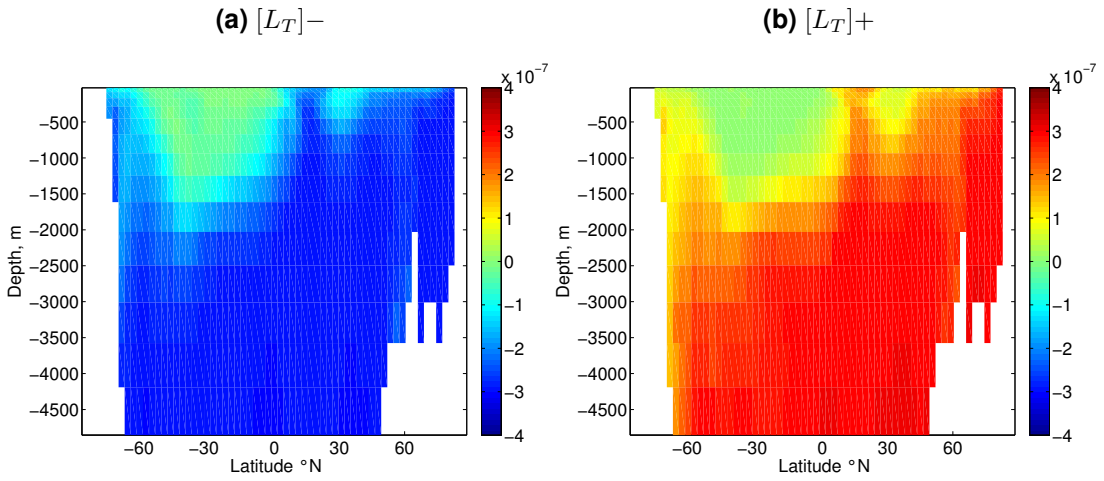

Figure 6.4: Meridional section of Fe_T ($mmol\ L^{-1}$) anomalies for total ligand concentration experiments

effects of source perturbations in the surface mixed layer Fe_T concentration are responsible for the responses seen in the zonal depth mean diagnostics. The indirect effects of these perturbations, such as alterations to export production and remineralisation distribution, are important and illustrate the value in the iron partitioning framework, results of which are covered later in this thesis.

The anomalies in the export production for the source experiments reveal how intricate the response can be. The response of export production to the atmospheric perturbations is straightforward. A reduction in the supply of iron to the surface mid-Atlantic results in a decrease in export production in the same region (Figure 6.5). An increase of atmospheric supply increases export production. It is clear that the atmospheric supply of iron controls biological activity in the mid-Atlantic in the model. The alterations made to the biological activity are reflected in export production and subsequent regeneration of exported organic material. The export production anomaly is consistent with the anomalies of total iron in the surface and intermediate waters (Figure 6.2). The sedimentary source perturbation experiments have a similar effect, decreasing and increasing export production with decreased and increased sedimentary source, but the location of the export production anomalies are focussed more on the South Atlantic and Southern Ocean.

Elucidating the drivers of Fe_T distribution changes for the experiment groups

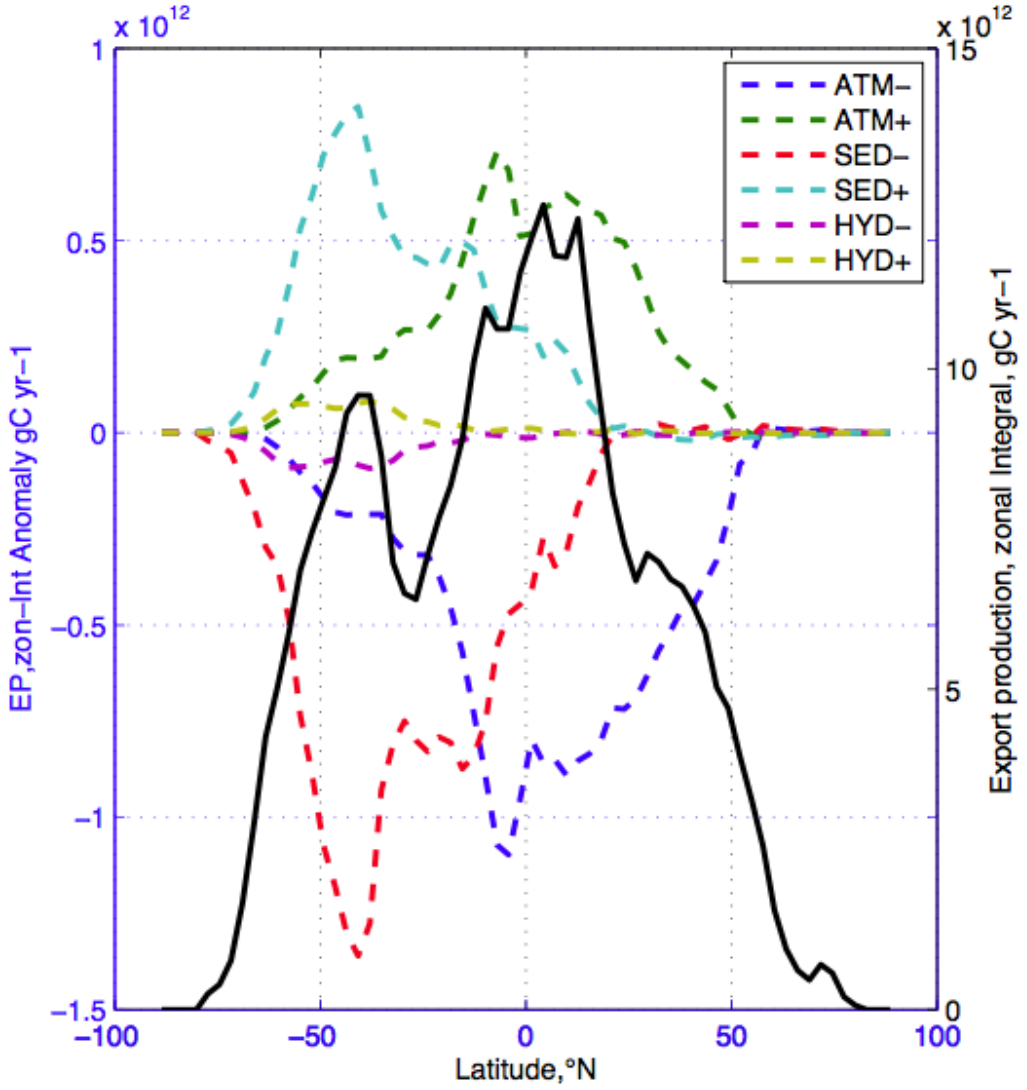

Figure 6.5: Zonal-depth mean plots of Fe_T anomalies from the Control run at three depths for the source experiments. From Left to right plots show zonal-depth mean values for the upper 120m,120-1800m and +1800m. Lines represent -50% and +50% perturbations for the three sources of iron, Atmospheric (ATM), Sedimentary (SED) and Hydrothermal (HYD).

is not straightforward. Looking at the zonal depth mean anomalies of Fe_T and the zonal mean export production provides limited analysis. It is necessary to further analyse the responses using the iron partitioning framework to better understand the drivers behind the iron cycle responses to these perturbations.

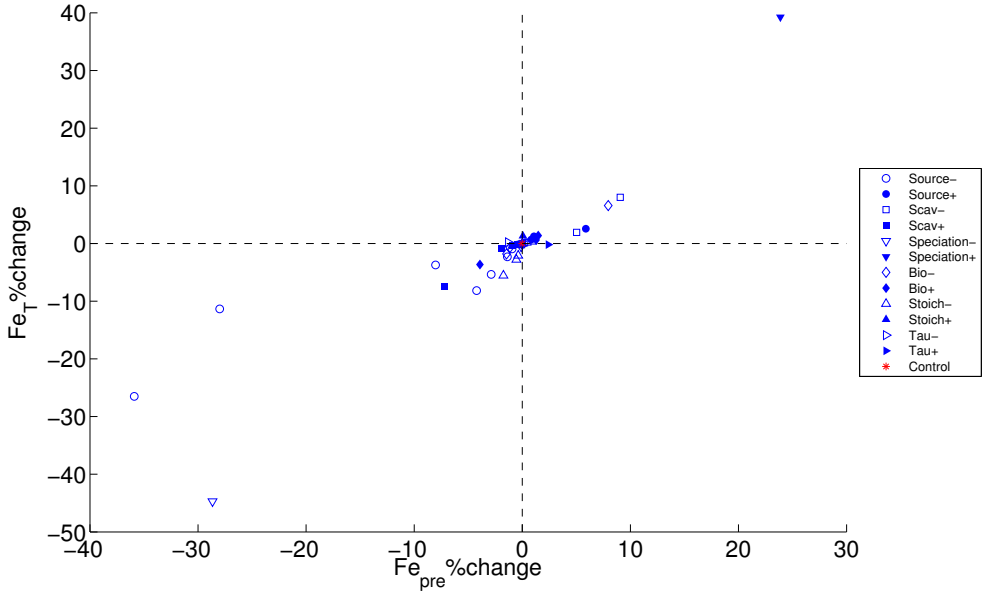

Figure 6.6: Scatter plot of all sensitivity experiments showing percentage change of Fe_T and Fe_{pre} from the control

6.3.2 What controls preformed iron?

The iron framework in Chapter 5 provides a new technique for understanding how the iron system is controlled in the oceans. From the control simulation discussed in Chapter 5, there are two balances that dictate the distribution of iron and magnitude of iron cycling:

- Total distribution is dictated by the distribution of preformed iron tracers, $Fe \approx Fe_{pre} + Fe_{sed} + Fe_{hyd}$.
- Regnerated iron and scavenging are approximately equivalent and to first order cancel out, $Fe_{reg} \approx -Fe_{scav}$.

. Here, the processes that have been found to be important for the partitioning of the preformed iron tracers are identified and explored using a combination of basin mean scatter plots, zonal-depth mean line plots and zonal mean sections.

As measured by percentage changes in $[Fe_T]$ and Fe_{pre}, the iron partitioning is most sensitive to reductions in iron sources and speciation changes (Figure

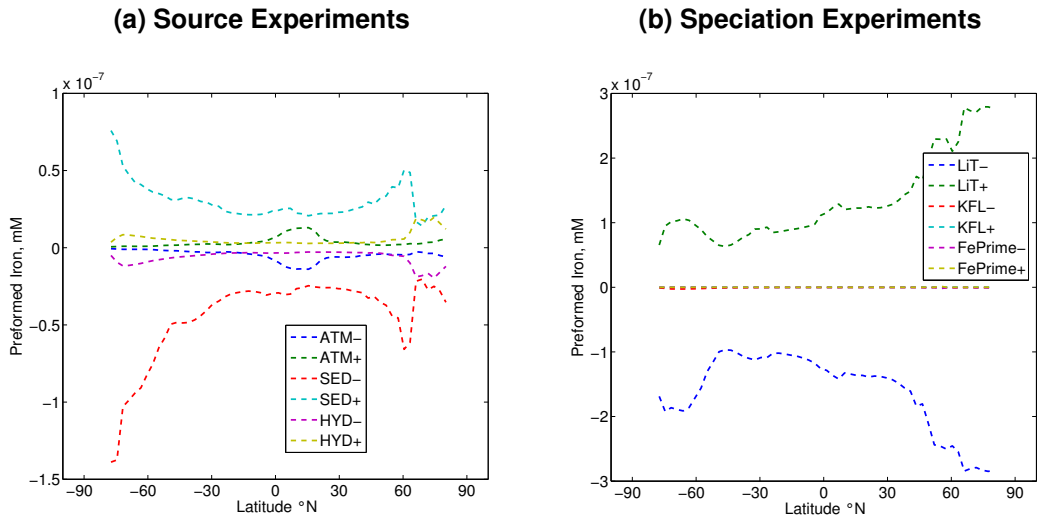

Figure 6.7: Zonal-depth mean plots of Fe_{pre} anomalies from the Control run for source and speciation experiment subsets.

6.6). Most of the other sensitivity tests perturb these output variables by less than 10%. Accordingly we focus on the effects of removing, decreasing and increasing the sources and the alteration of total ligand concentrations.

Zonal depth mean Fe_{pre} anomalies vary with latitude. Perturbation in the aeolian iron supply provides a small localised effect between 0 and 20°N (Figure 6.7a). Larger impacts on the Fe_{pre} occur over the entire basin from the perturbation of sedimentary iron supply rates. Anomalies in Fe_{pre} from the sediment supply experiments are particularly large in the high latitudes, illustrating that a major fraction of Fe_{pre} originates from sedimentary supply. The effect of total ligand concentration also significantly affects the Fe_{pre} concentrations, with a latitudinal dependence reflecting the subduction of Fe_{pre} and subsequent transport as North Atlantic Deep Water (Figure 6.7b).

Meridional sections further illustrate the effect of these iron source perturbation experiments, as well as providing a reference point for experiments altering the total iron-binding ligand concentrations, $[L_T]$. The cessation of atmospheric supply provides a significant, but localised, reduction of Fe_{pre} (Figure 6.8a) by 0.4 nM in the surface of the North Atlantic subtropical gyre. There is a greater integrated basin-wide effect from perturbation of the sediment supply. Turning off sedimentary supply reduces Fe_{pre} by 0.2 nM over the majority of the North

Atlantic Deep Water. A comparable reduction occurs in the Antarctic Bottom Water with the greatest reductions in the upper 1000m of the subpolar regions of the Atlantic (Figure 6.8b). The halving and doubling of sedimentary supply (Figures 6.8c and 6.8d) reveals its importance for Fe_{pre} via the supply to the mixed layer in high latitude, deep-water formation regions.

The sensitivity of Fe_{pre} to $[L_T]$ is also mechanistically related to these high-latitude deep-water formation regions. The iron system removes excess unassociated iron ions above the total ligand concentration through the joint processes of particle scavenging and precipitation. The Fe_{pre} concentrations are then set by the amount of ligand available in the mixed-layer in regions of subduction. When $[L_T]$ is reduced, there is accordingly a reduced amount of Fe_{pre} that can be subducted along with the dense water masses. Conversely, when $[L_T]$ is increased more Fe_{pre} is subducted and transported. The magnitudes of these anomalies linked to sediment perturbations are of a similar order to the cessation of sedimentary supply. There is only a small contribution of Fe_{sed}, however this inference depends on the attribution of sediment supplied iron to the Fe_{pre} pool.

6.3.3 What controls the regeneration imprint?

One of the key findings from the application of the iron framework is the absence of an imprint of regeneration of organic iron in total dissolved iron distributions. The ability of the system to regenerate organic iron in excess of the scavenging process is indicated by the regeneration excess, $Reg_{ex} = Fe_{reg} + Fe_{scav}$. If Reg_{ex} is positive, there is net regeneration of organic iron in excess of scavenging. Conversely, if Reg_{ex} is negative, the scavenging process exceeds regeneration. Another way to view the the Reg_{ex} concept is to use the ratio of the two tracers, $\frac{Fe_{reg}}{-Fescav}$, as an indicator of which of the two terms is the larger.

For the control run, there is excess regeneration, i.e. $Reg_{ex} > 0$, below regions of strong biological activity, such as in the mid-latitude Atlantic beneath the area

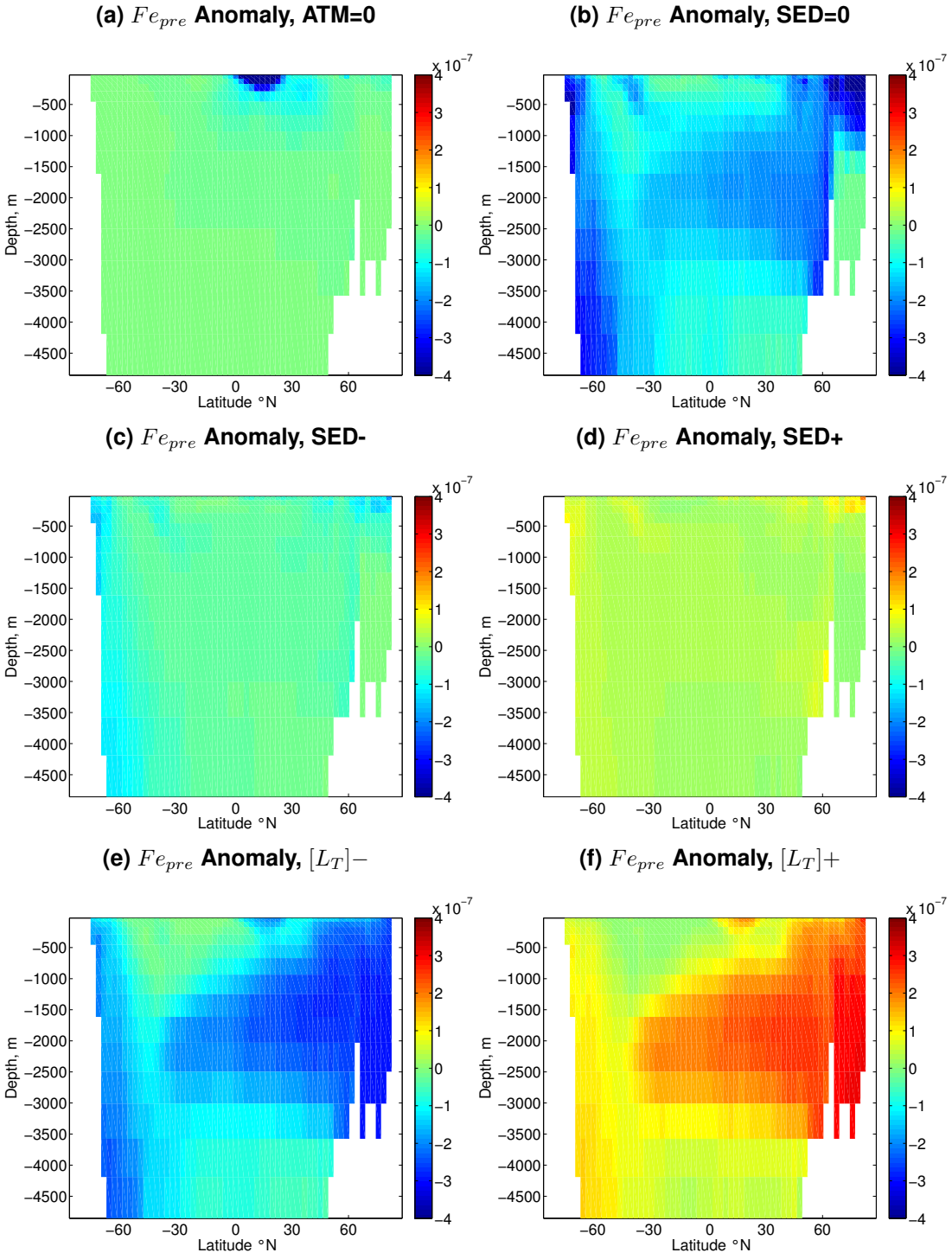

Figure 6.8: Meridional section of Fe_{pre} anomalies ($mmol\ L^{-1}$) for Atmospheric and sediment source and total ligand concentration experiments

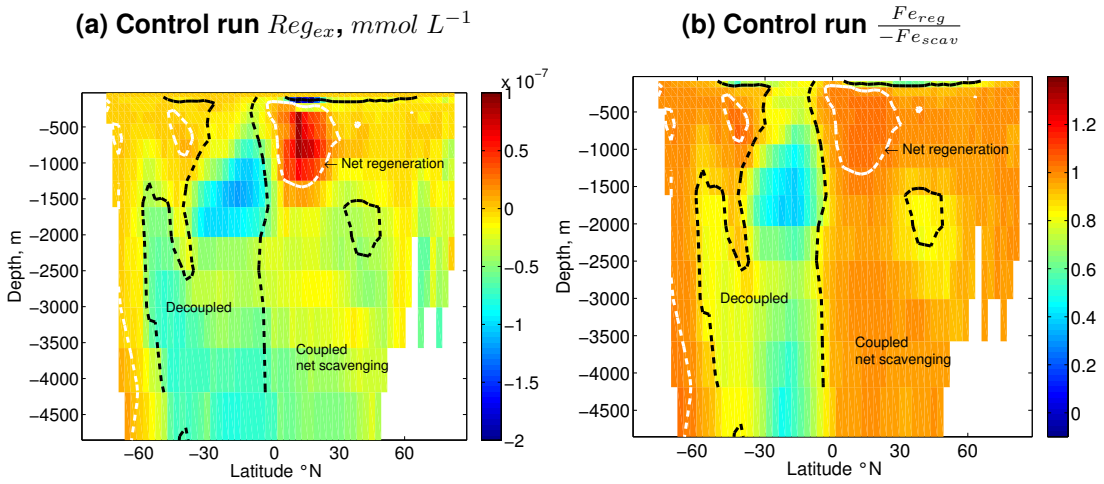

Figure 6.9: Meridional mean sections of Fe_{reg} and Fe_{scav} diagnostics from the control run, dashed white line indicates boundaries of "net scavenging" and "net regeneration" regimes. i.e $Reg_{ex} < 0$ are "net scavenging" regimes and $Reg_{ex} > 0$ are "net regeneration" regimes. The white dashed lines as a boundary between net scavenging and net regeneration regimes will be used in subsequent figures.

of high dust deposition (Figure 6.9a). Imprints of regeneration also occur in the deep water, such as the Antarctic Bottom Water in the South Atlantic. There is a bias towards negative Reg_{ex} in regions where the regeneration of organic iron is not as strong, such as beneath the subtropical gyre of the South Atlantic.

The imprint provided by Reg_{ex} is by definition sensitive to two main factors, Fe_{reg} and Fe_{scav}, which are themselves controlled by a range of processes and model parameters.

Fe_{reg} is sensitive to the biological stoichiometry, which affects the amount of inorganic iron that is fixed into organic material prior to export. The magnitude of export production also has a control on the overall amount of iron that is regenerated. There are a number of processes that can control these two aspects of the iron cycle. Source perturbations can affect the biological consumption of nutrients, as well as altering the saturation of organic ligand by changing Fe_T.

Fe_{scav} will be sensitive to three process, the first two rely on iron speciation as free inorganic iron is available to be scavenged:

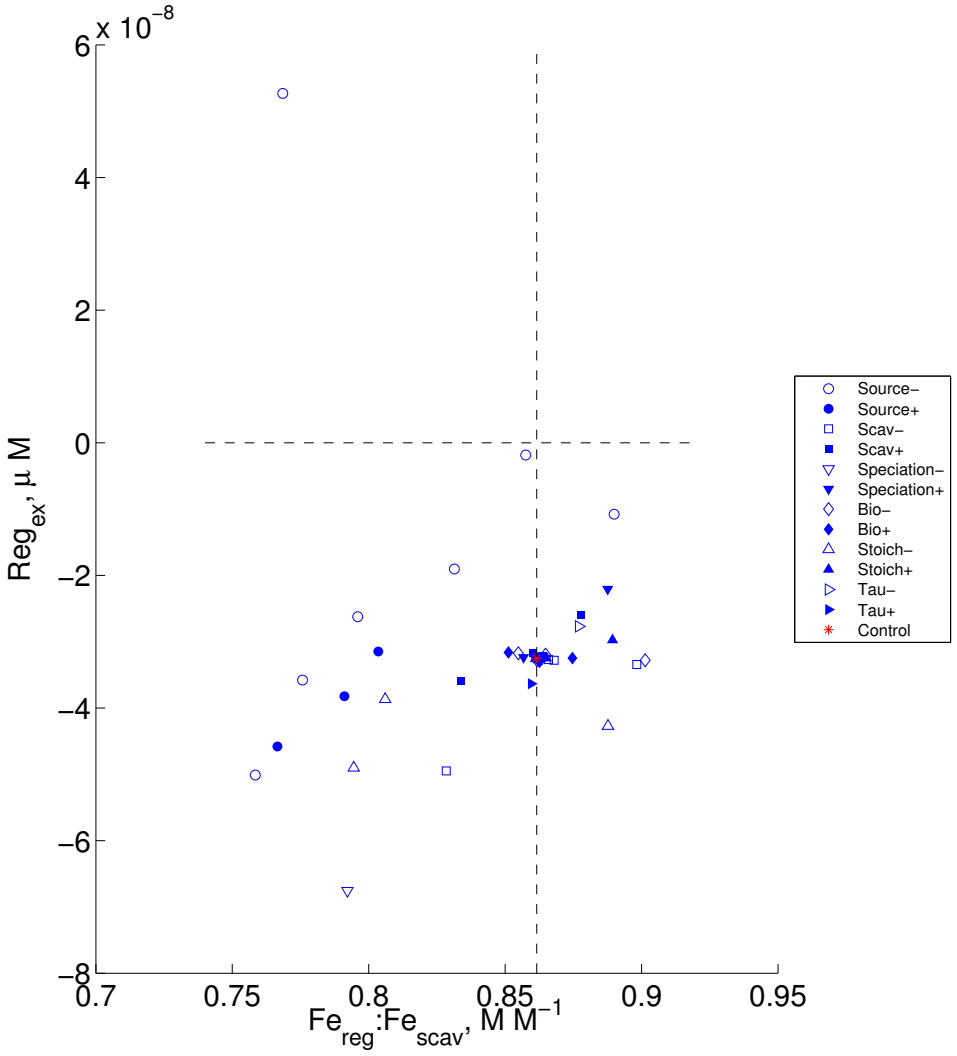

Figure 6.10: Scatter plot of all sensitivity experiments showing percentage change of Reg_{ex} and $\frac{Fe_{reg}}{-Fe_{scav}}$ from the control. Gridlines represent $\frac{Fe_{reg}}{-Fe_{scav}} = \frac{Fe_{reg}}{-Fe_{scav}\,control}$ and $Reg_{ex} = 0$, the latter is the boundary between net regeneration and net scavenging

- The availability of free iron for scavenging is partially controlled by the amount of iron in excess of ligand concentration. The excess iron will be exposed to scavenging.

- The ligand stability constant dictates the partitioning of iron between the free inorganic pool organic complexes. Weak stability constants result in weak associations with particles and allows higher proportion of iron to exist in the free inorganic form.

- Fe_{scav} is dependent on the scavenging rates that can be scaled by the presence of organic material.

The basin mean Reg_{ex} is approximately -0.03 nM, and the basin mean $\frac{Fe_{reg}}{-Fescav}$ = 0.86 (Figure 6.10). This implies that the parameter choices made for the control experiment result in a weak influence of Fe_{reg} on the total dissolved iron distributions. The perturbations of $\frac{Fe_{reg}}{-Fescav}$ and Reg_{ex} relative to the control run by the various sensitivity experiments are shown in Figure 6.10.

Atlantic mean Reg_{ex} is sensitive to source perturbations as well as stoichiometric changes and a reduction of $[L_T]$. These processes exacerbate the effect of the negative balance observed in the control run by decreasing Reg_{ex} from -0.03 nM to between -0.04 and -0.07 nM.

6.3.3.1 Effect of iron speciation on Reg_{ex}

Like most of the other iron framework tracers, Fe_{reg} and Fe_{scav} are affected significantly by the total ligand concentration, $[L_T]$. A reduction in the ligand concentration produces an imbalance of the regeneration and scavenging processes, as well as a decrease in Reg_{ex} beneath the dust plume in the Atlantic. However, the main consequences of this reduction in ligand concentration occurs in the deeper waters, with a significant increase in the magnitude of scavenging, indicated by the large negative anomaly of Reg_{ex} (Figure 6.11a). There is a basin-wide net scavenging extending over the whole of the sub-1400m deep Atlantic, rather than restricted in the deep Southern Ocean. An increase in the total ligand concentration accordingly enables

the net regeneration regime beneath the dust plume in the Atlantic to extend downwards and shift the majority of the deep Atlantic into a net regeneration region (Figure 6.11b).

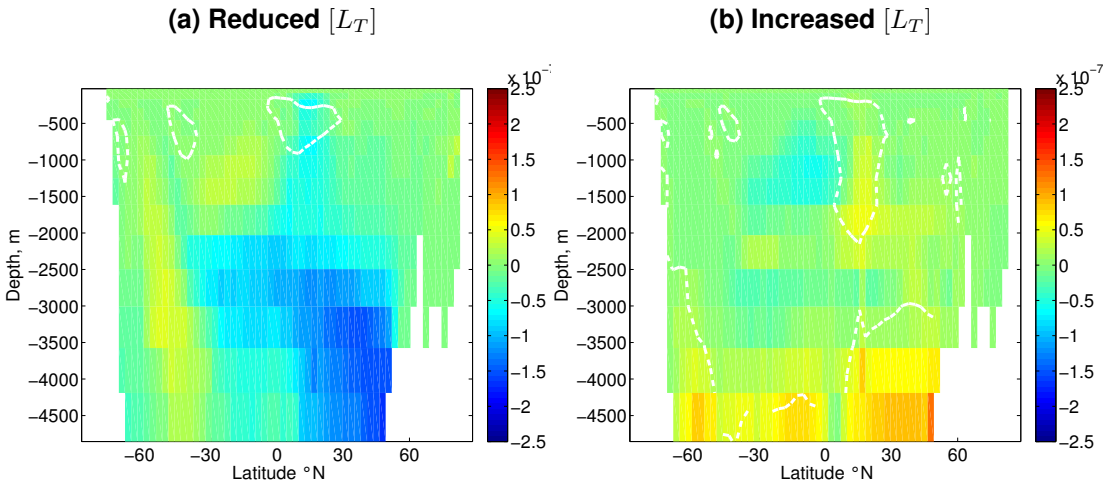

Figure 6.11: Meridional section of Reg_{ex} anomalies ($mmol\ L^{-1}$) for total ligand concentration experiments. White dashed line denotes the boundaries between net scavenging and net regeneration regimes determined by Reg_{ex} distribution.

These experiments imply the total ligand concentration is important in modifying the scavenging rate and allowing regeneration to be retained in organic complexes, instead of being scavenged onto particles. Increases in ligand concentration support regeneration and shift the basin towards a positive Reg_{ex}.

6.3.3.2 Sensitivity of Reg_{ex} to stoichiometry

The $Fe : P$ uptake ratio for the biological community is variable across the global ocean. There is a significant latitudinal variation determined by the ambient Fe_T concentrations in the surface water. Regions of high surface Fe_T concentrations allow the biological community to exhibit luxury uptake and utilise high levels of iron (Figure 6.12a). The efficiency of Fe_{reg} is strongly reliant on the ratio of iron in organic material, thus the application of a constant $Fe : P$, and the resulting reductions in Reg_{ex} limits the imprint of regenerated iron on total dissolved iron concentrations. The latitudes at which high $Fe : P$ ratios are seen (Figure 6.12a) are consistent with the latitudes where excess

(a) Comparison of variable and constant $Fe : C$ **(b) Anomaly in** Fe_{reg} **in** $Fe : P_{off}$ **experiment**

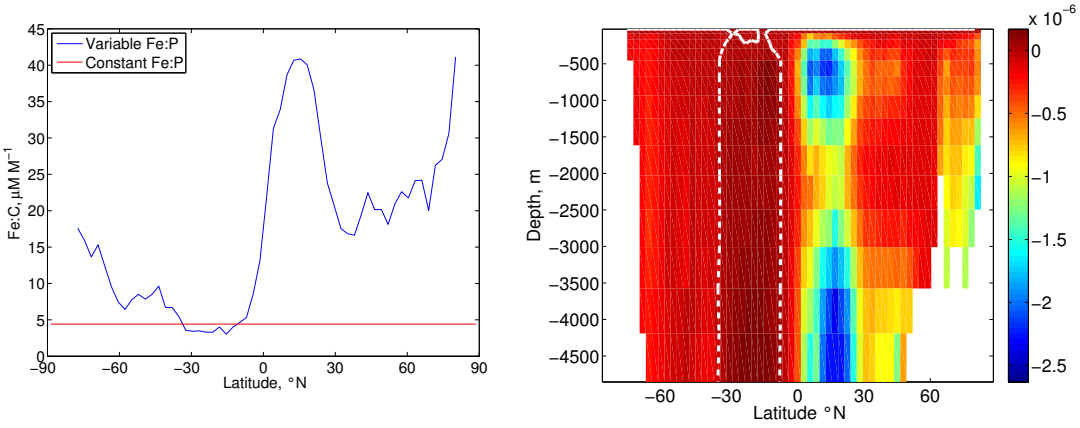

Figure 6.12: Figure demonstrating latitudinal variation of $Fe : C$**, note** $C : P = 117$**, and its effect on** Reg_{ex}**.**

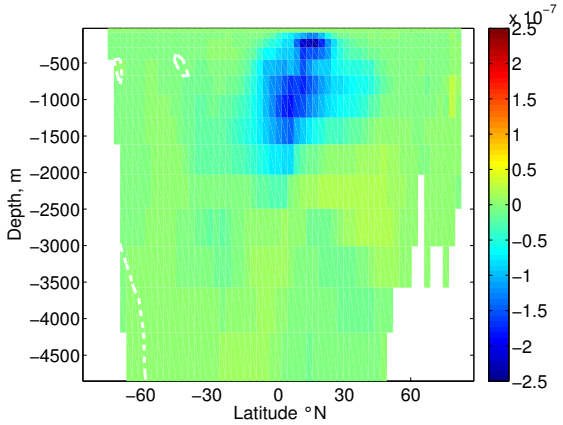

Figure 6.13: Plot of Reg_{ex} **anomaly (**$mmol\ L^{-1}$**) for constant** $Fe : P$ **experiment**

regeneration influences Fe_T (Figure 6.9a).

6.3.3.3 Effects of Sources on Reg_{ex}

Source perturbation experiments lead to complex responses of the regeneration and scavenging processes. Source experiments do not have a direct effect on the scavenging and regeneration regimes, but they do alter processes such as biological production and Fe_T (See Figure 6.2), which in turn affect the stoichiometry, export production and particle dependent scavenging rates. Export production increases or decreases the potential for regeneration, whereas Fe_T affects the magnitude of scavenging by determining the saturation of iron-binding ligands; any iron in excess of $[L_T]$

is available to the scavenging process.

The experiments in which the iron sources were removed produced varying results. The removal of the atmospheric source caused a basin mean decrease in Reg_{ex}, whereas the removal of the two benthic sources resulted in a significantly increased Reg_{ex} and a larger regenerated imprint.

The removal of the atmospheric source led to a decrease in Reg_{ex} of -0.25 nM in the low latitude, intermediate depth Atlantic (Figure 6.14a), where the largest supply of atmospheric iron occurs. This atmospheric supply drives significant biological community consumption and results in high $Fe : P$ ratios and high levels of export production. Hence, there is a strong regeneration signal in the waters beneath the dust plume. This is one of the few regions of the ocean where an imprint from regeneration is present in the control run, as revealed by Reg_{ex} in this region (Figure 6.9). The major driver of the reduction of Reg_{ex} is the decrease in export production (Figure 6.2), and therefore Fe_{reg} due to the reduced biological community consumption.

In addition to the effects on the biology, the regeneration imprint exists because of the physics of the region and the upstream biogeochemical regime in the Southern Ocean. In the control run, Fe_{reg} in the low latitude North Atlantic is relatively homogenous at all depths, however the regeneration imprint is only found at intermediate depths. The Antarctic Intermediate Water, subducted in the Southern Ocean and transported northwards, originates in an iron-poor region. The ligands carried in this water-mass are undersaturated. This free capacity to retain any regenerated iron allows Reg_{ex} to be positive in these intermediate depths. In contrast $[L_T]$ is saturated in North Atlantic Deep Water and Reg_{ex} remains below zero indicating the dominance of scavenging.

Removing the sedimentary source has an opposite effect to the removal of the atmospheric source. The region affected is the same as that affected by the atmospheric source, but removal of the sediment results in an increase in Reg_{ex} of 0.25 nM (Figure 6.14b). As discussed in section 6.3.2, the removal of the sedimentary source results in a decrease in the concentrations of Fe_{pre}.

A decrease in Fe_{pre}, particularly in the water mass formation region in the subpolar North Atlantic, results in undersaturation of ligands in subducted North Atlantic Deep Water. Once these undersaturated ligands have been transported they are then available for complexation with Fe_{reg} exported from overlying biological export regions. This extra capacity within the ligand pool provides a mechanism for Reg_{ex} to produce an imprint of regeneration processes on Fe_T distributions. The distribution of estimated ligand saturation (L_{sat}) by preformed iron (Figure 6.14e),

$$L_{sat} = L_T - Fe_{pre}, \tag{6.2}$$

within the control run illustrates the surfeit of iron within the North Atlantic Deep Water. The majority of the North Atlantic Deep Water has saturated ligand stock leading to a positive anomaly in L_{sat} (Figure 6.14f) when the sedimentary source is removed. Without the sediment source an increase of available ligands of 0.2 nM is flushed through the North Atlantic Deep Water, providing the capacity for a regeneration imprint to be more readily seen.

The hydrothermal source supplies mainly to deep waters, rather than shallower waters as for sedimentary sources. The effect of removing the hydrothermal source is similar to the removal of sedimentary source, but the distribution of the Reg_{ex} anomaly is instead located in the deep waters. The anomaly in Reg_{ex} spreads across much of the Atlantic basin at depths greater than 3000m with a magnitude up to 0.2 nM (Figure 6.14c). This anomaly creates an area of net regeneration throughout the deep Atlantic. The driver behind this excess regeneration is similar to the mechanism for the sediment source. The reduction of Fe_T results in an undersaturation of ligands in deep waters, where previously any excess regeneration was occurring above the concentration of $[L_T]$, and thus was susceptible to rapid scavenging. The undersaturation of the ligand is as a result of the reduction in Fe_T providing the capacity for regenerated iron to be retained in organic complexes protected from scavenging. This provision of undersaturated ligands enables a regeneration imprint to be seen in the deep waters throughout the basin.

Removal of both the benthic sources produces anomalies combining the

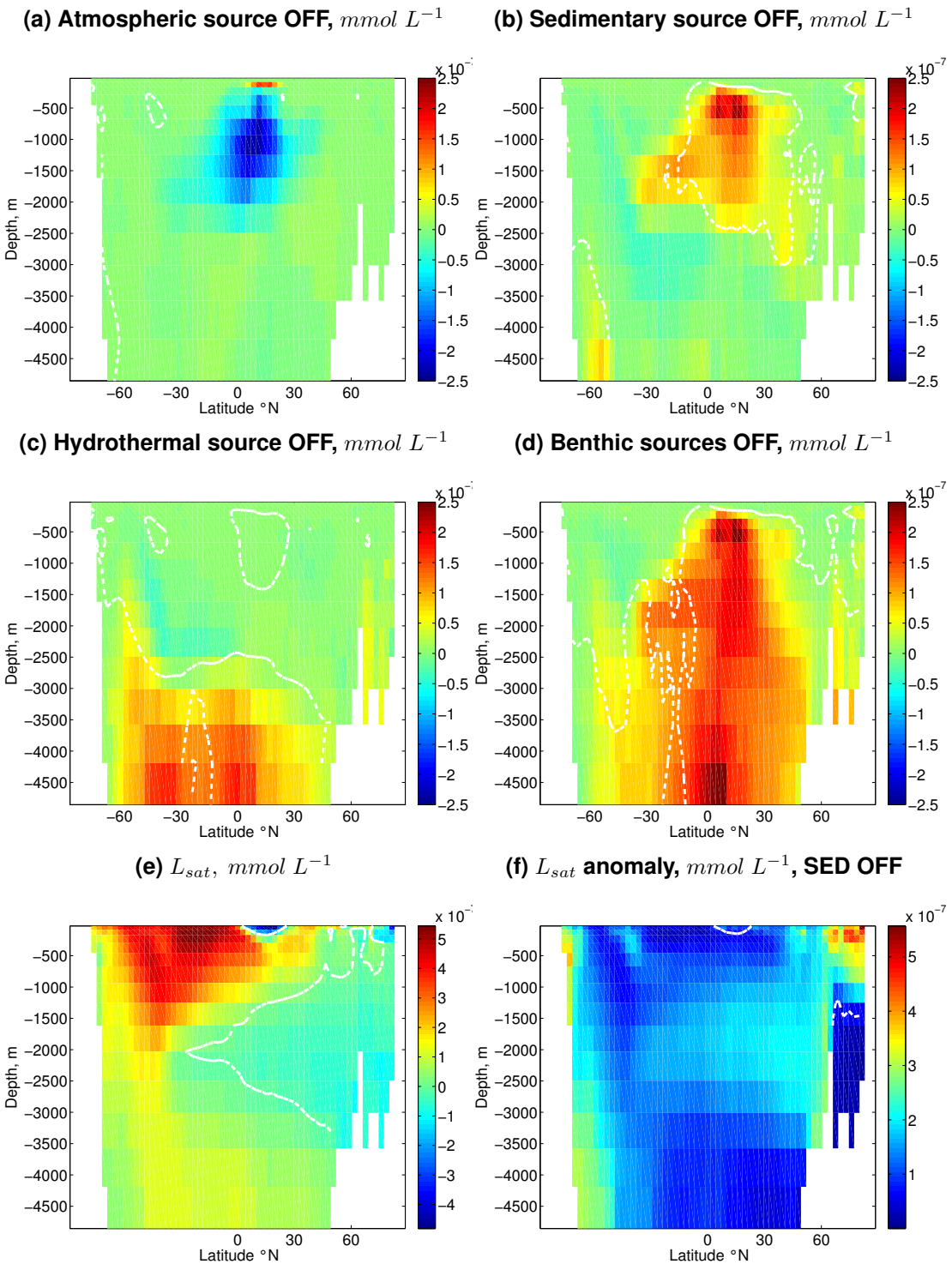

Figure 6.14: (a) to (d) Meridional section of Reg_{ex} anomalies ($mmol\ L^{-1}$) for stoichiometry and source experiments. White dashed line denotes the boundaries between net scavenging and net regeneration regimes determined by Reg_{ex} distribution. (e) & (f)Meridional section of control L_{sat} ($mmol\ L^{-1}$) and the anomaly of L_{sat} for the SED OFF scenario. White dashed line denotes $L_{sat} = 0$

effects of the separate sediment and hydrothermal sources (Figure 6.14d). The anomaly in Reg_{ex} reaches 0.25 nM and provides a regeneration imprint throughout much of the ocean, except for the Southern Ocean and subtropical gyre of the South Atlantic. Without benthic sources the ligand concentrations across much of the Atlantic remain undersaturated. The availability of these organic molecules to form complexes with regenerated iron provides a mechanism for Reg_{ex} to impact Fe_T distributions.

6.3.4 Comparison of iron and phosphate frameworks

With the development of the new iron framework it is important to know how the traditional macronutrient preformed and regenerated framework compares with it. To address this issue this section will answer two further questions:

1. How do the preformed and regenerated tracers relate to each other within the two frameworks, and what drives variations in the responses of the tracers to the model experiments?
2. Why are the responses by the preformed tracers of the two frameworks different?

6.3.4.1 Relationship between the preformed and regenerated tracers

The relationship between the preformed and regenerated tracers vary for the phosphate and iron partitioning frameworks. Within the phosphate framework there is a strong, consistent relationship between the magnitudes of P_{pre} and P_{reg} (Figure 6.15). Any perturbations in P_{pre} resulting from the model experiments is accompanied by an equivalent opposite perturbation in P_{reg}.

In contrast the relationship between Fe_{pre} and Fe_{reg} varies significantly between the model experiment runs (Figure 6.16). Two groups of experiments emerge from this initial analysis, one group tends to control Fe_{pre} and has a much smaller impact on Fe_{reg}, while the other group has strong controls on the magnitude of Fe_{reg} and little effect on Fe_{pre}.

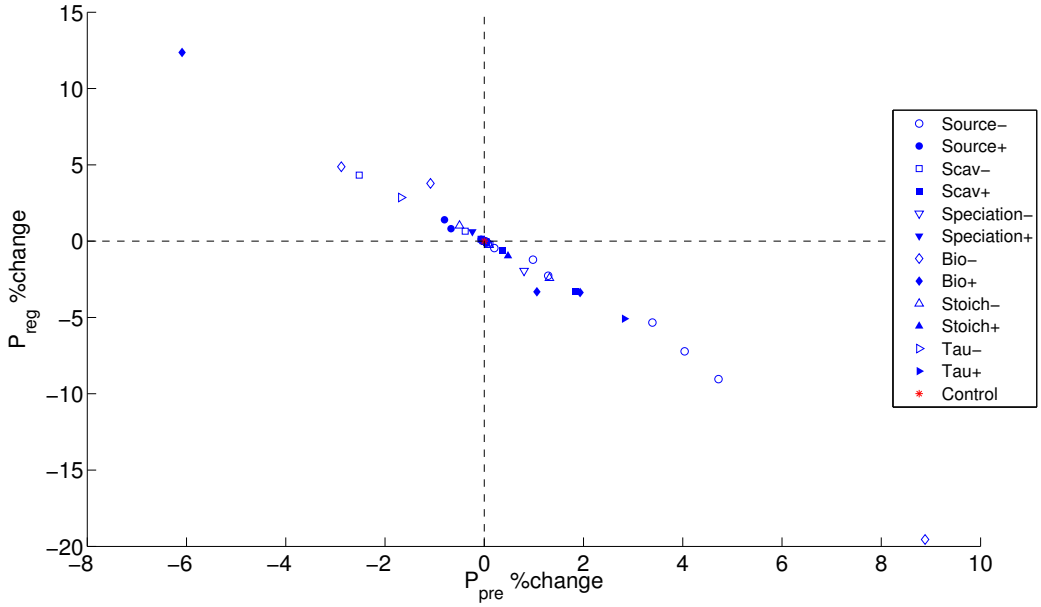

Figure 6.15: Plot showing anomalies in basin mean P_{pre} and P_{reg} for the model experiments

The benthic sources and the total ligand concentrations are the processes that most strongly control the preformed iron concentrations. These processes control the total dissolved iron concentrations in the surface mixed-layer. The sedimentary sources supply significant amounts of iron into the mixed layer, while the total ligand concentration determines the quantity of free inorganic iron that can be protected from processes, such as scavenging and precipitation, by forming organic complexes with ligands.

The experiments involving atmospheric source and stoichiometry perturbations tend to adjust the iron partitioning by affecting the concentrations of Fe_{reg}. The atmospheric source contributes to this pool by affecting the magnitude of organic material available for regeneration. This effect is achieved by aeolian iron fuelling large amounts of biological community production in the mid-latitude Atlantic. The stoichiometry experiments are able to adjust the amount of iron fixed within the organic material relative to phosphate. This process produces variability in the regeneration ratios of iron, whereas the ratio of phosphate fixed within organic matter does not change. The regenerated tracers both have similar responses to the model

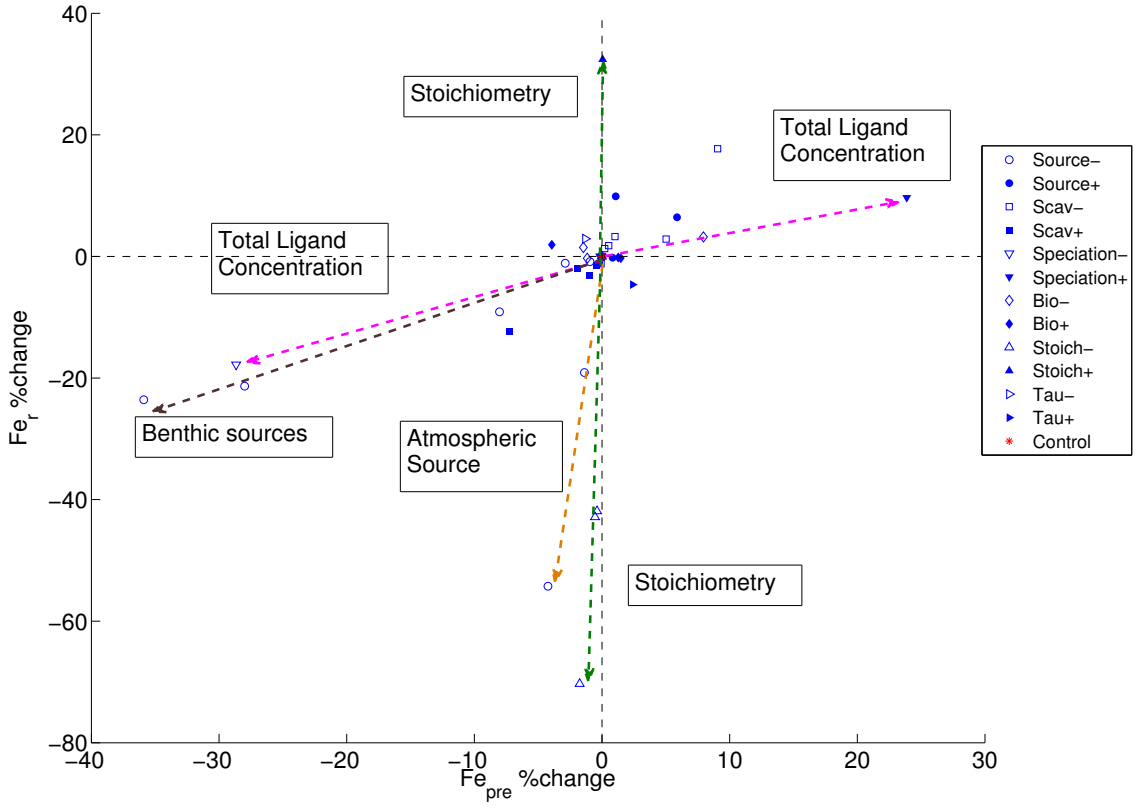

Figure 6.16: Plot showing anomalies in basin mean Fe_{pre} and Fe_{reg} and the effects of selected experiments. Dotted arrows and label boxes represent the spectrum of results for particular groups of experiments.

experiments, but the stoichiometry perturbations in particular allow much greater variation in the responses of Fe_{reg} relative to P_{reg}.

6.3.4.2 Variation in responses of Fe_{pre} and P_{pre} to model experiments

Despite the similarities in the concept of preformed nutrients and iron, there are contrasting processes that determine these concentrations, set the initial quantities of nutrients that are subducted and set the basin-scale preformed nutrient patterns. The only group of experiments that modify Fe_{pre} and P_{pre} in a consistent manner are those involving the biological system variables: biological community consumption rate, iron half-saturation constant and phosphate half-saturation constant (Figure 6.17). Total ligand concentration significantly alters Fe_{pre} concentrations without altering P_{pre}. The source perturbations all affect the two preformed tracers in opposing ways: when

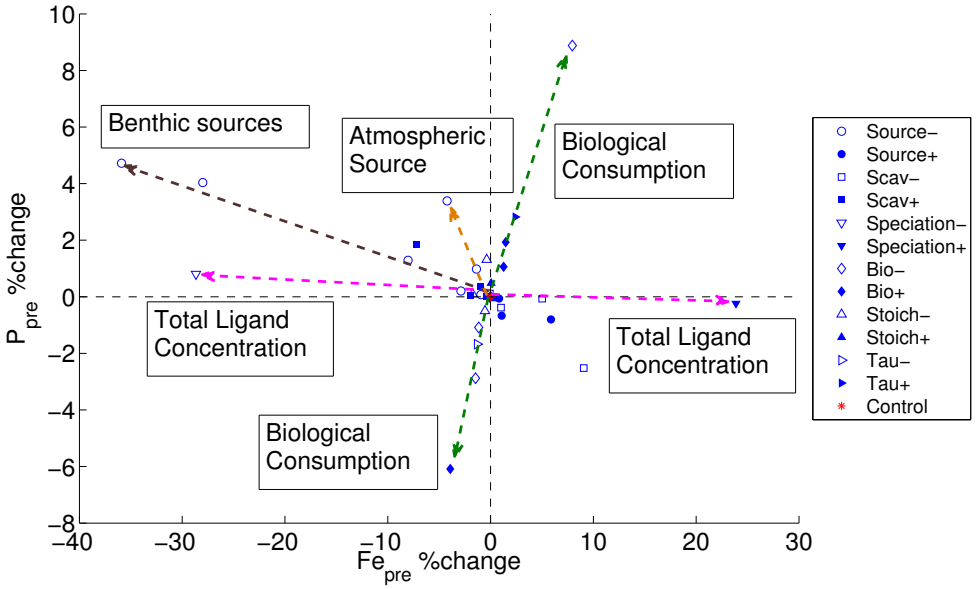

Figure 6.17: Plot showing anomalies in basin mean Fe_{pre} and P_{pre}. Dotted arrows and label boxes represent the spectrum of results for particular groups of experiments.

the Fe_{pre} tracer is reduced, there is an increase in P_{pre}, while conversely an increase in Fe_{pre} results in a decrease in P_{pre}.

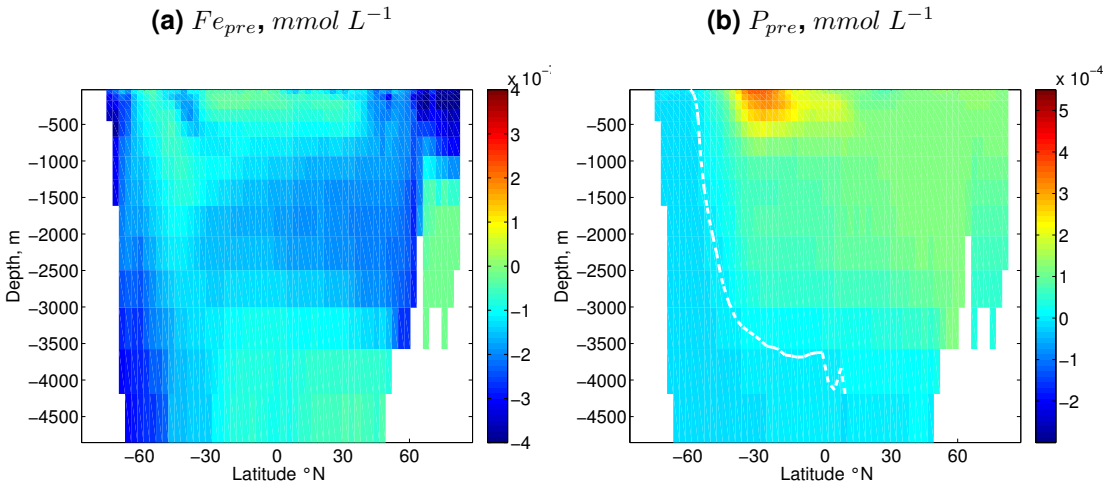

Figure 6.18: Meridional Atlantic sections of preformed tracer anomalies for the Sediment-OFF scenario for (a) Iron and (b) Phosphate

The mechanism behind this inverse relationship between the two preformed tracers derives from the relationship between Fe_T and PO_4 in the surface water. The source perturbation experiments result in alterations to the supply of iron to the surface mixed layer. A decrease in sedimentary iron supplied to

a region where PO_4 is depleted due to biological consumption decreases Fe_T, and hence Fe_{pre}, but increases P_{pre} concentrations as a result of iron-limitation of the biological community. This effect is seen strongly in the North Atlantic where the sediment source is strong. The reduction in sediment supply causes a strong negative anomaly in Fe_{pre} subducted into the North Atlantic Deep Water (Figure 6.18a). This negative anomaly is mirrored in P_{pre} which exhibits a strong positive anomaly in the same region (Figure 6.18b).

6.3.4.3 The regeneration imprint of phosphate

Previously in this chapter the concept of excess regeneration for iron has been discussed. With the phosphate preformed framework this concept does not apply. Due to the lack of a removal process for phosphate like scavenging, the regenerated phosphate contributes significantly to the total phosphate pool. The ratio of regeneration to total nutrient concentration for phosphate and iron, i.e,

$$P_{RR} = \frac{P_{reg}}{PO_4}, \tag{6.3}$$

$$Fe_{RR} = \frac{Reg_{ex}}{Fe_T}. \tag{6.4}$$

These quantities give an indication of the contribution to the total nutrient distribution. For iron we use the net regeneration, Reg_{ex}, signal as discussed in section 6.3.3.

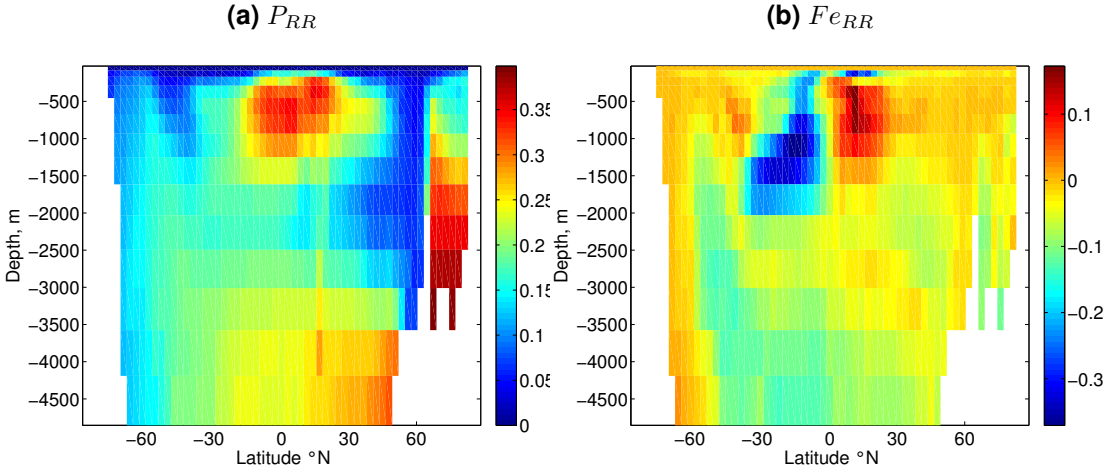

Figure 6.19: Control meridional Atlantic section of the fractional contribution of regenerated nutrient to total nutrient for phosphate and iron

In some regions P_{reg} contributes in excess of 30% of the PO_4 concentration, such as beneath the mid-latitude Atlantic dust deposition plume, and water deeper than 1500m in the subpolar North Atlantic 6.19a. The greatest imprint seen for Fe_{reg} is similarly beneath the mid-latitude Atlantic dust plume, where contributions of around 15% of Fe_T are evident 6.19b. For the majority of the rest of the Atlantic Fe_{RR} is either close to zero or negative. The imprint from Fe_{reg} does not occur, only the modification of Fe_T by scavenging is seen. The impact of scavenging is largest beneath the subtropical gyre of the South Atlantic, with a loss of Fe_T of 30% resulting from Reg_{ex}.

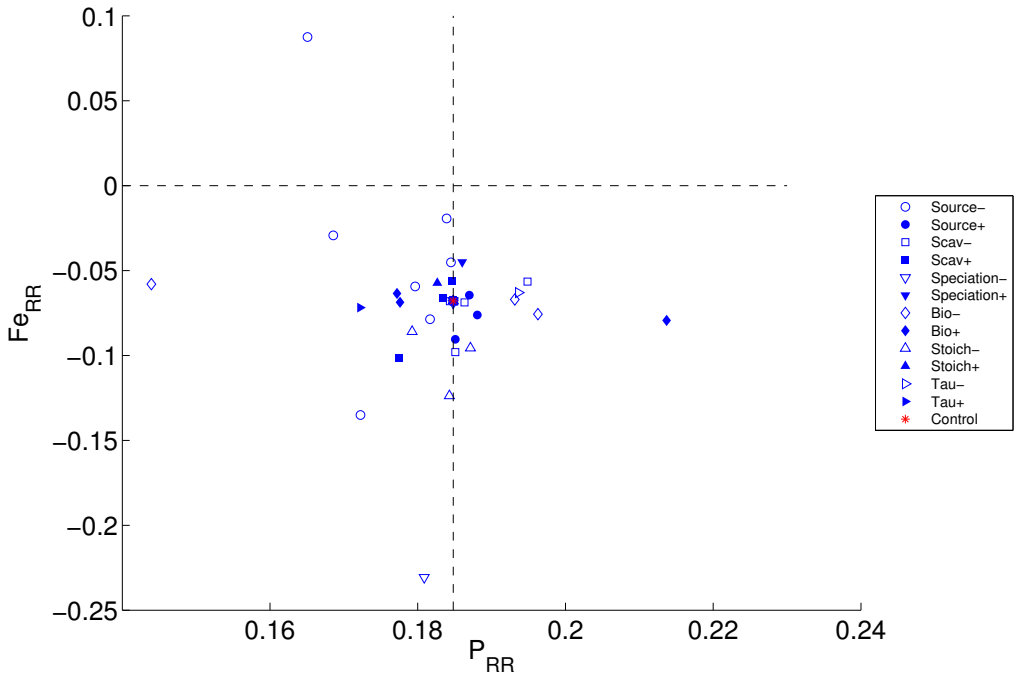

Figure 6.20: Plot showing basin mean Fe_{RR} and P_{RR} for the experiment runs for (a) Phosphate and (a) Iron

The iron source perturbation experiments along with the reduction in $[L_T]$ result in the biggest change to Fe_{RR} (Figure 6.20). The source perturbations cause some of the largest changes to P_{RR}, 0.01 to 0.02. The largest response is to perturbation in the biological community consumption rate (α) experiments, which cause changes to P_{RR} of 0.04.

Perturbation of the biological consumption rate results in opposing effects on P_{RR} and Fe_{RR} (Figure 6.21). The response of P_{RR} is derived from the effect of

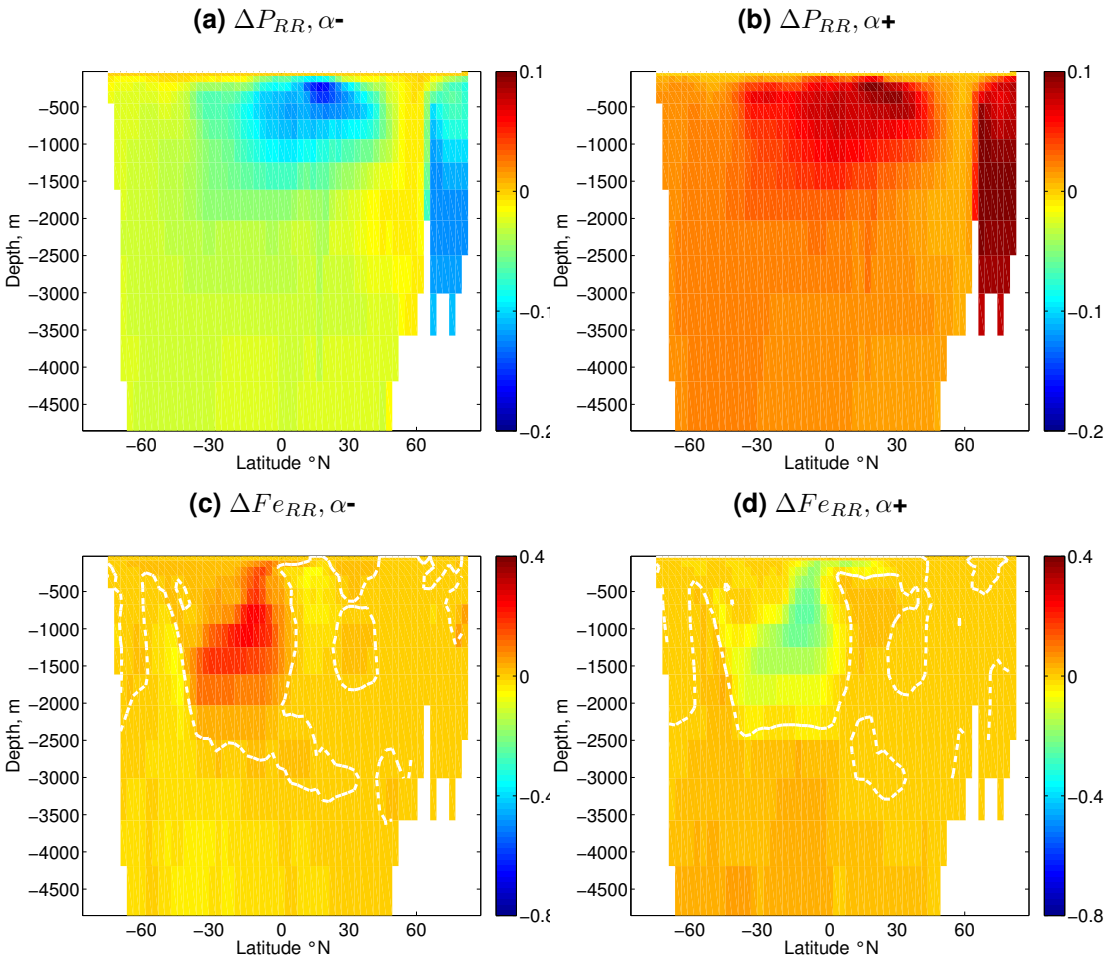

Figure 6.21: Meridional sections of P_{RR} and Fe_{RR} anomalies for biological consumption rate experiments. White dashed line denotes the zero contour

consumption rate changes on the overall export production. The decrease in biological consumption rate results in a reduction in P_{RR} of around 0.1 to 0.15% in the areas beneath the productive regions of the Atlantic: the mid-latitude Atlantic and subpolar North Atlantic (Figure 6.21a). The opposite effect is seen with an increase in biological consumption rate (Figure 6.21b). The overall basin-wide response of Fe_{RR} is very similar to the P_{RR} responses. The exception is the region underneath the subtropical gyre of the South Atlantic (Figures 6.21c and 6.21d). The result here is an indirect response of the system to Fe_T concentrations in the region. A reduced biological consumption rate results in increased concentrations of Fe_T. The response of the biology to higher Fe_T concentrations is to take up an increased amount of iron relative to phosphate (Figure 6.22). The increase in the $Fe : P$ ratio then provides an increased quantity of iron within the organic material that is being exported.

This effect results in an increase of Reg_{ex} and consequently an increase in Fe_{RR}, which despite the change remains negative. The opposite is true for reducing the biological consumption rate.

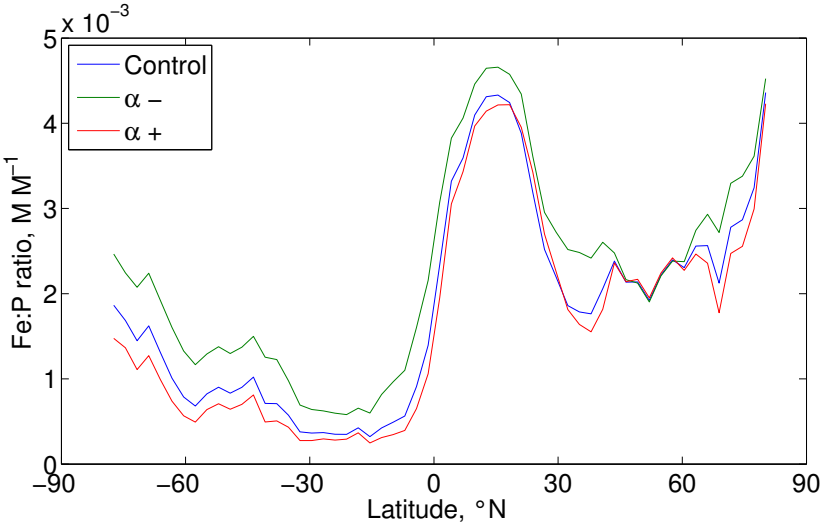

Figure 6.22: Latitudinal variation in zonal mean $Fe : P$ uptake ratio for biological consumption rate perturbations

When iron sources are removed, P_{RR} shows a response consistent with the damping of biological activity and export production by iron limitation; a consequence of reduced surface Fe_T concentrations. This simple response shown by phosphate is supported by the fact that the response of P_{RR} is very similar between the experiments where either atmospheric or benthic sources are removed (Figures 6.23a and 6.23b). The source anomalies are small relative to the biological consumption rate experiments, with maximum anomalies of around -0.1.

The response of Fe_{RR} to these experiments is more complex with opposing responses depending on the origin of the source that is removed. For a removal of atmospheric source there is a large reduction in Fe_{RR} of around -0.8 (Figure 6.23c). This is a combination of two effects, the first being reduction of surface Fe_T leading to reduced biological activity. Thus, there is lower export production and less available organic material for regeneration. The second is the reduction of $Fe : P$ ratios, also derived from the reduction of surface Fe_T. Any organic material regenerated at depth will therefore

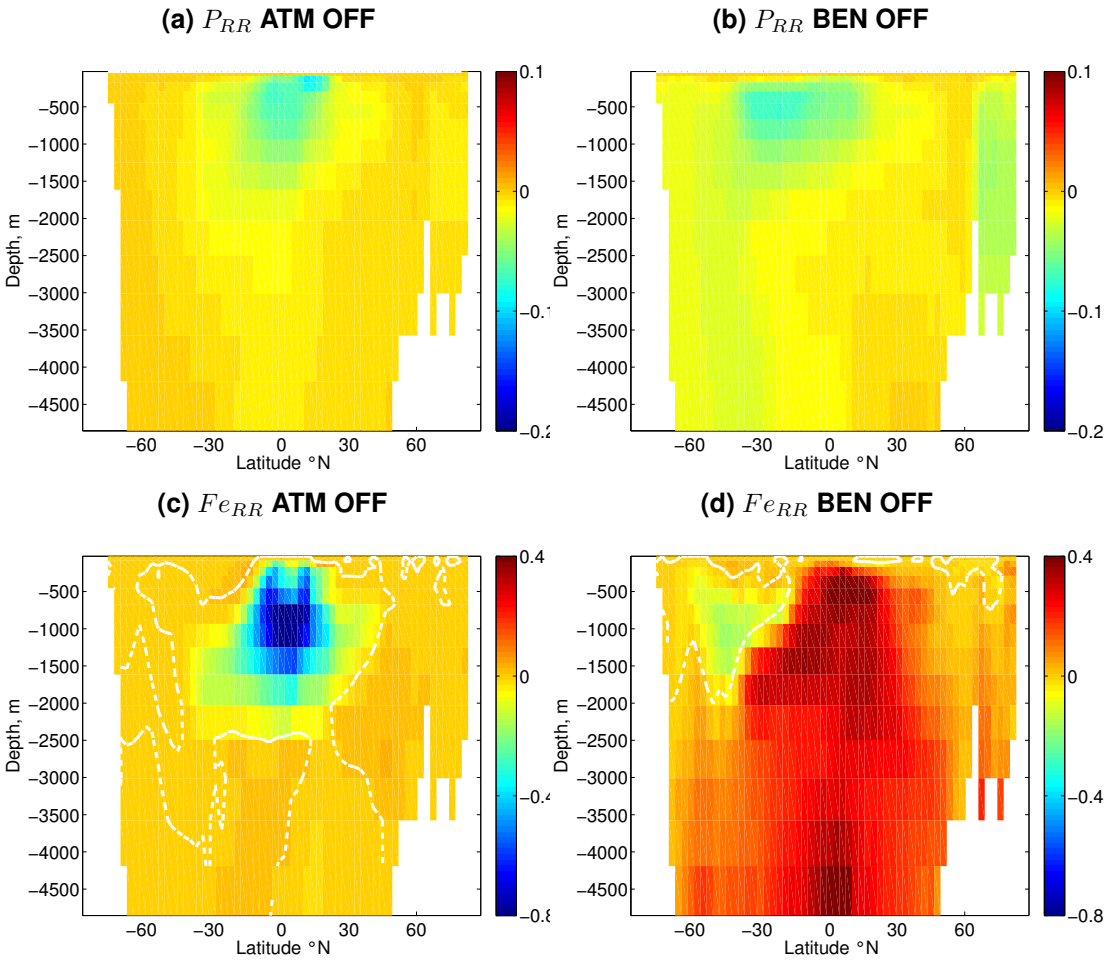

Figure 6.23: Meridional sections of P_{RR} and Fe_{RR} anomalies for iron source experiments. White dashed line denotes the zero contour.

have less iron available for recycling. Removal of the benthic sources has the opposite effect on Fe_{RR} as removal of the atmospheric source (Figure 6.23d). Reductions in the subsurface sources, though also impacting the biological consumption and export production, reduces the concentrations of Fe_T in subsurface water. This reduction of Fe_T means that more organic ligands become available for regenerated iron to form complexes beneath the surface. Low export production also produces reduced scavenging rates, further perturbing Fe_{RR} in favour of increased of Fe_{reg}. The anomalies seen for this increased regeneration imprint are between 0.2 and 0.4 for the deep water and intermediate water north of 20 °S.

6.4 Summary

The regional variability in iron sources and the amount of ligand available in these regions of iron supply are found to be very important in setting the basin-wide distribution of Fe_T. Though some of the drivers behind this distribution are hinted at from analysis of the preformed and regenerated tracers, a deeper look into the iron partitioning helped to elucidate this further.

Sedimentary iron sources was found to be a large contributor to the mixed layer preformed tracer, Fe_{pre}. The importance of ligand concentrations is also highly stressed. Perturbations to the sources impacted total iron distribution because of the localised effect of organic ligands. The parameterisation of sediment sources and total ligand concentration is crucial if the framework tested here is to be successful in the future.

The net effect of regeneration and scavenging is a crucial relationship that informs a lot about the characteristics of the total dissolved iron distribution. The imbalance between these two processes determines whether there is evidence of regeneration imprint on Fe_T distributions.

Ligand concentrations are the driving factor behind the imprint of regeneration. Ligands are often saturated due to iron from surface sources (aeolian and sedimentary), or shallow subsurface sources (sedimentary and hydrothermal). The presence of ligands in deep water leads to the formation of complexes with iron from hydrothermal sources. If ligand concentrations in subduction regions or hydrothermal source regions are saturated with dissolved iron then there is little capacity to retain Fe_{reg}.

Perturbation of subsurface sources of iron can lead to a propagation of positive L_{sat} anomaly from source regions, meaning that ligand concentration is in excess of Fe_{pre} and providing the capacity for an imprint tot regeneration to be retained.

Ligands are available to carry a regeneration imprint in the mid-latitude Atlantic

at intermediate depth. Water originating from the South Atlantic and Southern Ocean, which is low in Fe_T thus containing undersaturated ligands, is present here. The excessive supply of iron by the atmosphere allows very high $Fe:P$ ratios to be used by the biological community, leading to high levels of Fe_{reg}. This signal is evident in the mid-latitude Atlantic at intermediate depth but is not retained in deeper water. This is due to the variety in ligand capacity in waters originating from the Southern Ocean or North Atlantic.

Comparisons between the preformed and regenerated tracers for phosphate and iron have shown that P_{pre} and P_{reg} are very tightly coupled when viewed with respect to perturbations of the iron system parameters and biological system parameters. Contrastingly, there are significant variations in Fe_{pre} and Fe_{reg} that are far more varied and much less complimentary as for the phosphate framework.

The preformed tracers for phosphate and iron tend to have opposing responses to model perturbations. This is due to the inherent reliance of phosphate on iron limitation, resulting from a lack of total dissolved iron, to persist in the surface mixed layer.

The response of the iron and phosphate regenerated tracers is different. Regenerated phosphate responds in a consistent way to a reduction in iron sources. Whether atmospheric or benthic sources are reduced, a reduction in export production causes reductions of regenerated phosphate. The response of iron is sensitive to the perturbed source. A reduction in atmospheric iron reduces biological activity and consequently decreases Fe_{reg}, similar to P_{reg}. When benthic sources are removed, reduced Fe_T in the subsurface increases the capacity for regenerated iron to interact with organic ligands, leading to an increase in the ratio of Fe_{reg} relative to Fe_T.

Chapter 7

Conclusions

7.1 Key outcomes

A broad range of work was presented in this thesis. The first order relationship between the iron source distributions and the observed total iron distributions was discussed, before a method of quantifying scavenging rates of iron from direct measurements was presented to build on existing empirical techniques. Complementary to this work with observational data, significant progress was made towards improving the representation of iron within the MIT general circulation model. A new iron framework was employed using diagnostics from the improved MITgcm to reveal the drivers of the iron distribution. The key outcomes of this thesis are:

- There was value in using the ^{234}Th and ^{238}U derived rate constants for net adsorption and fallout to estimate the scavenging rates of trace metals (Honeyman et al., 1988). The equilibrium assumption necessary to derive these rates introduced errors of up to 60%, but was often much lower than this. The calculation of net adsorption rates was useful, but accompanying measurements of iron speciation will elucidate further the contributions to, and effects on, the organically complexed, colloidal, free inorganic iron and particulate iron.

- A significant relationship between observed scavenging rates and volcanic ash deposition was found; a strong correlation implies that when ash deposition occurs it can drive removal of iron from the water column through scavenging. This process was a previously unreported effect, which adds complexity to the response of the biological community to natural oceanic iron fertilisation events resulting from volcanic eruptions.

- In future I recommend that measurements of ^{234}Th and ^{238}U be combined with the measurement of a range of particulate material. The work in this thesis found that $[POC]$ and volcanic ash both have significant impacts on scavenging rates. This implies that other organic and inorganic particles will be important. Sampling for lithogenic particles, $[POC]$, calcium carbonate and biogenic silica, for example, will provide additional information as to the processes controlling scavenging.

- Development of the iron closure within the MITgcm has improved global correlation of total dissolved iron distribution from $R^2 = 0.05$ to $R^2 = 0.4$, in line with other more advanced biogeochemical general circulation models. This improvement was achieved by adding benthic sources following Aumont and Bopp (2006) and Tagliabue et al. (2010) and including biogenic and dust particle scavenging and coagulation. These changes enabled the MITgcm to strip out the increased quantities of iron resulting from the two new sources. Stoichiometry within the MITgcm became variable depending on total iron concentration, consistent with observations by Twining et al. (2004) and Strzepek et al. (2005) and speciation settings (Rue and Bruland, 1997) were modified to improve parameters, making them consistent with observational estimates.

- The parameter choices and additions to the iron closure presented here helped reconcile global dissolved iron measurements with the modelled iron fields. Though the skill of the MITgcm via R^2 was comparable to more complex biogeochemical models, there are still significant improvements in the representation of the iron speciation and iron sources that can be made. The combination of more complex representations of the

biological community and the iron chemistry improvements made here may improve further the reproducibility of the ever increasing database of oceanic dissolved iron measurements.

- Our new iron partitioning framework was a useful tool for understanding the interaction between preformed phosphate and preformed iron. Both tracers rely on residual concentrations in the surface mixed-layer. There are contrasting preformed signals of each nutrient. Phosphate dominates in waters of Southern Ocean origin, whereas iron dominates in regions from the North Atlantic, where sediment sources to the mixed layer are strong.

- Two key balances emerge from the iron partitioning framework.

    1. To first order, the total iron distribution was determined by the distribution of the mixed-layer preformed tracer (Fe_{pre}) and the new sedimentary (Fe_{sed}) and hydrothermal (Fe_{hyd}) tracers, i.e. $Fe_T \approx Fe_{pre} + Fe_{sed} + Fe_{hyd}$.

    2. The tracers that exhibit the largest magnitudes within the framework were regenerated iron (Fe_{reg}) and scavenging (Fe_{scav}). These two tracers nearly cancelled each other out, i.e. $Fe_{reg} \approx -Fe_{scav}$. The residual of these terms dictated whether the regeneration of organic iron can produce an imprint onto the total dissolved iron concentrations. For the majority of the Atlantic Ocean $Fe_{reg} + Fe_{scav} < 0$, which meant that there was no excess regeneration. The basin-wide distribution of total dissolved iron was not affected by regeneration of organic material.

- The balance between regeneration and scavenging implied by the new iron partitioning framework provided an alternative method of quantifying the scavenging rates of iron from observational data. When rates of regeneration of iron are calculated an estimate of scavenging could be made based on a near cancellation. Used in comparison with simple model experiments an error in this assumption can also be applied.

- The iron partitioning framework illustrated differences between the responses of regenerated iron and regenerated phosphate. Regenerated phosphate had a simple and direct response to reductions in biological community consumption and export production. If export production decreased, so did the imprint of regenerated phosphate on the subsurface phosphate distributions. These decreases in production can result from a reduction in any of the three modelled iron sources: atmospheric, sedimentary and hydrothermal supply. The response of regenerated iron was dependent on the source. The response to atmospheric source perturbations was the same as for phosphate. The response to the benthic sources was the opposite. Undersaturation of ligands in the vicinity of sources resulted from a reduction in iron supply. The undersaturated ligands were available for complexation with sinking biology-derived organic material, allowing an increased imprint of regenerated iron despite reduced export production.

  This signal was a result of the freeing up of subsurface organic ligands allowing an imprint of regeneration to be made, despite the reduction in total export production.

- Preformed iron in the mixed layer was strongly controlled by the shallow subsurface source of iron from the sediments. The iron partitioning framework did not explicitly represent a true partitioning of atmospheric, sedimentary and hydrothermal sources, but revealed the integrated contribution of all sources.

- Organic ligands play a central role in determining the dissolved iron distribution. Ligands form organic complex with inorganic free iron and increase the solubility of iron within the water column. These organic complexes then protect the iron from scavenging. Thus, the presence of ligands enhances the transport of iron-rich water throughout the Atlantic basin. I recommend in particular, that the development of an organic ligand tracer within general circulation models is crucial if meaningful advances in iron cycle modelling are to be made.

- The sedimentary and hydrothermal sources were also important factors in the determination of basin-wide total iron distribution. Effective parameterisation of these processes are crucial if one wants to truly represent the response of the basin-wide iron cycling to perturbations in physical, chemical and biological perturbations.

7.2 Open questions

This thesis provides three contributions to understand the cycling of iron in the Atlantic. The application of ^{234}Th and ^{234}U disequilibrium to calculate particle scavenging and fallout, along with custom calculation of errors associated with the equilibrium assumption, has reopened an avenue for observations of trace metal scavenging to be made. There were a number of questions that arise from this work:

- How can the revisitation of ^{234}Th and ^{234}U disequilibirum as an estimate of scavenging rates improve our mechanistic understanding of particle scavenging?

- What needs to be done to increase our understanding of element specific scavenging processes?

  ^{234}Th and ^{234}U measurements are often taken during biogeochemical research cruises. The aims of these measurements are to estimate carbon export from the surface mixed layer. With the addition of a few further measurements a much wider understanding of the drivers behind scavenging processes could be gained. Sampling of biogenic silica, calcium carbonate, lithogenic material, and some size fractionation of organic particulates will allow the relative contributions of each of these particles to be estimated. Combining ^{234}Th and ^{234}U measurements with trace metal measurements will also allow closer ties to be made between particle scavenging and trace metal chemistry. For example, combined studies are needed to identify the reliability of assuming adsorption rates

of ^{234}Th and iron are similar.

- Volcanic ash deposition: source or sink?

  This thesis presented evidence that volcano ash deposition to the ocean has a strong control on the scavenging and fallout rates of trace metals in the ocean. The question posed is analogous to the aims of Ye et al. (2010)'s atmospheric dust deposition mesocosm study, and follows on from Achterberg et al. (2013)'s findings of fertilisation of the biological community by the eruption. Further investigation into the net effect of volcanic ash deposition on the biological community is necessary to understand this periodical driver of biological activity.

- Do the developments of the MITgcm iron closure improve the representation of the oceanic ecosystem response to iron in more complex versions of the MITgcm?

  The changes made to the MITgcm iron closure in this thesis greatly improved the ability of the model to reproduce observed global iron concentrations. These improvements were made using a version of the MITgcm with a primitive representation of the biological community. The key question is how do these changes affect the more complex versions of the MITgcm that resolve multiple phytoplankton species and trophic levels of the marine ecosystem (Dutkiewicz et al., 2009).

- Are global total dissolved iron concentrations completely dependent on source processes?

  The application of the novel iron partitioning framework suggested that the global distribution of dissolved iron concentrations is almost entirely determined by the source processes. It is important that further investigation into this aspect of the thesis is carried out to ascertain how robust this assertion is, and will complement further iron source modelling work following Tagliabue et al. (2010, 2014)

- Does regeneration of organic iron matter?

The iron partitioning framework suggested that to first order there were very few regions of excess regeneration of organic iron above the levels of scavenging. The majority of the ocean did not see an imprint of regeneration of iron. The scavenging and regeneration processes, can each be very large relative to the transport of iron sources, but tend to cancel each other out. Scavenging was slightly larger than regeneration and there was net scavenging for much of the ocean. The balance between regeneration and scavenging was sensitive to total ligand concentration.

- Can we quantify scavenging rates from regenerated iron measurements?

  To look at the above issue from a different angle, the inferences made about the balance of regeneration and scavenging with the iron partitioning framework suggest that an estimate of the gross scavenging of iron can be made from measurements of regenerated iron. This assertion could be supported by running a survey of regenerated iron, ^{234}Th and ^{234}U in the oceans. These observations could be made in collaboration with other biogeochemical projects and, in combination with modelling studies, could improve the understanding, or viability, of the assertions made from the theoretical iron partitioning framework.

Bibliography

Achterberg, E. P., Moore, C. M., Henson, S. A., Steigenberger, S., Stohl, A., Eckhardt, S., Avendano, L. C., Cassidy, M., Hembury, D., Klar, J. K., Lucas, M. I., Macey, A. I., Marsay, C. M. and Ryan-Keogh, T. J. (2013), 'Natural iron fertilization by the eyjafjallajökull volcanic eruption', *Geophys. Res. Lett.* **40**(5), 921–926.

Amante, C. and Eakins, B. (2009), 'Etopo1 1 arc-minute global relief model: Procedures, data sources and analysis', *NOAA Technical Memorandum NESDIS NGDC-24* pp. 1–25.

Archer, D. and Johnson, K. (2000), 'A model of the iron cycle in the ocean', *Global Biogeochem. Cycles* **14**(1), 269–279.

Aumont, O. and Bopp, L. (2006), 'Globalizing results from ocean in situ iron fertilization studies', *Global Biogeochem. Cycles* **20**(2).

Aumont, O., Bopp, L. and Schulz, M. (2008), 'What does temporal variability in aeolian dust deposition contribute to seasurface iron and chlorophyll distributions?', *Geophys. Res. Lett.* **35**(7).

Baar, H. D., Boyd, P., Coale, K., Landry, M. H., Tsuda, A., Assmy, P., Bakker, D. C. E., Bozec, Y., Barber, R. T., Brzezinski, M. A., Buessler, K. O., Boye, M., Croot, P. L., Gervais, F., Gorbunov, M. Y., Harrison, P. J., Hiscock, W. T., Laan, P., Lancelot, C., Law, C. S., Levasseur, M., Marchetti, A., Millero, F. J., Nishioka, J., Nojiri, Y., van Oijen, T., Riebesell, U., Rijkenberg, M. J. A., Saito, H., Takeda, S., TImmermans, K. R., Veldhuis, M. J. W., Waite, A. M.

and Wong, C.-S. (2005), 'Synthesis of iron fertilization experiments: From the iron age in the age of enlightenment', *J. of Geophys. Res.* **110**.

Bacon, M. and Anderson, R. (1982), 'Distribution of thorium isotopes between dissolved and particulate forms in the deep sea', *Journal of Geophysical Research: Oceans (1978–2012)* **87**(C3), 2045–2056.

Balistrieri, L., Brewer, P. and Murray, J. (1981), 'Scavenging residence times of trace metals and surface chemistry of sinking particles in the deep ocean', *Deep Sea Research Part A. Oceanographic Research Papers* **28**(2), 101–121.

Baskaran, M., Santschi, P., Benoit, G. and Honeyman, B. (1992), 'Scavenging of thorium isotopes by colloids in seawater of the gulf of mexico', *Geochimica et Cosmochimica Acta* **56**(9), 3375–3388.

Benner, R., Louchouarn, P. and Amon, R. (2005), 'Terrigenous dissolved organic matter in the arctic ocean and its transport to surface and deep waters of the north atlantic', *Global Biogeochem. Cycles* **19**(2).

Bennett, S., Achterberg, E., Connelly, D., Statham, P., Fones, G. and German, C. (2008), 'The distribution and stabilisation of dissolved fe in deep-sea hydrothermal plumes', *Earth and Planetary Science Letters* **270**(3), 157–167.

Berelson, W. M., McManus, J., Coale, K. H., Johnson, K. S., Burdige, D., Kilgore, T., Colodner, D., Chavez, F., Kudela, R. and Boucher, J. (2003), 'A time series of benthic flux measurements from monterey bay, ca', *Cont. Shelf Res.* **23**, 457–481.

Berger, W. and Wefer, G. (1990), 'Export production: seasonality and intermittency, and paleoceanographic implications', *Global and Planetary Change* **3**(3), 245–254.

Boyd, P., Ibisanmi, E., Sander, S., Hunter, K. and Jackson, G. (2010), 'Remineralization of upper ocean particles: Implications for iron biogeochemistry', *Limnology and oceanography* **55**(3), 1271.

Boyd, P. W. and Ellwood, M. J. (2010), 'The biogeochemical cycle of iron in the ocean', *Nature Geosci* **3**(10), 675–682.

Boyle, E. (1997), 'What controls dissolved iron concentrations in the world ocean?–a comment', *Marine Chemistry* **57**(3), 163–168.

Boyle, E., Bergquist, B., Kayser, R. and Mahowald, N. (2005), 'Iron, manganese, and lead at hawaii ocean time-series station aloha: Temporal variability and an intermediate water hydrothermal plume', *Geochimica et Cosmochimica Acta* **69**(4), 933–952.

Boyle, E. and Jenkins, W. (2008), 'Hydrothermal iron in the deep western south pacific', *Geochimica et Cosmochimica Acta* **72**(12).

Brix, H., Gruber, N., Karl, D. and Bates, N. (2006), 'On the relationships between primary, net community, and export production in subtropical gyres', *Deep Sea Research Part II: Topical Studies in Oceanography* **53**(5), 698–717.

Broecker, W. (1974), 'No" a conservative water-mass tracer', *Earth and Planetary Science Letters* .

Broecker, W., Takahashi, T. and Takahashi, T. (1985), 'Sources and flow patterns of deepocean waters as deduced from potential temperature, salinity, and initial phosphate concentration', *Journal of Geophysical Research: Oceans (1978–2012)* **90**(C4), 6925–6939.

Bruland, K., Orians, K. and Cowen, J. (1994), 'Reactive trace metals in the stratified central north pacific', *Geochimica et Cosmochimica Acta* .

Bruland, K., Rue, E., Smith, G. and DiTullio, G. (2005), 'Iron, macronutrients and diatom blooms in the peru upwelling regime: brown and blue waters of peru', *Marine Chemistry* .

Burd, A. (2013), 'Modeling particle aggregation using size class and size spectrum approaches', *Journal of Geophysical Research: Oceans* .

Burd, A., Moran, S. and Jackson, G. (2000), 'A coupled adsorption–aggregation model of the poc/234th ratio of marine particles', *Deep Sea Research Part I: Oceanographic Research Papers* **47**(1), 103–120.

Chen, C. and Millero, F. (1986), 'Precise thermodynamic properties for natural waters covering only the limnological range', *Limnol. Oceanogr.;(United States)* **31**(3).

Coale, K. and Bruland, K. (1987), 'Oceanic stratified euphotic zone as elucidated by 234th: 238u disequilibria', *Limnol. Oceanogr* **32**(1), 189–200.

Coale, K., Fitzwater, S., Gordon, R., Johnson, K. and Barber, R. (1996), 'Control of community growth and export production by upwelled iron in the equatorial pacific ocean', *Nature* **397**, 621–624.

Coale, K. H., Johnson, K. S., Fitzwater, S. E., Gordon, R. M., Tanner, S., Chavez, F. P., Ferioli, L., Sakamoto, C., Rogers, P., Millero, F., Steinberg, P., Nightingale, P., Cooper, D., Cochlan, W. P., Landry, M. R., Constantinou, J., Rollwagen, G., Trasvina, A. and Kudela, R. (1996), 'A massive phytoplankton bloom induced by an ecosystem-scale iron fertilization experiment in the equatorial pacific ocean', *Nature* **383**(6600), 495–501.

Duce, R. and Tindale, N. (1991), 'Chemistry and biology of iron and other trace metals', *Limnol. Oceanogr* **36**(8), 1715–1726.

Dugdale, R. and Goering, J. (1967), 'Uptake of new and regenerated forms of nitrogen in primary productivity', *Limnol. Oceanogr* **12**, 196—206.

Dutay, J.-C., Jean-Baptiste, P., Campin, J.-M., Ishida, A., Maier-Reimer, E., Matear, R., Mouchet, A., Totterdell, I., Yamanaka, Y. and Rodgers, K. (2004), 'Evaluation of ocmip-2 ocean models' deep circulation with mantle helium-3', *Journal of Marine Systems* **48**(1), 15–36.

Dutkiewicz, S., Follows, M. J. and Bragg, J. G. (2009), 'Modeling the coupling of ocean ecology and biogeochemistry', *Global Biogeochem. Cycles* **23**(4), GB4017.

Dutkiewicz, S., Follows, M. and Parekh, P. (2005), 'Interactions of the iron and phosphorus cycles: A three-dimensional model study', *Global Biogeochem. Cycles* .

Dutkiewicz, S., Sokolov, A., Scott, J. and Stone, P. (2005), 'A three-dimensional ocean-seaice-carbon cycle model and its coupling to a two-dimensional atmospheric model: uses in climate change studies', *dspace.mit.edu* .

Elderfield, H. and Schultz, A. (1996), 'Mid-ocean ridge hydrothermal fluxes and the chemical composition of the ocean', *Annual Review of Earth and Planetary Sci.* **24**, 191–224.

Elrod, V., Berelson, W., Coale, K. and Johnson, K. (2004), 'The flux of iron from continental shelf sediments: A missing source for global budgets', *Geophys. Res. Lett.* **31**(12).

Falkowski, P., Ziemann, D., Kolber, Z. and Bienfang, P. (1991), 'Role of eddy pumping in enhancing primary production in the ocean'.

Farley, K., Maier-Reimer, E., Schlosser, P. and Broecker, W. (1995), 'Constraints on mantle 3he fluxes and deep-sea circulation from an oceanic general circulation model', *J. Geophys. Res.* **100**(B3), 3829–3839.

Field, C., Behrenfeld, M., Randerson, J. and Falkowski, P. (1998), 'Primary production of the biosphere: integrating terrestrial and oceanic components', *Science* **281**(5374), 237–240.

Foujols, M., Lévy, M., Aumont, O. and Madec, G. (2000), 'Opa 8.1 tracer model reference manual', *nora.nerc.ac.uk* p. 45.

Frogner, P., Gíslason, S. and Óskarsson, N. (2001), 'Fertilizing potential of volcanic ash in ocean surface water', *Geology* .
URL: *http://geology.gsapubs.org/content/29/6/487.short*

Garcia, H., Locarnini, R. A., Boyer, T., Antonov, J. I., Baranova, O. K., Zweng, M. M. and Johnson, D. R. (2010), 'World ocean atlas, 2009, volume 3: Dissolved oxygen, apparent oxygen utilization, and oxygen saturation', *NOAA Atlas NESDIS* **70**(3), 1–44.

Giarolla, E. (2005), 'The atlantic equatorial undercurrent: Pirata observations and simulations with gfdl modular ocean model at cptec', *Geophys. Res. Lett.* **32**(10), L10617.

Ginoux, P., Prospero, J., Torres, O. and Chin, M. (2004), 'Long-term simulation of global dust distribution with the gocart model: correlation with north atlantic oscillation', *Environmental Modelling & Software* **19**(2), 113–128.

Gislason, S., Hassenkam, T., Nedel, S., Bovet, N., Eiriksdottir, E., Alfredsson, H., Hem, C., Balogh, Z., Dideriksen, K. and Oskarsson, N. (2011), 'Characterization of eyjafjallajökull volcanic ash particles and a protocol for rapid risk assessment', *Proceedings of the National Academy of Sciences* **108**(18), 7307–7312.

Gledhill, M. and van den Berg, C. (1994), 'Determination of complexation of iron (iii) with natural organic complexing ligands in seawater using cathodic stripping voltammetry', *Marine Chemistry* **47**(1), 41–54.

Goldberg, E. (1954), 'Marine geochemistry 1. chemical scavengers of the sea', *The Journal of Geology* pp. 249–265.

Green, M., Aller, R., Cochran, J., Lee, C. and Aller, J. (2002), 'Bioturbation in shelf/slope sediments off cape hatteras, north carolina: the use of¡ sup¿ 234¡/sup¿ th, chl-¡ i¿ a¡/i¿, and br¡ sup¿¡/sup¿ to evaluate rates of particle and solute transport', *Deep Sea Research Part II: Topical Studies in Oceanography* **49**(20), 4627–4644.

Guo, L., Hung, C.-C., Santschi, P. and Walsh, I. (2002), '¡ sup¿ 234¡/sup¿ th scavenging and its relationship to acid polysaccharide abundance in the gulf of mexico', *Marine Chemistry* **78**(2), 103–119.

Henson, S., Lampitt, R. and Johns, D. (2012), 'Variability in phytoplankton community structure in response to the north atlantic oscillation and implications for organic carbon flux', *Limnology and oceanography* **57**(6), 1591.

Henson, S., Painter, S., Holliday, N. P., Stinchcombe, M. C. and Giering, S. L. (2013), 'Unusual subpolar north atlantic phytoplankton bloom in 2010: Volcanic fertilization or north atlantic oscillation?', *Journal of Geophysical Research: Oceans* **118**, 1–10.

Henson, S., Sanders, R., Madsen, E., Morris, P., Moigne, F. L. and Quartly, G. (2011), 'A reduced estimate of the strength of the ocean's biological carbon pump', *Geophys. Res. Lett.* **38**(4).

Homoky, W., John, S., Conway, T. and Mills, R. (2013), 'Distinct iron isotopic signatures and supply from marine sediment dissolution', *Nature communications* **4**, 2143.

Honeyman, B., Balistrieri, L. and Murray, J. (1988), 'Oceanic trace metal scavenging: the importance of particle concentration', *Deep Sea Research Part A. Oceanographic Research Papers* **35**(2), 227–246.

Honeyman, B. and Santschi, P. (1989), 'A brownian-pumping model for oceanic trace metal scavenging: Evidence from th isotopes', *Journal of Marine Research* **47**(4), 951–992.

Hutchins, D., DiTullio, G. and Bruland, K. (1993), 'Iron and regenerated production: Evidence for biological iron recycling in two marine environments', *Limnology and Oceanography* **38**(6), 1242–1255.

Ito, T. and Follows, M. (2005), 'Preformed phosphate, soft tissue pump and atmospheric co2', *Journal of Marine Research* **63**(4), 813–839.

Jackson, G. (1980), 'Phytoplankton growth and zooplankton grazing in oligotrophic oceans', *nature.com* **284**, 439–441.

Jenkins, W., Naveira, A., Schlosser, P., Lott, D. and Newton, R. (2007), 'Oceanic volcanic 3he: where is it going?', *AGU Fall Meeting* .

Jickells, T. and Spokes, L. (2002), 'Atmospheric iron inputs to the oceans, in the biogeochemistry of iron in seawater', *John Wiley, New York* **1**(1), 85–121.

Johnson, K., Gordon, R. and Coale, K. (1997), 'What controls dissolved iron concentrations in the world ocean?', *Marine Chemistry* **57**(3-4), 137–161.

Jones, M. and Gislason, S. (2008), 'Rapid releases of metal salts and nutrients following the deposition of volcanic ash into aqueous environments', *Geochimica et Cosmochimica Acta* **72**(15), 3661–3680.

Krauskopf, K. (1956), 'Factors controlling the concentrations of thirteen rare metals in sea-water', *Geochimica et Cosmochimica Acta* **9**(1), 1–B32.

Kuroda, Y. (2000), 'Variability of currents off the northern coast of new guinea', *Journal of oceanography* **56**(1), 103–116.

Lackner, K. (2003), 'A guide to co2 sequestration', *Science* **300**, 1677–1678.

Laes, A., Blain, S., Laan, P., Ussher, S., Achterberg, E. P., Treguer, P. and de Baar, H. J. W. (2007), 'Sources and transport of dissolved iron and manganese along the continental margin of the bay of biscay', *Biogeosciences* .

Lam, P., Ohnemus, D. and Marcus, M. (2012), 'The speciation of marine particulate iron adjacent to active and passive continental margins', *Geochimica et Cosmochimica Acta* **80**, 108–124.

Langmann, B. (2014), 'On the role of climate forcing by volcanic sulphate and volcanic ash', *Advances in Meteorology* **2014**(5), 1–17.

Langmann, B., Zakšek, K., Hort, M. and Duggen, S. (2010), 'Volcanic ash as fertiliser for the surface ocean', *Atmospheric Chemistry and Physics* **10**(8), 3891–3899.

Lauderdale, J. (2010), 'On the role of the southern ocean in the global carbon cycle and atmospheric co2 change', *Doctoral Thesis* pp. 1–280.

Lefèvre, N. and Watson, A. (1999), 'Modeling the geochemical cycle of iron in the oceans and its impact on atmospheric co2 concentrations', *Global Biogeochem. Cycles* **13**(3), 727–736.

Legendre, L. and Gosselin, M. (1989), 'New production and export of organic matter to the deep ocean: Consequences of some recent discoveries', *Limnology and oceanography* **34**(7), 1374–1380.

Liu, X. and Millero, F. (2002), 'The solubility of iron in seawater', *Marine Chemistry* **77**(1), 43–54.

Longhurst, A., Sathyendranath, S., Platt, T. and Caverhill, C. (1995), 'An estimate of global primary production in the ocean from satellite radiometer data', *Journal of Plankton Research* **17**(6), 1245–1271.

Luo, C., Mahowald, N. and Corral, J. D. (2003), 'Sensitivity study of meteorological parameters on mineral aerosol mobilization, transport, and distribution', *Journal of Geophysical Chemistry* .

Mackey, D., O'sullivan, J. and Watson, R. (2002), 'Iron in the western pacific: a riverine or hydrothermal source for iron in the equatorial undercurrent?', *Deep Sea Research Part I: Oceanographic Research Papers* **49**(5), 877–893.

Madec, G. (2008), 'Nemo ocean engine', *Note du Pole de modelisation* **27**.

Mahowald, N., Engelstaedter, S., Luo, C., Sealy, A., Artaxo, P., Benitez-Nelson, C., Bonnet, S., Chen, Y., Chuang, P. and Cohen, D. (2009), 'Atmospheric iron deposition: Global distribution, variability, and human perturbations*', *Annual Review of Marine Science* **1**, 245–278.

Mahowald, N., Muhs, D., Levis, S., Rasch, P., Yoshioka, M., Zender, C. and Luo, C. (2006), 'Change in atmospheric mineral aerosols in response to climate: Last glacial period, preindustrial, modern, and doubled carbon dioxide climates', *J. Geophys. Res.* **111**(D10), D10202.

Martin, J. (1990), 'Glacial-interglacial co2 change: The iron hypothesis', *Paleoceanography* **5**(1), 1–13.

Martin, J. and Fitzwater, S. (1988), 'Iron deficiency limits phytoplankton growth in the north-east pacific subarctic'.

Masotti, I., Moulin, C., Alvain, S., Bopp, L., Tagliabue, A. and Antoine, D. (2011), 'Large-scale shifts in phytoplankton groups in the equatorial pacific during enso cycles', *Biogeosciences* **8**(3), 539–550.

Mather, R., Reynolds, S., Wolff, G., Williams, R., Torres-Valdes, S., Woodward, E., Landolfi, A., Pan, X., Sanders, R. and Achterberg, E. (2008), 'Phosphorus cycling in the north and south atlantic ocean subtropical gyres', *Nature Geosci* **1**(7), 439–443.

Mayer, L. (1982*a*), 'Aggregation of colloidal iron during estuarine mixing: Kinetics, mechanism, and seasonality', *Geochimica et Cosmochimica Acta* **46**, 2527–2535.

Mayer, L. (1982*b*), 'Retention of riverine iron in estuaries', *Geochimica et Cosmochimica Acta* **46**, 1003–1009.

McGillicuddy, D. and Robinson, A. (1997), 'Eddy-induced nutrient supply and new production in the sargasso sea', *Deep Sea Research Part I: Oceanographic Research Papers* **44**(8), 1427–1450.

Mohamed, K., Steigenberger, S., Nielsdottir, M., Gledhill, M. and Achterberg, E. (2011), 'Dissolved iron (iii) speciation in the high latitude north atlantic ocean', *Deep Sea Research Part I: Oceanographic Research Papers* **58**(11), 1049–1059.

Moore, C. M., Mills, M. M., Achterberg, E. P., Geider, R. J., Laroche, J., Lucas, M. I., Mcdonagh, E. L., Pan, X., Poulton, A. J., Rijkenberg, M. J. A., Suggett, D. J., Ussher, S. J. and Woodward, E. M. S. (2009), 'Large-scale distribution of atlantic nitrogen fixation controlled by iron availability', *Nature Geosci* **2**(12), 867–871.

Moore, C., Mills, M., Arrigo, K., Berman-Frank, I., Bopp, L., Boyd, P., Galbraith, E., Geider, R., Guieu, C. and Jaccard, S. (2013), 'Processes and patterns of oceanic nutrient limitation', *Nature Geosci* .

Moore, J. and Braucher, O. (2008), 'Sedimentary and mineral dust sources of dissolved iron to the world ocean', *Biogeosciences* **5**(3), 631–656.

Moore, J., Doney, S., Glover, D. and Fung, I. (2001), 'Iron cycling and nutrient-limitation patterns in surface waters of the world ocean', *Deep Sea Research Part II:* **49**(1–3), 463–507.

Nielsdóttir, M., Moore, C., Sanders, R., Hinz, D. and Achterberg, E. (2009), 'Iron limitation of the postbloom phytoplankton communities in the iceland basin', *Global Biogeochem. Cycles* **23**(3).

Nozaki, Y., Horibe, Y. and Tsubota, H. (1981), 'The water column distributions of thorium isotopes in the western north pacific', *Earth and planetary science letters* **54**(2), 203–216.

Nyffeler, U., Li, Y.-H. and Santschi, P. (1984), 'A kinetic approach to describe trace-element distribution between particles and solution in natural aquatic systems', *Geochimica et Cosmochimica Acta* **48**(7), 1513–1522.

Painter, S., Henson, S., Forryan, A., Steigenberger, S., Klar, J., Stinchcombe, M. C., Rogan, N., Baker, A. R., Achterberg, E. P. and Moore, C. M. (2014), 'An assessment of the vertical diffusive flux of iron and other nutrients to the surface waters of the subpolar north atlantic ocean', *Biogeosciences* .
URL: *http://adsabs.harvard.edu/abs/2014BGeo...11.2113P*

Palter, J., Lozier, M., Sarmiento, J. and Williams, R. G. (2011), 'The supply of excess phosphate across the gulf stream and the maintenance of subtropical nitrogen fixation', *Global Biogeochemical Cycles* .

Parekh, P., Follows, M. and Boyle, E. (2005), 'Decoupling of iron and phosphate in the global ocean', *Global Biogeochem. Cycles* **19**(2).

Parekh, P., Follows, M. J. and Boyle, E. (2004), 'Modeling the global ocean iron cycle', *Global Biogeochem. Cycles* **18**(1), GB1002.

Paytan, A. and McLaughlin, K. (2007), 'The oceanic phosphorus cycle', *Chemical Reviews* **107**, 563–576.

Pelegri, J., Csanady, G. and Martins, A. (1996), 'The north atlantic nutrient stream', *Journal of oceanography* **52**(3), 275–299.

Pelegrí, J., Marrero-Díaz, A. and Ratsimandresy, A. (2006), 'Nutrient irrigation of the north atlantic', *Progress in Oceanography* **70**(2), 366–406.

Raven, J., Evans, M. and Korb, R. (1999), 'The role of trace metals in photosynthetic electron transport in o2-evolving organisms', *Photosynthesis research* **60**(2-3), 111–150.

Resplandy, L., Vialard, J., Lévy, M., Aumont, O. and Dandonneau, Y. (2009), 'Seasonal and intraseasonal biogeochemical variability in the thermocline ridge of the southern tropical indian ocean', *J. Geophys. Res.* **114**(C7), C07024.

Roussenov, V., Williams, R., Mahaffey, C. and Wolff, G. (2006), 'Does the transport of dissolved organic nutrients affect export production in the atlantic ocean?', *Global Biogeochem. Cycles* **20**(3).

Rue, E. and Bruland, K. (1997), 'The role of organic complexation on ambient iron chemistry in the equatorial pacific ocean and the response of a mesoscale iron addition experiment', *Limnology and oceanography* **42**(5), 901–910.

Santschi, P., Nyffeler, U., Li, Y. and O'Hara, P. (1986), 'Radionuclide cycling in natural waters: relevance of scavenging kinetics', *Sediments and Water Interactions* pp. 183–191.

Sarmiento, J. and Gruber, N. (2006), 'Ocean biogeochemical dynamics', *ocquim.qui.ufba.br* .

Savoye, N., Benitez-Nelson, C., Burd, A., Cochran, J., Charette, M., Buesseler, K., Jackson, G., Roy-Barman, M., Schmidt, S. and Elskens, M. (2006), '¡ sup¿ 234¡/sup¿ th sorption and export models in the water column: A review', *Marine Chemistry* **100**(3), 234–249.

Sawlan, J. and Murray, J. (1983), 'Trace metal remobilization in the interstitial waters of red clay and hemipelagic marine sediments', *Earth and planetary science letters* **64**(2), 213–230.

Schlosser, C., Klar, J., Wake, B., Snow, J. T., Honey, D. J., Woodward, E. M. S., Lohan, M. C., Achterberg, E. P. and Moore, C. M. (2014), 'Seasonal itcz migration dynamically controls the location of the (sub) tropical atlantic biogeochemical divide', *Proc. Natl. Acad. Sci. USA* .

Sedwick, P., Church, T., Bowie, A., Marsay, C., Ussher, S., Achilles, K., Lethaby, P., Johnson, R., Sarin, M. and McGillicuddy, D. (2005), 'Iron in the sargasso sea (bermuda atlantic timeseries study region) during summer: Eolian imprint, spatiotemporal variability, and ecological implications', *Global Biogeochem. Cycles* **19**(4).

Shaw, T., Gieskes, J. and Jahnke, R. (1990), 'Early diagenesis in differing depositional environments: The response of transition metals in pore water', *Geochimica et Cosmochimica Acta* **54**(5), 1233–1246.

Siegel, D., Maritorena, S., Nelson, N., Hansell, D. and Lorenzi-Kayser, M. (2002), 'Global distribution and dynamics of colored dissolved and detrital organic materials', *J. Geophys. Res.* **107**(C12), 3228.

Siegenthaler, U. and Sarmiento, J. (1993), 'Atmospheric carbon dioxide and the ocean', *Nature* **365**, 119–125.

Smith, K. (1978), 'Benthic community respiration in the nw atlantic ocean: in situ measurements from 40 to 5200 m', *Marine Biology* **47**, 337–347.

Soulsby, R. (1997), 'Dynamics of marine sands: a manual for practical applications', *Thomas Telford Books* .

Statham, P., German, C. and Connelly, D. (2005), 'Iron (ii) distribution and oxidation kinetics in hydrothermal plumes at the kairei and edmond vent sites, indian ocean', *Earth and planetary science letters* **236**(3), 588–596.

Stocker, T., Qin, D., Plattner, G.-K., Tignor, M., Allen, S., Boschung, J., Nauels, A., Xia, Y., Bex, V. and Midgley, P. (2013), 'Climate change 2013: The physical science basis. contribution of working group i to the fifth assessment report of the intergovernmental panel on climate change', *Cambridge University Press* .

Stohl, A., Prata, A., Eckhardt, S., Clarisse, L., Durant, A., Henne, S., Kristiansen, N., Minikin, A., Schumann, U. and Seibert, P. (2011), 'Determination of time-and height-resolved volcanic ash emissions and their use for quantitative ash dispersion modeling: the 2010 eyjafjallajökull eruption', *Atmospheric Chemistry and Physics* **11**(9), 4333–4351.

Stramma, L., Hüttl, S. and Schafstall, J. (2005), 'Water masses and currents in the upper tropical northeast atlantic off northwest africa', *J. Geophys. Res.* **110**(C12), C12006.

Stramma, L. and Schott, F. (1999), 'The mean flow field of the tropical atlantic ocean', *Deep Sea Research Part II: Topical Studies in Oceanography* **46**(1), 279–303.

Strzepek, R., Maldonado, M., Higgins, J., Hall, J., Safi, K., Wilhelm, S. and Boyd, P. (2005), 'Spinning the "ferrous wheel": The importance of the microbial community in an iron budget during the fecycle experiment', *Global Biogeochem. Cycles* **19**(4).

Suga, T. and Talley, L. (1995), 'Antarctic intermediate water circulation in the tropical and subtropical south atlantic', *Journal of Geophysical Research* .

Sullivan, R., Guazzotti, S., Sodeman, D. and Prather, K. (2007), 'Direct observations of the atmospheric processing of asian mineral dust', *Atmospheric Chemistry and Physics* **7**(5), 1213–1236.

Sunda, W. and Huntsman, S. (1995), 'Iron uptake and growth limitation in oceanic and coastal phytoplankton', *Marine Chemistry* **50**(1), 189–206.

Swift, J. (1984), 'The circulation of the denmark strait and iceland-scotland overflow waters in the north atlantic', *Deep Sea Research Part A. Oceanographic Research Papers* **31**(11), 1339–1355.

Tagliabue, A., Aumont, O. and Bopp, L. (2014), 'The impact of different external sources of iron on the global carbon cycle', *Geophys. Res. Lett.* .

Tagliabue, A., Bopp, L. and Aumont, O. (2009), 'Evaluating the importance of atmospheric and sedimentary iron sources to southern ocean biogeochemistry', *Geophys. Res. Lett.* **36**(13).

Tagliabue, A., Bopp, L., Dutay, J.-C., Bowie, A. R., Chever, F., Jean-Baptiste, P., Bucciarelli, E., Lannuzel, D., Remenyi, T., Sarthou, G., Aumont, O., Gehlen, M. and Jeandel, C. (2010), 'Hydrothermal contribution to the oceanic dissolved iron inventory: Supplementary material', *Nature Geosci* **3**(4), 252–256.

Tagliabue, A., Mtshali, T., Aumont, O., Bowie, A. R., Klunder, M. B., Roychoudhury, A. N. and Swart, S. (2012), 'A global compilation of dissolved iron measurements: focus on distributions and processes in the southern ocean', *Biogeosciences* **9**(6), 2333–2349.

Takahashi, T., Broecker, W. and Langer, S. (1985), 'Redfield ratio based on chemical data from isopycnal surfaces', *Journal of Geophysical Research: Oceans (1978–2012)* **90**(C4), 6907–6924.

Tarazona, J. and Arntz, W. (2001), 'The peruvian coastal upwelling system', *Coastal Marine Ecosystems of Latin America* **144**, 229–244.

Tegen, I., Werner, M., Harrison, S. and Kohfeld, K. (2004), 'Relative importance of climate and land use in determining present and future global soil dust emission', *Geophys. Res. Lett.* **31**(5).

Toggweiler, J., Gnanadesikan, A., Carson, S., Murnane, R. and Sarmiento, J. (2003), 'Representation of the carbon cycle in box models and gcms: 1. solubility pump', *Global Biogeochem. Cycles* **17**(1).

Toner, B., Fakra, S., Manganini, S., Santelli, C., Marcus, M., Moffett, J., Rouxel, O., German, C. and Edwards, K. (2009), 'Preservation of iron (ii) by carbon-rich matrices in a hydrothermal plume', *Nature Geosci* **2**(3), 197–201.

Turekian, K. (1977), 'The fate of metals in the oceans', *Geochimica et Cosmochimica Acta* **41**(8), 1139–1144.

Twining, B., Baines, S. and Fisher, N. (2004), 'Element stoichiometries of individual plankton cells collected during the southern ocean iron experiment(sofex)', *Limnology and oceanography* **49**(6), 2115–2128.

Volk, T. and Hoffert, M. (1985), 'Ocean carbon pumps: Analysis of relative strengths and efficiencies in ocean driven atmospheric co2 changes', *The Carbon Cycle and Atmospheric CO_2: Natural Variations Archean to Present* **32**, 99—110.

Weisberg, R. and Weingartner, T. (1988), 'Instability waves in the equatorial atlantic ocean', *Journal of Physical Oceanography* **18**(11), 1641.

Wen, L.-S., Santschi, P. and Tang, D. (1997), 'Interactions between radioactively labeled colloids and natural particles: Evidence for colloidal pumping', *Geochimica et Cosmochimica Acta* **61**(14), 2867–2878.

Williams, R. and Follows, M. (2003), Physical transport of nutrients and the maintenance of biological production, *in* M. Fasham, ed., 'Ocean Biogeochemistry', Global Change The IGBP Series (closed), Springer Berlin Heidelberg, pp. 19–51.

Williams, R., Roussenov, V. and Follows, M. (2006), 'Nutrient streams and their induction into the mixed layer', *Global Biogeochem. Cycles* **20**(1).

Wu, J., Boyle, E., Sunda, W. and Wen, L.-S. (2001), 'Soluble and colloidal iron in the oligotrophic north atlantic and north pacific', *Science* **293**(5531), 847–849.

Wu, J. and Luther III, G. (1995), 'Complexation of fe (iii) by natural organic ligands in the northwest atlantic ocean by a competitive ligand equilibration method and a kinetic approach', *Marine Chemistry* **50**(1), 159–177.

Yamamoto-Kawai, M., Carmack, E. and McLaughlin, F. (2006), 'Nitrogen balance and arctic throughflow', *Nature* .

Yang, Y., Liu, C., Hu, J. and Koga, M. (1999), 'Taiwan current (kuroshio) and impinging eddies', *Journal of oceanography* **55**, 609–617.

Ye, Y., Wagener, T., Völker, C., Guieu, C. and Wolf-Gladrow, D. (2011), 'Dust deposition: iron source or sink? a case study', *Biogeosciences* **7**, 9219–9272.

Ye, Y., Wagener, T., Völker, C., Guieu, C. and Wolf-Gladrow, D. A. (2010), 'Dust deposition: iron source or sink? a case study', *Biogeosciences Discussions* **7**(6), 9219–9272.

Yuan-Hui, L. (1981), 'Ultimate removal mechanisms of elements from the ocean', *Geochimica et Cosmochimica Acta* .

Zenk, W., Klein, B. and Schroder, M. (1991), 'Cape verde frontal zone', *Deep Sea Research Part A. Oceanographic Research Papers* **38**(1), S505–S530.

Zhu, X., Prospero, J., Millero, F., Savoie, D. and Brass, G. (1992), 'The solubility of ferric ion in marine mineral aerosol solutions at ambient relative humidities', *Marine Chemistry* **38**(1), 91–107.

Zhuang, G., Yi, Z., Duce, R. and Brown, P. (1992), 'Chemistry of iron in marine aerosols', *Global Biogeochem. Cycles* **6**(2), 161–173.